

Direct Photon Measurement in Proton-Proton and Deuteron-Gold Collisions

Meting van directe fotonen in proton-proton
en deuteron-goud botsingen

(met een samenvatting in het nederlands)

Proefschrift

ter verkrijging van de graad van doctor aan de Universiteit Utrecht
op gezag van de rector magnificus, prof. dr. J.C. Stoof, ingevolge het
besluit van het college voor promoties in het openbaar te verdedigen
op dinsdag 15 april 2008 des middags te 4.15 uur

door

Martinus Johannes Russcher

geboren op 20 januari 1980 te Gouda

Promotor: Prof. dr. T. Peitzmann

Co-promotor: Dr. A. Mischke

Dit werk maakt deel uit van het onderzoekprogramma van de Stichting voor Fundamenteel Onderzoek der Materie (FOM), die financieel wordt gesteund door de Nederlandse Organisatie voor Wetenschappelijk Onderzoek (NWO).

Contents

Introduction	1
1 Theoretical Background	5
1.1 Quantum Chromodynamics	6
1.1.1 Confinement versus Asymptotic Freedom	6
1.1.2 The Quark Gluon Plasma	8
1.1.3 Perturbative QCD and Factorization	11
1.2 Direct Photons	13
1.2.1 Prompt Photons at Next-to-Leading Order	14
1.2.2 Thermal Photon Production	15
1.2.3 Photons and Heavy Ion Collisions	19
2 Experiment	25
2.1 The Relativistic Heavy Ion Collider	25
2.2 The STAR Experiment	28
2.2.1 Time Projection Chamber	28
2.2.2 Barrel Electromagnetic Calorimeter	32
2.2.3 Barrel Shower Maximum Detector	38
2.2.4 Trigger Detectors	43
2.3 Data Acquisition	45
2.3.1 Trigger and DAQ	46
2.3.2 Data Sample	48
3 Data Analysis	51
3.1 Event Reconstruction	51
3.1.1 TPC Tracking and Vertex-finding	52
3.2 Event Selection	53
3.2.1 Beam Background	53
3.2.2 Vertex Position	55
3.2.3 Final Event Sample	55
3.3 Processing of BEMC Data	56

3.3.1	Noise Pedestals and Status Tables	57
3.3.2	Energy Calibration	58
3.3.3	Shower Reconstruction	60
3.4	Detector Simulation	66
3.4.1	GEANT	66
3.4.2	Detector Response Simulation	69
4	Neutral Pion Measurements	75
4.1	Raw Yield Extraction	75
4.1.1	Invariant Mass Spectra	76
4.1.2	Background Subtraction	78
4.2	Corrections	83
4.2.1	Corrections from a Single Particle Simulation	84
4.2.2	Acceptance	85
4.2.3	BEMC Trigger Efficiency	88
4.2.4	Photon Conversions	89
4.2.5	Simulated Mass Spectra and Energy Smearing	92
4.2.6	Pythia Studies	95
4.2.7	False Vetoes	98
4.2.8	Correction for Finite Bin Width	100
4.3	Results	101
4.3.1	Calculation of the Differential Cross Section	102
4.3.2	Neutral Pion Production in p+p and d+Au Collisions .	105
4.3.3	Systematic Uncertainties	109
5	Direct Photon Measurements	117
5.1	Inclusive Photons	119
5.1.1	Neutral Hadron Contamination	120
5.1.2	Background from Charged Particles	125
5.1.3	Photon Reconstruction Efficiency	127
5.2	Direct Photon Analysis	131
5.2.1	Double Ratio	131
5.2.2	Background from Hadronic Decays	132
5.2.3	Direct Photon Results	134
5.2.4	Systematic Uncertainties	137
6	Discussion	141
6.1	Neutral Pions in p+p Collisions	141
6.2	Nuclear Modification in d+Au collisions	147
6.3	Direct Photon Cross Sections	148
6.4	Comparison to Other Experiments	153

6.5 Outlook	159
Summary	165
Samenvatting	169
Acknowledgements	173
A Tabulated Results	175
B Coordinates and Kinematic Variables	179
C Neutral Pion Decay	183
D Acronyms	185
Bibliography	189

Introduction

The interest in studying collisions between ultra-relativistic heavy ions comes from the possibility to create a novel state of matter: the Quark Gluon Plasma (QGP). In ordinary matter, quarks and gluons are present only as bound states, mostly in terms of protons and neutrons. Quantum Chromodynamics, the theory of the strong interaction, predicts, however, that at extremely high temperature and density a transition will occur to the QGP. The quarks will decouple and can essentially behave as free particles, similar to electrons in an electromagnetic plasma. Cosmology states that the early universe, only a few microseconds after the Big Bang, was filled with a QGP. At present, the plasma might still form the very dense cores of neutron stars. The Relativistic Heavy Ion Collider (RHIC) at Brookhaven National Laboratory, NY provides collisions between heavy nuclei with the purpose of creating a QGP in the controlled environment of a laboratory.

One of the classical signatures of the QGP is the emission of thermally produced photons. The quarks in the plasma are in thermal equilibrium and will radiate photons, in some way similar to the light emitted by stars. The intensity of this radiation will then depend on the temperature of the matter. Since photons do not interact through the strong nuclear force, their mean free path is large compared to the size of the collision system. Therefore, the thermal photons can carry the information on the temperature of the plasma well outside the interaction region, which enables its detection. Obviously, the extraction of the thermal photon spectrum will require a detailed knowledge of all alternative sources of photons present in heavy ion collisions as well.

We have analyzed the photon production rates in proton-proton and deuteron-gold collisions. Both systems share multiple sources of photons with heavy ion collisions. However, the energy density reached in these reactions is too low to actually form a QGP and, consequently, thermal photons are not produced. The presented analysis constitutes a necessary baseline for the ultimate measurement of thermal photon production in heavy ion collisions.

The largest background in our analysis was caused by photons from decaying hadrons, in particular, by the process where a neutral pion decays into two photons. We have aimed to measure so called direct photons representing those photons which do not originate from such hadronic decays. Hence, the crucial first step was a measurement of the neutral pion yields. Although, in principal, the latter can be looked at as intermediate results, we will show how they have an interest of their own as well.

Outline

The first chapter of this thesis presents a summary of the theory of the strong interaction and the physics of the Quark Gluon Plasma. In addition, the concepts of perturbative Quantum Chromodynamics are introduced as we will make extensive use of its predictions in our discussion of the final results. The chapter concludes with a description of different sources of direct photons, particularly in the context of heavy ion collisions.

The experimental setup of the Solenoidal Tracker At RHIC (STAR) is the main subject of chapter 2. The focus is on the properties of the electromagnetic calorimeter and the shower maximum detector since the measurements with those detectors constitute the foundation of our analysis. After a brief overview of the data acquisition system at STAR, the conversion of the raw data to physical quantities is described in chapter 3. The framework which was used to simulate the response of the various detector components is treated there as well.

Chapters 4 and 5 present the techniques which were applied to reconstruct the neutral pion and direct photon spectra. This part explains the details of the analysis, including the necessary corrections and the evaluation of the systematic uncertainties. An accurate study of the latter turns out to be essential for a measurement of direct photons. Hence, the last sections of both chapters are exclusively devoted to this subject.

The final results on direct photon and neutral pion production will be presented in chapter 6. It includes a discussion of our main results in view of current theoretical calculations, as well as a comparison to results obtained by other experiments. The last part of this thesis contains an outlook to future direct photon analyses at STAR, especially when performed within the environment of ultra-relativistic heavy ion collisions.

The numerical data corresponding to our final results are given in terms of dedicated tables in appendix A. The general coordinate system of the detector is described in appendix B, along with frequently used kinematic variables. The decay process of a neutral pion into two photons plays a central role in the presented analysis and some aspects of the corresponding

kinematics are therefore discussed in appendix C. Finally, we hope to improve the readability of this thesis by including appendix D which lists most of the acronyms that will be introduced in the various chapters.

Chapter 1

Theoretical Background

The standard model of elementary particles is one of the most accurate fundamental theories in physics. It is a quantum field theory which reconciles the principles of quantum mechanics and special relativity in its description of elementary particles and their interactions. The standard model can be divided into two sectors:

- *electroweak*: the spontaneously broken $SU(2) \times U(1)$ gauge theory describing the electromagnetic and the weak nuclear force
- *strong*: the unbroken $SU(3)$ gauge theory corresponding to the strong nuclear force

The electroweak sector provides a unifying description of the electromagnetic and weak nuclear force between leptons and quarks in terms of four gauge particles: the electromagnetically charged W^+ and W^- , and the neutral Z and γ bosons. The standard model has been extremely successful as many of its predictions were confirmed by experiment with an astonishing precision.

The strong nuclear force manifests itself between particles which carry a quantum degree of freedom called color charge. In this case the corresponding gauge bosons are massless gluons (g) which not only couple to the color-charged quarks (q) but also interact among themselves. The latter gives Quantum Chromodynamics (QCD¹), the quantum field theory of the strong interaction, the characteristic features which will be discussed below. An extensive treatment of the principles of quantum field theory can be found in, e.g., [1, 2].

¹To improve readability, we have included appendix D which lists most acronyms used in this thesis.

1.1 Quantum Chromodynamics

Analogously to the theory of Quantum Electrodynamics (QED), the Lagrangian of QCD is given by

$$\mathcal{L} = -\frac{1}{4}(F_{\mu\nu}^a)^2 + \bar{\psi}(i\not{D} - m)\psi, \quad (1.1)$$

where the field strength tensor is defined as

$$F_{\mu\nu}^a = \partial_\mu A_\nu^a - \partial_\nu A_\mu^a + g_s f^{abc} A_\mu^b A_\nu^c, \quad (1.2)$$

and the covariant derivative

$$D_\mu = \partial_\mu - ig_s A_\mu^a t^a. \quad (1.3)$$

The tensors A_μ^a represent the gluon fields, similar to the photon field A_μ in QED, and the additional index a labels their color configuration. The structure constants of the group $SU(3)$ are denoted by f^{abc} and they are defined by the commutators of the Gell-Mann matrices t^a . In equation 1.1, the inner product of the covariant derivative with the Dirac matrices γ_μ is written as \not{D} . The strength of the color coupling is given by g_s . The fermion fields ψ have three color states: red (r), green (g), and blue (b). These fields represent the quarks of which currently 6 species are known to exist. The lightest and most common quarks are called *up* and *down*, and have a fractional electrical charge equal to $\frac{2}{3}$ and $-\frac{1}{3}$, respectively. The gluons carry one unit of color and one unit of anti-color, and form an octet of symmetric and antisymmetric color wave functions, such as

$$\frac{1}{\sqrt{2}}(r\bar{g} + g\bar{r}) \quad \text{and} \quad \frac{1}{\sqrt{2}}(b\bar{g} - g\bar{b}).$$

The Feynman rules of QCD can be derived from the Lagrangian above. The self-coupling of the gluons is a direct result of the non-vanishing structure constants f_{abc} of a non-Abelian gauge group, in this case the group $SU(3)$. Consequently, the QCD Lagrangian contains terms which are of third and fourth order in the gauge field A_μ^a , corresponding to three- and four-gluon interaction vertices.

1.1.1 Confinement versus Asymptotic Freedom

Although QCD predicts the existence of quarks and gluons, these particles have never been directly observed. All hadrons in fact appear to be color singlets, composed of quarks whose color charges cancel (e.g. $r\bar{r}$ or rgb). This

phenomenon is known as confinement of color and its mechanism is an integral part of any non-Abelian gauge theory with a sufficiently large coupling constant [3]. It has been demonstrated that an infinite amount of energy would be required to break up a singlet state into its colored components.

The coupling constant which appears in the QCD Lagrangian can be written as

$$g_s = \sqrt{4\pi\alpha_s} \quad (1.4)$$

where α_s is the analogue of the electromagnetic fine structure constant $\alpha = \frac{1}{137}$. It evolves according to a renormalization group equation, similar to the running of α in QED, and its dependence on the renormalization scale μ_R is given by:

$$\alpha_s(\mu_R^2) = \frac{\alpha_s(\mu_0^2)}{1 + \frac{\alpha_s(\mu_0^2)}{4\pi} \left(\frac{11}{3}N - \frac{2}{3}n_f\right) \ln(\mu_R^2/\mu_0^2)}, \quad (1.5)$$

for a $SU(N)$ gauge theory (i.e. N colors), n_f equal to the number of quark flavors, and μ_0 a reference point of the renormalization procedure. In case of 3 colors and defining $b_0 = 11 - 2n_f/3$, equation 1.5 is often rearranged as

$$\alpha_s(\mu_R^2) = \frac{2\pi}{b_0 \ln(\mu_R/\Lambda_{\text{QCD}})} \quad (1.6)$$

such that

$$1 = \frac{g_s^2 b_0}{8\pi^2} \ln(\mu_0/\Lambda_{\text{QCD}}) \quad (1.7)$$

with $\Lambda_{\text{QCD}} \sim 300$ MeV, the universal QCD scale which has to be determined from experiment.

When probed at small momenta or, equivalently, large distances, α_s becomes large and Feynman's diagrammatic perturbation theory, which is based on an expansion in α_s , cannot be applied. The coupling of QCD indeed contains a singularity as $\mu_R \rightarrow \Lambda_{\text{QCD}}$ in equation 1.6, which marks the lower limit of the perturbative regime. Nevertheless, the properties of the theory in this regime can be studied with an approximation known as lattice QCD. In this approximation the path integral approach of the continuum gauge theory presented above is replaced by a discrete expression which can be numerically evaluated on a four-dimensional Euclidean lattice.

The opposite limit, where $\mu_R \rightarrow \infty$, corresponds to large momenta and equation 1.5 implies that $\alpha_s(\mu_R^2) \rightarrow 0$, provided that n_f is not too large. This behavior of α_s is called asymptotic freedom and it makes it possible to evaluate the dynamics of the strong interaction with perturbation theory. The latter is essential for the derivation of the scattering cross sections, presented in sections 1.1.3 and 1.2, which we will use for the interpretation of our measurements in chapter 6.

1.1.2 The Quark Gluon Plasma

Ordinary matter consists of quarks and gluons, confined into hadrons by the strong nuclear force. However, lattice QCD predicts that at sufficiently high temperature and density a transition occurs to a phase where quarks and gluons are essentially free. This state of matter is the Quark Gluon Plasma (QGP). It is expected that the QGP existed in the early universe and that it might be present inside the dense cores of neutron stars. A thorough treatment of the physics of the QGP, including aspects of lattice QCD, can be found in [4, 5]. For the most recent developments of the field we refer to [6].

The scientific motivation to study the QGP is related to two key features of this exotic state of matter:

- *deconfinement*: the hadron wave functions in the plasma overlap and the color degrees of freedom manifest themselves over volumes larger than the size of hadrons
- *chiral symmetry restoration*: the (approximate) symmetry of the QCD Lagrangian between quarks with positive and negative chirality is restored

The latter is of particular interest as the spontaneous breaking of this symmetry is responsible for most of the visible mass in our universe.

Since the interaction with gluons leaves helicity unaltered, the chiral symmetry of the QCD Lagrangian for massless quarks leads to the conservation of helicity. It is known that quarks have a small though finite mass and this symmetry is explicitly broken. More specifically, the mass parameters of the two lightest quarks, the up and down quark, are equal to a few MeV/c^2 . However, the mass of the proton, a bound state of three quarks, is approximately equal to $1 \text{ GeV}/c^2$. The mechanism associated with the generation of these constituent quark masses is a spontaneous breaking of the chiral symmetry.

The ground state of QCD has a non-vanishing expectation value

$$\langle 0 | \bar{\psi} \psi | 0 \rangle = \langle 0 | \bar{\psi}_L \psi_R + \bar{\psi}_R \psi_L | 0 \rangle \neq 0, \quad (1.8)$$

where ψ_R denotes the field operator for the creation of a right-handed quark. The QCD vacuum thus contains $q\bar{q}$ pairs and a quark which propagates through this chiral condensate can have its helicity altered, as if it has a finite mass. The rate at which this happens is proportional to the vacuum expectation value in equation 1.8.

Over recent years much insight into the properties of the QGP has been gained from thermodynamic calculations on the lattice. To illustrate this, we consider the simplified picture where the QGP is an ideal gas of massless noninteracting quarks and gluons with the net baryon number equal to zero. The pressure P is then related to the temperature T of the plasma by

$$P = g_{\text{total}} \frac{\pi^2}{90} T^4, \quad (1.9)$$

and the energy density is given by

$$\epsilon = g_{\text{total}} \frac{\pi^2}{30} T^4. \quad (1.10)$$

In these equations, g_{total} represents the total degeneracy number of the quarks and gluons as a result of all possible flavors, spin states, and colors. The degrees of freedom associated with the color charges are absent in a gas of hadrons. A characteristic phase transition therefore occurs when the temperature of a gas of hadrons becomes larger than some critical temperature T_c .

Figure 1.1 shows results from lattice QCD calculations of the pressure as a function of the temperature of strongly interacting matter [7]. The individual curves represent different configurations of the QGP, namely, two and three flavors, two light and one heavier quark, and a pure $SU(3)$ gauge theory. The arrows indicate the results obtained in case of an ideal Stefan-Boltzmann gas. The curves indeed exhibit a sudden increase of the pressure (divided by T^4) when the temperature of the system exceeds T_c .

Figure 1.2 shows a sketch of the phase diagram of QCD matter in terms of the temperature and the baryon chemical potential μ . The dashed curve illustrates the region where the transition to the plasma phase is expected to be a continuous crossover and the full curve corresponds to a first order phase transition. The critical temperature near $\mu = 0$, which is close to the conditions of matter produced in collisions at RHIC, is approximately 170 MeV. However, the critical baryon chemical potential μ_c , which marks the region of the phase transition at the lowest temperatures, is poorly known.

The detailed exploration of the phase diagram of QCD matter has been the primary goal of many nuclear collision experiments over the past 20 years. In sections 1.2.2 and 1.2.3 we will discuss how a study of direct photon production in heavy ion collisions could contribute to this effort.

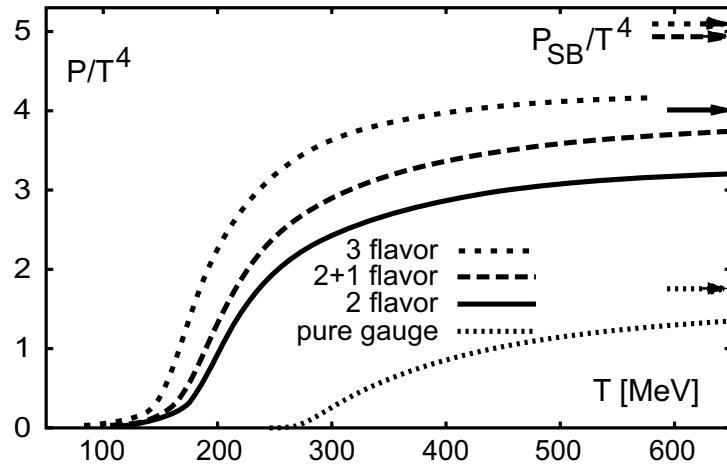


Figure 1.1: The pressure P , divided by the nominal T^4 dependence, of QCD matter as a function of the temperature of the system. The curves are results from lattice QCD calculations (see text) and the arrows indicate the results in case of a Stefan-Boltzmann gas (see equation 1.9).

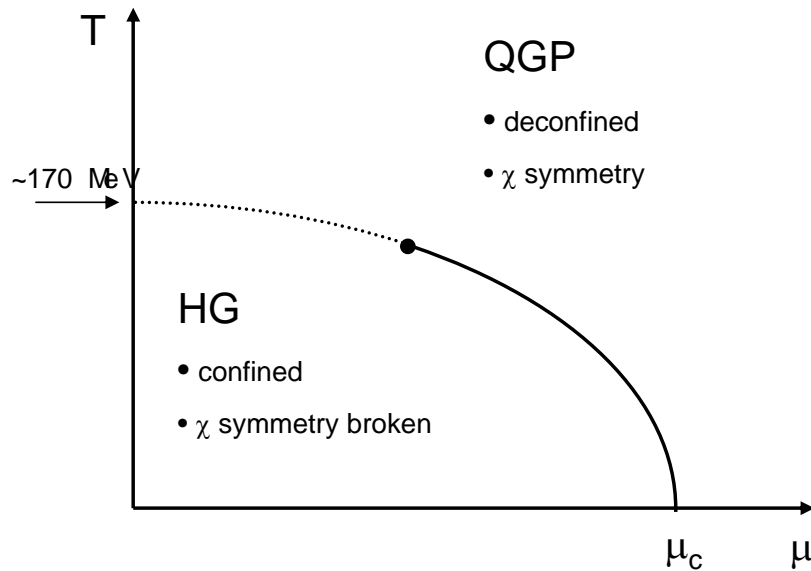


Figure 1.2: The phase diagram of QCD matter. It shows the hadron gas (HG) phase and the QGP phase, as a function of temperature T and baryon chemical potential μ . The variables T_c and μ_c mark the critical temperature and chemical potential, respectively.

1.1.3 Perturbative QCD and Factorization

In the regime of large momentum transfers the use of perturbative QCD² (pQCD) is validated by the phenomenon of asymptotic freedom. However, more is needed to calculate physical quantities, such as differential cross sections, and meaningfully compare those to measurements. Confinement restricts the quarks into hadrons and experimental tests of QCD therefore involve the interaction and detection of hadrons, e.g. protons or pions, instead of quarks. The actual mechanism which binds the quarks is governed by non-perturbative effects which are, at least up till now, not well understood.

The concept of factorization in pQCD is that for a large class of physical observables the long-distance and the short-distance dynamics can be separated in a universal way. Qualitatively, this means that the collision of hadrons can be related to a perturbatively calculable scattering of partons. The non-perturbative effects are then isolated from the hard scattering, independent of the particular partonic process which is treated.

To illustrate the above, consider inclusive single-particle production of a hadron C in a collision between the hadrons A and B :

$$A + B \rightarrow C + X. \quad (1.11)$$

When we denote the energy and momentum of the hadron in the final state by E and p , respectively, the factorized cross section of this process can be written as

$$\begin{aligned} E \frac{d^3\sigma}{d^3p} &= \sum_{abcd} \int dx_a dx_b dz_c \phi_{a/A}(x_a, \mu_I^2) \phi_{b/B}(x_b, \mu_I^2) \\ &\times \frac{s}{\pi z_c^2} \frac{d\hat{\sigma}}{dt}(\mu_I, \mu_R, \mu_F) \frac{D_{C/c}(z_c, \mu_F^2)}{\pi z_c} \delta(s + t + u) \end{aligned} \quad (1.12)$$

with the factor $d\hat{\sigma}/dt$ equal to the hard scattering cross section at the parton level, $a + b \rightarrow c + d$, and s , t , and u the corresponding Mandelstam variables (see appendix B). The sum runs over all the flavors, including gluons, of the incoming and outgoing partons. The parton density function (PDF) $\phi_{a/A}(x_a)$ gives the probability to find a parton of flavor a in hadron A with a fraction x_a of the longitudinal momentum of the hadron, and similar for $\phi_{b/B}(x_b)$. The fragmentation function $D_{C/c}(z_c)$ represents the probability that the hadronization of the outgoing parton c results in a collinear hadron C with a momentum fraction z_c with respect to the parton. The momentum scales μ_R , μ_I , and μ_F are the renormalization, the initial state factorization,

²See, for example, the review in [8].

and the final state factorization scale, respectively. The scale μ_F will also be referred to as the fragmentation scale.

At higher orders in perturbation theory, singularities will be encountered when evaluating the scattering amplitude of the partonic process $d\hat{\sigma}/dt$. For example, when an outgoing quark emits a gluon nearly collinear to its own momentum. The factorization theorem states that these collinear divergences factorize up to all orders in α_s and can be absorbed in the fragmentation functions. Similar arguments hold for the parton distribution functions with respect to initial state radiation. The partonic scattering amplitude then is an infrared and collinear safe quantity which depends on the specific choice of μ_I and μ_F . As such, it no longer contains any long-distance effects and, in particular, it is independent of the specific hadrons involved in the interaction.

The parton densities $\phi_{a/A}$ and $\phi_{b/B}$, and the fragmentation function $D_{C/c}$, which appear in equation 1.12, incorporate all the sensitivity to infrared and collinear processes which was present in the original cross section. They depend on the specific hadron, the factorization scales μ_I and μ_F , but by no means on the actual partonic process $d\hat{\sigma}/dt$. The latter corresponds to the aspect of universality which allows to determine these functions in one process and use the result in any other process.

Fortunately, the dependence of the parton densities and fragmentation functions on their respective scales, μ_I and μ_F , can be calculated perturbatively. In case of the parton distribution $\phi_{i/h}$ for parton i in a hadron h , for example, this evolution is described by a set of integro-differential equations, the DGLAP equations [9], as

$$\mu_I^2 \frac{d}{d\mu_I^2} \phi_{i/h}(x, \mu_I) = \sum_j \int_x^1 \frac{d\xi}{x} P_{ij}(x/\xi) \phi_{j/h}(\xi, \mu_I) \quad (1.13)$$

where the sum runs over all flavors, including the gluon, and the $P_{ij}(x/\xi)$ are splitting functions, derived from the amplitude of the process where a parton of type j emits a parton i . Note that each of the functions in the above equation depends on the scale μ_R as well, through the evolution of the strong coupling α_s as given by equation 1.5.

Ideally, the parton densities are determined from an experiment where x and μ_I can be accurately constrained. Note that in particular the deep-inelastic scattering (DIS) of an electron on a proton is suitable for this purpose. Subsequently, the measured distributions are parametrized and evolved to different values of μ_I using the DGLAP equations. Likewise, the initial parameterizations of the fragmentation functions are based on experimental observations at a given scale μ_F . Their evolution with μ_F can be calculated

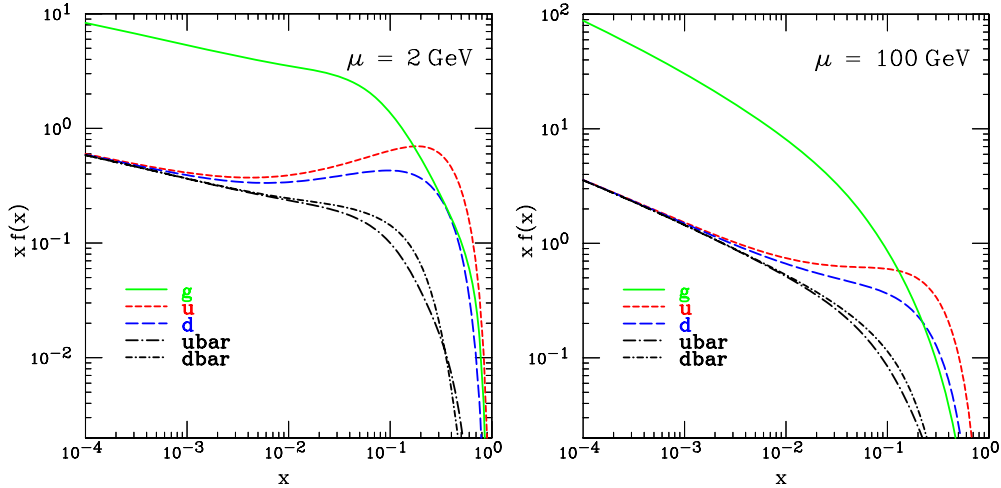


Figure 1.3: Parton density functions from the CTEQ collaboration shown for two different factorization scales: $\mu_I = 2 \text{ GeV}/c$ (left) and $\mu_I = 100 \text{ GeV}/c$ (right). The figures were taken from [10].

perturbatively as well, using a similar set of evolution equations, as discussed in e.g. [11] and [12]. Figure 1.3 shows the parton distribution functions of the proton for two different momentum scales μ . These parameterizations were obtained by the CTEQ collaboration in a global QCD analysis of interactions such as DIS, Drell-Yan scattering, and inclusive jet production in proton-antiproton collisions [10].

The formalism introduced in this section provides the necessary tools to determine the differential cross sections of inclusive neutral pion production in p+p collisions at next-to-leading order (NLO) accuracy. Furthermore, we will discuss the calculation of direct photon production at next-to-leading order below. In chapter 6, we will use these calculations in our discussion of the final experimental results.

1.2 Direct Photons

In this thesis direct photons are defined as those photons which are directly produced by the scattering of charged particles and do not originate from hadronic decays. At the Born level $\mathcal{O}(\alpha\alpha_s)$, the scattering processes which generate direct photons are given by the Feynman diagrams in figure 1.4. The left diagram represents quark-gluon Compton scattering and the right diagram shows the quark-antiquark annihilation process³

³The Feynman diagrams in this thesis were generated with the Axodraw package [13].

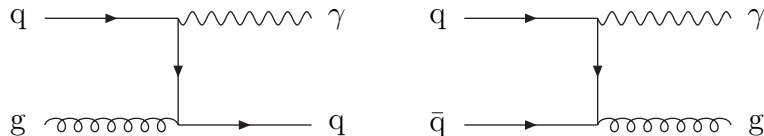


Figure 1.4: Born level diagrams for direct photon production. The left diagram represents quark-gluon Compton scattering, the right quark-antiquark annihilation.

At higher orders in perturbation theory, the photons which are produced in the fragmentation process of an outgoing parton should also be considered. The perturbative scattering mechanism, at lowest order given by the Feynman diagrams in figure 1.4, and the fragmentation component constitute the source of what is often referred to as prompt photons. The calculation of the pQCD cross section for prompt photon production at next-to-leading order will be the subject of the next section. Additional sources of direct photons are expected to be present in the hot and dense matter which exists shortly after the collision of ultra-relativistic heavy ions. These thermally produced photons will be discussed in section 1.2.2. Finally, all separate mechanisms of direct photon production will come together in the context of heavy ion collisions in section 1.2.3.

1.2.1 Prompt Photons at Next-to-Leading Order

At next-to-leading order in α_s , there is no clear distinction between the prompt photons which are directly produced and the contribution from the fragmentation of the outgoing partons. When calculating the NLO diagrams for prompt photon production, collinear singularities will be encountered which are then absorbed in the parton-to-photon fragmentation functions. Only the sum of these two components is a physical quantity, the separate contributions have a non-vanishing dependence on the chosen regularization scheme ($\overline{\text{MS}}$ in this thesis) as well as on the fragmentation scale μ_F .

Consider the two diagrams in figure 1.5. The left diagram is an example of a Bremsstrahlung process and is part of the NLO pQCD corrections to the Born diagrams in the previous section. The production of a collinear photon by the fragmentation of an outgoing quark is shown on the right. Note that the distinction between these topologies indeed disappears when the Bremsstrahlung photon is emitted parallel to the quark. The NLO expression of the direct component of prompt photon production can be found in [14, 15, 16] and that of the fragmentation component in [17, 18].

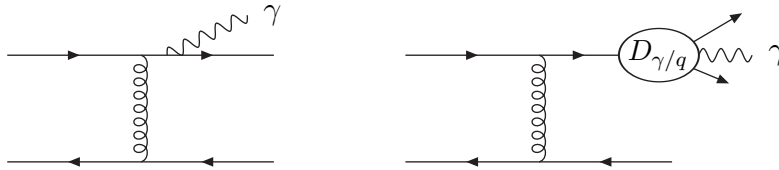


Figure 1.5: Examples of Bremsstrahlung (left) and fragmentation (right) photon contribution to direct photon production at next-to-leading order.

In figure 1.6, the results from a complete NLO calculation of the prompt photon differential cross section are shown as a function of transverse momentum p_T [19]. These curves were obtained by a calculation where the scales were chosen such that $\mu_I = \mu_R = \mu_F$ and the value of the common scale is equal to μ . Figure 1.7 shows the relative size of the fragmentation component $D_{\gamma/q}$ to the total cross section. Even though it appears as a higher order process ($\mathcal{O}(\alpha\alpha_s^2)$), the fragmentation photons significantly contribute over the entire p_T range considered here. This is a consequence of the anomalous behavior of $D_{\gamma/q}$ which yields a term $\sim \ln(p_T^2/\Lambda_{\text{QCD}}^2)$ from the integral over the momentum of the radiating quark [20]. From equation 1.6 it is clear that this collinear logarithm effectively cancels the additional factor of α_s in the hard scattering amplitude. The final contribution from fragmentation is therefore $\mathcal{O}(\alpha\alpha_s)$ which is the leading order in the calculation.

1.2.2 Thermal Photon Production

The quarks in a QGP will emit photons similar to, for instance, the thermal radiation produced by stellar objects. However, we will consider these thermal photons in the context of the hot and dense matter produced in ultra-relativistic heavy ion collisions. The possible formation of a QGP after such a collisions occurs in a volume which is small compared to the mean free path of the photon. Hence, contrary to the light emitted by stars, these thermal photons are not thermalized themselves.

At leading order in perturbation theory, the production mechanism of direct photons in the QGP is again given by the Born diagrams in figure 1.4. The energy of the quarks and gluons in an equilibrated plasma is distributed according to

$$n_F(E) = \frac{1}{e^{E/T} + 1} \quad \text{and} \quad n_B(E) = \frac{1}{e^{E/T} - 1}, \quad (1.14)$$

the Fermi-Dirac and Bose-Einstein distributions, respectively, in the limit of a vanishing chemical potential. Convoluting the matrix elements of the two

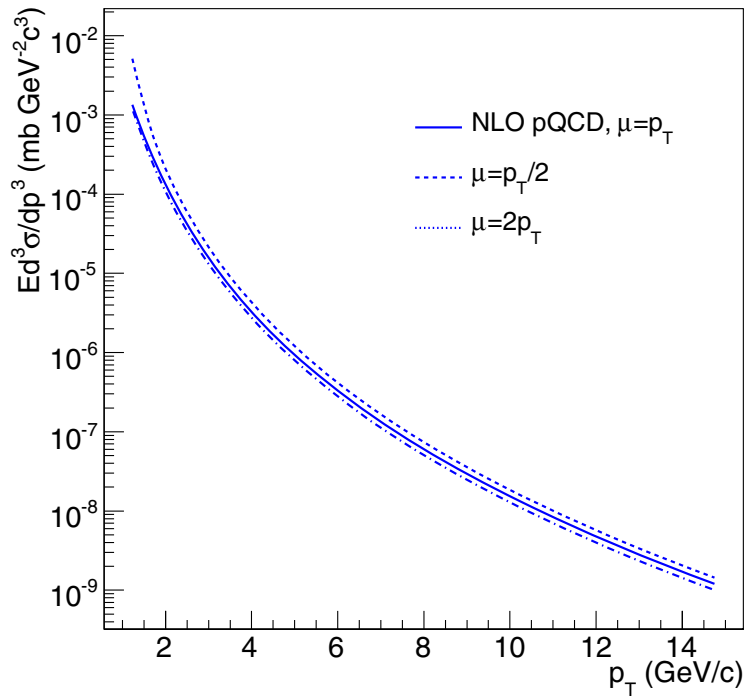


Figure 1.6: Prompt photon cross section in p+p collisions at next-to-leading order. The different curves correspond to alternative choices of the common scale [19].

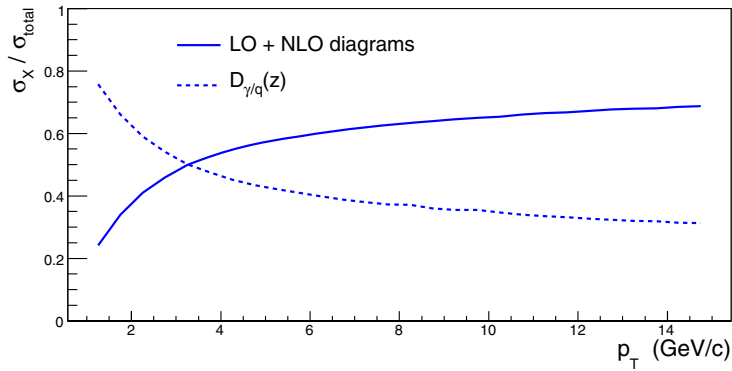


Figure 1.7: The relative contribution of the fragmentation process ($D_{\gamma/q}$) and the pQCD hard scattering process to the total prompt photon cross section. Both contributions are shown as a function of the p_T of the produced photon [19].

elementary photon production processes with these thermal distributions, the following expressions were derived [21, 22] for the photon production rate per unit volume R :

$$E \frac{dR}{d^3p}(\text{qg} \rightarrow \gamma\text{q}) = \frac{5}{9} \frac{\alpha\alpha_s}{6\pi^2} T^2 e^{-E/T} \left\{ \ln \frac{4ET}{k_c^2} + 0.0460 \right\} \quad (1.15)$$

$$E \frac{dR}{d^3p}(\text{q}\bar{\text{q}} \rightarrow \gamma\text{g}) = \frac{5}{9} \frac{\alpha\alpha_s}{3\pi^2} T^2 e^{-E/T} \left\{ \ln \frac{4ET}{k_c^2} - 2.1472 \right\}. \quad (1.16)$$

In these equations, E and p are the energy and momentum of the radiated photon, and T is the temperature of the matter. We will assume, here and in what follows, that E is large with respect to the temperature of the system. The parameter k_c satisfies $T^2 \gg k_c^2 > 0$ and regulates the divergence which occurs when the Mandelstam variables u and t approach zero.

An alternative derivation of the photon production rate in the QGP comes from field theory at finite temperature. It has been shown [23] that

$$E \frac{dR}{d^3p} = -\frac{1}{(2\pi)^3 E} \frac{1}{e^{E/T} - 1} \text{Im} \Pi_\mu^\mu(E) \quad (1.17)$$

where $\text{Im} \Pi_\mu^\mu$ equals the imaginary part of the contracted photon polarization tensor, also known as its self-energy. The two diagrams on the left in figure 1.8 illustrate how the leading order diagrams of direct photon production in vacuum follow from $\Pi^{\mu\nu}$ in combination with the appropriate cutting rules. The $\mathcal{O}(\alpha\alpha_s^2)$ Bremsstrahlung and inelastic pair annihilation $\text{qq}\bar{\text{q}} \rightarrow \gamma\text{q}$ processes have been shown to contribute effectively at the same order as a result of the enhanced emission of collinear photons. The expressions for the photon rate in equations 1.15 and 1.16 are therefore incomplete. The definition in equation 1.17, however, is exact up to all orders in α_s and up to the first order in α .

It was argued that at finite temperature the vacuum propagators and vertices, as shown in figure 1.5 for example, should be replaced by expressions which incorporate the effects of the medium[24]. An example of a diagram which should be included for the evaluation of the in-medium polarization tensor is shown in figure 1.8 (c). The filled circle indicates an effective quark propagator which is obtained from a Schwinger-Dyson resummation of diagrams, up to all orders in the coupling constant, containing a single hard loop:

$$\text{---} \bullet \text{---} = \text{---} \rightarrow \text{---} + \text{---} \rightarrow \bullet \text{---} \quad (1.18)$$

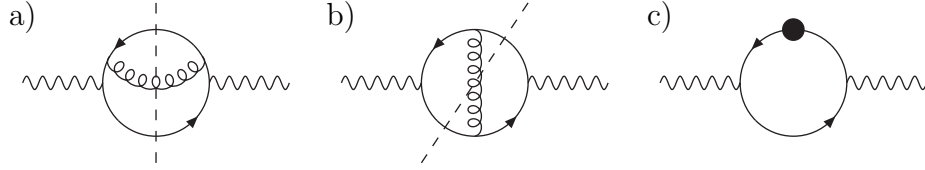


Figure 1.8: Feynman diagrams contributing to the photon polarization tensor $\Pi^{\mu\nu}$ in vacuum (a,b) and an example of a diagram containing a resummed quark propagator in the HTL formalism (c). The dashed lines illustrate how the use of cutting rules yields the $\mathcal{O}(\alpha\alpha_s)$ topologies as given by figure 1.4

This effective theory is used to replace the vacuum perturbation theory in case of soft or thermal quark momenta. Hence, it is referred to as the Hard-Thermal-Loop (HTL) formalism.

In the calculation of the HTL photon rate, the soft regime is separated from the hard regime by a momentum scale q_c which satisfies $g_s T \ll q_c \ll T$. When the quark momentum is larger than q_c , the vacuum approach is used and the parameter k_c in equations 1.15 and 1.16 is replaced by q_c . In case that the momentum is smaller than q_c , the HTL resummation technique is used resulting in a medium-modified expression for $\Pi^{\mu\nu}$ and a corresponding photon production rate. The IR divergence disappears since the quark acquires a thermal mass as a result of the collective behavior of the hot medium, as expressed by the diagrams in equation 1.18. The final result then is no longer dependent on the separation scale q_c .

The exact 1-loop HTL calculation has to be carried out numerically and results in a photon rate, in the specific case of two quark flavors, given by

$$E \frac{dR}{d^3p} = \frac{5}{9} \frac{\alpha\alpha_s}{2\pi^2} T^2 e^{-E/T} \left\{ \ln \frac{2.912}{g_s^2} \frac{E}{T} \right\}. \quad (1.19)$$

By comparing the above formula to those in equations 1.15 and 1.16 it appears that the IR cutoff scale k_c is effectively replaced by a term $\sim g_s T$ which is indeed of the order of the thermal quark mass. For some time, equation 1.19 has been considered the complete $\mathcal{O}(\alpha\alpha_s)$ result.

The 2-loop contribution to the HTL rate follows from polarization diagrams similar to the ones in figure 1.8 (a,b) but now with the gluon propagator replaced by a dressed propagator. The two quark-quark-gluon vertices are responsible for an additional factor g_s^2 . However, it has been demonstrated [25] that the resummation of the gluon propagator leads to a term $\sim g_s^2$ in its denominator which precisely cancels this additional factor. These diagrams, as well as higher order HTL diagrams, therefore yield a similar contribu-

tion to the photon rate and seem to cause a breakdown of the perturbative technique.

Fortunately, much progress was made when it turned out that near-collinear photon emissions were significantly suppressed as a result of interference effects in multiple soft scatterings, the analogue of the famous Landau-Pomeranchuk-Migdal (LPM) effect in QED [26]. Hence, 1-loop, 2-loop, and even multi-loop HTL diagrams could be consistently resummed and a complete $\mathcal{O}(\alpha_s)$ result for the photon rate was obtained [27].

1.2.3 Photons and Heavy Ion Collisions

Thus far we have discussed the following sources of what was defined as direct photons:

- prompt photons directly produced in the perturbative part of the initial hard scattering
- prompt photons originating from the non-perturbative hadronization process of an outgoing parton (fragmentation photons)
- thermal photons radiated by a QGP in thermal equilibrium

All of these are expected to contribute to the direct photon rate in ultra-relativistic heavy ion collisions in a non-trivial way.

The formation of a QGP can possibly be established by colliding heavy ultra-relativistic nuclei. Once such a state of matter is formed, the production of thermal photons can provide information on the temperature evolution of the system and thus, on the equation of state which governs the QCD phase diagram. In addition, photons have the advantage that their mean free path is extremely large compared to the size of the produced system and they leave the interaction region unscathed. These are the primary reasons to study direct photon production in the environment of heavy ion collisions. However, a QGP which is produced in the laboratory is not stable, it will inevitably expand and cool down. Eventually, as a consequence of the principle of confinement, ordinary hadronic matter remains.

The space-time evolution of the hot and dense matter is often described by means of relativistic hydrodynamics (see, e.g., the contribution by Kolb and Heinz to [5] for an overview). As an illustration, consider the energy-momentum tensor

$$T^{\mu\nu} = (\epsilon + P) u^\mu u^\nu - P g^{\mu\nu} \quad (1.20)$$

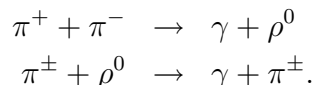
where ϵ equals the energy density, u^μ the four-velocity $\partial x^\mu / \partial \tau$ with proper time τ , and $g^{\mu\nu}$ the metric tensor. Assuming that the expansion of the system

is Lorentz boost invariant in the longitudinal direction (the Bjorken scenario [28]) and using that $\partial_\mu T^{\mu\nu} = 0$ it follows that

$$\frac{d\epsilon}{d\tau} + \frac{\epsilon + P}{\tau} = 0. \quad (1.21)$$

Figure 1.9 shows how ϵ and T vary with τ in case of this simplified hydrodynamical model [29]. Note that these curves can be derived from equation 1.21 combined with equations 1.9 and 1.10. Shortly after the collision, in case the critical temperature T_c is exceeded, the system enters the QGP phase and cools down until T_c is reached. At this point, hadronization sets in and the Mixed Phase (MP) is formed, in which deconfined matter and hadrons coincide. When all partons are confined, the Hot Hadron Gas (HHG) remains which then further expands up to the point where the hadrons cease to interact, the so called freeze-out.

The production rate of thermal photons in a QGP has been discussed in section 1.2.2. However, these results were obtained at a finite but fixed temperature. Moreover, the charged hadrons in the HHG constitute a source of thermal radiation as well, see e.g. [21] or [30], via scattering processes such as



Even from the simplified picture shown in figure 1.9, it is clear that the final thermal photon rates will then depend on, for instance, the formation time of the QGP (τ_0), the initial temperature T_0 , and the duration of the separate stages of the collision.

Figure 1.10 shows the results of a recent calculation of photon production in central Au+Au collisions at $\sqrt{s_{NN}} = 200$ GeV [31]. Such a calculation combines the previously discussed thermal photon rates with the space-time evolution of the collision system. The contribution of prompt photons is included as the differential cross section in p+p collisions, scaled with the nuclear overlap function T_{AA} from a Glauber model (see e.g. [32]) of Au+Au interactions. The calculation indicates that the prompt component will dominate the direct photon yield at high transverse momentum (p_T), whereas thermal radiation will constitute the largest part of the yield below $p_T \sim 3$ GeV/ c .

A Note on Effects in Cold Nuclear Matter

The calculation presented in figure 1.10 included the scaling factor T_{AA} to account for the increase in the number of scatterings as compared to a single

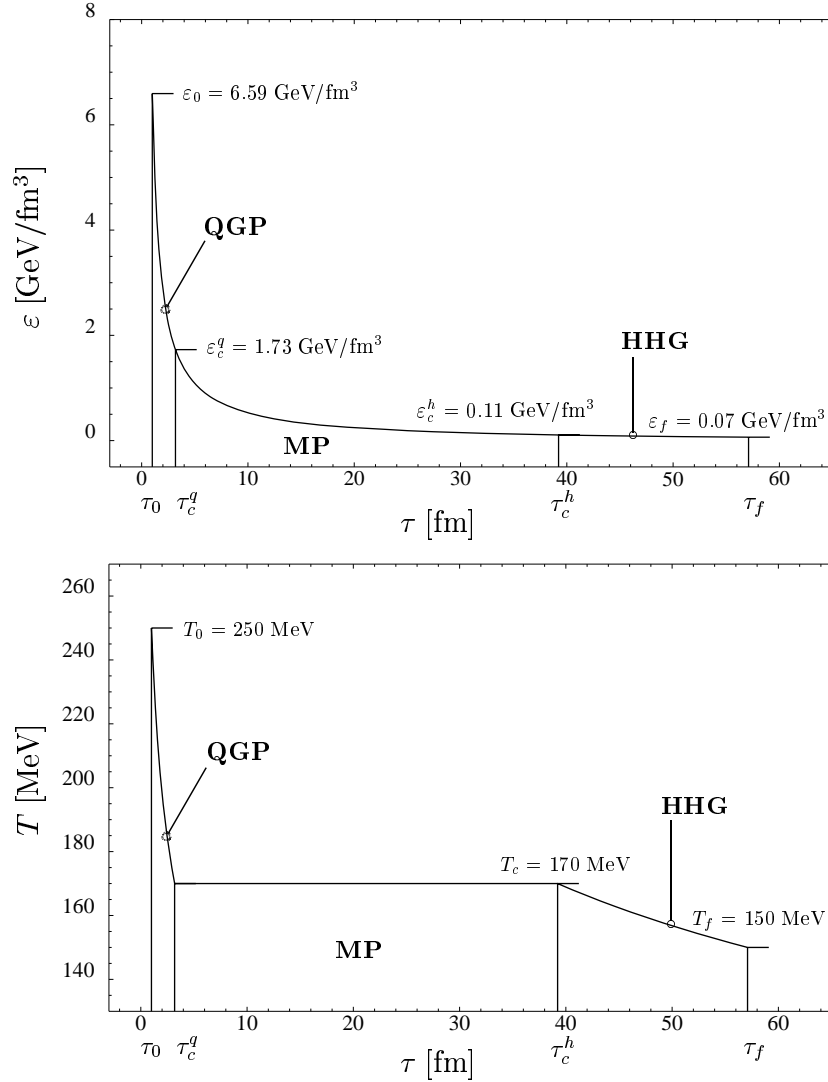


Figure 1.9: Evolution of temperature (bottom) and energy density (top) in an ultra-relativistic heavy ion collision according to a hydrodynamics framework (figure taken from [29]).

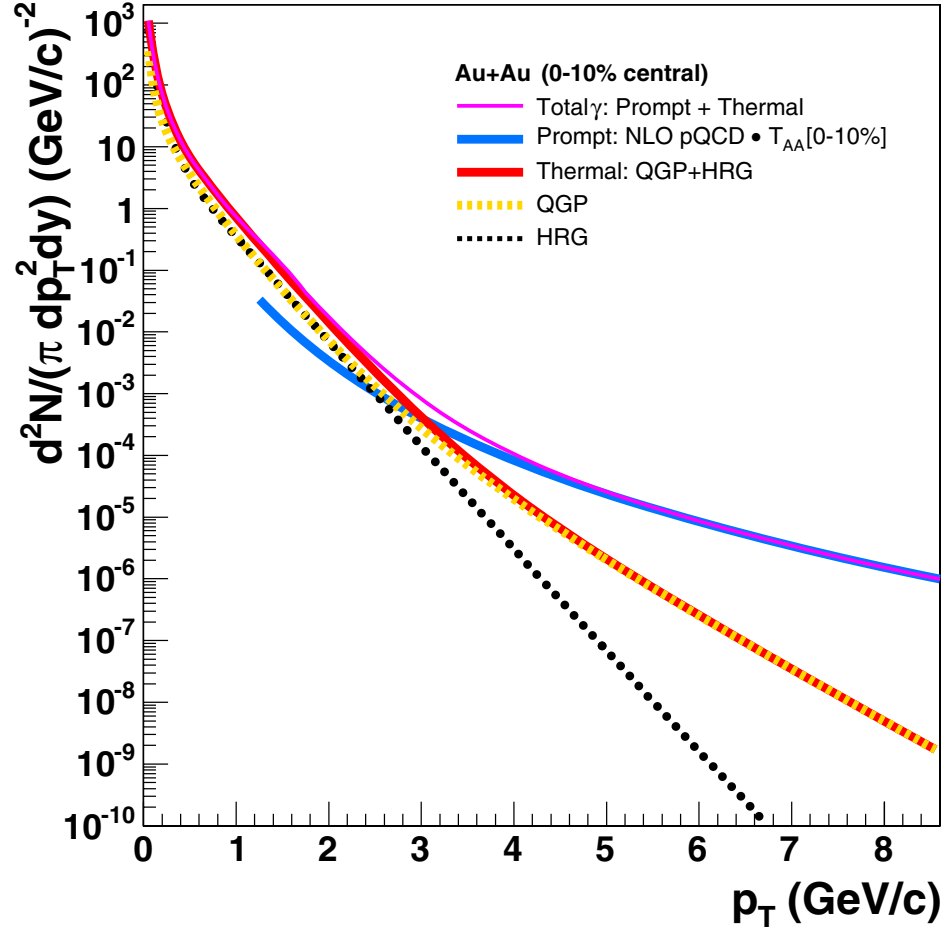


Figure 1.10: Photon production rates in central Au+Au collisions at $\sqrt{s_{NN}} = 200 \text{ GeV}$ as a function of p_T . The curves represent the contribution from the QGP, the HRG (written as HRG in the legend), and a NLO pQCD calculation of prompt photon production. The latter was scaled with the nuclear thickness function T_{AA} for central (0-10%) Au+Au collisions. The initial temperature and the formation time in the hydrodynamical model were equal to $T_0 = 590 \text{ MeV}$ and $\tau_0 = 0.15 \text{ fm}/c$, respectively. The figure was taken from [31].

p+p collision. It is not evident that this model leads to a sufficiently accurate description of the particle yields in ultra-relativistic collisions involving heavy nuclei. Even without the presence of a hot and dense medium in the final state of the collision, there are several phenomena which can lead to a suppression or an enhancement of particle production rates. Next to the assumed parameters of the hydrodynamical calculation, those phenomena cause an additional uncertainty of the thermal photon excess which needs to be reduced by experiments.

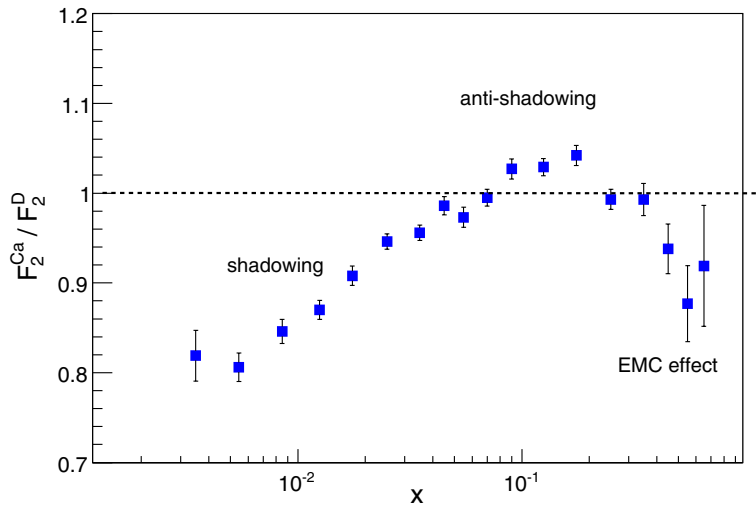


Figure 1.11: Nuclear effects in the fixed-target scattering reaction $\mu + \text{Ca}$ ($E_\mu = 100 \text{ GeV}$) compared to the scattering on deuterium, given in terms of the ratio of nuclear structure functions, $F_2^{\text{Ca}}/F_2^{\text{D}}$. The parton momentum fraction labels the horizontal axis (Data from the NMC collaboration [35]).

Among the known effects in cold nuclear matter are those which are coupled to the modification of the nuclear structure functions, as compared to an incoherent superposition of the partonic density functions. When the cross section of scattering on a nucleus is expressed relative to that on a nucleon, multiple nuclear effects have been identified [33, 34]. Figure 1.11 shows the cross section determined from deep-inelastic scattering of a muon on a calcium target, relative to the same reaction on a deuterium target [35]. The variable x denotes the momentum fraction of the parton with respect to the nucleon. Three distinct regions are indicated in the figure. The suppression of the cross section in the low x region is generally referred to as shadowing, the enhancement at intermediate x as anti-shadowing, and the depletion in the region $x > 0.3$ is the EMC effect, named after the

European Muon Collaboration [36].

The theory of the Color Glass Condensate (CGC) provides a description of the initial state of an ultra-relativistic nucleus in terms of a collective (classical) gluon field [37]. When probing the nucleus at increasingly smaller x , the density of gluons eventually saturates as a result of non-linear evolution effects (gluon recombination versus splitting). This saturation would put a natural bound on the total cross section of hadronic scattering processes thereby solving what is called the small x problem. It has been argued that the CGC has considerable implications for the production rates of particles in heavy ion collisions (see e.g. [38]).

The Cronin effect [39] leads to an enhancement of particles in p+A (or d+A) collisions. However, in contrast to the previously mentioned modifications of nuclear densities, it is not necessarily an initial state effect. It is believed to be caused by multiple soft scatterings of the parton on its way in and out of a nucleus. This enhancement has been observed at RHIC, in particular in case of charged hadron production in the transverse momentum range $2 < p_T < 6 \text{ GeV}/c$ [40].

In order to eventually isolate the thermal photon contribution from the total photon yield determined in an experiment, it is essential that these possible modifications of the particle yields are quantitatively under control. In addition, it should be stressed that prompt photons are an extremely suitable tool to study the initial conditions of heavy nuclei themselves. Their production mechanism is sensitive to the gluon density in the gold nucleus at leading order, as can be seen from the left Feynman diagram in figure 1.4. Moreover, it has a reduced uncertainty from the non-perturbative fragmentation as compared to the production of hadrons. In fact, these are the main motivations for our experimental study of direct photon production in d+Au collisions.

Chapter 2

Experiment

2.1 The Relativistic Heavy Ion Collider

The Relativistic Heavy Ion Collider (RHIC) at Brookhaven National Laboratory [41] (BNL) was designed and constructed to generate collisions of heavy ions and polarized protons with the following two objectives:

- the study of the Quark Gluon Plasma created in ultra-relativistic heavy ion collisions at a maximum center-of-mass energy of 200 GeV per nucleon pair ($\sqrt{s_{NN}} = 200$ GeV)
- the study of the spin structure of the proton with polarized proton-proton collisions (p+p) up to $\sqrt{s} = 500$ GeV

Although the latter was not the primary motivation of the analysis presented in this thesis, it should be stressed that direct photon production in p+p collisions is one of the most promising probes to unravel the proton spin puzzle (see e.g. [42]).

A schematic overview of the RHIC complex is shown in figure 2.1 and a detailed report on the design performance and mode of operation can be found in [43]. The heavy ions (and deuterium ions) were generated with the Pulse Sputter Ion source in the Tandem van de Graaff facility with charge $Q = -1e$. The ions were accelerated twice, first from ground potential to +15 MV and subsequently, after passing through a series of stripping foils, back to ground potential. Upon exit of the Tandem van de Graaff, the ions were further stripped and transferred to the Booster synchrotron, in case of Au ions with an energy equal to 1 MeV/nucleon and net charge $Q = +32e$. After an acceleration to 95 MeV/nucleon in the Booster, the ions were once again stripped ($Q = +77e$) on their way to the Alternating Gradient Synchrotron (AGS) and only the two K-shell electrons remained. Before injection

into the RHIC rings, the AGS was used to generate the final bunches of ions with an energy equal to 10.8 MeV/nucleon. In the transfer line from AGS to RHIC, the remaining electrons were removed as well which led to $Q = +79e$ in case of Au, and $Q = +39e$ in case of Cu. The (polarized) protons were generated in the Linear Accelerator facility (LINAC) and injected into the Booster with an energy equal to 200 MeV.

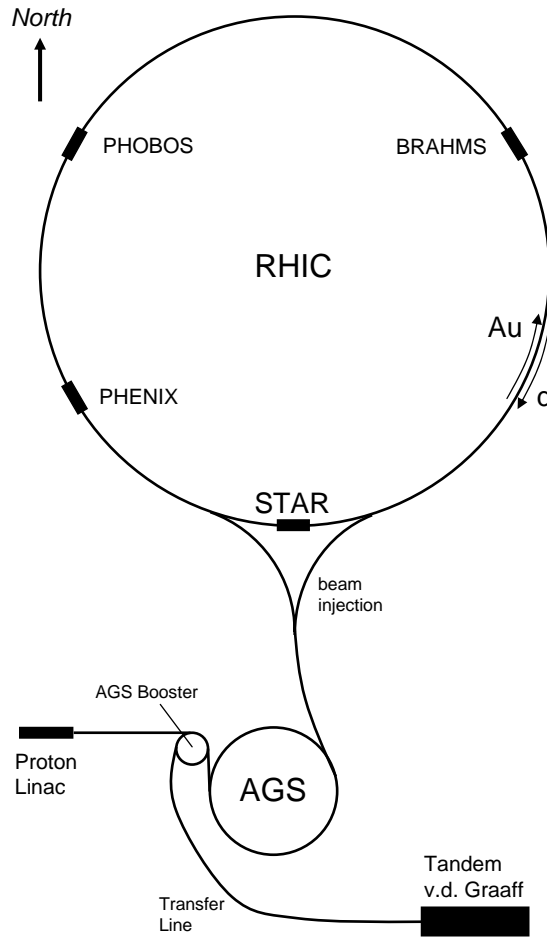


Figure 2.1: A schematic view of the RHIC accelerator complex at BNL.

Each of the two 3.8 km RHIC rings (one in each direction) was capable of storing and accelerating a maximum of ~ 110 ion bunches¹, to a top energy of

¹However, during the d+Au run, pressure rises created unacceptable background and beam lifetime issues which required a return to the storage of 55 bunches per beam.

Run	year	species	E (GeV/nucleon)	\mathcal{L}	$\langle \mathcal{P} \rangle$
Run-1	2000	Au+Au	27.9	$< 0.001 \mu\text{b}^{-1}$	
		Au+Au	65.2	$20 \mu\text{b}^{-1}$	
Run-2	2001–2002	Au+Au	100.0	$258 \mu\text{b}^{-1}$	
		Au+Au	9.8	$0.4 \mu\text{b}^{-1}$	
		p+p	100.0	1.4pb^{-1}	14%
Run-3	2003	d+Au	100.0	73nb^{-1}	
		p+p	100.0	5.5pb^{-1}	34%
Run-4	2003–2004	Au+Au	100.0	$3530 \mu\text{b}^{-1}$	
		Au+Au	31.2	$67 \mu\text{b}^{-1}$	
		p+p	100.0	7.1pb^{-1}	46%
Run-5	2004–2005	Cu+Cu	100.0	42.1nb^{-1}	
		Cu+Cu	31.2	1.5nb^{-1}	
		Cu+Cu	11.2	0.02nb^{-1}	
		p+p	100.0	29.5pb^{-1}	46%
		p+p	204.9	0.1pb^{-1}	30%
Run-6	2006	p+p	100.0	93.3pb^{-1}	58%
		p+p	31.2	1.05pb^{-1}	50%
Run-7	2006–2007	Au+Au	100.0	$7250 \mu\text{b}^{-1}$	

Table 2.1: The delivered integrated luminosity \mathcal{L} with RHIC in the period 2000–2007 (data taken from [47]). The last column shows the average polarization $\langle \mathcal{P} \rangle$ in case of p+p collisions.

100 GeV per nucleon in case of heavy ions and 250 GeV per proton. Table 2.1 lists the completed RHIC runs to date, the accelerated species, and the energy per nucleon. In addition, the last two columns show the delivered luminosity \mathcal{L} and the average polarization $\langle P \rangle$ of the proton bunches. The two RHIC beams intersect at six locations equally distributed around the ring, four of which correspond to locations of the main experiments: BRAHMS, PHENIX, PHOBOS, and STAR. An overview of these experiments is given in [44].

The presented analysis was performed with data recorded by the STAR experiment during the 2003 d+Au run [45] and the 2005 p+p run [46]. The data collected from p+p reactions was averaged over the four possible configurations with respect to bunch polarization ($\uparrow\uparrow, \uparrow\downarrow, \downarrow\uparrow, \downarrow\downarrow$) such that the residual polarization was negligible.

2.2 The STAR Experiment

The Solenoidal Tracker At RHIC (STAR) is a large acceptance experiment, primarily designed to investigate strongly interacting matter at high energy density in a search for signatures of the QGP. Many observables have been and will be studied in order to understand the possible formation of the QGP and its properties. Hence, the STAR experiment was equipped with multiple dedicated detectors to perform high precision tracking, momentum analysis, and particle identification, particularly of charged hadrons in the high multiplicity environment of an ultra-relativistic heavy ion collision. Furthermore, it provides electromagnetic calorimetry almost continuously over the full azimuthal angle and over a pseudo-rapidity range $-1 < \eta < 2$.

A picture of the complete STAR detector is shown in figure 2.2. The experimental setup of all detector components is described in [48] and references therein. Because this direct photon analysis was performed with the mid-rapidity calorimeter and central time projection chamber as the main detectors, these will be described in more detail below. In addition, section 2.2.4 summarizes the properties of the general STAR trigger detectors. The data acquisition will be the main subject of section 2.3. Finally, we would like to refer to appendix B for the definition of the STAR coordinate system which is useful to interpret the dimensions of the various detectors.

2.2.1 Time Projection Chamber

The Time Projection Chamber [49] (TPC) constitutes the core of the STAR experiment. The TPC is a 4.2 m long cylinder which is concentric with the beam line. A layout of the STAR TPC is shown in figure 2.3. It has an

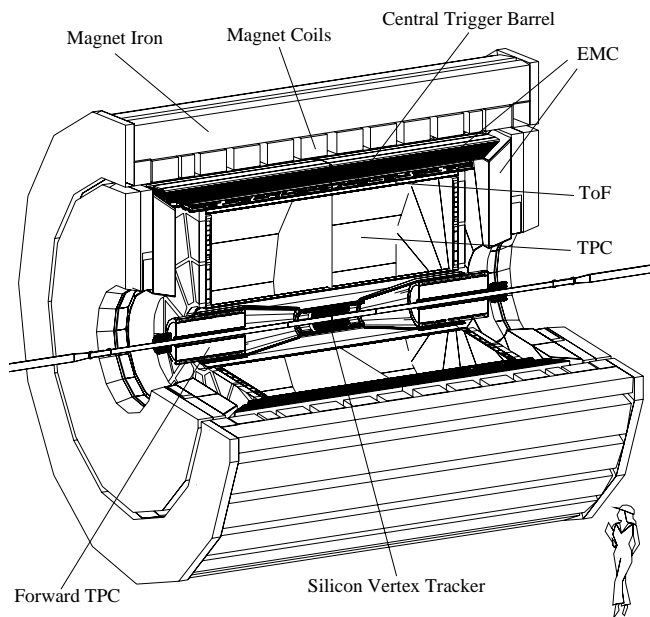


Figure 2.2: The STAR detector at RHIC.

active volume with an inner radius of 0.5 m and an outer radius of 2 m. Hence, it extends over $-2.0 < \eta < 2.0$ at $r = 0.5$ m and $-1.0 < \eta < 1.0$ at $r = 2.0$ m while covering the full azimuthal angle: $0 < \phi < 2\pi$. The chamber is filled with a mixture of two gases, 90% Ar and 10% CH₄, approximately 2 mbar above atmospheric pressure. A central membrane divides the volume at $z = 0$ and is kept at a high voltage with respect to the detection planes at $z = \pm 210$ cm, resulting in an electrical field equal to ± 135 V/cm \hat{z} .

A charged particle traversing the gas loses energy as a result of ionization, thereby leaving free electrons in its wake. These electrons then drift in the direction of the uniform electric field to the detection planes which are both equipped with a thin Multi-Wire Proportional Chamber (MWPC). Each of the MWPCs consists of 45 pad rows extending from the inner to the outer radius and is highly segmented in ϕ , yielding a total of 136,608 pads.

Figure 2.4 illustrates the method of operation of the MWPCs. The electrons are collected on a gating grid (top panel) until it is opened in case a triggered event occurs (bottom panel). They are then accelerated to the high-voltage anode wires and generate an avalanche of ionization. These positive ions temporarily induce an image charge on the pads which is amplified, digitized, and assigned to consecutive time intervals. The sampling rate of the readout system corresponds to 9.4 MHz, the sampling depth has

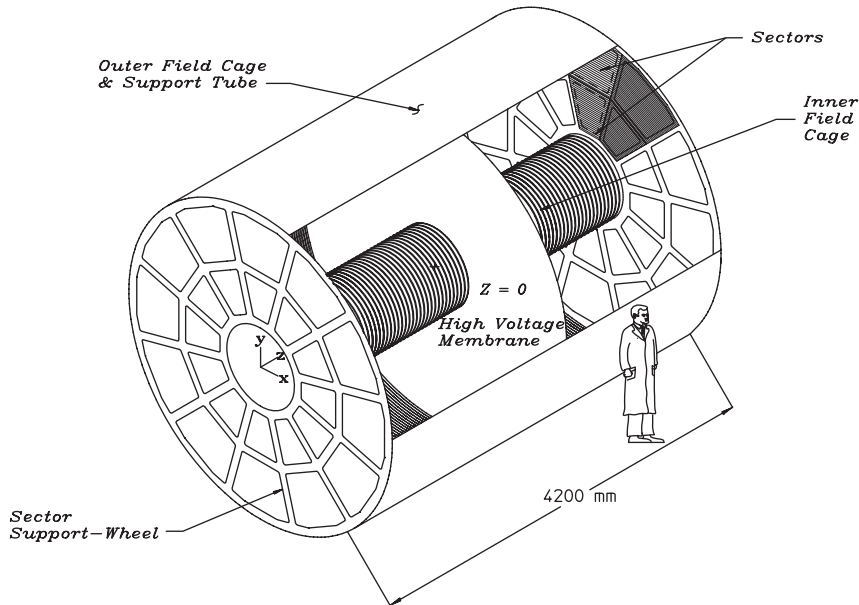


Figure 2.3: The STAR Time Projection Chamber.

a maximum of 512 time buckets.

The STAR magnet [50] provides a uniform 0.5 T field² along the RHIC beam line in both directions: \hat{z} as well as $-\hat{z}$. Next to suppressing the transverse diffusion of the drifting electrons, the field causes the ionizing particles to follow a helical trajectory. The curvature of the tracks defines their transverse momentum by the equality $p_T = eBr$, with r equal to the gyration radius, e the charge of the particle, and B the magnetic field strength. The x and y coordinates of the tracks follow from the precise location of the MWPC pads, z can be determined from the time of readout in combination with the drift velocity. Hence, the TPC can be used to reconstruct the three-dimensional trajectory of a particle as well as its momentum. In addition, the characteristic energy loss along the track of the particle dE/dx is known from the Bethe equation [52]. Figure 2.5 shows how the measured values appear as bands around the theoretical prediction making the TPC a very powerful tool for particle identification below $\sim 2 \text{ GeV}/c$.

The p_T resolution of the TPC degrades with increasing p_T as a result of the reduced curvature of the tracks: $\Delta p_T/p_T$ equals approximately 3%

²The field strength was equal to 0.25 T before 2001.

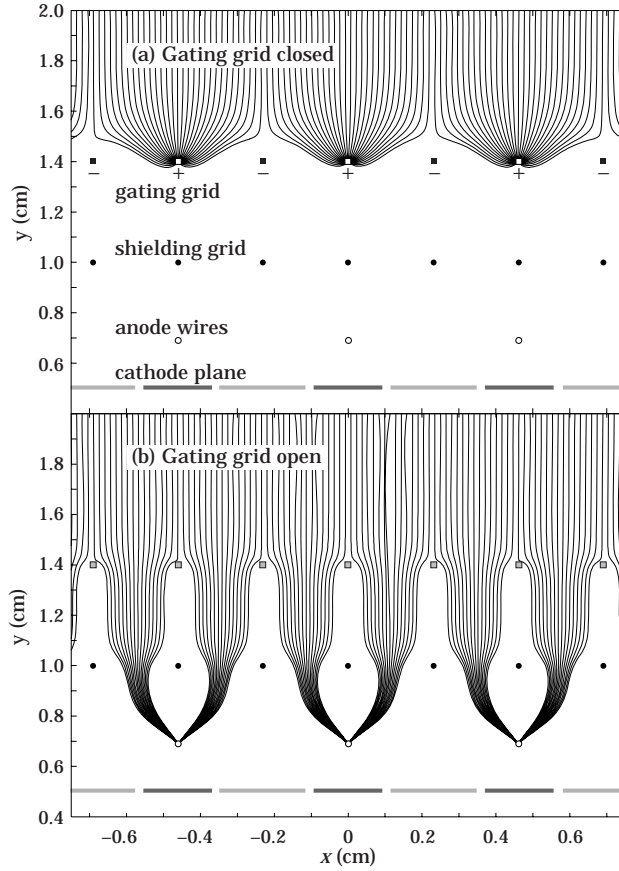


Figure 2.4: Mode of operation of a typical MWPC. The coordinate axes do not correspond to the STAR coordinate system. The figure was taken from [51].

at $p_T = 1 \text{ GeV}/c$ and 7% at $p_T = 4 \text{ GeV}/c$ with an approximately linear dependence on p_T in between. The dE/dx resolution depends on the gas gain which in turn depends on the pressure in the TPC. Therefore, the gain is carefully monitored with a ^{55}Fe source outside the main chamber. The electrical field, the pressure, and the composition of the gas determine the drift velocity (typically $5.5 \text{ cm}/\mu\text{s}$) of the electrons which therefore varies over time. During the recording of data, a laser system is used to calibrate this velocity on a daily basis. The laser beams, embedded in the tracks from a genuine collision, ionize the gas at a known location and the time to detection on the MWPC planes gauges the drift velocity.

The general resolution of the TPC improves when a particle crosses an increasing number of pad rows. Hence, the effective acceptance of tracks is limited to approximately $-1.4 < \eta < 1.4$. The reconstruction efficiency depends on the quality constraints of a track and rapidly approaches a value

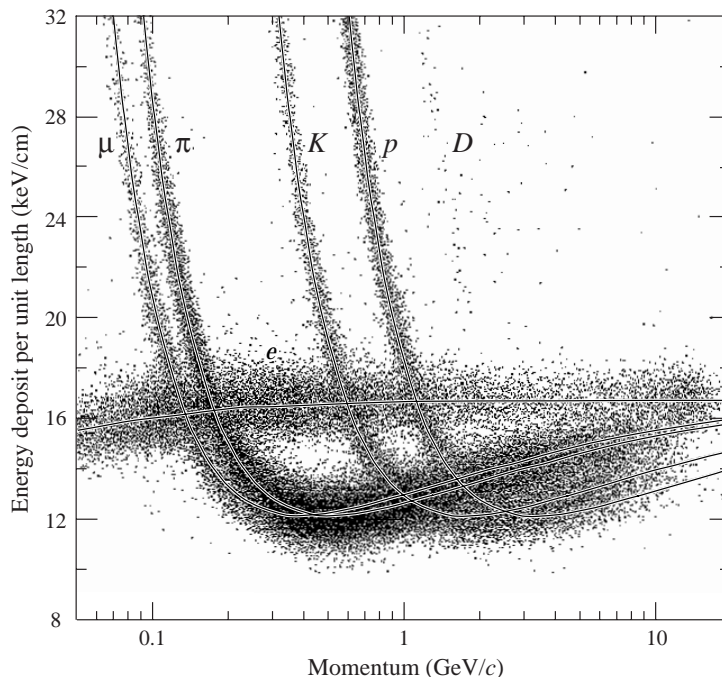


Figure 2.5: The energy loss dE/dx in a TPC as a function of momentum. The curves through the data correspond to calculations with the Bethe formula (figure from [51]).

larger than 96% above $p_T = 1 \text{ GeV}/c$. The primary use of the TPC in our direct photon analysis was to reconstruct the collision vertex and to reduce the contamination of our photon sample by charged particles. Furthermore, the energy calibration of the calorimeter was performed with identified electrons tracked in the TPC. It was therefore advantageous that the acceptance of the TPC extended well beyond that of the calorimeter which was used to detect the photons.

2.2.2 Barrel Electromagnetic Calorimeter

The Barrel Electromagnetic Calorimeter [53] (BEMC) is a scintillator-lead sampling calorimeter located outside the TPC³ and within the STAR magnet coils, as can be seen from figure 2.2. Its active volume has a pseudo-rapidity coverage equal to $-1 < \eta < 1$ and it extends 2π in azimuth. The inner radius of the BEMC, determined at the front plate, is equal to 223.5 cm, its outer

³In between the TPC and the BEMC are the Central Trigger Barrel [54] and the Time Of Flight detector [55] which were not directly used for the analysis presented in this thesis.

radius is at $r = 263$ cm (back plate). The position of the BEMC within the STAR experiment is shown in figure 2.6.

Mechanical Design

The BEMC consists of two half barrels, each with a length equal to 293 cm and 257 cm at the back and front plate, respectively. A half barrel contains 60 identical modules with $\Delta\eta = 1.0$ and $\Delta\phi \approx 0.10$ (6°) which are approximately 26 cm wide. Figure 2.7 shows the layout of a single module in the west barrel: $0 < \eta < 1$. The top of the figure illustrates the view of the last scintillator tile such that the separate calorimeter towers are visible. Each module contains 40 towers of dimension $\Delta\eta \times \Delta\phi = 0.05 \times 0.05$ rad, yielding a total of 4800 towers in the east and west barrel combined. The towers are projective with respect to the origin of the STAR coordinate system and increase in absolute size from $\eta = 0$ outward. Figure 2.8 shows two towers from modules which are adjacent in ϕ . Note that in between the modules there is a 5.6 mm gap which can lead to distortions in the shower development near the module boundaries.

Starting from the inner radius of the BEMC, the first part of the detector is the ~ 19 mm aluminum front plate. This is followed by a stack of 10 layers, alternating lead and scintillating material (Kuraray SCSN81). The outer stack consists of another 15 layers of lead and 16 layers of scintillator, organized in a similar manner. In between these stacks there is a shower-maximum detector which will be discussed below. All layers are 5 mm thick except for the first two scintillating layers which are 6 mm thick and constructed with an additional readout. The latter corresponds to the Barrel Preshower detector [53] which was not operational when the presented data were recorded⁴. The material of the layers was chosen to provide sufficient friction and the stack is held at a pressure of ~ 1 bar to assure stability of the calorimeter in all directions.

The area of a single scintillator tile is equal to that of a BEMC module. However, to ensure optical isolation, a groove was made between calorimeter towers by cutting 95% through the material which was subsequently filled with an opaque epoxy. In addition, a thin black line was painted on the tile opposite to the isolation groove reducing the optical cross talk to a level smaller than 0.5%. A wavelength shifting (WLS) fiber is embedded in the tile for each single tower, as shown for the top megatile (Sc21) in figure 2.7. The light output of all 21 WLS fibers are routed to the back plate of the

⁴In the future the Barrel Preshower detector will contribute to similar analyses as it improves the discrimination of hadronic and electromagnetic cascades in the BEMC.

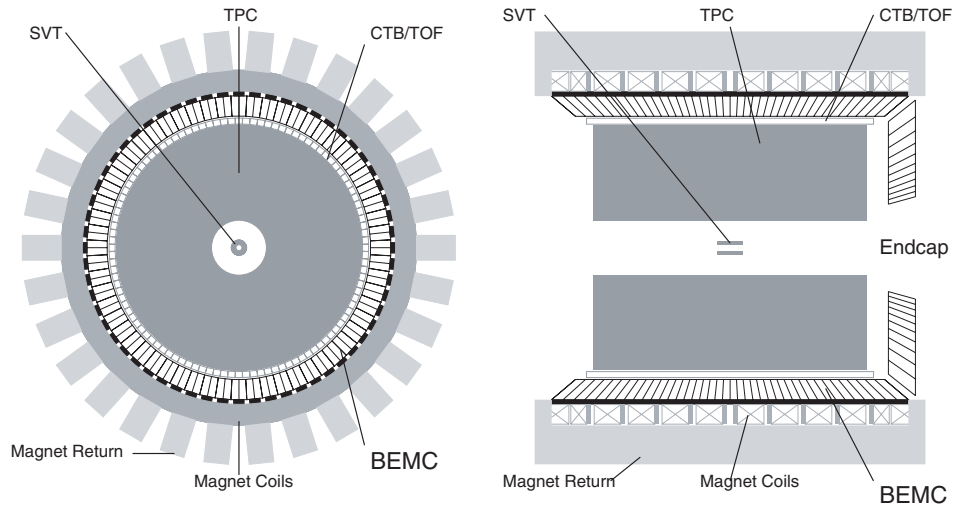


Figure 2.6: The position of the BEMC with respect to other STAR detector components. A cross section perpendicular to the beam line is shown on the left, the right shows the cross section in the plane $x = 0$.

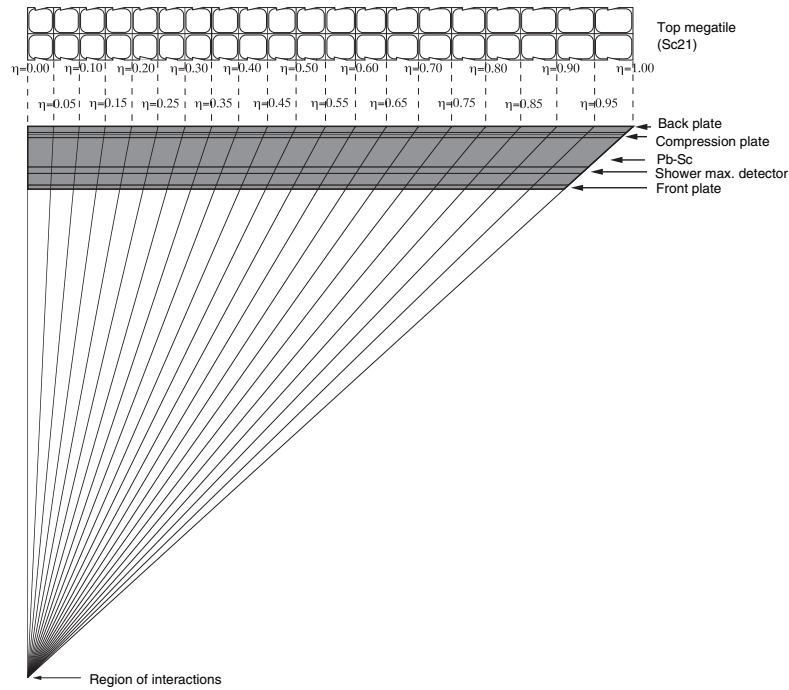


Figure 2.7: The cross section of a BEMC module in the (r, z) plane. The top of the figure shows the outermost megatile, as seen along r .

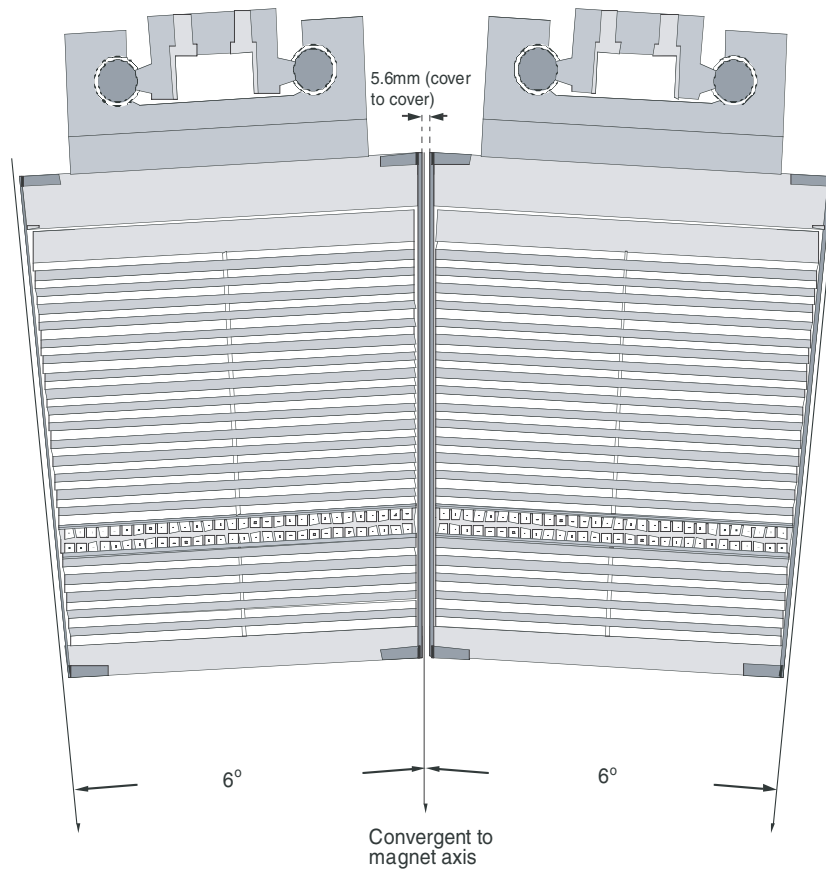


Figure 2.8: A cross section of two adjacent BEMC towers and the Barrel Shower Maximum Detector which is located after the first 5 scintillator tiles.

module and terminate in separate optical connectors. A 2.1 m long multi-fiber optical cable transports the light output to an optical connector inside large boxes mounted on the outer surface of the STAR magnet. In these boxes, the light coming from the 21 separate WLS fibers of a single tower is guided to a single photo-multiplier tube (PMT).

The PMTs of the BEMC are of the type *Electron Tube Inc. model 9125B* and were required to have a quantum efficiency of at least 10% at $\lambda = 420$ nm upon installation. The mean efficiency was found to be 13.3%. Only PMTs which had a non-linearity less than 2% at a peak current of 20 mA were installed. The high voltage on the 11 dynodes is regulated by a Cockroft-Walton type base which provides a voltage division ratio of $\{2 : 1 : 1 : 1 : 1 : 1 : 1 : 1 : 2 : 3 : 4 : 3\}$. The high voltage on these bases can be remotely steered through a serial slow controls network. Further details on the BEMC optical structure, its mechanical design, as well as performance estimates can

be found in [53].

Mode of Operation

The BEMC was designed to measure the energy and position of photons, electrons, and positrons which traverse the active material of the detector. When a photon (with energy greater than ~ 10 MeV) enters the BEMC, it interacts with the absorber material (Pb) predominantly through the process of electron-positron pair production in the nuclear field. These secondary electrons and positrons then lose energy as a result of Bremsstrahlung up to the point where ionization dominates, as shown in figure 2.9, and the particles are fully absorbed. Evidently, the Bremsstrahlung photons can convert into electron-positron pairs again until their energy is low enough for absorption by the atoms (< 10 MeV). Hence, an electromagnetic cascade, also referred to as shower, is generated in the calorimeter volume. When the primary incident particle is an electron or positron, a similar cascade is initiated starting directly from the Bremsstrahlung process.

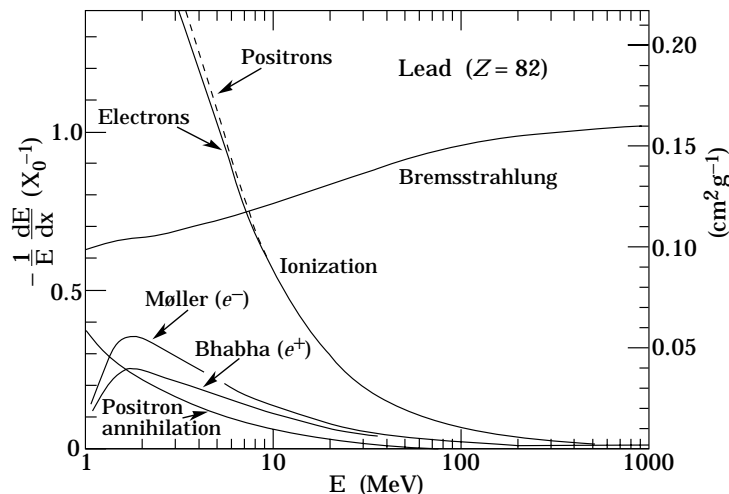


Figure 2.9: Energy loss for the different interactions of positrons and electrons with lead (figure taken from [51]).

The interaction probability of an electron or a photon is determined by the amount of radiation lengths (X_0) it traverses. In case of lead, one unit of X_0 corresponds to 0.56 cm. The probability that a photon converts before it has reached a depth d in the material is given by

$$P_{\text{conv}} = 1 - e^{-\frac{7}{9}td} \quad (2.1)$$

with $t_d = d/X_0$ and the mean free path of the photon is equal to $9/7X_0$ [51]. The radial depth of the active BEMC volume is approximately equal to $21 X_0$ and electromagnetic showers will therefore be fully absorbed. The characteristic transverse (η, ϕ) expansion of the shower is often expressed as the Molière radius R_M . When fully absorbed, an approximate 90% (99%) of the energy of the incident particle will be contained in a cylinder of radius R_M ($3.5R_M$). In case of lead, $R_M \approx 1.5$ cm which is sufficiently small to suppress the physical overlap of nearby showers. In addition, it allows for a precise determination of the shower axis. To suppress the total cost of construction, the transverse dimensions of a BEMC tower were approximately 6–9 times larger than R_M . Hence, the BEMC was equipped with the Barrel Shower Maximum Detector to increase the spatial segmentation, as will be discussed below.

As the electrons and positrons in the shower pass through the scintillator, light is induced which is collected on the WLS fibers of the tower. The energy resolution of the calorimeter is subject to fluctuations of the light output of the scintillator tiles. Dedicated tests of the optical signal in the separate layers and a full system test with cosmic rays showed that on average 3 photo-electrons are produced per minimum ionizing particle per scintillator layer. In case of an ideal sampling calorimeter this would correspond to

$$\Delta(E)/E \approx \frac{14\%}{\sqrt{E/\text{GeV}}} \oplus 1.5\%. \quad (2.2)$$

In reality, the resolution is worse as a result of, for example, cross talk between towers and radiation damage to the scintillator (yellowing).

Although the BEMC was designed to constrain electromagnetic showers, a hadron traversing the detector can also initiate a cascade through the nuclear interaction. The typical hadronic interaction length λ_I is very large though compared to the size of the towers: $\lambda_I \sim 35 \text{ g cm}^{-2} A^{1/3}$ with A the atomic mass number. Hence, most hadrons will just pass through the calorimeter and in case of charged hadrons a minimal amount of energy will be lost as a result of ionization. These particles are referred to as minimum ionizing particles (MIP). Occasionally a nuclear interaction will occur and, for example, neutral pions are created which directly decay, predominantly into two photons, and an electromagnetic cascade starts. Hence, the longitudinal as well as the transverse profile of the hadronic cascades in the BEMC will be very irregular compared to that of exclusively electromagnetic cascades. This irregular shower pattern is commonly used to discriminate between the two types of showers.

Electronics and Hightower Trigger

The signal processing and digitization of the analog output of the PMTs occurs in 30 electronics crates located on the outer surface of the STAR magnet (c.f. Magnet Return in figure 2.6). The resulting 12 bit ADC⁵ values, one for each tower and 4800 in total, are pipelined and ready to be sent to the main STAR data acquisition system (DAQ) for every bunch crossing of the RHIC beams. When a signal arrives which triggers these data to be released, the output of all 30 crates is transferred to a central electronics crate, the Tower Data Collector (TDC). It is stored with an identifier, also referred to as a token, to await the possible readout by the DAQ system.

The BEMC is of great importance to the STAR physics program, mainly because of the following two reasons. First of all, the detector is fast and can be read out every consecutive RHIC bunch crossing. Next to that, it measures the total energy of particles and can therefore identify rare collisions with a highly energetic photon, electron, or even a jet in the final state. To implement this functionality in the main STAR trigger system, the BEMC front end electronics provide two kinds of trigger primitives. The first set corresponds to the summed energy in a patch of 4×4 towers (300 patches total) which is truncated to 6 bit numbers. The second collection of 300 primitives also consists of 6 bit numbers, each of them representing the single largest tower signal in a given patch. The latter corresponds to the BEMC hightower trigger which was essential for the presented analysis, its 6 bit primitive is referred to as a hightower trigger bit.

To calculate the primitive which holds the energy deposition in a single tower, the location of the noise pedestals can be uploaded to the BEMC crates. In addition, each digitizer board has a mask which can be set to exclude individual towers from the decision making. These manipulated data can be sent to the STAR trigger system within 700 ns of the RHIC bunch crossing, fast enough to participate in the final L0 trigger decision (see section 2.3.1). Further details with respect to the logic of the BEMC trigger algorithms can be found in, e.g., [56].

2.2.3 Barrel Shower Maximum Detector

The Barrel Shower Maximum Detector (BSMD) is a proportional counter with gas amplification and a two-dimensional cathode strip readout. It is embedded in the BEMC between the inner and outer stack of lead-scintillator layers, as can be seen from figure 2.7. Hence, it has a similar coverage:

⁵ADC stands for Analog-to-Digital Converter and also refers to the digital number which represents the analog charge signal.

$-1 < \eta < 1$ and $0 < \phi < 2\pi$. The BSMD is located at a depth which varies from $4.6X_0$ at $\eta = 0$ up to $7.1X_0$ at $\eta = 1$, as seen from the origin. This region corresponds to the part of the BEMC where the energy deposition per unit length dE/dx of an electromagnetic cascade is near its maximum⁶ (see equation 2.6). The latter served the intended functionality of the BSMD, namely, to improve the overall spatial resolution by means of a reconstruction of the transverse profile of the showers. The ultimate goal was to separate electromagnetic from hadronic showers and to resolve the individual cascades of two nearby photons which is the signature of a neutral pion at high p_T (see appendix C).

Mechanical Design and Electronics

Figure 2.10 shows a (partial) cross section of a BSMD module which coincides with the BEMC module in terms of its (η, ϕ) dimension. The volume between the two readout planes is filled with a mixture of gases: 90% Ar and 10% CO₂. The lower readout plane in the figure is the BSMD eta-plane (BSMDE) and is closest to the beam line, the upper plane is the BSMD phi-plane (BSMDP). In front of each of the planes, 30 high voltage (~ 1.4 kV) tungsten anode wires with a $50 \mu\text{m}$ diameter run from $\eta = 0$ to $\eta = \pm 1$ through as many continuously grounded aluminum extrusions.

There are 300 cathode strips in a single BEMC module. The 150 BSMDE strips are adjacent in \hat{z} and have $\Delta\phi \sim 0.1$, which equals the width of a single module. The 150 BSMDP strips are organized in 10 patches with $\Delta\eta \times \Delta\phi \sim 0.1 \times 0.1$ rad, each patch containing 15 strips contiguous in $\hat{\phi}$ and covering 2×2 calorimeter towers. The strips come on a copper-backed board which is attached to the extrusion with a $100 \mu\text{m}$ thick epoxy to provide the necessary electrical insulation and to seal the chamber.

The signal transmission lines are printed in the circuit board and run from the cathode strips to a front end electronics board located at $\eta = 1$. This board contains a pre-amplifier to preserve the typically very small BSMD signals (~ 7 fC/MIP). The amplified signals are subsequently buffered in a switch capacitor array of 126 time buckets. When an event is triggered, the analog readout is multiplexed 80:1 to external digitization crates outside the STAR magnetic field. Finally, a 10 bit ADC value for each of the 36000 BSMD channels is available, approximately $200 \mu\text{s}$ after the corresponding RHIC bunch crossing. We have listed some essential BSMD design parameters in table 2.2.

⁶In practice, an additional amount of material equal to $\sim 1.0X_0$ had to be taken into account, most of it belonging to the Central Trigger Barrel which is directly in front of the BEMC (see also section 4.2.4).

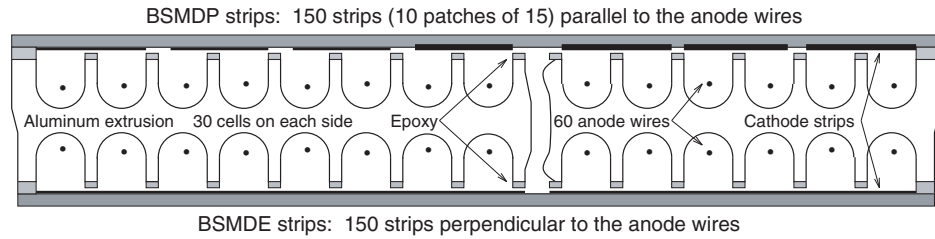


Figure 2.10: A partial cross section of a BSMD module. The figure shows 7 BSMDP strips extending in ϕ whereas a complete patch has 15 adjacent BSMDP strips and 10 such patches fill up a module. The BSMDE strips extend in the η direction which can be thought of as perpendicular to the presented view.

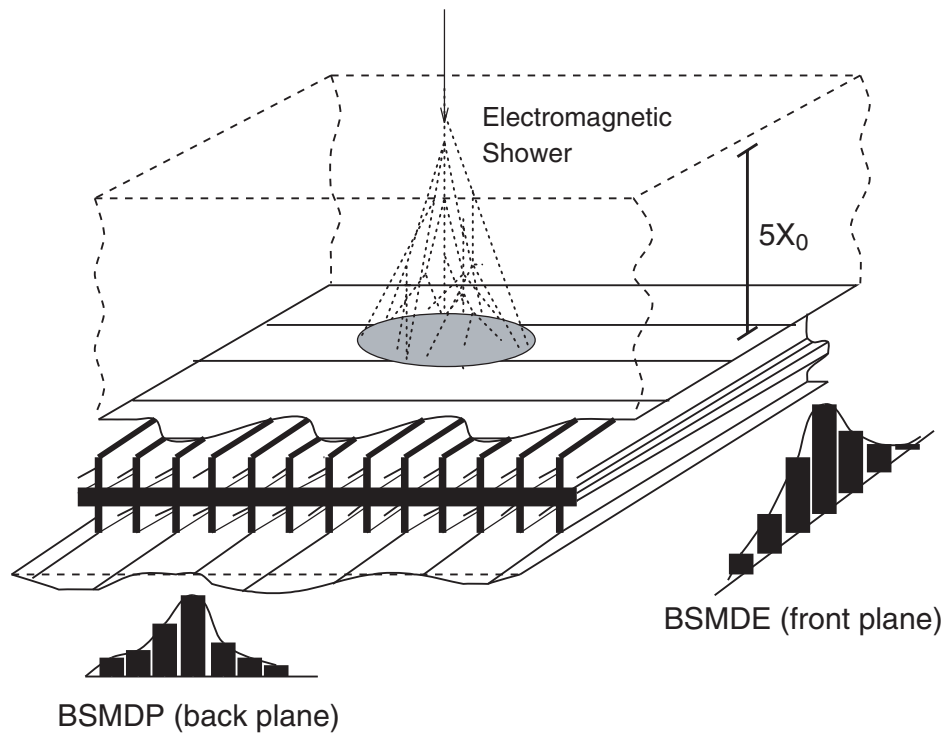


Figure 2.11: Illustration of the reconstruction of an electromagnetic shower with the BSMD. The first layers ($\sim 5X_0$) of BEMC material are shown as well as the aluminum extrusions, the cathode strips, and the high voltage anode wires.

chamber depth inside BEMC	$\sim 5X_0$ at $\eta = 0$
rapidity coverage (single module)	$\Delta\eta = 1$
azimuthal coverage (single module)	$\Delta\phi = 6^\circ$
occupancy (p+p)	$\approx 1\%$
occupancy (Au+Au)	$\approx 5\text{--}25\%$
	(depending on threshold and centrality)
chamber depth (cathode to cathode)	20.6 mm
anode wire diameter	50 mm
gas mixture	90% Ar and 10% CO ₂
gas amplification	3000
signal length	110 ns
BSMDE strip width (pitch)	1.46 (1.54) cm for $ \eta < 0.5$ 1.88 (1.96) cm for $ \eta > 0.5$
BSMDP strip width (pitch)	1.33 (1.49) cm
number of strips per module	300
total number of modules	120
total number of readout channels	36000

Table 2.2: The BSMD design parameters.

Mode of Operation

An incident electron or photon initiates an electromagnetic cascade in the BEMC absorber. When the charged constituents (e^+ , e^-) of the cascade cross the BSMD chamber, they will ionize the gas along their track. The liberated electrons proceed towards the anode wires and the ions towards the aluminum extrusion. When the electrons approach the wire, the electrical field ($\sim r^{-1}$) accelerates them to an energy which is large enough to produce secondary ionization. This finally results in an ionization avalanche in the gas volume near the wires. The number of electron-ion pairs created in this avalanche is proportional to the number of electrons from the primary ionization. The gas amplification of the BSMD highly depends on the anode voltage and typically lies within the range 3000–5000. The ions in the avalanche induce an image charge on the cathode strips which is subsequently read out through the transfer lines in the PC board. The collected charge serves as a measure of the local intensity of the shower and can eventually be used to reconstruct the lateral profile of the energy deposition. The electrons induce a sufficiently large current on the anode wires to be used as a fast trigger on electromagnetic showers. However, the finer segmentation ($\Delta\eta \times \Delta\phi = 0.05 \times 0.05$ rad) and better energy resolution of the BEMC based hightower trigger have made this functionality obsolete.

Figure 2.11 illustrates the use of the BSMD to reconstruct the lateral shower profile and the location of impact. The BSMDP constrains the ϕ coordinate of the shower (hence phi-plane) and the BSMDE the η coordinate. The energy resolution was determined from a beam test [57] and given by

$$\Delta E/E = 12\% + \frac{86\%}{\sqrt{E/\text{GeV}}} \quad (2.3)$$

in case of the eta-plane. A similar result, with the constant term equal to 15%, was obtained for the phi-plane. The position resolution during the beam test was found to be

$$\Delta x = 2.4 \text{ mm} + \frac{5.6}{\sqrt{E/\text{GeV}}} \text{ mm} \quad (2.4)$$

using a center-of-gravity method which weighted the strip position with the amplitude of the detected signal.

BSMD Calibration

The final energy scale calibration of the BEMC towers was carried out when the detector was in place, usually when the recording of data in a specific RHIC run (c.f. table 2.1) was finished. This calibration procedure is summarized in section 3.3.2. However, the BSMD has presently not been calibrated in situ. The remainder of this section illustrates the method which was used to obtain the current calibration coefficients of the BSMD channels.

The total induced charge Q on the strips is given by

$$Q = Q_e N_e, \quad (2.5)$$

where Q_e is the charge corresponding to a single ionizing particle and N_e the multiplicity of charged particles in the shower at the position of the BSMD gas layer. The latter depends on the location of the chamber as well as the initial energy E_0 of the particle which caused the shower. It can be shown [58] that N_e follows the longitudinal energy loss distribution

$$\frac{dE}{dt} = E_0 b \frac{(bt)^{bt_{\max}} e^{-bt}}{\Gamma(bt_{\max} + 1)} \quad (2.6)$$

with $t = x/X_0$ equal to the distance along the shower axis in terms of radiation lengths X_0 . The position of the shower maximum t_{\max} can be approximated by

$$t_{\max} \approx \ln(E_0/E_c) + \delta. \quad (2.7)$$

In case of an initial electron $\delta = -0.5$ and $\delta = 0.5$ for a photon initiated shower, E_c is the critical energy (9.59 MeV for lead), and the parameter b is approximately 0.5 [51]. The total accumulated charge can then be written as

$$Q = A Q_e \left(b \frac{(bt_s^{bt_{\max}} e^{-bt_s})}{\Gamma(bt_{\max} + 1)} \right) E_0 \quad (2.8)$$

where t_s is equal to the position of the BSMD gas layer in radiation lengths. Note that the non-linearity of the detector is now fully contained in the factor between the brackets.

Subsequently, the product of A and Q_e was determined using the test beam electrons [57] where the energy (E_0) and the material in front of the BSMD (t_s) were known. The average induced charge on the strips was found to be equal to $6.6 Q_e$ per 1 GeV of the incident electron beam. However, earlier measurements resulted in a smaller value, namely $6.0 Q_e$, although this experiment was equipped with a different type of shower maximum detector [59]. A dedicated simulation of the detector indicated that the coefficient could be somewhat larger than $6.6 Q_e$ [60]. Hence a relative uncertainty of 10% was assigned to the overall energy scale of the BSMD.

2.2.4 Trigger Detectors

The fundamental trigger conditions which were used to select events for our analysis sample were based on the signals of two extremely fast detectors. First of all, at approximately ± 20 m outside the RHIC interaction regions, Zero Degree Calorimeters [61] (ZDC) were installed, as shown by figure 2.12. As indicated, the ions are bent by the RHIC dipole magnet and continue their way in the collider. However, when a collision occurs, in this analysis between a deuterium and a gold ion, evaporation neutrons remain almost parallel (< 2 mrad) to the beam line and hit the ZDCs.

The ZDCs are calorimeters composed of tungsten plates ($2\lambda_I$ in total) with wavelength shifting fibers in between. The latter route the Čerenkov light to a PMT after which the signal is digitized. The ZDCs are extremely fast, the main spread in the transit time of light is a result of the passage along the optical fibers. Its design goal was to achieve a time-of-flight resolution better than ~ 200 ps.

The detection of neutrons passing through the ZDC serves as an indicator of a hadronic collision. Moreover, the multiplicity of neutrons can be used to extract information on the impact parameter of these collisions. Finally, the ZDCs can be used to detect the interaction vertex by measuring the delay of the PMT signal with respect to the RHIC bunch crossing time. The above makes the ZDC a valuable trigger detector which can operate at the fastest

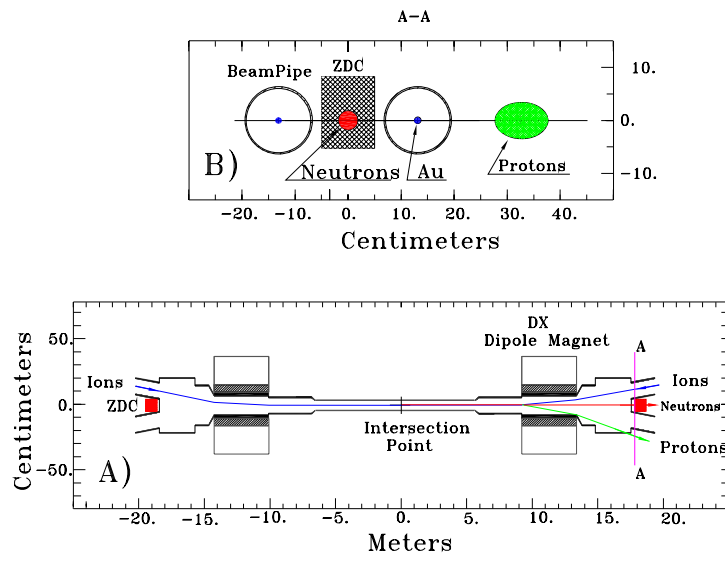


Figure 2.12: A cross section in the (x, y) plane at the location of the ZDCs (B) and a cross section in the (x, z) plane at $y = 0$ (A).

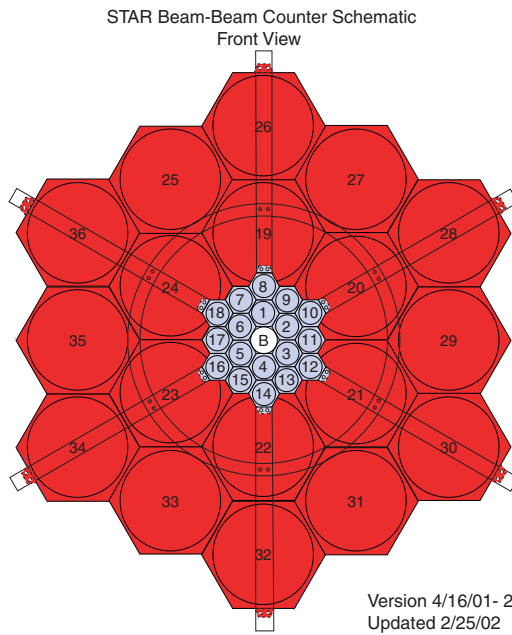


Figure 2.13: The BBC as seen from the beam line.

level of the STAR trigger system. The signal in the east ZDC as well as its timing information was the main input of the minimum bias definition in d+Au collisions, as explained in section 2.3.2.

A different set of trigger detectors is required in order to detect the collision of two protons. These are the Beam-Beam Counters (BBC) which are scintillators mounted around the beam axis at ± 374 cm from the nominal interaction region $z = 0$ [62]. The scintillator tiles are shown schematically in figure 2.13 in case of a single BBC. The 36 small inner hexagonal tiles (18 on both sides of STAR) cover a pseudo-rapidity interval approximately equal to $3.4 < |\eta| < 5.0$, and similar for the large tiles with $2.1 < |\eta| < 3.6$. Wavelength shifting fibers are embedded in the scintillating tiles and the optical signal is transported through a clear fiber to a PMT and subsequently digitized.

Upon a proton-proton collision, the charged remnants are focused in the forward direction and hit the BBC tiles which generates the scintillation light. The minimum bias baseline trigger of our data sample from p+p collisions was a coincident signal of the east and west BBC. The coincidence requirement was important to suppress false triggers coming from beam backgrounds. In principle, the BBCs could be used to trigger on d+Au collisions as well. However, it was found that the ZDC based trigger was approximately 10% more efficient.

2.3 Data Acquisition

The data which were analyzed for this research were recorded during the 2003 d+Au run (Run-3) and the 2005 p+p run (Run-5) at RHIC (see table 2.1). Such a run period typically lasts for one up to a few months and can be divided into separate beam stores (or fills). After injection, the intensity of the beam degrades, according to an exponential decay law, and the beam will therefore last a limited number of hours.

During a beam store, the recorded data was segmented in multiple runs and each of these runs corresponded to approximately 30 minutes of beam time. In the course of a run, typically 10^5 collisions were triggered. The collected data which was associated with a single triggered collision is referred to as an event. The further processing of these events is the subject of chapter 3. The sampled raw data and the system which was used to steer its recording will be discussed below.

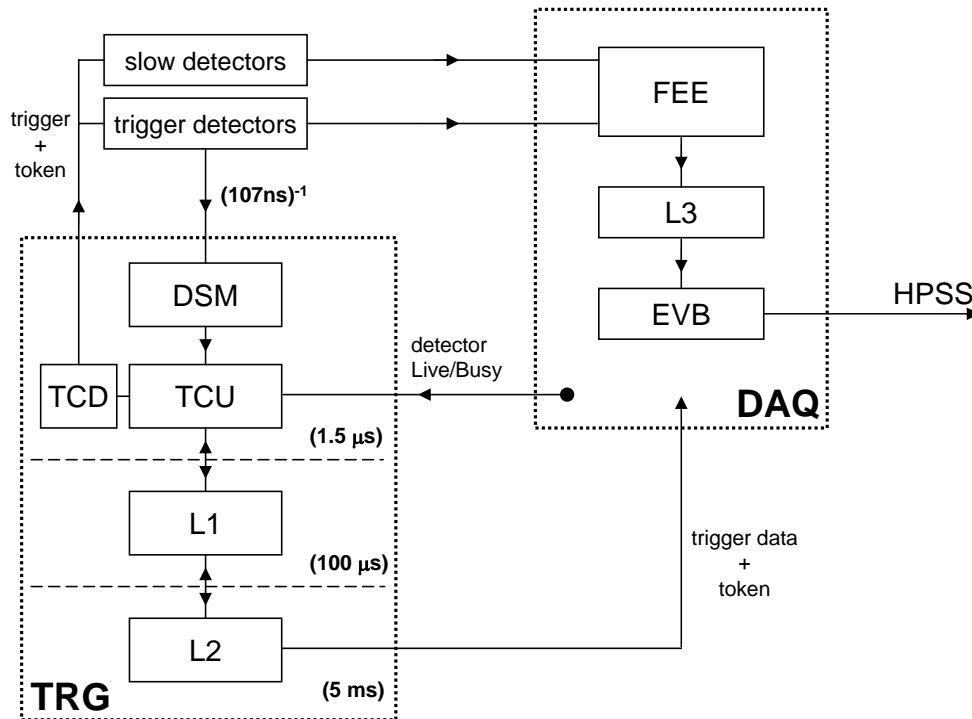


Figure 2.14: A schematic representation of the STAR data acquisition (DAQ) and trigger system (TRG).

2.3.1 Trigger and DAQ

The STAR trigger system [54] (TRG) was used to analyze the digitized signals from the fast trigger detectors at a rate equal to the RHIC bunch crossing frequency (~ 10 MHz). Based upon these signals, the decision was made whether to begin the cycle of amplification, digitization, and acquisition for the slow detectors, or to abort the event. These slower detectors, such as the TPC, were operating with a typical maximum rate of 100 Hz. Therefore, the trigger system had to facilitate a reduction of the event rate by almost 5 orders of magnitude.

In figure 2.14, the flow of data through TRG is schematically shown. For every bunch crossing, the data from the fast detectors were sent to the Data Storage and Manipulation (DSM) boards, a multi-layer pipeline designed as a fast decision tree. The final DSM output, a set of 16 bits each of them indicating whether a certain condition was met, was then passed on to the Trigger Control Unit (TCU) where it was combined with the detector status

bits (Live/Busy) into a trigger word. This trigger word was mapped onto an action word, containing information on which detectors should be triggered to perform a given action. A pre-scale system was used to suppress very frequent trigger types, thereby providing bandwidth to rare events.

Once a trigger was issued, a token was released by the TCU to serve as a unique event identifier up to the point where the decision was made to either store or abort the event. Subsequently, the action word, trigger word, and token were sent to the Trigger and Clock Distribution (TCD) network, combined with the RHIC strobe and sent to the detectors to start the digitization of the buffered signals. This part of the TRG is referred to as Level 0 (L0) and it was capable of issuing triggers within $1.5 \mu\text{s}$ of the corresponding collision.

During the digitization process, the higher level trigger systems (L1,L2) had up to a few milliseconds to perform further analysis on the available data. L1 and L2 could either accept or abort events, thereby notifying the relevant detector subsystems through the TCU as well as the data acquisition system [63] (DAQ). However, the triggered events which constituted the data sample used for this analysis had no constraints at L1 and L2 and were therefore always accepted at these levels.

Based on the token received from L2, DAQ collected and processed the data coming from the various STAR subsystems, as indicated in figure 2.14. The size of the data volume which was processed was dominated by the output of the tracking detectors, in particular by the TPC and was as large as 30 MB per central Au+Au event. The input rate of events to DAQ was limited by the TPC front-end electronics to approximately 100 Hz. The main task of the STAR DAQ system was to reduce the throughput of data to at most 50 MB/s before it could be stored on tape (HPSS) at the RHIC Computing Farm [64].

This reduction was achieved, first of all by a zero-suppression of the raw data and additionally, by applying an additional filter to the events, the L3 trigger [65]. When the event was accepted by L3 as well, the Event Builder (EVB) started to collect all relevant information and prepared the transfer of the constructed event to HPSS. Finally, the token was released to the trigger system and available for re-use.

The STAR trigger framework allowed to trigger on different event types simultaneously. Before the start of a new run, a trigger configuration was chosen which contained multiple trigger definitions. Such a trigger definition corresponded to a collection of requirements on the input bits of the TCU and had its own pre-scale value, calculated based upon the assigned bandwidth. When these requirements, as well as the pre-scale condition, were fulfilled, the event was labeled with a unique identifier. The STAR trigger framework

was designed such that a single event could have multiple identifiers.

2.3.2 Data Sample

To measure the cross section of a process such as $p+p \rightarrow \pi^0 + X$, it is essential to trigger on collisions with the least possible bias towards the final state of the interaction. These are referred to as minimum bias (MB) collisions and constituted the fundamental data sample of our measurement.

Minimum Bias Events

The MB trigger in p+p collisions accepted events which caused coincident signals in both BBCs. The timing difference between the east and the west BBC was used as a measure for the z component of the interaction vertex and constrained by the trigger to a predefined window. In case of d+Au collisions, the MB trigger required at least one neutron to be detected in the east ZDC, where the Au-nuclei entered the interaction region from the west (c.f. figure 2.1). Note that this trigger did not require coincident hits on both sides of the interaction region, increasing its susceptibility to beam background events. Hence, the vertex position of the event was restricted by the timing difference between the hit in the east ZDC and the RHIC strobe which signals the bunch crossings.

The part of the p+p hadronic cross section to which the BBC trigger was sensitive has been measured with a Vernier-scan [67] and was equal to $26.1 \pm 0.2(\text{stat.}) \pm 1.8(\text{sys.}) \text{ mb}$, which amounts to $87 \pm 8\%$ of the non-singly diffractive cross section [68]. The d+Au hadronic cross section has not yet been measured at RHIC. A Monte-Carlo Glauber calculation [69], using the Hulthén wave-function of the deuteron [70], resulted in $2.21 \pm 0.09 \text{ b}$ and the ZDC efficiency was found to be $95 \pm 3\%$ [40].

Hightower Triggered Events

Even with the full bandwidth of the DAQ system available to the MB trigger, the integrated luminosity would not have been sufficient for the reconstruction of particle spectra at large values of transverse momentum (p_T). Because these spectra are rapidly decreasing with p_T , the likelihood of an event with a high p_T particle in the final state of the interaction is relatively small. To enrich the data sample with these rare events, the hightower trigger selected MB events which had a large deposition of transverse energy (E_T) in a single BEMC tower. More detailed information on the hightower trigger is given in section 2.2.2.

collision	trigger	threshold		\mathcal{L}
		6 bit ADC	E_T (GeV)	
d+Au	MB	-	-	$17.0 \mu\text{b}^{-1}$
	HT1	8	2.5	$200 \mu\text{b}^{-1}$
	HT2	13	4.5	$1720 \mu\text{b}^{-1}$
p+p	MB	-	-	0.34nb^{-1}
	HT1	13	2.6	650nb^{-1}
	HT2	17 (20)	3.5 (4.2)	2830nb^{-1}

Table 2.3: The integrated luminosities and the trigger thresholds (in terms of 6 bit trigger ADCs as well as E_T) for the Run-3 d+Au and Run-5 p+p data. The data obtained with the threshold $E_T = 4.2 \text{ GeV}$ was not used in this analysis.

Table 2.3 lists the final integrated luminosities for the Run-3 d+Au and Run-5 p+p data set. Two different thresholds, labeled hightower-1 (HT1) and hightower-2 (HT2), were set on the 6-bit trigger ADCs to cover a broad and continuous range in p_T . Using the average gain of the towers, these thresholds can be converted to the E_T values shown in the table. The HT1 as well as the MB event rates were suppressed with a pre-scale in order to optimally distribute the available DAQ bandwidth over the various triggers.

Chapter 3

Data Analysis

The reconstruction of electromagnetic showers in the BEMC was the first step in our analysis of neutral pion and direct photon production. In this chapter, we will discuss the conversion of the raw data to our final sample of photon candidates, as well as the selection criteria which have been applied to optimize the quality of the data set. The simulation framework, used to determine the required corrections to the measured photon and neutral pion signals, will be introduced in the final part of this chapter.

3.1 Event Reconstruction

For each run the raw detector and trigger data were split up in relatively small files and written to the HPSS facility. This made parallel processing of the data possible during which the raw event was converted to the MuDST¹. This event format provided an easy access to more physical quantities such as the energy and position of hits and the location of the event vertex. The production of the MuDST events was a collaborative effort, requiring massive resources in terms of data storage and CPU capacity. A particularly demanding task was the reconstruction of tracks in the TPC and the determination of their common vertex. A summary of the employed routine is given below, however, a more detailed description can be found in [49].

Although the reconstruction of the showers in the BEMC was an integral part of the MuDST production, the raw ADC values of the towers and strips were saved at this stage as well. Hence, it was possible to repeat the shower reconstruction afterwards, with the produced MuDST events as an input. This approach was essential, first of all, because the final calibration of the

¹MuDST stands for Micro Data Summary Tape, reflecting the compact format which holds the event data.

BEMC towers required the full information of the TPC tracks which was available after the production of the MuDST events. Next to that, the end user was able to process the BEMC data with different implementations of the analysis software. The latter was used to optimize the algorithmic performance and to evaluate systematic dependencies on specific cuts and settings. The shower reconstruction algorithm will be discussed in section 3.3.3.

3.1.1 TPC Tracking and Vertex-finding

A charged particle which traversed the TPC volume liberated electrons in the TPC gas. Due to the applied electrical field, these electrons then drifted towards the end cap of the TPC where the induced signal was converted to an ADC value for consecutive time bins. This ADC value, the location of the pad, and the time bin in which the charge was collected were translated into a TPC pixel and the pixels which were close in space and time, were grouped into clusters. After the unfolding of pixels from intersecting tracks, the final TPC hits were created. The above manipulation of TPC data was already performed with the L3 software (see section 2.3). The hits were input to the Time Projection Chamber Tracker (TPT), the offline track reconstruction algorithm which was used for the production of the MuDSTs.

The TPT algorithm started in the outermost pad row, where the density of TPC hits was lowest, by identifying small groups of hits which overlapped in time. A straight line was used to characterize such a group of hits and this line was extrapolated to the next pad row. When a hit was close to the point of extrapolation, a basic helical trajectory was assigned as a first segment of the track. After all hits in the outermost pad row were processed, the algorithm continued with the next pad row inward.

Subsequently, the preliminary helices were extrapolated in both directions across the TPC volume and additional hits were added to the track segment. The segments were then combined into tracks, again using a helix to describe the path of the particle in the STAR magnetic field. A statistically robust refit of these tracks was performed with a Kalman filter [66] and resulted in a global track which contained, for example, the momentum and charge of the particle, its energy loss (dE/dx) in the TPC gas, and the χ^2 of the Kalman fit.

Finally, the primary event vertex was determined by extrapolating all global tracks to the center of the STAR detector and minimizing their distance to an initially chosen position, the vertex seed. The sum of all distances was minimized by varying this position and the procedure was repeated with an updated seed. The above was carried out iteratively until a stable pri-

mary vertex position was found. Global tracks were then refit, including the primary vertex as an additional fit point. The latter incorporated the momentum distortion which was caused by the scattering and energy loss in the volume between the vertex and the first pad row. This significantly improved the momentum resolution of the resulting primary tracks.

3.2 Event Selection

After the production of the MuDST files, the first step in selecting an event sample for data analysis was the run-by-run quality assurance. This was based on quantities such as the average number of BEMC hits per event and the level of beam background as determined with a study of abort gap events [71]. Abort gaps correspond to empty beam buckets of the collider. When an event was triggered in coincidence with the crossing of such an empty bucket, this could not be the result of a genuine collision. Hence, an analysis of such abort gap events could be used to monitor the level of beam background during a beam store. The above, in combination with the quality label assigned during the actual recording of the raw data, resulted in a final list of runs which was suitable for further analysis. The size of the data sample was further reduced by imposing constraints on characteristic properties of a single event.

3.2.1 Beam Background

A prominent background to the measurement of photons in the BEMC was caused by the scattering of the deuteron beam halo on material located approximately 40 m upstream of the STAR interaction region. Highly energetic particles which were produced in this reaction propagated almost parallel to the beam and deposited large amounts of energy in the BEMC. Since these particles entered the STAR detector from the side, their tracks were not reconstructed by the TPT. Nevertheless, an asymmetry in the azimuthal distribution of the TPC clusters was observed which matched the expected pattern of these background tracks.

The anomalous showers in the BEMC could not be distinguished from genuine photons originating from the event vertex and thus constituted a problematic background to a photon measurement. Because the background clusters in the BEMC were relatively energetic, the most significant contamination was that of the hightower triggered data. Figure 3.1 shows the total energy measured with the BEMC versus the summed p_T of tracks in the TPC for HT1 d+Au events. A sizeable number of events is visible with a large

deposition of energy in the BEMC but relatively little summed momentum in the TPC. The full line in the figure indicates the cut which was used to exclude these background events from the data sample:

$$\frac{E(\text{BEMC})}{E(\text{BEMC}) + p_T(\text{TPC})} < 0.8 \pm 0.1. \quad (3.1)$$

The quoted uncertainty in this expression will be used in later chapters to evaluate the systematic dependence of the final results on this cut. Note that the absence of entries with a BEMC energy smaller than approximately 2.5 GeV is a consequence of the HT1 trigger threshold.

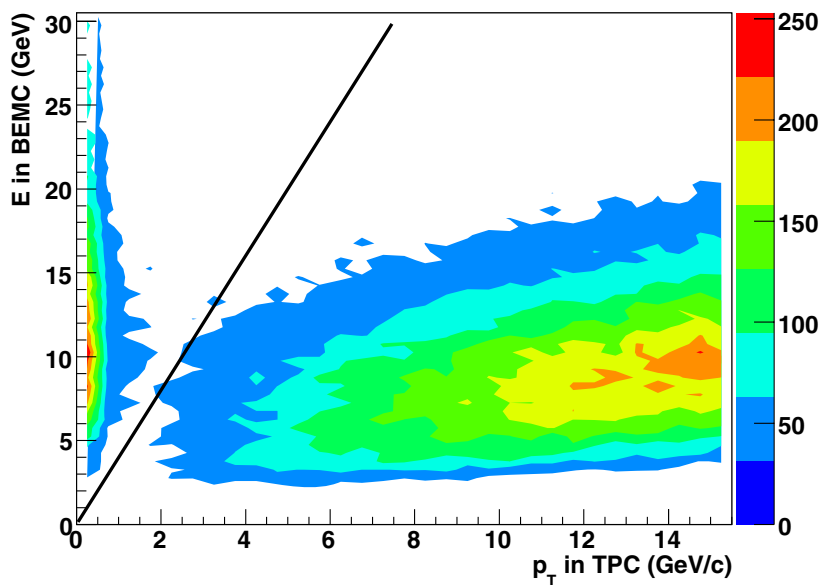


Figure 3.1: The total energy per event measured with the BEMC versus the summed p_T of tracks reconstructed with the TPC for HT1 events. The full line represents the cut which was used to eliminate these background events.

The level of beam background in the Run-5 p+p data was not as prominent as in the Run-3 d+Au data. This was partially due to the minimum bias (MB) trigger in p+p which required a coincident signal of the BBCs, as opposed to the d+Au run where a stand-alone signal in the east ZDC was sufficient to fulfill the MB condition. In addition, a more accurate monitoring of the beam background conditions during the p+p run contributed to the quality of these data as well. Before the start of Run-6, additional shielding was installed on both sides of the STAR interaction region to further reduce the background caused by the beam halo.

3.2.2 Vertex Position

The reconstructed vertex of the event was constrained to a narrow interval around the center of the STAR detector ($z = 0$). This vertex cut served multiple purposes. First of all, since the BEMC towers were projective with respect to $z = 0$, it was more likely that the longitudinal development of the shower was confined to a single tower. In addition, it effectively lowered the amount of material in front of the BEMC because a large fraction of this material was located at $\eta > 1$ (see section 4.2.4 on photon conversions). Finally, it increased the reconstruction efficiency of tracks which became smaller towards the edges of the active TPC volume. The spread of the vertex position in the plane perpendicular to the beam line was constrained by the transverse extension of the beams themselves. The x and y values were required to be within 5 cm of the beam line and this condition was satisfied by effectively all triggered events.

The TPC vertex was reconstructed for $93 \pm 1\%$ of the MB d+Au events. The position resolution was better than 1 cm for all three coordinates [40, 71] and constant within the vertex window $-60 < z < 60$ cm which was used for this analysis. For p+p collisions, the vertex position based on the BBC timing difference was used to select events. Due to the definition of the MB trigger, every recorded p+p event had a reconstructed BBC vertex position and consequently the vertex-finding efficiency was 100%, contrarily to a TPC vertex finding efficiency of approximately 63%. A linear transformation was necessary to map the BBC timing difference to the correct z value. The primary TPC vertex was used to determine the parameters of this map and the resulting correlation was 1.009 ± 0.001 and is shown in figure 3.2.

Although p+p events were selected based on their BBC timing difference, the TPC vertex was used for the analysis whenever it was successfully reconstructed. This was the case for effectively all hightower triggered events and for approximately 63% of the MB events. For the fraction of p+p events without a TPC vertex, the BBC information was used instead. However, the position resolution of the BBCs was not negligible, namely 43.9 ± 0.2 cm, and was accounted for as explained in section 4.2.1.

3.2.3 Final Event Sample

The size of the final data sample, after the run-based quality assurance and the event cuts discussed above, is given in table 3.1. Note that the average pre-scale factors (see section 2.3.2) for a certain trigger condition can be easily obtained from the table by taking the ratio of the integrated luminosity \mathcal{L} with respect to that of the HT2 trigger. The MB events were suppressed

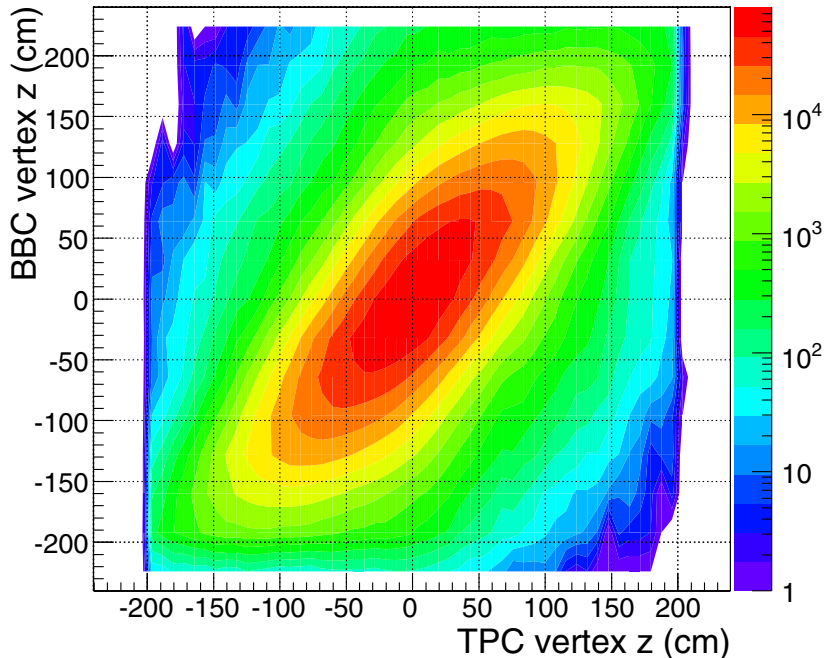


Figure 3.2: Reconstructed vertex z based on the BBC timing difference versus the primary TPC vertex for minimum bias p+p collisions.

by a pre-scale factor ps_i^{MB} to enable readout bandwidth for the recording of the events satisfying the HT2 condition. The number of MB events that would have resulted in the HT2 data sample was therefore equal to the sum of these MB pre-scale factors. The integrated luminosity sampled with the HT2 trigger could then be calculated as

$$\mathcal{L} = \sigma_{\text{MB}}^{-1} \sum_{i=1}^{N_{\text{ev}}^{\text{MB}}} ps_i^{\text{MB}} \quad (3.2)$$

where the summation was carried out over all MB events recorded when the hightower trigger was active. The parameter σ_{MB} corresponds to the part of the total cross section which was captured by the MB trigger (see section 2.3.2).

3.3 Processing of BEMC Data

Before the photon candidates could be reconstructed from the BEMC data, the raw ADC values were converted to energies for all towers and strips.

collision	trigger	number of events	\mathcal{L}
d+Au	MB	6.3×10^6	$2.7 \mu\text{b}^{-1}$
	HT1	2.0×10^5	$111 \mu\text{b}^{-1}$
	HT2	1.1×10^5	$1064 \mu\text{b}^{-1}$
p+p	MB	2.3×10^6	0.09nb^{-1}
	HT1	5.1×10^5	72nb^{-1}
	HT2	4.1×10^5	282nb^{-1}

Table 3.1: The size of the data sample after the run-based quality assurance and the event cuts.

For this conversion, the calibration coefficients of the channels had to be determined as well as the ADC value of the pedestal. In addition, a status code was assigned to individual channels such that the energy could be set to zero for dead and malfunctioning strips and towers. All this information was stored in a central database in terms of dedicated tables which were marked with a timestamp to account for the time dependence of these values.

3.3.1 Noise Pedestals and Status Tables

The position and width of the noise peaks followed from an analysis of the raw BEMC data. For every channel a spectrum of ADC values was generated and the peak was fit with a Gaussian distribution. A typical example of an ADC spectrum of a single BSMD channel is shown, together with the result of the fit, in figure 3.3. Relatively few events were required to measure the mean and width of the peaks with high precision. The drift of these values over time was investigated as well and found to be negligible.

To determine the status of the towers and strips, the raw ADC values were accumulated for short time intervals of the RHIC run, typically once per beam store, and a status code was assigned based on several criteria. These included the goodness of the fit to the noise peak, its position and width, and the number of ADC counts above a threshold. The latter was used to identify towers which fired with an abnormally high frequency (hot towers) as well as those which fired significantly below average (cold and dead towers). The data from such towers were excluded from further analysis.

The average percentages of dead and malfunctioning towers were approximately 3% and 10% for p+p and d+Au collisions, respectively. For the BSMD the approximate percentages were 10% for the phi-plane and 17% for the eta-plane during both RHIC runs. Many of these strips were dead due to high-voltage failures of the anode wires which affected an entire module.

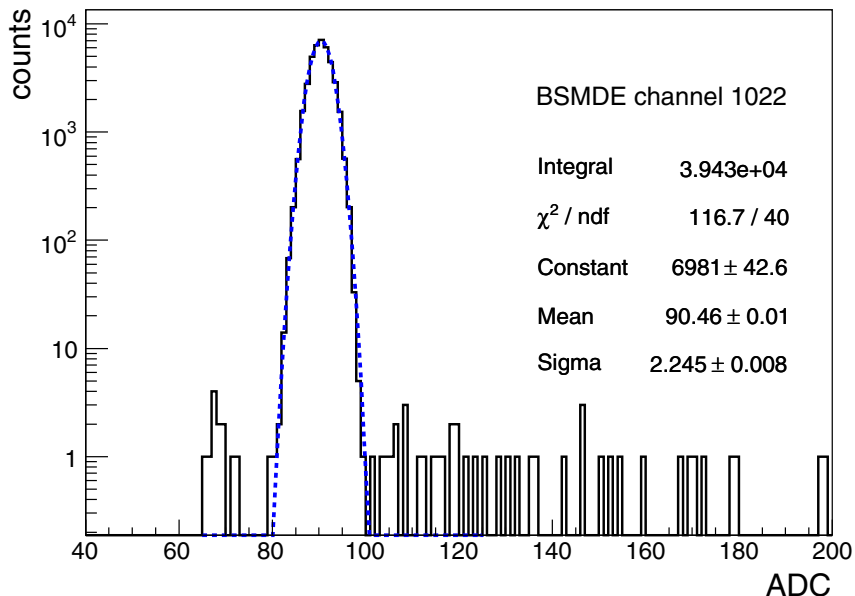


Figure 3.3: The raw ADC spectrum of a single BSMD strip for $\sim 4 \times 10^4$ p+p events and the Gaussian fit (dashed line) to the noise peak.

Consequently, there was a significant spatial overlap of bad channels from both BSMD planes.

3.3.2 Energy Calibration

The high-voltage for each of the tower PMTs was set at the beginning of a RHIC run before the actual recording of data started. The desired full-scale energy (30 GeV for p+p and 60 GeV for d+Au) and the dynamic range of the ADCs (0–4095) were translated into a nominal high-voltage. Subsequently, the E_T response as a function of η was equalized. To achieve the latter, tower ADC spectra from dedicated minimum bias runs were fit with an exponential function in a region well above the pedestal. The slopes of these functions were used as a measure of the tower gains, which was validated by the linear response of the BEMC. The high-voltage of each of the corresponding PMTs was adjusted to match the slopes to the intended η dependence: proportional to the inverse of $(1 + 0.056 \eta) \sin \theta$. The presence of the factor $1 + 0.056 \eta$ was due to an artifact of the detector itself and is explained in [72], the factor $\sin \theta$ was applied to obtain a constant E_T response over the entire BEMC acceptance. The above routine was carried out iteratively until convergence

was reached and consequently, the effective E_T thresholds of the hightower trigger were uniform as a function of η .

Offline BEMC Calibration

The offline calibration of the BEMC was accomplished in three steps which we will summarize below. Further information on the BEMC calibration can be found in [73]. After the production of the MuDST files, the full information from the detectors was available for further analysis. The first step of the analysis was performed making use of minimum ionizing particles (MIP), energetic charged hadrons which deposit a minimal amount of energy (~ 20 MeV) due to ionization of the detector material. These MIPs were identified as isolated BEMC hits with an associated track in the TPC. After the removal of background contributions, the most probable value of the pedestal-subtracted ADC distribution was translated into a calibration coefficient by means of the calculation described in [72].

The second step involved the measured momentum of electrons, identified through their energy loss (dE/dx) in the TPC. The electrons were grouped for multiple intervals of η and the ratio of their momentum and tower energy (p/E) was plotted as a function of the distance of the projected track to the center of the tower: $R = (\Delta\phi^2 + \Delta\eta^2)^{1/2}$. The R dependence of the p/E distribution, caused by the leakage of energy to neighboring towers, was determined in a GEANT simulation of the detector and corrected for. Hence, for each interval of η , the cumulative p/E distributions were Gaussian. The factor which was used to set the mean of these distributions equal to unity was then applied to the calibration coefficients from the MIP analysis. Note that an ideal calibration would indeed imply that $p/E = 1$ in case of electrons.

Finally, the overall distribution of the ratio of tower energy and TPC momentum (E/p) was formed for all electrons which passed through the center of the tower ($R < 0.003$). This time E was calculated with the updated calibration coefficients from the second step. A Gaussian distribution was fit and a correction factor for E was derived such that the ultimate distribution was centered exactly at 1, as shown in figure 3.4.

Although the MIP-based calibration already provided the absolute energy scale for each individual tower, the determination of the global energy scale and the η dependence of the gains by means of electrons was preferred. The MIP peak resided at relatively low energy where the energy resolution was poor and the signal distorted by noise. A small absolute error on the calibration coefficient would therefore cause a large relative error on higher values of E . This is in contrast to the electron-based calibration for which all electron momenta were required to be larger than 1.5 GeV/ c , thus providing

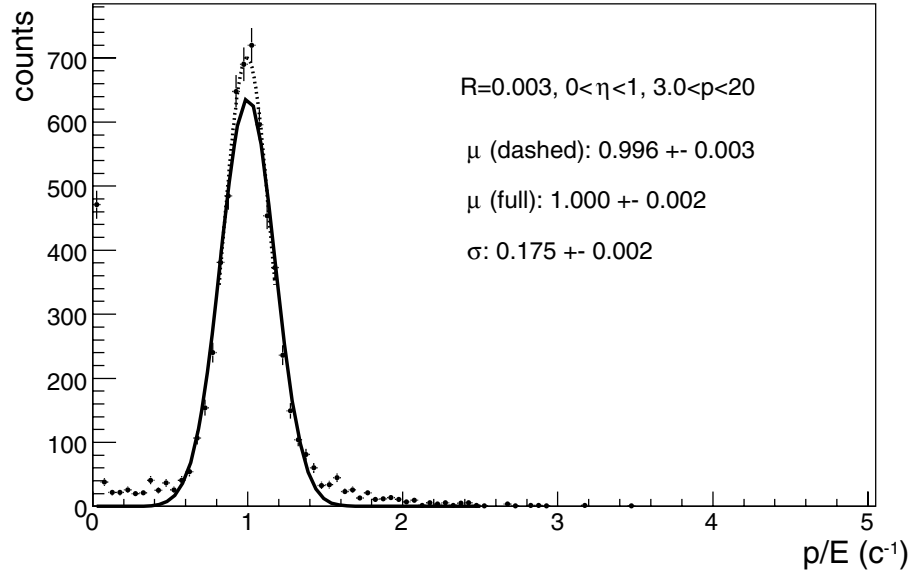


Figure 3.4: The final p/E distribution of the p+p 2005 calibration analysis. The full (dashed) line is the Gaussian fit with (without) the residual background subtracted. The parameters R , η , and p are explained in the text and μ and σ represent the mean and width of the fit, respectively.

a more accurate extrapolation to higher energies. The final uncertainty on the global BEMC energy scale was 5% (4%) for d+Au (p+p) collisions and was predominantly caused by the remaining contamination of the electron sample with charged hadrons.

3.3.3 Shower Reconstruction

The energy E of a hit was calculated from the raw ADC values as

$$E = C_1(\text{ADC} - \text{PED}) + C_2(\text{ADC} - \text{PED})^2 \quad (3.3)$$

where PED is the location of the pedestal and C_i the calibration coefficients. The coefficient C_2 was zero for the towers as a result of their linear energy response. When the status table indicated that a specific channel was not functioning properly, the hit was excluded from further analysis by setting its energy to zero.

The energy of a photon was generally spread out over multiple towers and strips due to the transverse expansion of electromagnetic cascades in the calorimeter material. To recover the total energy, the position of impact, and the lateral profile of the shower, clusters of adjacent hits were formed for the towers and both BSMD planes. When clusters from different subsystems

could be associated with a single incident particle, they were combined into a photon candidate.

Clustering Algorithm

The clustering was performed in each of the subsystems separately. For a single module, a list was created in which the hits were sorted with respect to their energies. The algorithm scanned through the list, starting with the most energetic hit. When its energy was greater than the threshold value E_{seed} , it constituted the first element of a cluster and was removed from the list. The remainder of the list was then searched for hits which were adjacent to the cluster and above a second threshold E_{add} . When such a hit was encountered, it was added to the cluster and removed from the list as well. In case that no (more) adjacent hits were found or when the maximum number of hits in a cluster N_{max} was reached, the above was repeated for the next-most energetic hit. The default settings used for this analysis are given by table 3.2. During the MuDST production, BSMD hits were rejected whenever their pedestal-subtracted ADC was less than 1.5 times the width of the noise peak (zero-suppression). Hence, the effective threshold E_{add} for the BSMD was ~ 0.03 GeV.

subsystem	E_{seed} (GeV)	E_{add} (GeV)	N_{max}
BEMC	0.35	0.035	4
BSMDE	0.20	0.0005	5
BSMDP	0.20	0.0005	5

Table 3.2: The parameters used for the clustering algorithm.

A tower was considered to be adjacent to a cluster when both shared either a border or a corner. In case of the BSMDP, only strips which were contiguous in the azimuthal direction ($\hat{\phi}$) could be added to the cluster. For a single module, the strips in the BSMDE extended only in η and consequently there was no ambiguity in the definition of adjacency. Since there were sizeable gaps (5.6 mm) between the modules, the development of the showers across the module edges was distorted. Hence, a reconstructed cluster only contained hits from one specific module.

The position \vec{x} and the energy E of a cluster were calculated as

$$E = \sum_i E_i \quad (3.4)$$

$$\vec{x} = \sum_i \frac{E_i \vec{x}_i}{E} \quad (3.5)$$

where E_i is the energy in channel i and \vec{x}_i its two-dimensional coordinate (η, ϕ) . Note that the radial coordinate was effectively constant for each of the subsystems.

Next to the splitting of reconstructed showers near the module boundaries, the clustering algorithm led to other artifacts. It was possible that a single shower deposited energy in two neighboring BSMDP sub-modules such that two clusters were found instead of one. Fluctuations in the energy response of a single strip gave rise to an anomalous splitting of clusters as well. At large energies however, the presence of two nearby clusters in the BEMC was similar to the signature of genuine neutral pions. These cluster splitting effects could therefore lead to an artificial enhancement of the neutral pion yields. The correction for these artifacts was an integral part of our efficiency determination, as discussed in section 4.2.1.

Figure 3.5 gives an illustration of typical clusters in the BSMDE in case of a single incident photon (a), two photons originating from a decaying neutral pion (b), and the splitting of the shower due to a malfunctioning strip (c). Note that even when both photons from a decaying pion deposited energy in a single strip, it was assigned to the cluster which contained the most energetic strip.

Photon Candidates

Since the clustering was performed independently, the clusters from the BEMC, BSMDE, and BSMDP were associated with photon candidates afterwards. For this analysis, the photon candidates were required to consist of three clusters, one in each of the subsystems. The BEMC cluster constrained the energy of the shower and the clusters in the BSMDE and BSMDP determined the shower axis in terms of η and ϕ , respectively.

The association of the clusters to a photon candidate was not a straightforward procedure. The encountered ambiguity is illustrated in figure 3.6 for two photons (γ_1 and γ_2) initiating a cascade in the same tower patch. The unfolding of the BEMC cluster, which in this case consists of three towers, has to be done based on the BSMD clusters. However, the BSMD provides no direct distinction between the actual shower axes, (η_1, ϕ_1) and (η_2, ϕ_2) , and the erroneous shower axes, (η_1, ϕ_2) and (η_2, ϕ_1) . Nevertheless, the energy of the clusters should be equal when both are a result of the same shower and the optimum combination of the clusters i and j is the one which minimizes the energy asymmetry

$$S_{ij} = \frac{|E_{\eta_i} - E_{\phi_j}|}{E_{\eta_i} + E_{\phi_j}}, \quad (3.6)$$

where E_{η_i} is the BSMDE energy for cluster i and correspondingly for E_{ϕ_j} .

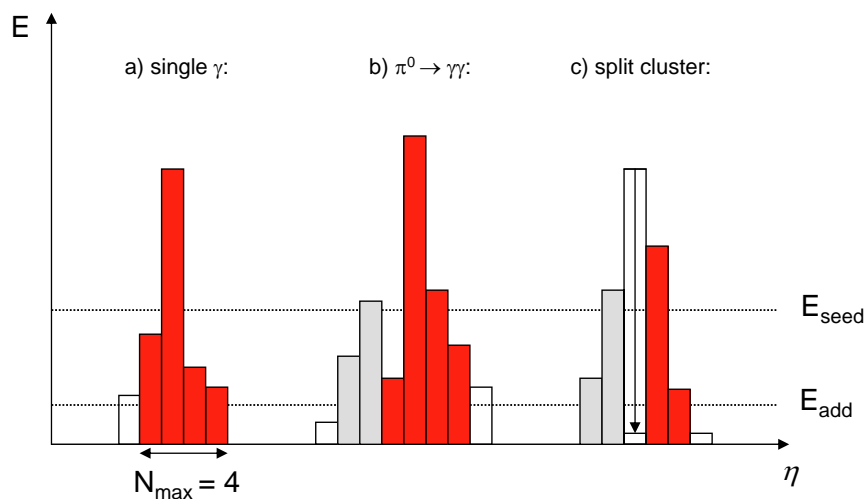


Figure 3.5: Schematic representation of the clustering algorithm in the BSMDE.

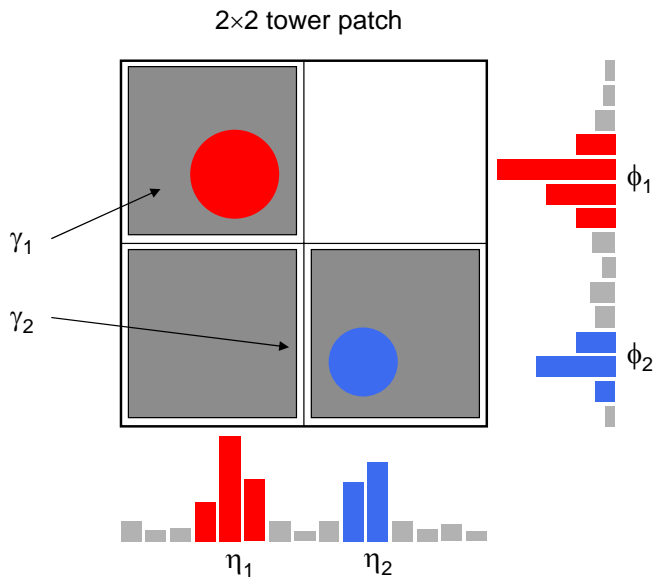


Figure 3.6: Illustration of the assignment of clusters to the photon candidates.

In practice, this assignment problem was addressed with the `ASSNDX` routine from the CERN program library [74].

The matrix S_{ij} was determined for combinations of BSMD clusters in the separate tower patches. After the minimization, the energy and position of photon candidate (k, l) was given by

$$E(k, l) = \frac{E_{\eta_k} + E_{\phi_l}}{\sum_i E_{\eta_i} + \sum_j E_{\phi_j}} \times E_{\text{patch}} \quad (3.7)$$

$$\vec{x}(k, l) = (\eta_k, \phi_l), \quad (3.8)$$

with E_{patch} the energy of the BEMC cluster in the patch. The above, when combined with the information on the primary event vertex, constrained the four-momenta of the photon candidates.

Selection Criteria of Photon Candidates

Although the active volume of the BEMC during Run-3 and Run-5 extended from $\eta = 0.0$ to $\eta = 1.0$, only photon candidates were considered which were reconstructed within $0.1 < \eta < 0.9$. Besides the unavoidable presence of edge effects, the choice of this specific range was supported by the following observations. First of all, the MIP spectra for towers with $\eta > 0.9$ contained a large amount of background which complicated the calibration. This was confirmed by the scale corrections derived with the TPC electron calibration which were as large as 17%, compared to 0–2% for the other η intervals. In addition, the amount of material between the calorimeter surface and the interaction region increases rapidly for $\eta > 0.9$ as can be seen from the conversion study in section 4.2.4. Hence, a proper treatment of photon reconstruction in this part of the detector would either require detailed knowledge of the location and amount of this material or introduce a significant systematic uncertainty on the final results.

To exclude the showers of charged particles, a charged particle veto (CPV) was applied based on the tracks in the TPC. For each photon candidate the distance to the closest global track D_{track} was determined as

$$D_{\text{track}} = |\vec{x}_{\text{track}} - \vec{x}_\gamma| \quad (3.9)$$

with \vec{x}_{track} the coordinate of the helical projection of the track onto the BEMC and \vec{x}_γ the position of the photon candidate. Candidates were rejected from the photon sample when D_{track} was smaller than a certain value D_{CPV} . A relatively large value of D_{CPV} would yield a photon sample with a high purity but with lower efficiency due to the frequent rejection of genuine photons. Contrarily, a small value of D_{CPV} increases the efficiency but inevitably leads

to a lower purity. Since a high purity of the sample was more important for a proper reconstruction of the γ_{incl} spectrum than it was for the π^0 analysis, alternative values of D_{CPV} were applied, as can be seen from table 3.3.

Only photon candidates which had a reconstructed cluster in both BSMD planes were accepted for further analysis. Furthermore, to suppress hadronic background as well as the contamination caused by split clusters, the following constraints on the transverse shower profile were alternately applied:

- SC0 := $(N_{\text{min}}(\eta) \geq 1 \wedge N_{\text{min}}(\phi) \geq 1)$
- SC1 := $(N_{\text{min}}(\eta) \geq 1 \wedge N_{\text{min}}(\phi) \geq 2) \vee (N_{\text{min}}(\eta) \geq 2 \wedge N_{\text{min}}(\phi) \geq 1)$
- SC2 := $(N_{\text{min}}(\eta) \geq 2 \wedge N_{\text{min}}(\phi) \geq 2)$

where $N_{\text{min}}(\eta)$ equals the required minimum number of strips in a BSMDE cluster, and likewise for the BSMDP. The purity of the photon candidate sample was significantly improved by changing the cut from SC0 up to SC2, but only at the cost of efficiency. This is illustrated in figure 3.7 which shows the results of a simulation of single photons and charged pions inducing a shower in the BEMC. The left panel demonstrates that the relative abundance of charged pions decreased upon requiring an increasing number of strips in a cluster. The graphs in the right panel show the number of simulated photons which led to more than one cluster in the BEMC, relative to that same number in case of SC0 (split cluster fraction). This fraction was reduced as well by strengthening the cut on the shower shape (SCX).

The results in this thesis were obtained with SC1 as the nominal constraint on the transverse shower profiles. Nevertheless, a repetition of the full analysis with the alternative cuts, SC0 and SC2, proved to be a valuable tool to investigate the sensitivity to hadronic backgrounds as well as split clusters. Table 3.3 lists the final set of cuts which led to the main results presented in this thesis.

	γ	π^0
rapidity	$0.1 < y < 0.9$	-
fiducial volume	$0.1 < \eta < 0.9$	$0.1 < \eta < 0.9$
CPV	$D_{\text{CPV}} = 15 \text{ cm}$	$D_{\text{CPV}} = 5 \text{ cm}$
BSMD shower	SC1	SC1

Table 3.3: The nominal cuts on the properties of the photon candidates used for the reconstruction of the direct photon spectrum (γ) and the neutral pion spectrum (π^0).

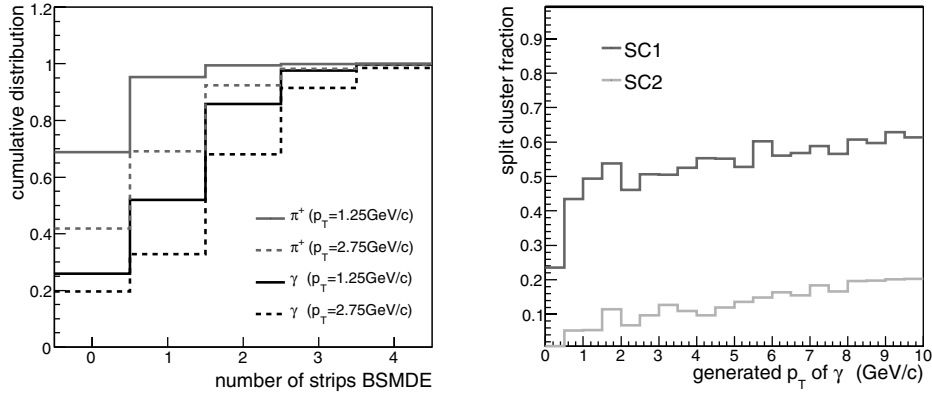


Figure 3.7: The results from a Monte-Carlo simulation. Left panel: the cumulative distribution of the number of strips in a BSMDE cluster for charged pions and single photons. The p_T values in the plot refer to the momentum reconstructed with the BEMC. Right panel: the split cluster fraction (defined in the text) of photons as a function of the generated Monte-Carlo p_T for different shower shape cuts SCX.

3.4 Detector Simulation

It was unavoidable that photon candidates were lost as a result of, for example, limited coverage of the detector, finite energy resolution, and specific analysis cuts. In order to meaningfully compare the results of this analysis to theoretical calculations as well as data from other experiments, such inefficiencies had to be accounted for. A Monte-Carlo (MC) simulation of the detector response provided a way to determine the appropriate correction factors.

3.4.1 GEANT

The GEometry ANd Tracking package [75] (GEANT) was used to describe the passage of elementary particles through matter and in particular through the STAR geometry. The GEANT package handles the interaction of particles with the implemented material and their decay processes, while keeping track of the energy deposition in the various components of the STAR detectors. The package provides the simulation of a large number of physical processes such as Bremsstrahlung, Compton scattering, and the ionization of detector material by moving charged particles. For all particles in the event, the probability that a certain process occurs is sampled from the total cross section of that process. After an interaction, the probability of the final state

is determined from the corresponding differential cross sections. The generated particle trajectories as well as the energy loss in the sensitive detector volumes are recorded and subsequently used as analog input to a simulation of the digitization procedure.

Many properties of the BEMC, such as the sampling resolution of energy in the towers, were accurately simulated. However, the shower development of particles in dense material has been an outstanding issue of GEANT. Discrepancies between the detected shower in the BEMC and the results from a GEANT simulation were already reported in [57]. The CDF experiment, which utilizes a very similar gaseous wire-proportional counter [76], found that the transverse shower profile measured in the test beam runs was not reproduced by GEANT as well [77]. Moreover, the observation of many high-energy physics experiments has been that the showers generated with the GEANT package appear to be narrower than the detected showers.

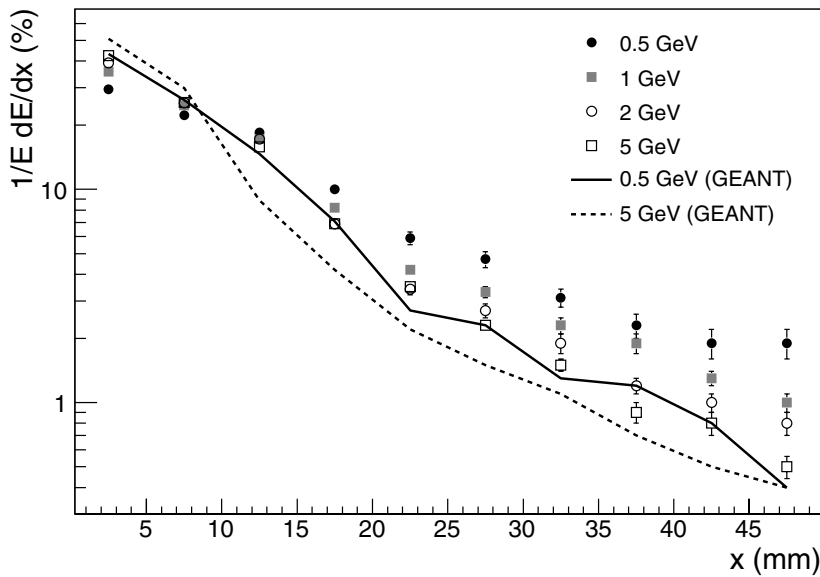


Figure 3.8: Transverse shower profiles of electrons from the test beam compared to a GEANT simulation (data taken from [57]).

A comparison between the measured profiles of electrons in the BSMD and a GEANT simulation is shown in figure 3.8. Especially at lower electron energies, the dispersion of the simulated BSMD showers deviates from the experimental observation. The latter significantly affected the calculated efficiency of the clustering algorithm. Because a larger amount of energy was deposited in the center of the shower, the threshold value E_{seed} was more

frequently exceeded. On the other hand, the strips contiguous to the centroid contained less energy which effectively raised the threshold E_{add} . This property of the simulation was discovered when N_{min} , the required minimum number of strips in the BSMD clusters of a photon candidate, was varied simultaneously for simulated and experimental data.

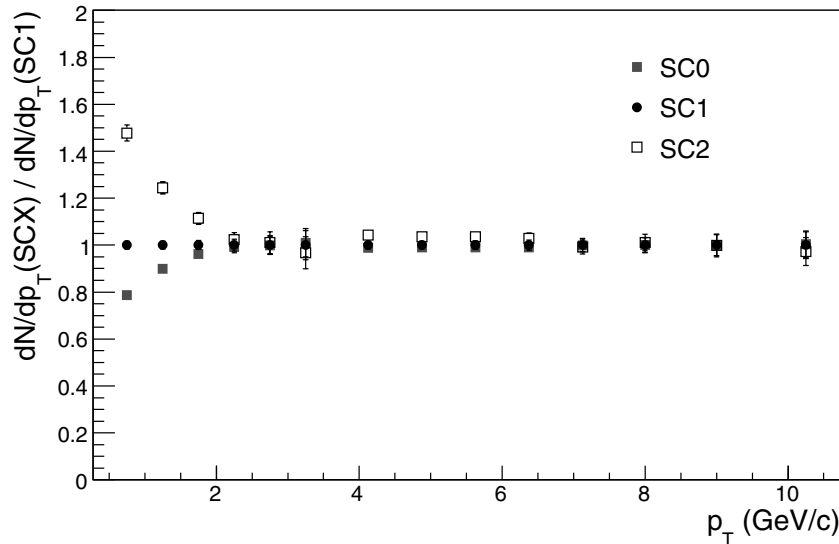


Figure 3.9: A comparison of the fully corrected inclusive photon spectra for different cuts on the BSMD shower. The data points are for minimum bias ($p_T < 4\text{GeV}/c$) and HT1 ($p_T > 4\text{GeV}/c$) p+p collisions.

In figure 3.9 the difference is shown of the corrected inclusive γ spectra for three different cuts on N_{min} . The focus is on the low p_T part of the spectrum where the threshold effects played a crucial role and the discrepancies appeared to be largest. The presence of at least one strip in each of the BSMD clusters, which is the minimum condition for this analysis, resulted in the smallest yield. This was most likely due to the overestimation of the clustering efficiency as described above. However, requiring additional strips in the cluster counteracts the previous and increased the corrected yield. For neutral pions the discrepancies were found to be larger. First of all, because they were reconstructed from pairs of photons (see section 4.1) and the calculated efficiency affects the π^0 reconstruction more or less quadratically. In addition, the p_T of each of the two decay photons was smaller than the original π^0 p_T , which increased the sensitivity to this effect as well.

At the time of writing this thesis no proper simulation of the shower development in the BEMC was available. Nevertheless, future analyses of

photon and neutral pion production at STAR would most certainly benefit from a fast Monte-Carlo simulation of the transverse component of the shower using parametrizations of experimentally determined profiles as an input.

3.4.2 Detector Response Simulation

The next step in the simulation of the experimental setup was the conversion of the energy losses in the sensitive material of the detectors to digitized signals (ADC). These signals were then stored in the default event format and fed to the same reconstruction chain as was used for the experimental data. A complete simulation of the transport and processing of the induced signals in the detectors would be tremendously time-consuming and not efficient for this analysis. Therefore the TPC Response Simulator (TRS) was used to convert the ionization energy loss of the charged particles in the gas, as determined by GEANT, to TPC hits.

The TRS consisted of computational methods to account for

- the transport (drift) of ionization electrons to the readout pads
- the amplification and charge collection on the MWPC wires
- the induction of a time-dependent analog signal on the readout pads
- the conversion of the analog signal to an ADC value

After the last step, the data format was equivalent to that of a TPC pixel and could therefore serve as an input to the TPT (see section 3.1.1). A detailed discussion of the TRS, including the various response functions, can be found in [78].

BEMC Simulation

As a first step, the GEANT energy deposit ΔE in a BEMC tower was converted to the number of initial photoelectrons at the PMT cathode n_{pe} with the equation

$$n_{\text{pe}} = \Delta E \left(\frac{n_{\text{pe}}}{\Delta E} \right)_{\text{MIP}} \quad (3.10)$$

where the fraction on the right equals the number of produced photoelectrons (63) per equivalent MIP energy (0.02 GeV). The statistical fluctuation of n_{pe} was included by replacing this value with a number sampled from a Poisson distribution. To account for the secondary PMT statistics as well,

the multiplication factor K^i (see e.g. [79]) for dynode i was calculated based on its relative voltage V^i as

$$K^i = V^i \left(\frac{g}{\prod_{i=1}^M V^i} \right)^{1/M} \quad (3.11)$$

with g the cumulative PMT gain over M dynodes:

$$g = C^{-1} S(\eta) \left(\frac{\Delta E}{n_{\text{pe}}} \right)_{\text{MIP}}. \quad (3.12)$$

In this equation, C is the calibration coefficient determined by the offline electron calibration and $S(\eta)$ represents a parametrization of the sampling fraction as a function of pseudo-rapidity. The number of electrons at each of the dynodes n_e^i followed from the relation

$$n_e^{i+1} = \mathcal{P}(K^i n_e^i) \quad (3.13)$$

where \mathcal{P} denotes sampling from a Poisson distribution and $n_e^0 = n_{\text{pe}}$. Finally, the simulated ADC value was determined as

$$\text{ADC} = g n_e^{M+1} \prod_{i=1}^M \frac{1}{K^i} + \mathcal{G}(\mu, \sigma) \quad (3.14)$$

with $\mathcal{G}(\mu, \sigma)$ a random value from a Gaussian distribution with mean μ and width σ . These were the values for the pedestal peak which were stored in the central database. Instead of carrying out the complete simulation of the multiplication over all dynodes, the loop was interrupted when the number of electrons was larger than 100. This significantly reduced the computing time, the statistical fluctuation of the final signal on the anode was in this case evaluated with the procedure explained in [80].

For the BSMD, the assumption was made that the statistical fluctuations of the digitized signal were due to the sampling resolution in the gas layer only. These fluctuations were therefore already taken into account by the GEANT simulation of the number of electrons and positrons ionizing the BSMD gas mixture. The digital signal of the individual strips followed directly from

$$\text{ADC} = C^{-1} S(\eta) \Delta E, \quad (3.15)$$

with ΔE the ionization energy loss from GEANT, $S(\eta)$ the sampling fraction, and C the calibration coefficient, all of which were determined separately for the BSMDE and BSMDP. Note that the coefficient of the non-linear term

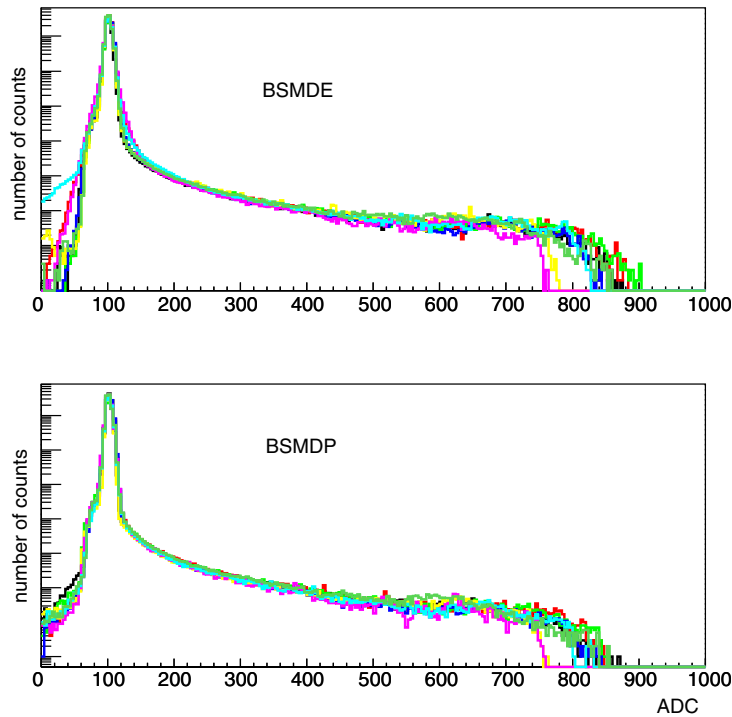


Figure 3.10: The saturation effect observed for the BSMD signal in HT2 data. The separate histograms are cumulative ADC distributions corresponding to the eight individual readout crates. The ADC values of each individual channel were shifted such that the noise pedestals were centered at $\text{ADC} = 100$. Note, however, that this is close to their actual location such that the saturation indeed occurs at ADC values equal to ~ 800 .

(see section 2.2.3) was omitted in the simulation. However, its effect on the final results turned out to be negligible.

To incorporate the limited dynamic range of the converters, a cutoff was applied to the simulated ADC at 4095 and 1023 for the BEMC and BSMD, respectively. In case of the BEMC, this value corresponds to an energy which is far outside the range considered for the results presented in this thesis. However, recent investigations indicate that the BSMD signal already saturates at lower ADC values, typically within 750–850, corresponding to electromagnetic showers with a total energy deposition of 10–15 GeV. This saturation effect is illustrated by the ADC spectra in figure 3.10. Note that the noise peaks of the channels were artificially set at 100 to enable a comparison between the individual spectra. In practice, the BSMD pedestals were spread out approximately from 50 to 150 ADC counts. This indicates that most of the channels suffered from the saturation effect and that this can not be

attributed to the limited dynamic range.

In p+p and d+Au collisions, the frequency of hits in a single BSMD strip was very low. Consequently, the saturation effects were not observed when the spectra of the individual channels were analyzed. Each cumulative distribution in figure 3.10 though, represents the combined spectra of 2250 BSMD channels and in this case the saturation is evident. The origin of the distorted ADC spectra is presently not well understood. Nevertheless, to estimate the possible consequences for a reconstruction of the photon showers, we have implemented a fixed cutoff at an ADC count equal to 650 in our simulations. Subsequently, the full analysis was repeated and the observed variation of the final results was found to be negligible given the current experimental uncertainties.

The energy measurements in the BEMC and BSMD were subject to resolution effects which were not automatically included in the discussed simulation routine. The experimental data were recorded over a longer period of time, typically a few months, which seriously challenged the stability of the various detector components. For example, the gain of the photo-multiplier tubes can change in the course of the measurement and the light output of the scintillator tiles fluctuates as a result of temperature variations and radiation damage (see e.g. [81]). The dependence of the BSMD gas gain on the atmospheric pressure is shown in figure 3.11. The fluctuations of the daily average barometric pressure in Mt. Sinai, NY, which is only a few miles from BNL, are well within 1000 hPa and 1030 hPa [82]. The latter would correspond to a relative change in amplitude (mV) of the signal of $\sim 8\%$.

To account for the above, and more importantly for the systematic errors on the relative calibration of the towers, the calibration coefficients in the simulation were modified using

$$C' = C \times \mathcal{G}\left(1 + \delta, \frac{\sigma(C)}{C}\right) \quad (3.16)$$

with C' the new coefficient and \mathcal{G} a number sampled from a Gaussian distribution with mean $1 + \delta$ and width $\sigma(C)/C$. The parameter δ was used to evaluate the uncertainty caused by the systematic error on the global energy scale (see section 3.3.2). The relative uncertainty of the tower gains $\sigma(C)/C$ was $7 \pm 2\%$ and $10 \pm 2\%$ for the p+p and the d+Au run, respectively. These values were chosen based on the following observations.

The width of the p/E distribution, as shown in figure 3.4, was a convolution of $\sigma(C)/C$ with the momentum resolution of the TPC as well as the energy resolution of a single tower. It was well reproduced with the values quoted for $\sigma(C)/C$, for separate bins in electron momentum. In case of the BSMD, the spread in the gains was estimated from the variation of the total

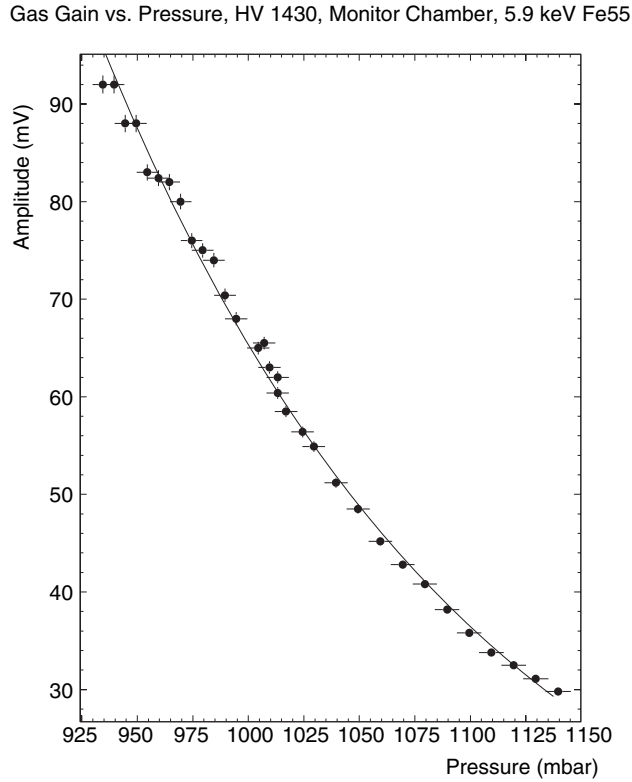


Figure 3.11: The effect of atmospheric pressure variations on the BSMD gas gain [60].

signal of single strips. Although these spectra contained the ADC values accumulated over approximately 10 million d+Au events, the poor energy resolution of the BSMD, combined with the low occupancy, made it difficult to produce an accurate estimate. Therefore a rather conservative error was assigned to the final number, $20 \pm 10\%$. Finally, the consistency of the simulated π^0 peak widths and those obtained from the experimental data, which will be discussed in section 4.2.5, served as an overall validation of this approach.

Chapter 4

Neutral Pion Measurements

Neutral pions were reconstructed from the photon candidate sample by means of their decay to two photons: $\pi^0 \rightarrow \gamma\gamma$. This channel is favorable for π^0 reconstruction because of its large branching ratio $\Gamma_{\pi^0 \rightarrow \gamma\gamma}/\Gamma = 98.8\%$. The mean lifetime of the π^0 is of the order of 10^{-16} s such that its decay vertex effectively coincides with the interaction vertex of the event. The invariant mass m_{inv} of a pair of photons was calculated as

$$m_{\text{inv}} = \sqrt{(p_{\gamma_1} + p_{\gamma_2})^2} = \sqrt{2E_{\gamma_1}E_{\gamma_2}(1 - \cos\psi)} \quad (4.1)$$

where p_{γ_i} denotes the four-momentum, E_{γ_i} the energy of the photon candidates, and ψ the opening angle between them. For two photons produced in a single π^0 decay, the value of m_{inv} is then equal to the π^0 mass: $m_{\pi^0} = 135.0$ MeV.

4.1 Raw Yield Extraction

Due to the large multiplicity of produced particles in high energy nuclear collisions, many of the possible pairs did not consist of two photons coming from the same reaction $\pi^0 \rightarrow \gamma\gamma$. Hence, it was not possible to directly identify neutral pions. Instead, the π^0 yield was extracted from the invariant mass distribution of all combinations of photon candidates, over many events. In this distribution the π^0 signal emerged as a peak on top of a background largely formed by combinations of candidates which did not both originate from the same π^0 decay. A thorough understanding of the behavior of the various components of this background turned out to be essential for a reliable extraction of the raw π^0 yield.

4.1.1 Invariant Mass Spectra

A large part of the background in the invariant mass spectra was formed by combinations of uncorrelated photons. This background increased quadratically with the multiplicity of photon candidates in an event. However, the number of neutral pions was only proportional to that multiplicity and therefore the π^0 signal relative to the underlying background improved when the multiplicity decreased. This is confirmed by figure 4.1 which shows the spec-

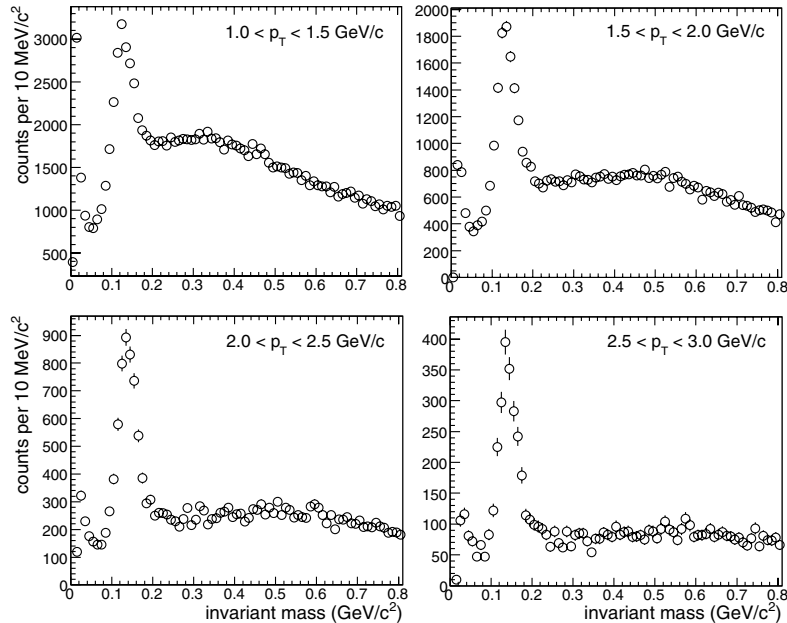


Figure 4.1: Invariant mass distributions for pairs of photons for minimum bias d+Au events for different bins in p_T .

tra of m_{inv} for consecutive p_T intervals of the photon pair. The π^0 peak is clearly visible, spread around the theoretical value of the π^0 mass as a result of the finite detector resolution. The figure illustrates that for increasing values of p_T , where the multiplicity of photon candidates was lower, the peak-to-background ratio became larger, as expected.

In addition to the above, there was a component of the invariant mass background which was formed by correlated pairs of photons. Especially for neutral pions at high p_T it was important to consider the topology of the event. A high p_T π^0 was likely to be part of a jet. The presence of this jet introduced angular correlations between pairs of photon candidates, even when they did not come from the same mesonic decay. Furthermore, the

fragments of the jet could deposit additional energy near the photon showers which might affect the reconstructed m_{inv} of the pairs. A study of the possible consequences of these effects will be presented in section 4.2.6.

Finally, the erroneous splitting of BSMD clusters, as described in section 3.3.3, generated a background consisting of pairs of fake photon candidates. This component is visible in figure 4.1 in terms of the enhancement of pairs on the left side of the π^0 mass peaks. The opening angle ψ between the two parts of a split cluster was relatively small, typically 1° , which led to correspondingly small values of m_{inv} . Because the finite granularity of the BSMD constituted an absolute lower limit to ψ , the reconstructed invariant mass of this component increased for larger values of p_T . Eventually, the contribution from these split clusters migrated underneath the π^0 peak, which complicated the extraction of the signal. The cut on the energy asymmetry of pairs which will be discussed next, as well as the shower shape cut described in section 3.3.3, were successfully applied to suppress this distortion of the mass spectrum.

Asymmetry Cut

Prior to the extraction of the π^0 yield, a cut was applied to the energy asymmetry $Z_{\gamma\gamma}$ of each invariant mass pair which required that

$$Z_{\gamma\gamma} = \frac{|E_{\gamma_1} - E_{\gamma_2}|}{E_{\gamma_1} + E_{\gamma_2}} \leq 0.7, \quad (4.2)$$

where E_{γ_i} is the energy of the photon i . The kinematics in appendix C demonstrate that the theoretical distribution of $Z_{\gamma\gamma}$ is flat for the decay $\pi^0 \rightarrow \gamma\gamma$. However, since the photon candidate spectrum was steeply falling with increasing p_T , random combinations had an energy asymmetry which was enhanced towards $Z_{\gamma\gamma} = 1$. Figure 4.2 shows the cumulative distribution of $Z_{\gamma\gamma}$ for pairs of photon candidates in case that

- both candidates originated from the same simulated π^0 and the invariant mass was reconstructed within the π^0 mass window (top)
- both candidates were the result of a single simulated photon causing a split cluster (middle)
- both candidates were reconstructed from the d+Au data and with m_{inv} outside the π^0 mass window: $0.08 < m_{\text{inv}} < 0.2 \text{ GeV}/c^2$ (bottom)

The first of these three corresponds to the signal which we aimed to measure. The other two represent typical background contributions. The vertical line

in the figure indicates the cut which was used to eliminate a large fraction of these background pairs from the m_{inv} spectra, while maintaining an efficiency of approximately 70%.

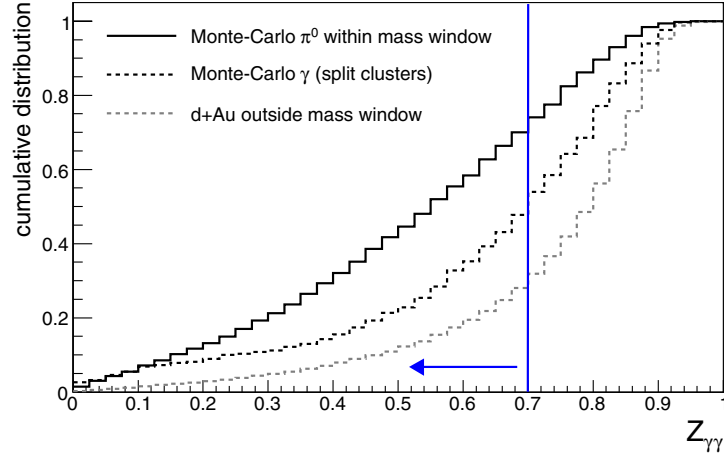


Figure 4.2: The cumulative distribution function of $Z_{\gamma\gamma}$ for the three cases described in the text together with the imposed constraint on the photon pairs: $Z_{\gamma\gamma} \leq 0.7$ (vertical line).

There was an additional advantage of such a cut on $Z_{\gamma\gamma}$. It served as a (p_T dependent) lower limit to the energy of the showers used for the m_{inv} combinations. Since the energy resolution of both the calorimeter towers and the BSMD channels improved with increasing energy, this led in general to a better mass resolution.

4.1.2 Background Subtraction

The next step in the reconstruction of the π^0 yield was the extraction of the mass peak from the invariant mass histograms. The combinatorial background had to be subtracted and the total number of entries of the remaining peak was defined as the uncorrected (raw) π^0 yield in each p_T interval.

Fit Method

To subtract the combinatorial background, the function

$$f_{\text{bg}}(x) = ax + bx^2 + cx^3. \quad (4.3)$$

was fit to the invariant mass distributions. The fit was restricted to the interval $0.0 < m_{\text{inv}} < 0.8 \text{ GeV}/c^2$ with the π^0 and η peak regions excluded.

The excluded window corresponding to the η mass peak was fixed, for all p_T bins and triggers, at $0.48 < m_{\text{inv}} < 0.65 \text{ GeV}/c^2$ and the π^0 mass window was temporarily set equal to $0.08 < m_{\text{inv}} < 0.24 \text{ GeV}/c^2$. The function f_{bg} was then subtracted from the invariant mass spectra and a Gaussian distribution

$$f_{\text{peak}}(x) = ce^{-(x-\mu)^2/2\sigma^2}. \quad (4.4)$$

was used to fit to the remaining peak. A second iteration was performed, this time with the excluded π^0 mass window given by $\{\mu - 3\sigma, \mu + 3\sigma\}$ and μ and σ equal to the parameters obtained from the first iteration.

The parameters μ and σ in equation 4.4 represent the mean and width of f_{peak} , respectively, and were also used to obtain the final integration interval around the π^0 mass peak: $\{\mu - 3\sigma, \mu + 3\sigma\}$. The total number of counts in this interval was defined as the raw π^0 yield. As a cross-check, the distributions were also fit with the sum of both functions. The resulting yields were found to be consistent with the former.

Figures 4.3 and 4.4 show mass distributions for different intervals in p_T in case of p+p and d+Au collisions, respectively. Also shown are the sum of f_{bg} and f_{peak} as well as the peak which remained after the subtraction of the fit to the combinatorial background. These figures clearly illustrate how the HT1 and HT2 trigger (middle and lower row of histograms, respectively) enhanced the reconstructed π^0 yield at higher values of p_T .

The statistical error on the raw π^0 yield could not be determined in a straightforward way because we did not measure the signal S directly, but the sum of signal and background $S + B$ instead. Therefore the error $\sigma(S)$ was approximated by

$$\begin{aligned} \sigma^2(S) &\approx \sigma^2(S + B) + \sigma^2(B) \\ &= S + 2B, \end{aligned} \quad (4.5)$$

where S is the content of the π^0 peak and B the size of the underlying background. Because B was determined from a fit with the π^0 peak region excluded, the two terms on the right in equation 4.5 were assumed to be statistically uncorrelated¹. Next to that, the assumption was made that $\sigma^2(B) = B$ remained a decent measure for the true statistical variance of B . This led to our final estimate of the statistical error on the raw π^0 yield: $\sigma(S) = \sqrt{S + 2B}$. An additional uncertainty was the specific choice of the function f_{bg} as a description of the background shape underneath the peak. This will be addressed in section 4.3.3 in terms of a systematic error on the final π^0 spectrum.

¹This assumption is clearly an approximation since the entries in the m_{inv} histograms represent pairs of candidates. A single candidate can therefore contribute to the distribution multiple times, for different values of m_{inv} .

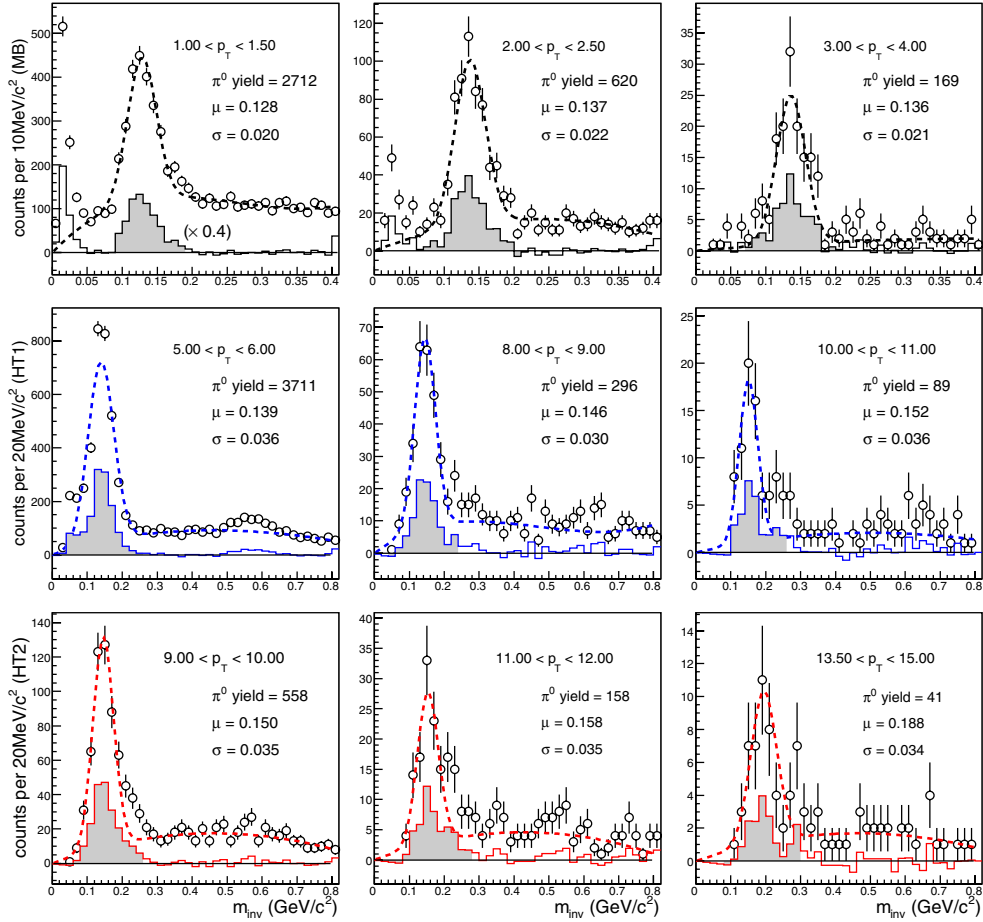


Figure 4.3: Invariant mass distributions obtained from p+p data. Typical examples of the yield extraction from minimum bias (top row), HT1 (middle), and HT2 (bottom) data for different intervals in p_T (GeV/c). The dashed line is the sum of f_{bg} and f_{peak} . The open symbols represent the raw invariant mass distribution and the filled histograms the scaled ($\times 0.4$) π^0 signal after the subtraction of f_{bg} . The raw π^0 yield is listed for each bin in p_T together with the mean μ and width σ (both in GeV/c²) of the π^0 mass peak. In addition, several distributions show an enhancement corresponding to the mass peak of the η meson ($m_\eta \approx 0.55$ GeV/c²) which also has a decay channel into two photons.

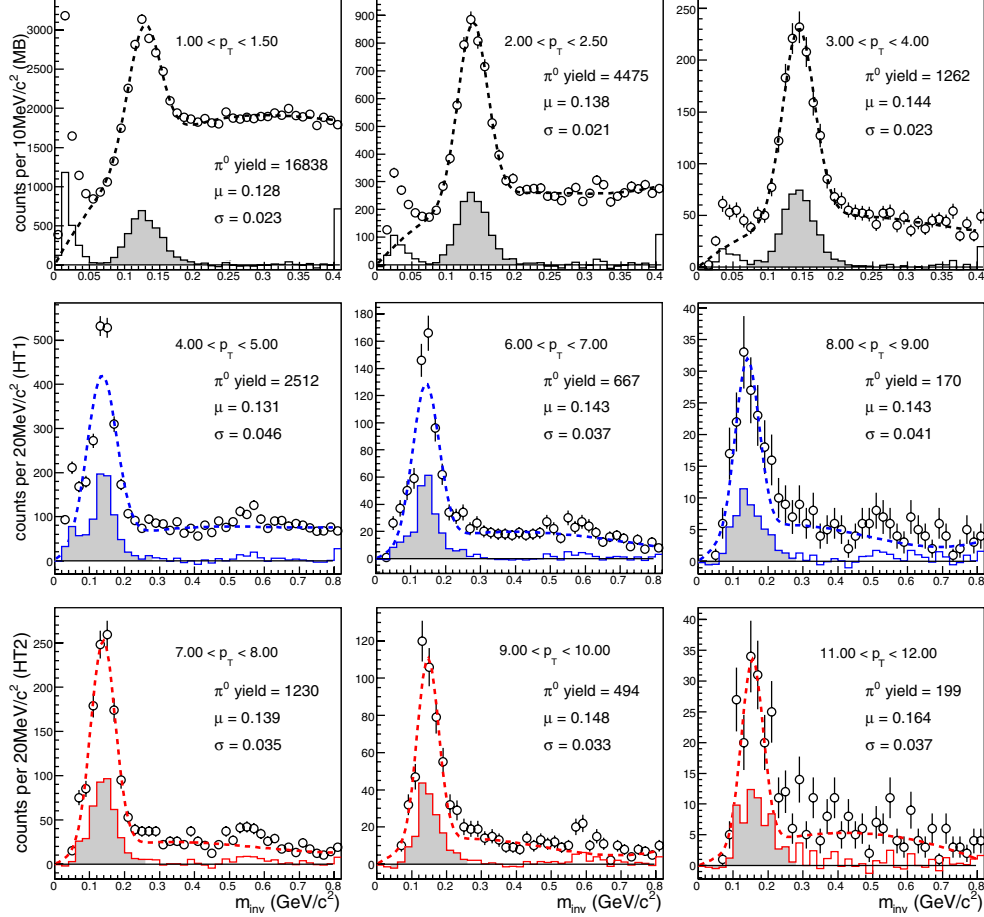


Figure 4.4: Invariant mass distributions obtained from d+Au data. Typical examples of the yield extraction from minimum bias (top row), HT1 (middle), and HT2 (bottom) data for different intervals in p_T (GeV/ c). The dashed line is the sum of f_{bg} and f_{peak} . The open symbols represent the raw invariant mass distribution and the filled histograms the scaled ($\times 0.4$) π^0 signal after the subtraction of f_{bg} . The raw π^0 yield is listed for each bin in p_T together with the mean μ and width σ (both in GeV/c^2) of the π^0 mass peak. In addition, several distributions show an enhancement corresponding to the mass peak of the η meson ($m_\eta \approx 0.55 \text{ GeV}/c^2$) which also has a decay channel into two photons.

A Note on Event Mixing

An analysis of mixed events is an established technique to reproduce the combinatorial background in the invariant mass spectra. Events with similar properties, such as particle multiplicity, primary vertex position, and trigger type, are grouped in separate classes. Subsequently, for each individual class, m_{inv} is determined for pairs of photons which do not come from the same event. Hence, the corresponding mass spectrum only contains pairs of fully uncorrelated photons.

This method generally reproduces a large part of the combinatorial background, especially at lower values of p_T . However, it was already pointed out in section 4.1.1 that the topology of the event as well as certain detector artifacts significantly contributed to the background in the vicinity of the π^0 mass peak. The spatial correlations of such components will be absent, by definition, in a study of the mixed events. This is illustrated in figure 4.5, which demonstrates the discrepancy in the mass distributions from the HT1 p+p data and the mixed event technique.

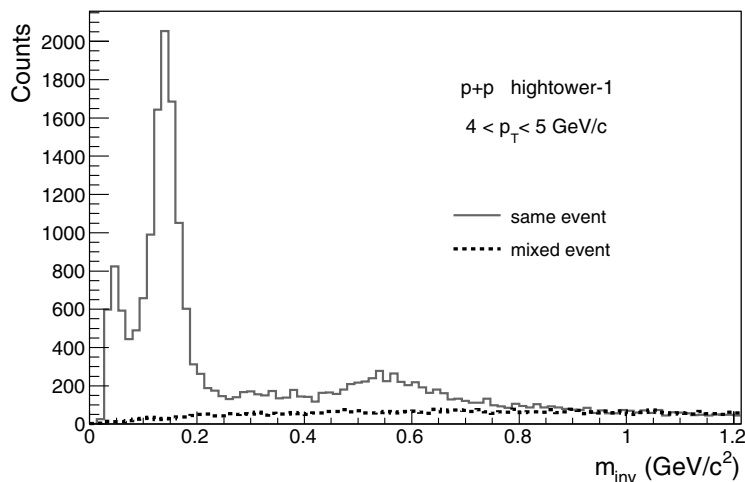


Figure 4.5: A comparison of m_{inv} spectra obtained from HT1 p+p data and from mixed events.

An alternative approach, extending the conventional event mixing routine, was to rotate the coordinates within one of the mixed events in order to align their jet axes. This leads to angular correlations similar to those in jets between the photon candidates in two, otherwise fully uncorrelated, events. Such a procedure was successfully applied in an independent analysis of π^0 production with the BEMC [56].

4.2 Corrections

Neutral pions were generated within a GEANT description of the experiment and the response of the various detector components was simulated following the procedures described in section 3.4.2. The resulting data were stored in an event format equivalent to that of the real experiment such that the π^0 reconstruction could be performed within the same framework as was used to process the experimental data. The p_T dependent reconstruction efficiency ϵ_{reco} was defined as

$$\epsilon_{\text{reco}}(p_T) = \frac{N_{\text{raw}}^{\pi^0}(p_T)}{N_{\text{true}}^{\pi^0}(p_T)} \quad (4.6)$$

where $N_{\text{true}}^{\pi^0}$ is the generated input distribution of pions and $N_{\text{raw}}^{\pi^0}$ the raw yield from those simulated events, both evaluated at the same value of p_T .

The above definition of $\epsilon_{\text{reco}}(p_T)$ heavily relied on a realistic simulation of the detector response. In addition, it introduced a dependence on the specific choice of $N_{\text{true}}^{\pi^0}(p_T)$. Since the neutral pion spectra were a final result of this analysis, the input distribution used in the first iteration was a fit to the pQCD calculation presented in section 1.1.3. Subsequently, a fit to the fully corrected spectrum provided a weight factor which was assigned to the individual events. This was an iterative procedure which had to be carried out multiple times until convergence was reached. The consistency of the simulated and experimental conditions was confirmed by comparing several essential observables, which will be discussed in more detail below.

It is important to stress that there were no additional constraints on the reconstructed momenta of the pions which were included in $N_{\text{raw}}^{\pi^0}(p_T)$. Hence, $\epsilon_{\text{reco}}(p_T)$ contained implicit corrections for effects such as the smearing of energy as a result of the finite detector resolution and merging of the π^0 decay photons at high p_T . This was the case, not only for the analysis of π^0 production, but more generally, for all reconstruction efficiencies in this thesis. In principle it is not correct to refer to $\epsilon_{\text{reco}}(p_T)$ as a reconstruction efficiency. It represents a convolution of acceptance as well as detection and reconstruction efficiencies. Since the purity in terms of the p_T of the reconstructed pions was not explicitly considered, $\epsilon_{\text{reco}}(p_T)$ could very well be larger than unity. Nevertheless, we will maintain the definition of $\epsilon_{\text{reco}}(p_T)$ as a reconstruction efficiency during the remainder of this thesis.

Ideally not only the full detector setup and the response of all its components should be simulated, but also the specific topology of the events which were analyzed. The presence of other particles and their spatial correlations can lead to, for instance, cluster overlaps and false charged particle vetoes which could possibly distort the measurement. Consequently, a full

simulation of p+p and d+Au events would be appropriate but the required resources, in terms of data storage and processing, will be extremely large. The final correction factors were therefore determined from a Monte-Carlo (MC) simulation of a single input particle per event. It was assumed that the multiplicity of particles produced in p+p and d+Au collisions was sufficiently small such that this approach was justified. Indeed, the typical occupancy of the BEMC for these events was smaller than $\sim 5\%$. In addition, a systematic study of simulated p+p collisions was used to validate this assumption. The corresponding results will be discussed in section 4.2.6.

4.2.1 Corrections from a Single Particle Simulation

To correct the π^0 spectrum in p+p as well as d+Au collision, a single pion per event was generated with the following kinematic properties:

- $0 < p_T < 20 \text{ GeV}/c$
- $-0.3 < y < 1.2$
- $0 < \phi < 2\pi$
- $dN/dp_T = dN/dy = dN/d\phi = \text{constant}$

Only events with the decay $\pi^0 \rightarrow \gamma\gamma$ were analyzed and the yield was afterwards corrected for the complementary branching ratio. The input distributions were chosen to be flat to obtain similar statistics over the entire phase space. Each event was assigned a weight factor to match the simulated to the experimental p_T distributions, iteratively, as mentioned earlier.

The primary vertex was simulated with a Gaussian spread in z around the nominal interaction point. An additional weight factor was applied to the events to match the simulated vertex distribution to the measured distribution. Figure 4.6 shows the resulting agreement of the simulated vertex positions (z) and the position obtained from experiment. However, for the π^0 reconstruction from the p+p data, the timing information from the BBC was used whenever there was no TPC vertex available (see section 3.2.2). Therefore the BBC resolution ($43.9 \pm 0.2 \text{ cm}$) was implemented in the MC simulation for the same fraction (37%) of minimum bias events.

The inverse correction factor $\epsilon_{\text{reco}}(p_T)$, for the default cuts defined in section 3.2 and table 3.3, is shown in figure 4.7 for minimum bias as well as hightower triggered p+p collisions. It was used to correct for inevitable losses of neutral pions as a result of

- the finite geometrical acceptance

- malfunctioning detector channels and module spacing
- photon conversions in the material in front of the BEMC
- the hightower trigger inefficiency

as well as losses which were related to the specific aspects of the reconstruction method, such as

- the selected fiducial volume of the BEMC
- the shower reconstruction algorithm and the constraint on the lateral shower profile
- the exclusion of pairs with large energy asymmetry $Z_{\gamma\gamma}$
- the limited π^0 mass window used to extract the raw yield

and additionally, for the artificial gain and loss of neutral pions due to p_T shifts caused by the finite energy resolution of the detector.

It was important that these effects were taken into account simultaneously in order to incorporate possible correlations between them. For example, the hightower trigger condition biased the π^0 decay photons to larger $Z_{\gamma\gamma}$ (see figure 4.13) and therefore to smaller opening angle ψ which in turn challenged the energy and position resolution of the BSMD. Nevertheless, it is instructive to consider the dominant effects separately. This is the main objective of the following sections. The corrections for finite bin width and the false CPV rejections were applied separately and will be discussed below as well.

4.2.2 Acceptance

During the p+p and d+Au run, half of the BEMC ($0 < \eta < 1$) was instrumented. However, a particle with its rapidity within the range $0 < y < 1$ could still miss the detector due to the spread in the event vertex. In case of neutral pions there were additional losses, mostly near the edges of the BEMC, when at least one of the decay photons remained undetected. The geometrical acceptance ϵ_{geom} was defined as the fraction of particles with a given p_T and y directed towards the fiducial volume of the detector:

$$\epsilon_{\text{geom}}(p_T, y) = \frac{N_{\text{onto}}^{\pi^0}(p_T, y)}{N_{\text{true}}^{\pi^0}(p_T, y)}, \quad (4.7)$$

where $N_{\text{true}}^{\pi^0}$ again equals the total number of generated pions and $N_{\text{onto}}^{\pi^0}$ those which had both their decay photons within the fiducial range of the BEMC.

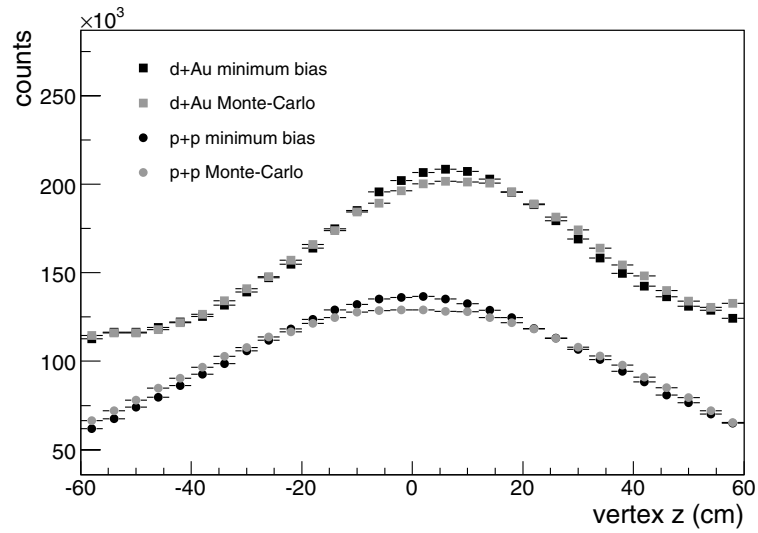


Figure 4.6: The distributions of the primary event vertex obtained from minimum bias p+p and d+Au collisions compared to the simulated distributions.

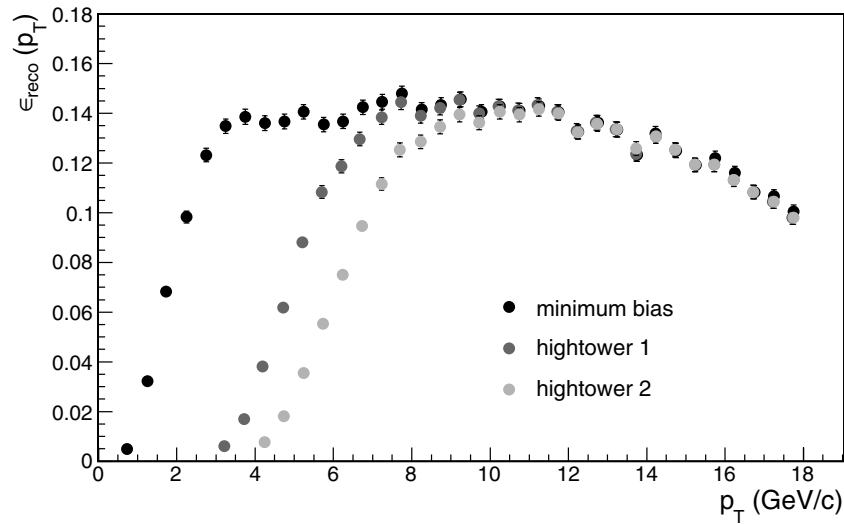


Figure 4.7: The reconstruction efficiency $\epsilon_{\text{reco}}(p_T)$ of neutral pions in p+p collisions for MB, HT1, and HT2 triggered events.

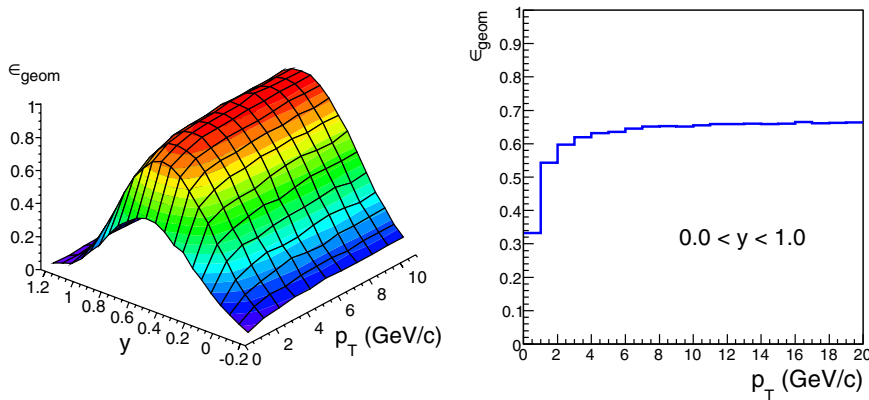


Figure 4.8: The geometrical acceptance ϵ_{geom} for neutral pions, using photon candidates with $0.1 < \eta < 0.9$, as a function of π^0 p_T and y (left panel) and ϵ_{geom} integrated over $0 < y < 1$ (right panel). These results were obtained for d+Au events.

Figure 4.8 shows ϵ_{geom} with the requirement that both decay photons hit the BEMC in the fiducial range $0.1 < \eta < 0.9$. The p_T dependence follows from the kinematics of the π^0 decay. As p_T decreases, the decay angle between the photons becomes larger and it is more likely that one of them misses the calorimeter thereby reducing the acceptance.

Even when both of the decay photons were within the BEMC acceptance, it wasn't always possible to detect the showers. The acceptance was further reduced by dead or malfunctioning towers and BSMD strips of which the data was discarded, in experiment as well as simulation (see section 3.3.1). The time dependence of these hardware failures was simulated by randomly assigning database timestamps to the MC events. These timestamps were sampled from their respective distributions as obtained from the p+p and d+Au data sets, thereby reproducing the fraction of masked towers within $\sim 0.5\%$.

Since the trigger pre-scale factors were allowed to vary over runs, the timestamps of hightower triggered events followed a distribution which differed from the distribution in case of minimum bias events. Therefore, the correction factors for MB, HT1 and HT2 data were determined from different MC data samples, each of them generated with the appropriate timestamp distributions.

4.2.3 BEMC Trigger Efficiency

The hightower trigger was simulated by implementing the same decision algorithm as discussed in section 2.3.2 on the raw ADC values from the Monte-Carlo data. It was therefore essential to use the actual tower calibration coefficients to calculate the ADC value corresponding to the energy deposition from GEANT. In addition, the resolution effects already had to be taken into account at the ADC level because they influenced the trigger decision, especially around the threshold value. The simulation framework of the BEMC, which is explained in detail in section 3.4, complied with both demands.

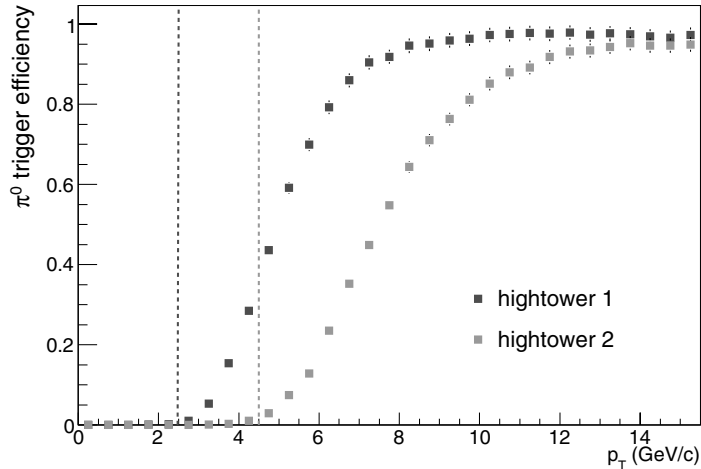


Figure 4.9: The HT1 and HT2 trigger efficiencies in d+Au collisions versus p_T of a π^0 , as determined from a MC simulation. The dashed vertical lines represent the effective trigger thresholds in terms of the transverse energy deposition in a single tower.

The hightower trigger efficiency for neutral pions produced in d+Au collisions is shown in figure 4.9. The vertical dashed lines indicate the effective E_T thresholds of the trigger. The graphs were calculated from the simulated events by dividing the raw π^0 yield for which the trigger condition was satisfied by the total raw π^0 yield. Events triggered by BEMC towers which were masked out during the recording of the data, were also discarded in the simulation. Because these were only a small fraction ($< 0.5\%$) of the total number of active towers, the asymptotic values of the hightower trigger efficiency were very close to 100%.

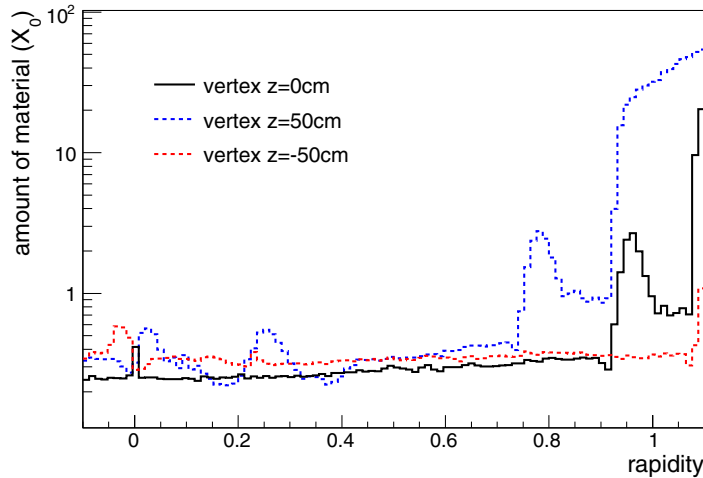


Figure 4.10: The amount of material, in terms of radiation length X_0 , in front of the BEMC ($r < 223.5$ cm) for different values of the event vertex z as a function of rapidity. These results were obtained with the GEANT description of the 2005 geometry of the STAR detector.

4.2.4 Photon Conversions

The probability P_{conv} that a photon converts in a medium was already given by equation 2.1. Consequently, the probability $P_{\text{conv}}^{\pi^0}$ that a π^0 was not detected because at least one of its decay photons converted is given by

$$P_{\text{conv}}^{\pi^0} = 2P_{\text{conv}}(1 - P_{\text{conv}}) + P_{\text{conv}}^2. \quad (4.8)$$

Because the material of the STAR detector was implemented in GEANT, the reconstruction efficiency ϵ_{reco} implicitly contained a correction for π^0 losses due to conversions. However, the accuracy of this correction was directly related to the uncertainty of the amount of material in front of the BEMC.

Figure 4.10 shows the cumulative amount of material between the BEMC front plate and three different production vertices of simulated particles, as a function of their rapidity. The plot clearly illustrates that a reduction of the traversed material was obtained by constraining the vertex to a narrow region around $z = 0$. Next to that, the histogram for $z = 0$ (which means that rapidity is equal to η) motivates the choice of the fiducial cut $0.1 < \eta < 0.9$ as it reduced the amount of encountered material even further.

During the 2005 p+p run, approximately 20% of all material was located within $r < 60$ cm. Most of this material was part of the SVT, SSD, and the TPC Inner Field Cage (IFC). The geometry description of the first two of

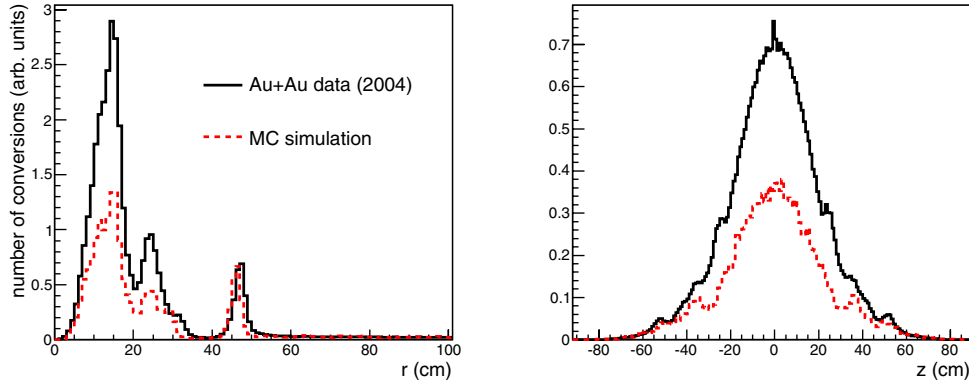


Figure 4.11: Left panel: The number of photon conversions as a function of the radial coordinate r . Right panel: The number of photon conversions as a function of z . (data from [85]).

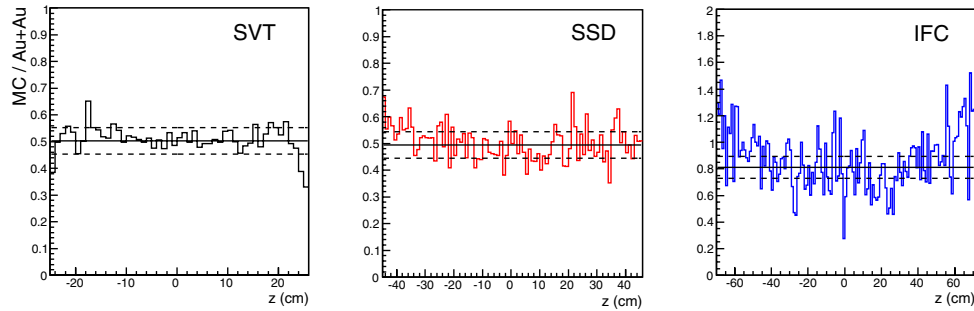


Figure 4.12: The ratio of the conversion probability determined in a MC simulation and the 2004 Au+Au data for the SVT, SSD, and IFC as a function of z . The results of the fit (full line) and the estimated uncertainty (dashed line) are listed in table 4.1.

	P_{conv}		$P_{\text{conv}}^{\text{MC}}/P_{\text{conv}}^{\text{Au+Au}}$	location
	d+Au	p+p		
SVT	0.043 ± 0.004	0.038 ± 0.004	0.50 ± 0.05	$0 < r < 20$ cm
SSD	0.006 ± 0.001	0.034 ± 0.003	0.50 ± 0.05	$20 < r < 40$ cm
IFC	0.005 ± 0.001	0.005 ± 0.001	0.81 ± 0.08	$40 < r < 55$ cm

Table 4.1: Photon conversions in the inner part ($r < 55$ cm) of the STAR detector. The symbols are explained in the text.

these detectors was a complex composition of silicon strips, support structures, and readout electronics. The other 80 % could largely be attributed to the CTB which was directly in front of the BEMC. It was observed that the simulation failed to reproduce the number of conversion in the inner part of the STAR detector [84].

Figure 4.11 shows that a large fraction of conversions detected in 2004 Au+Au collisions were not seen in the Monte-Carlo study. Both these histograms were normalized in the region $60 < r < 100$ cm where the TPC gas constituted a homogeneous medium which could be accurately simulated. Since these results were obtained with the geometry description of the STAR detector for the 2004 Au+Au run, they could not be directly translated into a correction factor for this analysis.

The probability P_{conv} was determined from the simulation in case of photon conversions in the SVT, SSD, and the IFC, separately. Their respective position is given in table 4.1 and can be correlated with the three peaks in the left panel of figure 4.11. These numbers were calculated for photons with $0.1 < y < 0.9$, which hit the calorimeter in its fiducial volume, $0.1 < \eta < 0.9$. In addition, the position of the event vertex was distributed according to the measured distribution. Consequently, the final numbers for P_{conv} , listed in table 4.1, constitute an effective probability, only valid for the sample of photons which we aimed to measure and for the corresponding distribution of the event vertices.

The number of simulated conversions relative to that number obtained from the Au+Au data, $P_{\text{conv}}^{\text{MC}}/P_{\text{conv}}^{\text{Au+Au}}$, was determined for the regions associated with the SVT, SSD, and the IFC. These data are given by the table as well. Figure 4.12 shows this ratio as a function of z together with the fit applied to these histograms and the estimated uncertainty. Photons which passed through these detectors outside the shown z range, were not of interest because they would either miss the fiducial volume of the BEMC or fall outside the selected rapidity range. The simulated probabilities P_{conv} were divided by the corresponding ratio $P_{\text{conv}}^{\text{MC}}/P_{\text{conv}}^{\text{Au+Au}}$ and summed over the subsystems. Upon comparing these numbers to the initial conversion probabilities, correction factors for the missing material, denoted by c_{miss} , were derived which were equal to 1.05 ± 0.01 and 1.08 ± 0.02 in case of the photon spectra in p+p and d+Au events, respectively. For the neutral pion spectra, we used equation 4.8 and estimated that the necessary corrections were equal to 1.10 ± 0.02 (p+p) and 1.15 ± 0.03 (d+Au). The photon attenuation length in most absorbers rapidly approaches a constant for energies greater than ~ 100 MeV [51]. Hence, these correction factors were assumed to be independent of photon p_T . Note that terms of order P_{conv}^2 were neglected, an approximation which is valid for sufficiently small conversion probabilities.

4.2.5 Simulated Mass Spectra and Energy Smearing

The effects discussed above could not account for the total loss of neutral pions. Even when both decay photons caused a shower in the active part of the detector, the efficiency was still subject to certain artifacts of the shower reconstruction algorithm and to the analysis cuts which were applied to the photon candidates and their invariant mass combinations. These had to be evaluated in conjunction with the finite resolution of the detector in order to properly account for their influence on the raw π^0 yield. Hence, it was extremely important that the experimental conditions were accurately simulated.

The energy asymmetry $Z_{\gamma\gamma}$ was a key observable which was not only sensitive to the energy measured in the calorimeter towers but also to the unfolding of BSMD clusters caused by neutral pions at high p_T . The consistency of the measured $Z_{\gamma\gamma}$ distribution and the simulation is illustrated by figure 4.13. Although the theoretical distribution of $Z_{\gamma\gamma}$ is flat, two distinct features are present in these histograms.

First of all, all distributions are suppressed when approaching $Z_{\gamma\gamma} = 1$. This is a direct consequence of the energy threshold which was applied in the shower reconstruction. This threshold was absolute and the observed effect is therefore larger for pairs with lower values of p_T . The latter are even more suppressed as a result of the kinematics of the π^0 decay (see appendix C). Since the minimum opening angle ψ_{\min} was largest for low p_T pions, and in particular for very asymmetric decays, their decay photons were more likely to miss the calorimeter.

Furthermore, in case of the distribution for hightower-2 triggered collisions (HT2), an enhancement towards more asymmetric decays can be observed for the p_T interval which is closest to the trigger threshold ($6 < p_T < 7 \text{ GeV}/c$). Because most of the energy of a π^0 decaying with $Z_{\gamma\gamma}$ close to unity was deposited in a relatively small volume, the hightower requirements were more often fulfilled for these asymmetric decays. The overall agreement of the experimental distributions with the simulated values adds to the conclusion that the actual experimental conditions were accurately reproduced with our simulation framework.

Similar to the energy asymmetry, the measured widths and positions of the π^0 mass peak differed from the theoretical values as well. Again this was due to the finite energy and position resolution of the detector. The invariant mass pairs were measured at an energy distributed around a certain nominal value. In combination with the steeply falling π^0 spectrum, this led to bin migrations, predominantly towards higher values of energy and therefore towards higher m_{inv} . Indeed it was observed that the measured

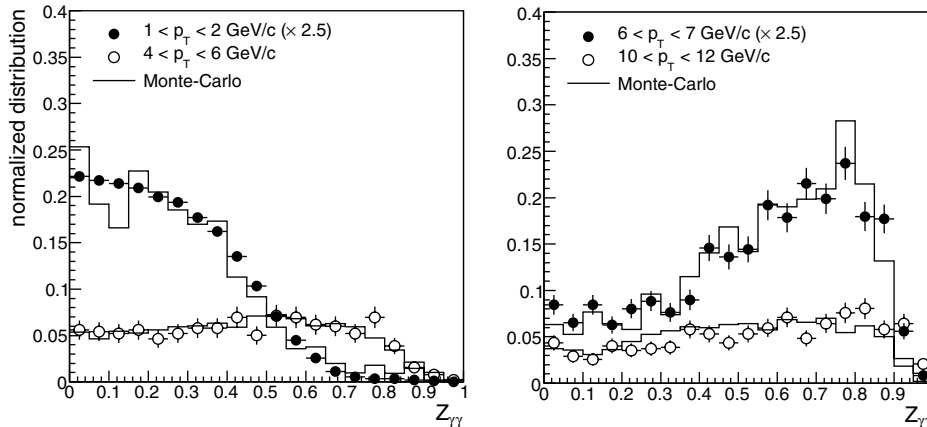


Figure 4.13: The energy asymmetry $Z_{\gamma\gamma}$ for minimum bias (left panel) and HT2 (right panel) d+Au collisions compared to the results from the Monte-Carlo simulation.

peak positions exceeded $m_{\pi^0} = 135.0 \text{ MeV}/c^2$ over a large p_T range. This can be seen from the graphs in figure 4.14 in case of minimum bias as well as hightower triggered p+p and d+Au collisions. The dashed line indicates the theoretical value of the π^0 mass. The agreement with the Monte-Carlo results was obtained only after implementing the additional spread of the gains, as discussed in section 3.4.2.

The finite energy resolution did not just modify the properties of the invariant mass distributions. It also significantly affected the final value of the reconstruction efficiency ϵ_{reco} . The net flow of reconstructed pions to higher values of p_T increased the efficiency (while reducing the purity) and the size of this flow had a strong dependence on the shape of the input distribution of particles. To handle this phenomenon correctly, an accurate fit to the reconstructed and fully corrected π^0 yield was required. We should point out that the increase of the raw yield by this energy smearing effect was not uniquely a feature of the π^0 analysis. The reconstruction efficiencies in case of photons and neutral hadrons, to be discussed in the next chapter, were defined analogously and were therefore subject to energy smearing as well.

A NLO pQCD calculation was used to parametrize the π^0 yield in a first

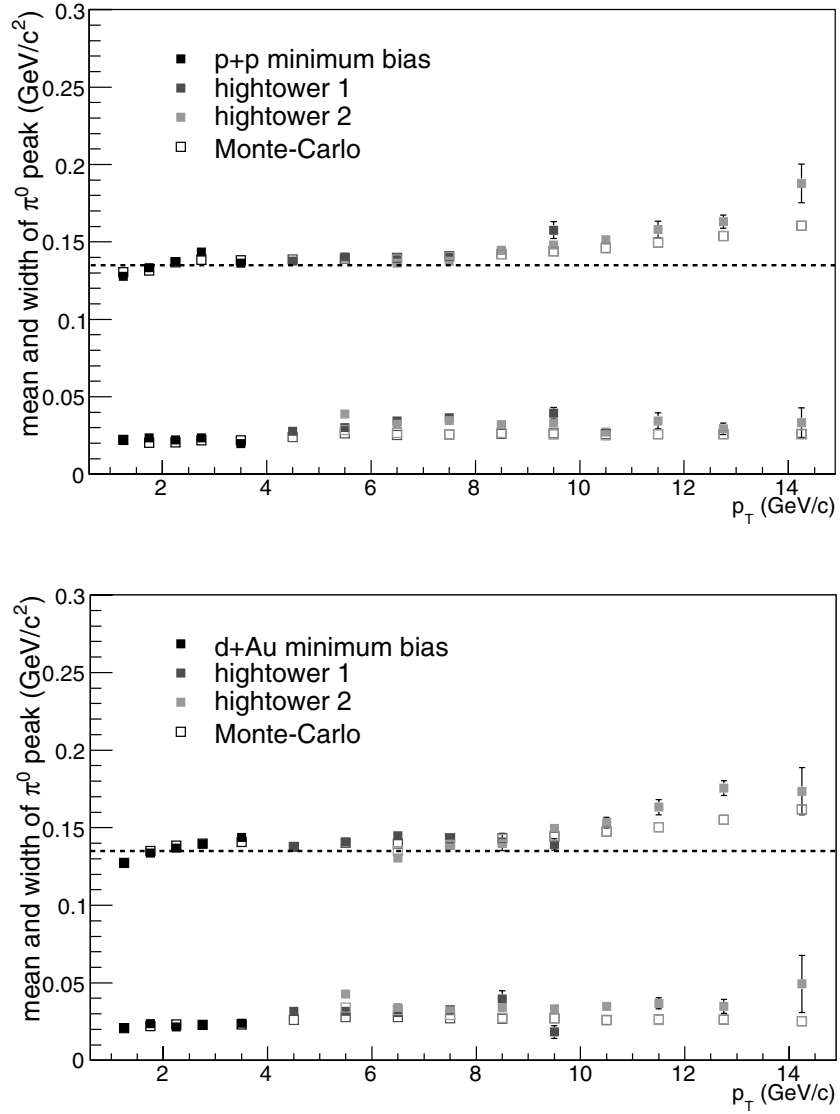


Figure 4.14: Results obtained from p+p (upper panel) and d+Au (lower panel) data. A comparison of the mean (upper graphs) and width (lower graphs) of the π^0 peak and the results from the Monte-Carlo simulation. The dashed line indicates the theoretical π^0 mass: $135.0 \text{ MeV}/c^2$.

	a	b	c	n	m
d+Au	51.0	3.8	6.6	-8.9	-7.8
p+p	373.0	81.2	5.6	-8.9	-8.4

Table 4.2: The final parameters of f_{yield} (see equation 4.9) obtained from a fit to the fully corrected π^0 yield $Ed^3N/d^3p(\text{GeV}^{-2}c^3)$ from d+Au collisions and the cross section $Ed^3\sigma/d^3p(\text{mb GeV}^{-2}c^3)$ in p+p collisions.

iteration. Subsequently, the function

$$\begin{aligned}
 f_{\text{yield}}(x) &= a \xi(x) \left(\frac{1}{1+x} \right)^n + b (1 - \xi(x)) \left(\frac{1}{1+x} \right)^m \\
 \xi(x) &= \frac{1}{e^{2(x-c)} + 1}
 \end{aligned}
 \tag{4.9}$$

was fit to the fully corrected p_T spectrum. The shape defined by the function $a(1+x)^{-n}$ provided an accurate description of the part of the spectrum at lower as well as higher values of p_T . However, the value of the exponents significantly differed and therefore the function $\xi(x)$ was used to provide a transition between the two p_T ranges. Figure 4.23 shows the result of the fit to the corrected π^0 yield in p+p collisions (top panel) together with the ratio of those data and f_{yield} , and likewise for figure 4.24 in case of d+Au collisions. The parameters, obtained after the final iteration of the full analysis, are listed in table 4.2.

4.2.6 Pythia Studies

A high p_T π^0 produced in nuclear collisions is often part of a jet. To study the possible effects of the jet structure of an event on the reconstructed π^0 yield, we have used the Monte-Carlo event generator Pythia [86]. Approximately 2×10^6 p+p collisions were generated at $\sqrt{s_{NN}} = 200$ GeV with a parton momentum exchange of at least 15 GeV/c, the rapidity of the outgoing partons within $-0.5 < y < 1.5$, and the collisions vertex equal to (0, 0, 0). This resulted in $\sim 3 \times 10^4$ events containing at least one π^0 in the direction of the west BEMC ($0 < \eta < 1$) with $p_T > 8$ GeV/c. All particles which were produced in a jet-like cone $R = (\Delta\phi^2 + \Delta\eta^2)^{1/2} < 1.0$ around this π^0 were stored and processed through the GEANT description of the STAR detector. The possible decay processes of the particles were handled by GEANT as well.

On the left panel of figure 4.15 the generated π^0 yield is shown as a function of p_T . The dashed line was a fit of an exponential function to those data. The right panel demonstrates that the invariant mass background in

these events was enhanced in the region around the π^0 mass peak. This was caused by the angular correlation of the photon candidates in a jet and the fact that a smaller opening angle ψ leads to a smaller value of m_{inv} . The absence of these correlations in the conventional mixed event technique and the resulting discrepancy of the mass distributions were already discussed in section 4.1.2.

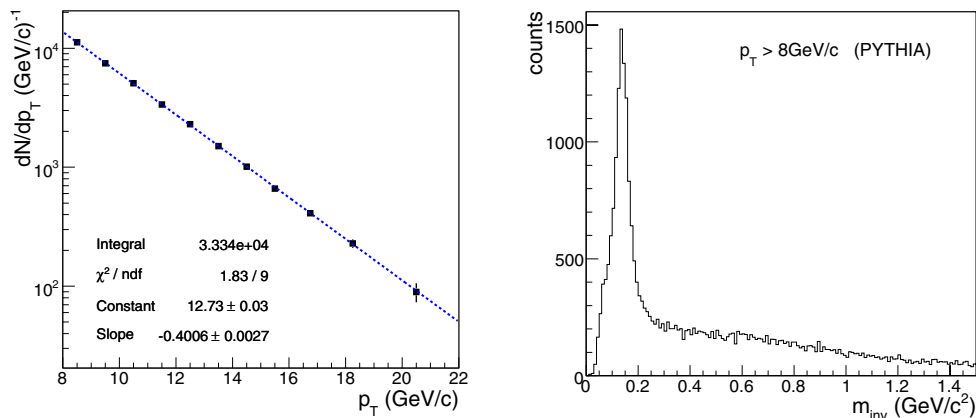


Figure 4.15: Results from a Pythia simulation. Left panel: the generated distribution of neutral pions and the parameters of a fitted exponential function (dashed line). Right panel: the m_{inv} distribution for pair p_T greater than 8 GeV/ c .

Additionally, a sample of events was produced, similar to the above, but containing only a single π^0 per event with dN/dp_T equal to a constant. Afterwards, the events were weighted with the exponential fit described above such that the effective input distribution matched the one from the Pythia simulation. Figure 4.16 shows the invariant mass spectra as obtained from both samples of simulated data. In case of the Pythia spectra, the combinatorial background was subtracted by applying the default routine described in section 4.1.2. The figure demonstrates that the remaining shape of the mass peak was consistent with the single-particle-per-event Monte-Carlo. In addition, figure 4.17 shows the comparison of the position and width of the π^0 peak for different p_T bins. The consistency between the invariant mass distributions obtained from the separate MC samples supported our initial argument that the corrections to the raw data could be extracted from a simulation of single particles per event.

It should be stressed here that the results from the study of Pythia events could not be used to correct the experimental data for a variety of reasons. First of all, the shape of the input distribution of pions was not realistic and limited in p_T . In addition, the simulation was performed with all detector

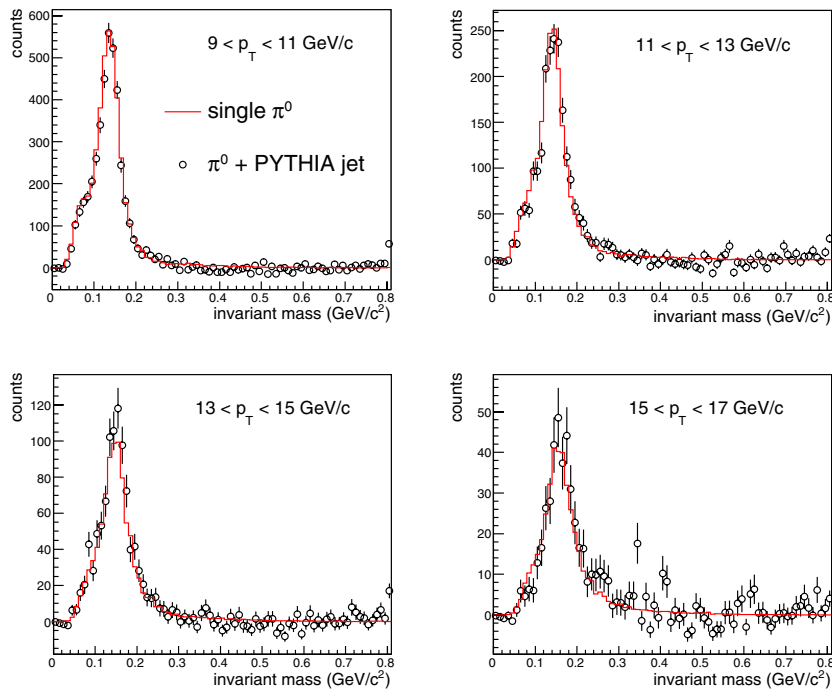


Figure 4.16: Invariant mass distributions for Pythia jets and from the simulation of a single π^0 per event. In case of the spectra from Pythia, the combinatorial background was subtracted.

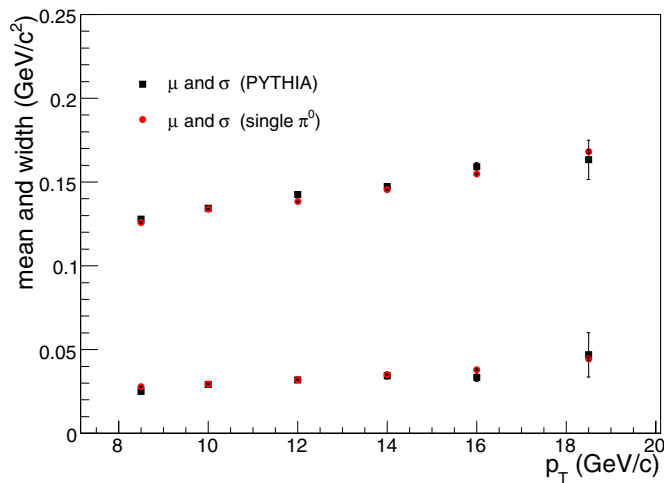


Figure 4.17: The mean (upper graphs) and width (lower graphs) of the π^0 mass peak from the Pythia simulation compared to the results from the Monte-Carlo study based on a single π^0 per event.

channels properly functioning, no vertex spread, and relatively loose cuts in order to statistically improve the results. The small difference in the π^0 yield extracted from the Pythia mass distributions, as compared to the simulation of single pions, will be addressed in section 4.3.3.

4.2.7 False Vetoes

The neutral pion yields were corrected for losses caused by accidental charged particle vetoes (CPV) applied to clusters from genuine photons. To determine the fraction of neutral pions which was lost as a result of these random rejections, the distance of any of the two photons to the closest track (D_{track}) was determined separately for MB, HT1, and HT2 events. The obtained distribution of D_{track} , accumulated over all events, is shown in figure 4.18. The peak of this distribution near $D_{\text{track}} = 0$ signals the presence of charged particles in the sample. The CPV criterion which was applied in our π^0 analysis excluded all pairs with $D_{\text{track}} < 5$ cm. However, in case only one of the two clusters had a charged track within the CPV radius, the other could still contribute in combination with the remaining clusters.

The background of random associations followed from a fit with the function

$$f_{\text{rnd}}(x) = axe^{-bx} \quad (4.10)$$

in the range $20 < D_{\text{track}} < 50$ cm. This range was found to be well outside the D_{track} distribution of simulated charged pions which indicates that the fit was applied to the random component of the distribution only. The resulting shape of f_{rnd} is shown by the dashed curve in figure 4.18 .

The calculation was performed for all p_T bins and all trigger classes separately. The area below the fit in the region $0 < D_{\text{track}} < 5$ cm was considered to be an estimate of the π^0 losses as a result of false vetoes. The correction term ϵ_{CPV} was then defined as the ratio of the accepted pairs, i.e. those with $D_{\text{track}} \geq 5$ cm, and the total number of neutral clusters. The latter was determined as the integral of the D_{track} distribution for $D_{\text{track}} \leq 20$ cm, summed with the area underneath the fit for $D_{\text{track}} < 20$ cm. Equations 4.15 and 4.16 illustrate how the term ϵ_{CPV} was used to correct the raw π^0 yield.

Figure 4.19 shows ϵ_{CPV} as a function of p_T for HT2 p+p events. The full line and the parameters correspond to a fit with the function

$$f_{\text{cpv}}(x) = c + dx. \quad (4.11)$$

The value of f_{cpv} can be interpreted as the fraction of true photon pairs which satisfied the CPV criterion: $D_{\text{track}} > 5$ cm. The final parameters of f_{cpv} are listed for completeness in table 4.3.

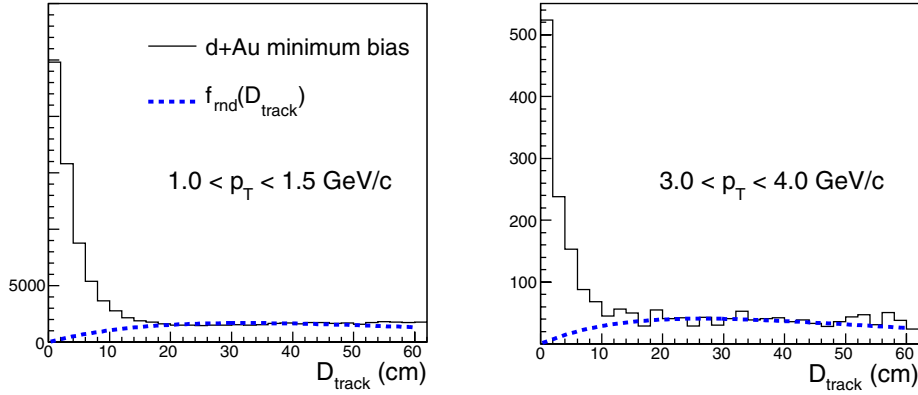


Figure 4.18: The distribution of D_{track} in case of minimum bias d+Au events for two typical p_T bins. The dashed line is the result of the fit with the function defined in equation 4.10.

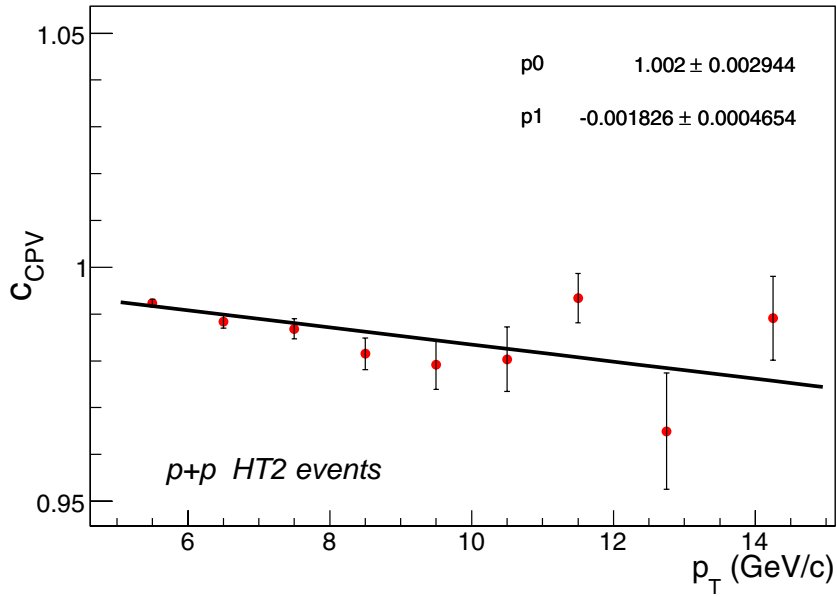


Figure 4.19: The p_T dependence of ϵ_{CPV} in case of HT2 p+p events. The full line is a fit with a the function f_{CPV} as defined in equation 4.11, the resulting parameters for d+Au and p+p, as well as for all trigger types, are listed in table 4.3.

system	par.	MB	HT1	HT2
p+p	c	0.997 ± 0.002	1.001 ± 0.002	1.002 ± 0.003
	d	0.000 ± 0.001	-0.0017 ± 0.0004	-0.0018 ± 0.05
d+Au	c	0.996 ± 0.001	0.996 ± 0.002	0.995 ± 0.002
	d	-0.0005 ± 0.0004	-0.0007 ± 0.0005	-0.0005 ± 0.0003

Table 4.3: The parameters of the fit to ϵ_{CPV} with the function f_{CPV} defined in equation 4.11.

Not all rejections of photon pairs from a genuine π^0 were caused by random overlaps. In principle there was a possibility that one of those two photons converted early enough such that the electron and positron tracks were reconstructed in the TPC. In that case, the π^0 could not be reconstructed. However, the correction of the data with ϵ_{reco} already accounted for losses due to conversions (see section 4.2.1) and therefore these were not considered here.

4.2.8 Correction for Finite Bin Width

The center of the p_T bins of the extracted π^0 yield did not represent the mean p_T value in that bin. This was a consequence of the combination of a steeply falling p_T spectrum and the finite width of the bins. The choice was made to apply a correction to the measured yield, instead of shifting the p_T value of the point. The former was more convenient since eventually the ratios of different spectra had to be calculated.

The true invariant yield Y_{true} at the center of a bin ($p_T = p_0$) was defined as

$$Y_{\text{true}} = \frac{dN}{p_T dp_T}(p_0) \quad (4.12)$$

and the measured yield as

$$Y_{\text{meas}} = \frac{N(p_0)}{p_0 \Delta} \quad (4.13)$$

where $N(p_0)$ represents the π^0 yield after applying all previously described corrections and Δ is the width of the bin at p_0 . This led to the following correction factor c_{bin} in order to account for the overestimate of the yield as

a result of the finite bin width:

$$\begin{aligned} c_{\text{bin}}(p_0) &= \frac{Y_{\text{true}}}{Y_{\text{meas}}}(p_0) \\ &= \frac{Y_{\text{true}}(p_0)}{\frac{1}{p_0 \Delta} \int_{p_0 - \Delta/2}^{p_0 + \Delta/2} p_T Y_{\text{true}}(p_T) dp_T}. \end{aligned} \quad (4.14)$$

The fit to the measured spectrum with f_{yield} (see equation 4.9) was used to parametrize Y_{true} . The derived correction factor approaches unity for higher values of p_T where the yield falls off less rapidly. An exception was when the width of the bin increased, which enhanced the deviation from the true yield.

4.3 Results

The fully corrected Lorentz invariant differential π^0 yield per minimum bias collision was derived as

$$E \frac{d^3 N}{d^3 p} = \frac{1}{2\pi p_T} \frac{d^2 N}{dp_T dy} = \frac{1}{2\pi p_T} \frac{1}{N_{\text{ev}}^{\text{MB}}} \frac{1}{K(p_T)} \frac{N_{\text{raw}}^{\pi^0}(p_T)}{\Delta p_T \Delta y}, \quad (4.15)$$

where

$$K(p_T) = \epsilon_{\text{reco}}(p_T) c_{\text{miss}}^{-2} \epsilon_{\text{vert}} \epsilon_{\text{CPV}} c_{\text{bin}}^{-1} \frac{\Gamma_{\gamma\gamma}}{\Gamma}, \quad (4.16)$$

and with the various symbols defined as

- $N_{\text{raw}}^{\pi^0}(p_T)$ the uncorrected π^0 yield per p_T bin
- $N_{\text{ev}}^{\text{MB}}$ the number of accepted minimum bias events
- $\epsilon_{\text{reco}}(p_T)$ the p_T dependent reconstruction efficiency
- ϵ_{vert} the vertex finding efficiency (d+Au only)
- c_{miss} the single photon correction for conversions in the missing material
- ϵ_{CPV} the correction for false vetoes of photon pairs
- c_{bin} the correction for finite bin width
- $\Gamma_{\gamma\gamma}/\Gamma$ the branching ratio of the process $\pi^0 \rightarrow \gamma\gamma$
- $\Delta p_T, \Delta y$ the width of the p_T and y bin, respectively

In case of hightower triggered events, the above equations were modified to account for the pre-scaling of the minimum bias and HT1 event rates. Therefore, $N_{\text{ev}}^{\text{MB}}$ was replaced by the equivalent number of minimum bias events which would have resulted in the HT2 data sample. The latter was equal to the sum over all events of the minimum bias pre-scales ps_i^{MB} and given by

$$N_{\text{ev}}^{\text{HT2}} = \sum_{i=1}^{N_{\text{ev}}^{\text{MB}}} \text{ps}_i^{\text{MB}}. \quad (4.17)$$

Since the HT1 event rate was pre-scaled as well, the expression for $N_{\text{ev}}^{\text{HT1}}$ which was used is

$$N_{\text{ev}}^{\text{HT1}} = \sum_{i=1}^{N_{\text{ev}}^{\text{MB}}} \text{ps}_i^{\text{MB}} / \text{ps}_{\text{eff}}^{\text{HT1}} \quad (4.18)$$

with

$$\text{ps}_{\text{eff}}^{\text{HT1}} = \sum_{i=1}^{N_{\text{ev}}^{\text{HT1}}} \text{ps}_i^{\text{HT1}} / N_{\text{ev}}^{\text{HT1}}. \quad (4.19)$$

The available statistics were not sufficient to determine $N_{\text{raw}}^{\pi^0}$ differentially in p_T and y simultaneously. Therefore, it was assumed that near mid-rapidity the production of neutral pions was independent of y , just like the input distribution of the Monte-Carlo analysis used to determine $\epsilon_{\text{reco}}(p_T)$. A validation of this assumption followed from the consistency of the raw π^0 yield from experiment and simulation for different values of y and integrated over p_T , as shown by figure 4.20. The figure also illustrates the selected range of rapidity y of neutral pions, $0.1 < y < 0.9$, which was used in case of p+p as well as d+Au collisions.

The second implicit assumption in equation 4.15 was that the contribution to the π^0 yield from events without a reconstructed vertex was negligible. This was confirmed with a HIJING [83] simulation of d+Au collisions within the GEANT framework. The per-event π^0 yield in events without a primary vertex was indeed more than an order of magnitude lower, as illustrated by figure 4.21. Hence, the possible effect on the value of the invariant yield was found to be smaller than 0.2% for $p_T > 1 \text{ GeV}/c$.

4.3.1 Calculation of the Differential Cross Section

For a collision of two protons, the total cross section σ_{tot} can be divided into an elastic and an inelastic cross section:

$$\sigma_{\text{tot}} = \sigma_{\text{el}} + \sigma_{\text{inel}} \quad (4.20)$$

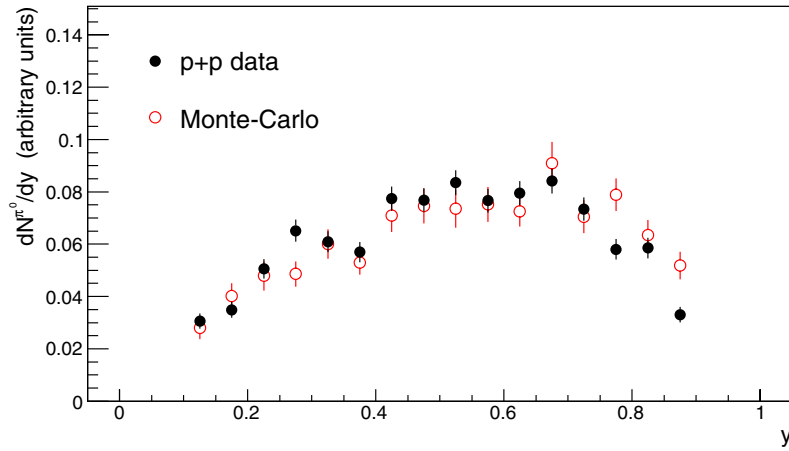


Figure 4.20: A comparison of $dN_{\text{raw}}^{\pi^0}/dy$ from p+p data and from the Monte-Carlo simulation.

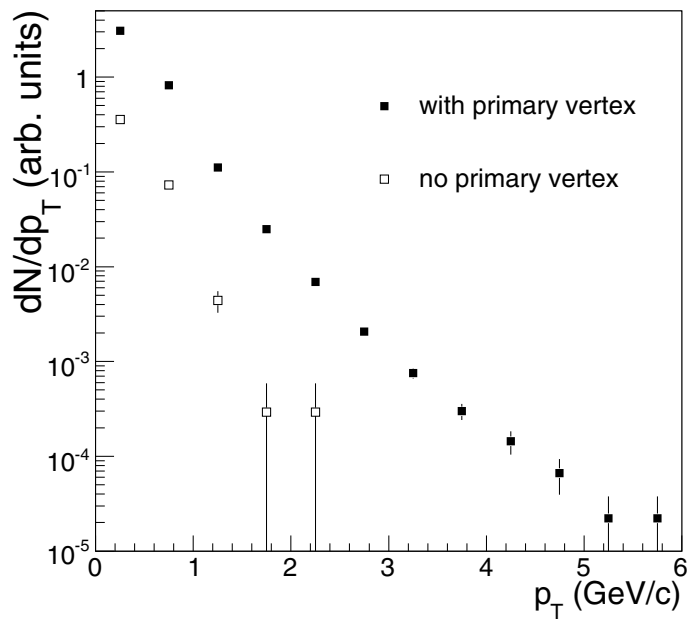


Figure 4.21: The π^0 yield per event from HIJING events with and without a reconstructed primary vertex.

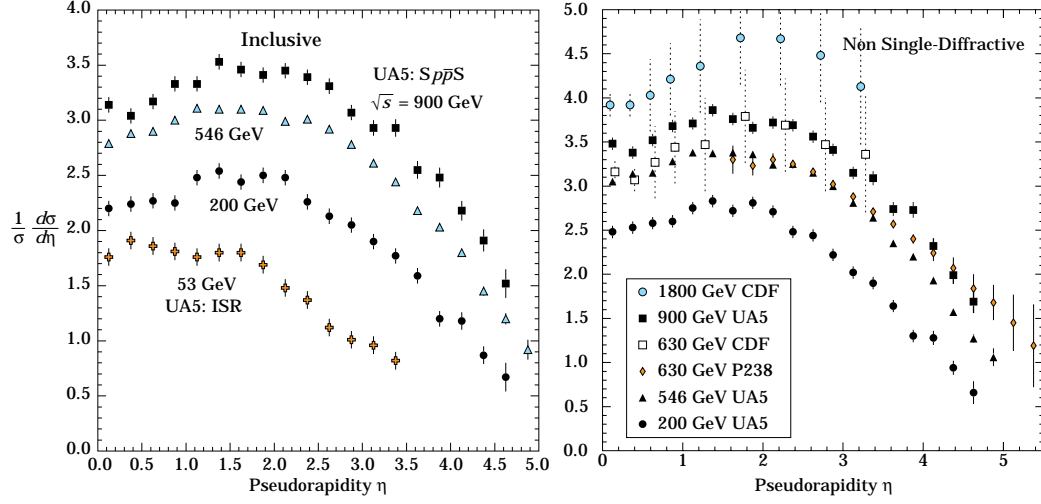


Figure 4.22: The charged particle yields versus η measured by the UA5 collaboration. The left (right) panel shows the results in case of inelastic (NSD) interactions (figure from [51]).

The inelastic part consists of a single-diffractive (SD), double-diffractive (DD), and non-diffractive cross section (ND). The sum of the DD and ND cross sections is defined as the non-single-diffractive cross section (NSD).

Starting from the invariant yield, it follows that

$$\begin{aligned}
 \frac{dN}{dp_T} &= \frac{1}{\sigma_{\text{BBC}}} \frac{d\sigma_{\text{BBC}}}{dp_T} \\
 &= \frac{1}{\sigma_{\text{BBC}}} \frac{d\sigma_{\text{inel}}}{dp_T} \times \left(\frac{d\sigma_{\text{NSD}}}{dp_T} / \frac{d\sigma_{\text{inel}}}{dp_T} \right) \times \left(\frac{d\sigma_{\text{BBC}}}{dp_T} / \frac{d\sigma_{\text{NSD}}}{dp_T} \right) \\
 &= \frac{\epsilon_{\text{BBC}}}{\sigma_{\text{BBC}}} \frac{d\sigma_{\text{inel}}}{dp_T} \times \left(\frac{d\sigma_{\text{NSD}}}{dp_T} / \frac{d\sigma_{\text{inel}}}{dp_T} \right) \quad (4.21)
 \end{aligned}$$

where $d\sigma_{\text{BBC}}/dp_T$ is the differential cross section for BBC triggered collisions. In general, $d\sigma_{\chi}/dp_T$ was defined as the differential cross section for the process $p + p \rightarrow \pi^0 + X$ for interactions of type χ . Additionally, we have used in the last step above that the BBC efficiency was defined as

$$\epsilon_{\text{BBC}} = \left(\frac{d\sigma_{\text{BBC}}}{dp_T} / \frac{d\sigma_{\text{NSD}}}{dp_T} \right), \quad (4.22)$$

which corresponds to the fraction of $d\sigma_{\text{NSD}}/dp_T$ satisfying the minimum bias condition as described in section 2.3.2. In what follows, we will demonstrate that the ratio of $d\sigma_{\text{NSD}}/dp_T$ and $d\sigma_{\text{inel}}/dp_T$ approximately equals unity.

The UA5 collaboration have measured the charged particle multiplicity in $p + \bar{p}$ collisions at $\sqrt{s_{NN}} = 200$ GeV as a function of pseudo-rapidity [87]. The experimental results are shown in figure 4.22 in case of inelastic collisions (left panel) and NSD collisions (right panel). From these data we estimated that

$$\left(\frac{d\sigma_{\text{inel}}}{d\eta} \Big/ \frac{d\sigma_{\text{NSD}}}{d\eta} \right) \approx (0.9 \pm 0.1) \times \frac{\sigma_{\text{inel}}}{\sigma_{\text{NSD}}} \quad (4.23)$$

in the range $0.0 < \eta < 1.0$. The same collaboration measured that $\sigma_{\text{SD}} = 4.8 \pm 0.5 \pm 0.8$ mb and $\sigma_{\text{inel}} = 41.8 \pm 0.6$ mb [88], which implies that

$$\left(\frac{d\sigma_{\text{inel}}}{d\eta} \Big/ \frac{d\sigma_{\text{NSD}}}{d\eta} \right) \approx 1.02 \pm 0.2. \quad (4.24)$$

In practice, the contribution from SD collisions falls off more rapidly with increasing p_T and results from a Pythia simulation have demonstrated that the ratio in equation 4.24 effectively equals unity for p_T values greater than 1.2 GeV/c [71]. After substituting this result in equation 4.21, the differential cross section of inclusive π^0 production in inelastic p+p collisions follows as

$$E \frac{d^3\sigma_{\text{inel}}}{d^3p} = \frac{\sigma_{\text{BBC}}}{\epsilon_{\text{BBC}}} \frac{1}{2\pi p_T} \frac{d^2N}{dp_T dy}. \quad (4.25)$$

This is the expression which we have used to convert our Lorentz invariant yields into cross sections.

4.3.2 Neutral Pion Production in p+p and d+Au Collisions

Figure 4.23 shows our measurement of the inelastic differential cross section of the process $p + p \rightarrow \pi^0 + X$ as given by equation 4.25. Figure 4.24 shows the Lorentz invariant yield of inclusive π^0 production in d+Au collisions which was defined by equations 4.15 and 4.16. The lower panels in both figures present those same data divided by a fit with the function defined in equation 4.9.

In nucleus-nucleus collisions, the production of particles is often expressed in terms of the nuclear modification factor R_{AB} which can be defined as

$$R_{\text{AB}} = \frac{dN/dp_T}{T_{\text{AB}} d\sigma_{\text{inel}}/dp_T}. \quad (4.26)$$

The overlap function T_{AB} of nucleus A and nucleus B was determined with a Monte-Carlo Glauber calculation [69]. The result in case of d+Au collisions was given by

$$T_{\text{dAu}} = \sigma_{\text{inel}}^{-1} \langle N_{\text{bin}} \rangle \quad (4.27)$$

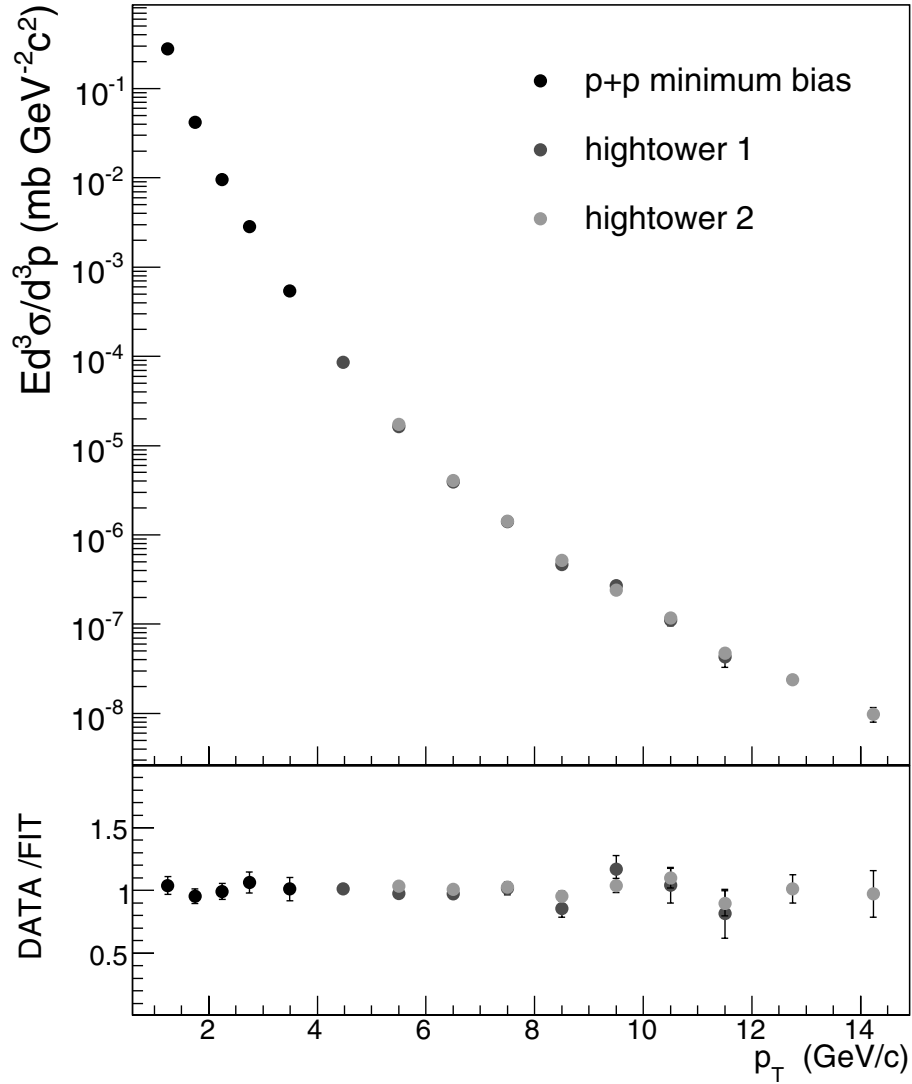


Figure 4.23: Top panel: the inclusive π^0 cross section $Ed^3\sigma/d^3p$ as a function of p_T for $\sqrt{s_{NN}} = 200$ GeV p+p collisions for the rapidity interval $0.1 < y < 0.9$. Bottom panel: the cross section divided by a fit (see equation 4.9). The error bars in both panels represent the statistical uncertainty only.

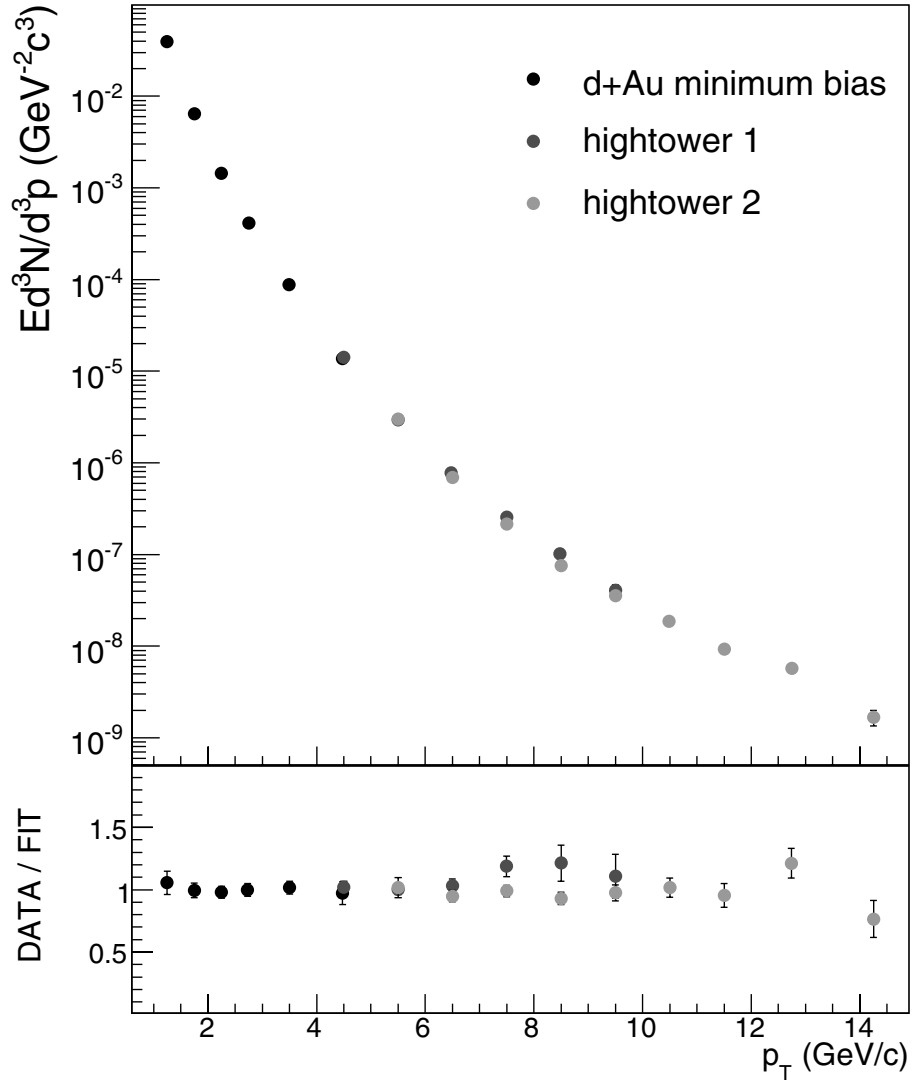


Figure 4.24: Inclusive neutral pion production in d+Au collisions at $\sqrt{s_{NN}} = 200$ GeV for the rapidity interval $0.1 < y < 0.9$. The error bars represent the statistical uncertainty only. Top panel: inclusive π^0 invariant yield Ed^3N/d^3p as a function of p_T (see equation 4.15) for minimum bias, HT1, and HT2 triggered collisions. Bottom panel: the same data divided by a fit (see equation 4.9).

where $\sigma_{\text{inel}} = 42 \text{ mb}$, the inelastic p+p cross section, and $\langle N_{\text{bin}} \rangle = 7.5 \pm 0.4$. The latter represents the number of binary collisions, that is, the total number of collisions between any two nucleons in the Glauber calculation. In general, T_{dAu} and $\langle N_{\text{bin}} \rangle$ are functions of the impact parameter \vec{b} . However, as we have analyzed our d+Au data without a bias towards the collision centrality, these dependences have been integrated out. The measured differential cross section of π^0 production in p+p collisions was used for the term $d\sigma_{\text{inel}}/dp_T$ in equation 4.26. Figure 4.25 shows the nuclear modification factor R_{dAu} as a function of p_T .

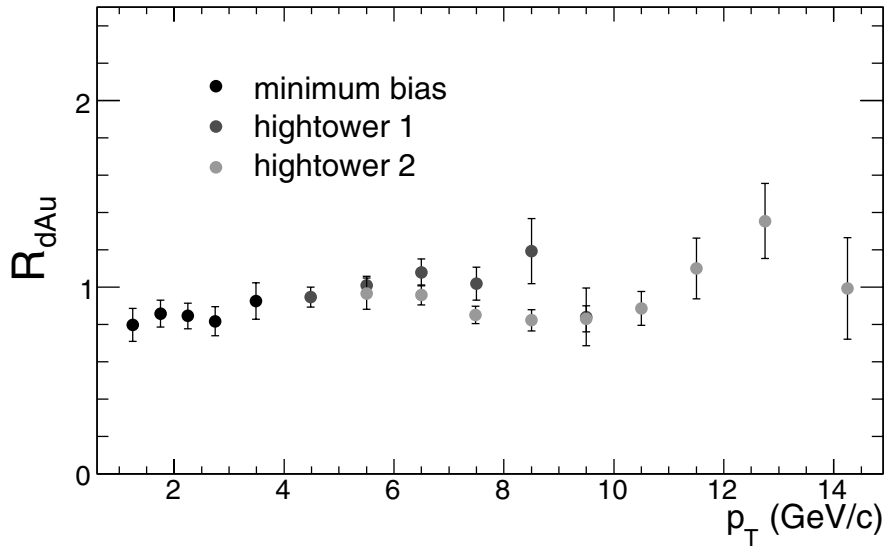


Figure 4.25: The nuclear modification factor R_{dAu} as a function of p_T . The shown error bars correspond to statistical uncertainties only.

Note that all error bars in this section represent the statistical uncertainties of the data points only. The systematic uncertainties will be discussed in detail below. The results are shown separately for the three classes of triggered events: minimum bias, HT1, and HT2. In principle it would be possible to combine the separate results in the p_T regions where they overlap. However, these data were statistically correlated, the size of this correlation strongly depending on the value of the trigger pre-scale factors (see section 2.3.2). Therefore, for the discussion of our results in chapter 6, those data points were selected which had the smallest statistical uncertainty. Nevertheless, the spectra obtained from the different data samples were found to be consistent in the p_T region where they overlapped, as can be seen from the figures. The final data points are listed in appendix A.

4.3.3 Systematic Uncertainties

The systematic uncertainties of the measured differential cross section (p+p), the invariant yield (d+Au), and the nuclear modification factor for π^0 production (R_{dAu}) are listed together in table 4.4. The total systematic error was dominated by the uncertainty coming from the energy calibration of the BEMC and BSMD, and more specifically, by the uncertainty of the overall energy scale of these detectors. In the next chapter, the direct photon yields will be discussed in terms of a ratio of the γ_{incl} and π^0 spectrum, as determined from the same data set. In this measurement, the calibration uncertainty largely canceled and the part of the systematic error which was caused by the π^0 yield extraction turned out to be of particular importance. These two sources of uncertainty and the corresponding errors will be discussed in more detail below.

The uncertainties which were caused by the normalization and the correction for conversions in the missing material were already discussed before (see sections 2.3.2, 4.2.4, and 4.3.2). The errors originating from the pre-scale correction have been determined in an independent analysis of the same data [56]. The relative difference of the γ_{incl} spectra, observed in the overlap region of the HT1 and HT2 triggered data, exceeded the value (3%) which was reported there for the HT1 spectra. We assigned a larger systematic error (5%) to account for the effect. A possible explanation for this discrepancy could be the different criteria used to select the event sample. In case of the d+Au π^0 spectrum, the beam background removal was included as a source of uncertainty by varying the applied event cut around its nominal value (see section 3.2.1). The systematic uncertainties of the final results caused by the correction for false charged particle vetoes were found to be negligible.

The uncertainties on the normalization of $R_{\text{d+Au}}$ followed straightforwardly from those of the p+p and d+Au measurements. The contributions resulting from the π^0 yield extraction routine, the systematic error on ϵ_{reco} , the correction for the missing material, and the relative uncertainty of the tower gains, were conservatively added in quadrature as well. Since the results from the p+p and d+Au data were obtained with the same energy calibration of the BSMD, the corresponding uncertainty canceled upon taking the ratio of the spectra in terms of R_{dAu} .

The calibration of the BEMC towers was performed separately for the d+Au and the p+p data. However, there was no reason to believe that the corresponding systematic errors on the BEMC energy scale were fully uncorrelated. Adding the quoted errors in quadrature would lead to a relative error on R_{dAu} of approximately 45% at $p_T = 10.5 \text{ GeV}/c$ thereby seriously reducing the significance of the measurement. A reduction of the separate uncertain-

p_T (GeV/ c)	p+p		d+Au		R_{dAu}	
	3.5	10.5	3.5	10.5	3.5	10.5
<i>correlated</i>						
BEMC energy scale	23.7%	28.3%	29.6%	35.4%	12.0%	14.1%
BEMC gain spread	2.4%	2.4%	3.5%	3.5%	4.2%	4.2%
BSMD energy scale	11.2%	4.5%	11.2%	4.5%	-	-
BSMD gain spread	7.4%	1.4%	7.4%	1.4%	-	-
missing material	1.8%	1.8%	2.6%	2.6%	3.2%	3.2%
<i>uncorrelated</i>						
ϵ_{reco} (sys.)	4.0%	4.0%	4.0%	4.0%	-	-
ϵ_{reco} (stat.)	2.0%	1.5%	2.0%	2.0%	2.8%	2.5%
beam background	-	-	< 1%	3.5%	< 1%	3.5%
π^0 yield extraction	5.0%	7.1%	5.0%	7.1%	7.1%	10.0%
<i>normalization</i>						
σ_{BBC}	6.9%	6.9%	-	-	6.9%	6.9%
ϵ_{BBC}	9.2%	9.2%	-	-	9.2%	9.2%
ϵ_{vert}	-	-	1.1%	1.1%	1.1%	1.1%
pre-scale	-	5.0%	-	5.0%	-	7.1%
$\langle N_{\text{bin}} \rangle$	-	-	-	-	5.3%	5.3%
<i>total</i>						
point-to-point	28.2%	30.0%	33.5%	37.1%	15.2%	18.6%
normalization	11.5%	12.5%	1.1%	5.1%	12.7%	14.6%
statistical	9.8%	7.3%	4.8%	7.3%	10.9%	10.4%

Table 4.4: The relative uncertainties of the neutral pion differential cross section (p+p), the invariant yield (d+Au), and the nuclear modification factor (R_{dAu}). The numbers are grouped in terms of point-to-point (in p_T) correlated, point-to-point uncorrelated, and overall normalization uncertainties. Note that the energy scale uncertainty of R_{dAu} was exclusively derived (see text) and therefore does not follow from the quadratic subtraction of the uncertainties of the separate spectra.

ties could be accomplished by means of an energy calibration based on the π^0 peak position. However, this would require more detailed knowledge on the background underneath the peak which, if not properly simulated, might introduce a shift in the peak position.

To estimate the relative uncertainty between the two data sets, we use the reconstructed peak positions (μ), after subtraction of the background, from the minimum bias data. They are compared to the results of the respective Monte-Carlo simulations in figure 4.26. The outer two dashed curves show the sensitivity of μ to a change in the global p+p energy scale by $\pm 4\%$. The expected difference between the reconstructed π^0 masses from the d+Au and p+p data was small, as indicated by the two full lines in the figure. This same difference is larger in case of the measured values of μ , though still significantly smaller than the uncertainty indicated by the two dashed curves. Moreover, these curves represent the error on the p+p energy scale only, incorporating the error for d+Au as well would yield an uncertainty which is even ~ 1.5 times larger. To avoid such an overestimate of the systematic error on R_{dAu} , we have estimated that the calibration uncertainty in the d+Au data, relative to that of the p+p data, was not larger than 2%. The size of this uncertainty is illustrated by the band around the full lines in the figure.

Finally, the stability of the π^0 spectra upon variation of the analysis cuts was investigated in order to trace hidden systematic uncertainties. The cut on the energy asymmetry was varied as $Z_{\gamma\gamma} = 0.7 \pm 0.1$ and two alternative fiducial volumes for the photon candidates were used: $0.0 < \eta < 1.0$ and $0.2 < \eta < 0.8$. Furthermore, the vertex cut was varied ± 10 cm around the nominal value. We have added the corresponding fluctuations in quadrature which resulted in a 4% (and hence negligible) error on the π^0 spectrum, for both collision systems. This error was our estimate of the remaining systematic uncertainty of our efficiency correction factor ϵ_{reco} . Since the simulation framework and the method to determine ϵ_{reco} were identical in p+p as well d+Au collisions, we have assumed that a full cancellation occurred with respect to our measurement of R_{dAu} .

Calibration Uncertainty

The simulation framework which was used to evaluate the systematic uncertainty related to the energy calibration has already been discussed in section 3.4.2. The parameters in equation 3.16 were separately varied based on the error of the global energy scale (δ) as well as the estimated spread in the channel-to-channel relative calibration ($\sigma(C)/C$). Subsequently, the full analysis was repeated and the variation relative to the nominal settings was

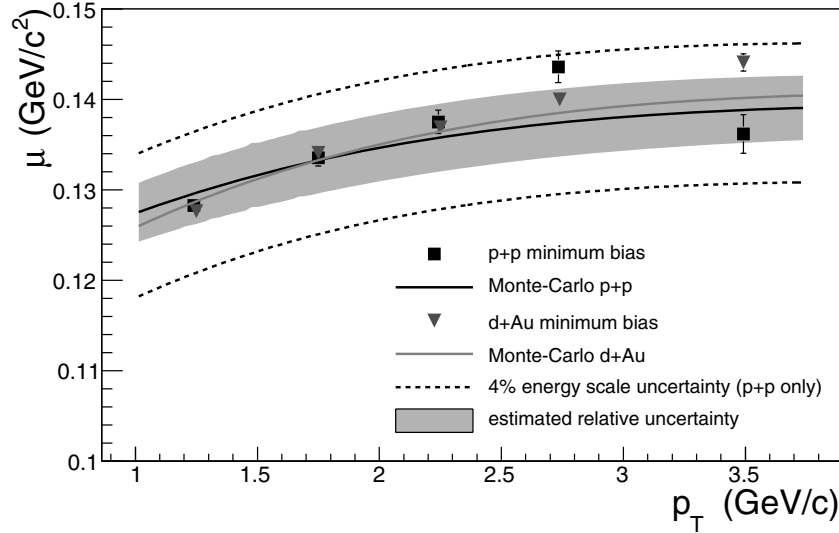


Figure 4.26: The reconstructed π^0 mass (μ) as a function of p_T for d+Au and p+p minimum bias collisions. The results from the corresponding Monte-Carlo simulations are shown as well. The two dashed curves indicate the uncertainty on the reconstructed π^0 mass as a result of the error on the BEMC energy scale in case of p+p collisions. The shaded band is our derived estimate of the relative uncertainty of the respective overall energy scales in the two data sets.

used as an estimate of the corresponding uncertainty.

The dashed lines in figures 4.27 and 4.28 represent the uncertainty on the measured π^0 cross section in p+p collisions attributed to the error on the overall energy scale of the BEMC and BSMD, respectively. The upper graphs in both figures correspond to an overestimate of the experimental energy scale, leading to a larger π^0 yield in both cases. From these figures it is evident that the systematic uncertainties were correlated for different values of p_T . The large contribution associated with the error on the BEMC energy scale (4%) was a consequence of the shape of the π^0 spectrum which falls off rapidly with increasing p_T . A relatively small shift in the measured energy causes a large change of the raw yield.

The uncertainty caused by the error on the BSMD energy scale was most prominent at low values of p_T . This was a result of the energy thresholds of the clustering algorithm (E_{seed} and E_{add}). These thresholds would be more frequently exceeded if there was an overestimate of the BSMD energy scale. In case of single photons, this effect vanishes for large values of p_T . The energy corresponding to the centroid of the BSMD cluster would always be

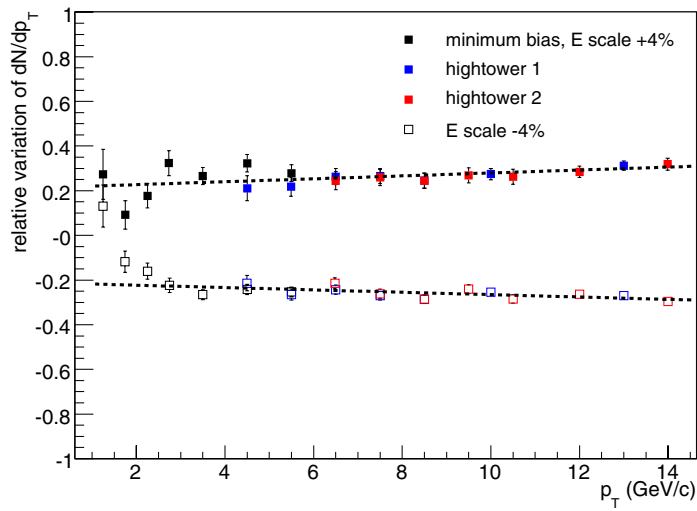


Figure 4.27: The relative change of the measured π^0 yield in case that the absolute BEMC energy scale (GeV/ADC) would have been 4% too large (upper curve) and 4% too small (lower curve).

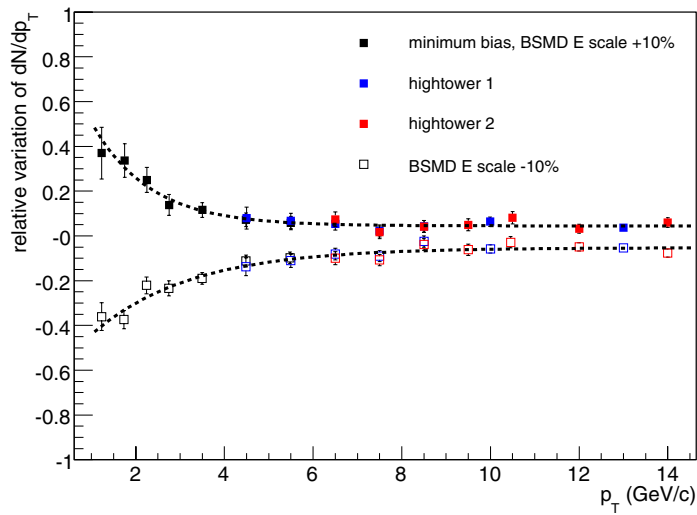


Figure 4.28: The relative change of the measured π^0 yield in case that the absolute BSMD energy scale (GeV/ADC) would have been 10% too large (upper curve) and 10% too small (lower curve).

greater than E_{seed} , regardless whether the energy was off by 10% or not, and likewise for the adjacent channels. However, for the decay photons of the π^0 similar arguments hold since the cut on $Z_{\gamma\gamma}$ constituted a lower limit to their energies which became higher with increasing p_T . Hence, this uncertainty had a relatively small contribution at high p_T .

Neutral Pion Yield Extraction

The final goal of the presented analysis was to measure the direct photon yields in p+p and d+Au collisions. Since the photons produced by the process $\pi^0 \rightarrow \gamma\gamma$ were the largest background to the direct photons, the errors in table 4.4 are of great relevance for that measurement as well. However, it can be shown (see section 5.2.4) that the largest uncertainties discussed above, namely those associated with the energy calibration, were of secondary importance to the direct photon measurement. They effectively canceled upon calculating the double ratio, as defined by equation 5.10 in the next chapter. Consequently, the systematic uncertainty from the π^0 yield extraction routine was one of the dominant contributions to the total systematic error in the direct photon analysis.

Part of the systematic error associated with the extraction of the raw π^0 yield was related to the unknown shape of the background underneath the π^0 mass peak. A Pythia study was performed to check whether the applied polynomial fit successfully removed the background at higher values of p_T where a π^0 was likely to be part of a jet. The jet is characterized by the angular correlation of its constituents which in turn leads to background pairs near the π^0 peak. The results of this study were presented in section 4.2.6 above and implied that the possible distortions of the measurement were relatively small. Figure 4.29 shows the reconstruction efficiency obtained from the Pythia simulation compared to the results from the single-particle-per-event simulation. The dashed line represents the estimated uncertainty (5%) which was used to account for the possible effects of this jet structure on the extracted π^0 yield. We have included this uncertainty for the HT1 and HT2 spectra only ($p_T > 5 \text{ GeV}/c$).

Additionally, the invariant mass range which was used to integrate the π^0 peak was varied. The results are shown in figure 4.30 for the alternative integration intervals $\{\mu - 3\sigma, \mu + 2\sigma\}$, $\{\mu - 2\sigma, \mu + 3\sigma\}$, and $\{\mu - 2\sigma, \mu + 2\sigma\}$. When the result of the fit with f_{bg} would be exactly equal to the combinatorial background, the final result could still be sensitive to this variation in cases where the shape of the π^0 peak was different from the simulated mass spectra. The dashed lines in the figure correspond to the uncertainty as determined from the d+Au data. Similar results were found

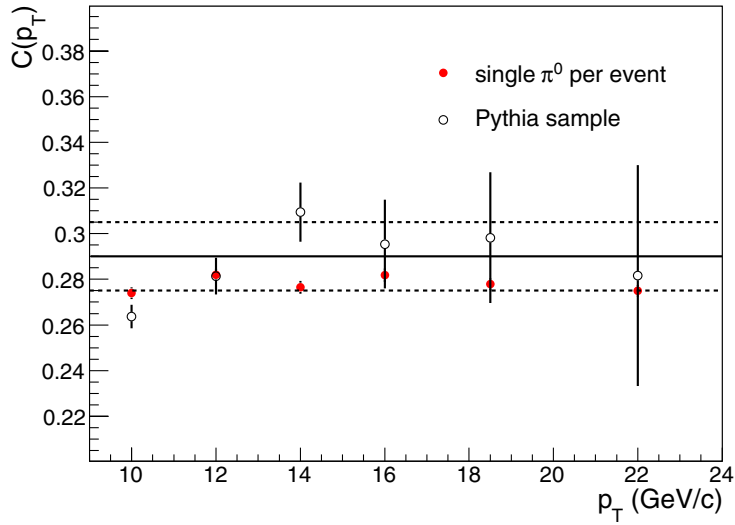


Figure 4.29: The reconstruction efficiency (denoted by $C(p_T)$) as a function of p_T from the Pythia simulation compared to the single-particle-per-event Monte-Carlo. The dashed lines demonstrate the corresponding systematic uncertainty which was assigned to the final results.

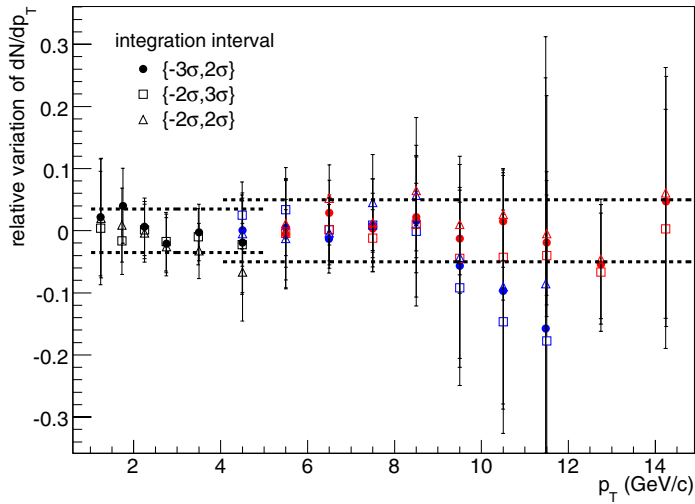


Figure 4.30: The relative variation of the π^0 spectrum for different definitions of the π^0 peak integration interval. The dashed lines represent our estimate of the uncertainty. Note that the data points outside this uncertainty band were not included in our final results.

for the p+p data and both were added to the uncertainty from the Pythia study, in quadrature. The latter resulted in the values listed in table 4.4.

Chapter 5

Direct Photon Measurements

A common approach to measure direct photon production in hadronic collisions is based on a direct identification of isolated photons. An isolation criterion is used to reject photon candidates, typically by requiring less than a certain minimal amount of background energy in a cone around them. However, the implementation of an isolation cut in a high multiplicity environment would introduce additional complications. Since our final goal was to provide results which could serve as a reference to the direct photon rates in heavy ion collisions, an alternative method was preferred. Our strategy was to measure the direct photon signal indirectly, as the ratio of all photons to the simulated background. This background mainly consists of photons coming from hadronic decays, in particular those from the process $\pi^0 \rightarrow \gamma\gamma$ ($\sim 80\%$). Hence, an accurate measurement of the π^0 spectrum was an important first step in the presented direct photon measurement.

Figure 5.1 outlines the followed approach. The sample of photon candidates (γ_{cand}) served as the main input, as in case of the reconstruction of the π^0 spectrum, however, with the alternative constraints listed in table 3.3. After subtracting the contamination by charged particles and neutral hadrons, the raw inclusive photon sample was corrected to account for, for example, the limited acceptance and the finite detector resolution. In parallel, the total yield of photons from π^0 , η , and $\omega(782)$ decays was simulated where a phenomenological scaling law (m_T scaling) was assumed for the η and $\omega(782)$ spectra. The direct photon yield finally followed after subtracting the decay photon yield from the inclusive photon yield, written schematically as

$$\gamma_{\text{dir}} = \gamma_{\text{incl}} - \gamma_{\text{decay}}. \quad (5.1)$$

This equation corresponds to the subtraction of two numbers which are generally large compared to the direct photon signal. The relative systematic

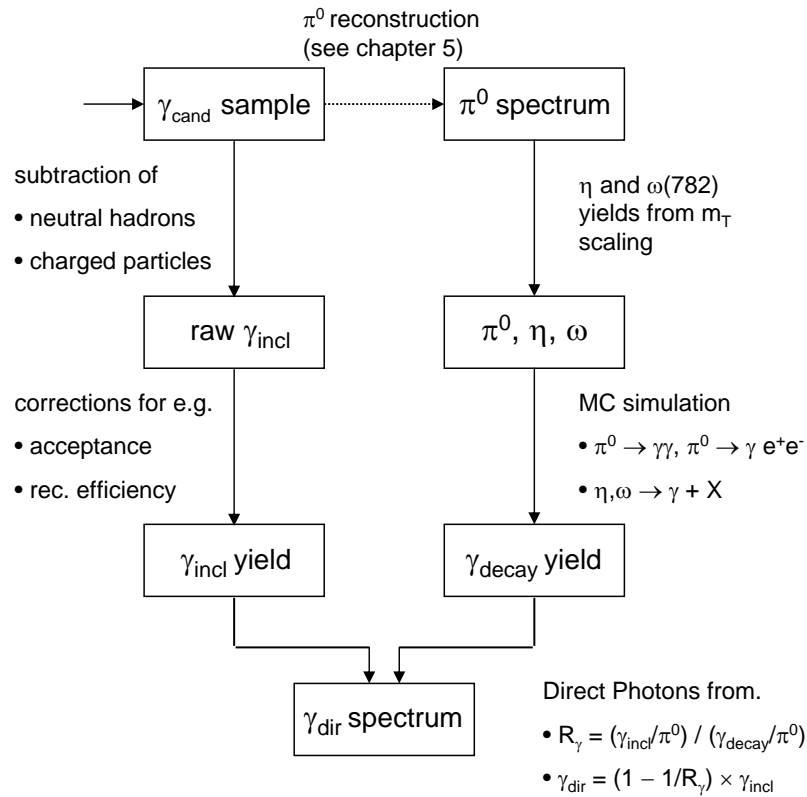


Figure 5.1: The flow of the direct photon analysis.

uncertainties of the two components on the right side of equation 5.1 therefore needed to be well under control.

To exploit the fact that the inclusive photon and decay photon yields have many positively correlated uncertainties, we studied the direct photon yield in terms of the double ratio R_γ :

$$R_\gamma = \frac{\gamma_{\text{incl}}/\pi^0}{\gamma_{\text{decay}}/\pi^0} \quad (5.2)$$

where the numerator equals the point-to-point ratio of the measured spectra of inclusive photons and neutral pions. The denominator is the simulated background contribution from decay processes divided by the parametrized π^0 yield. It follows that

$$R_\gamma = 1 + \frac{\gamma_{\text{direct}}}{\gamma_{\text{decay}}} \quad (5.3)$$

which therefore serves as an indicator of a direct photon signal ($R_\gamma > 1$).

The absolute direct photon yields can subsequently be determined as

$$\gamma_{\text{direct}} = (1 - R_\gamma^{-1}) \times \gamma_{\text{incl}} \quad (5.4)$$

where the systematic uncertainties which canceled in the double ratio will have to be included again.

5.1 Inclusive Photons

The reconstruction of the γ_{incl} spectrum was in many ways similar to that of the neutral pions described in the previous chapter. The uncorrected γ_{incl} spectrum was extracted from the same data sample, using identical event cuts and the same sample of photon candidates. However, there were no rigorous constraints on the purity of the photon candidates used for the π^0 invariant mass analysis. Remaining contributions from charged particles and neutral hadrons could be identified afterwards, in terms of the combinatorial background in the mass distributions. In contrast to the latter, the uncorrected inclusive photon sample $N_{\text{incl}}^{\text{raw}}$ was obtained from an explicit subtraction of such backgrounds:

$$N_{\text{incl}}^{\text{raw}} = (1 - C_0) (1 - C_\pm) N_{\text{cand}} \quad (5.5)$$

where the correction terms C_0 and C_\pm represent the fractional contamination by neutral hadrons and charged particles, respectively, to the yield of photon candidates N_{cand} .

The Lorentz-invariant yield of inclusive photons was defined, analogously to that of neutral pions in equations 4.15 and 4.16, as

$$\frac{1}{2\pi p_T} \frac{d^2 N}{dp_T dy}(p_T) = \frac{1}{2\pi p_T} \frac{1}{N_{\text{ev}}^{\text{MB}}} \frac{1}{K(p_T)} \frac{N_{\text{incl}}^{\text{raw}}(p_T)}{\Delta p_T \Delta y}, \quad (5.6)$$

The correction term in the denominator is given by

$$K(p_T) = \epsilon_{\text{reco}}^\gamma(p_T) c_{\text{miss}}^{-1} \epsilon_{\text{vert}} \epsilon_{\text{CPV}}^\gamma c_{\text{bin}}^{-1}. \quad (5.7)$$

The two factors in the expression for $K(p_T)$ which did not already appear in the formula for the π^0 invariant yield are

- $\epsilon_{\text{reco}}^\gamma(p_T)$ the single photon reconstruction efficiency
- $\epsilon_{\text{CPV}}^\gamma$ the correction for false vetoes in case of single photon candidates

The inverse correction factor $\epsilon_{\text{reco}}^\gamma$ contained the convoluted effects on the inclusive photon yield from the limited acceptance, the detection and reconstruction efficiency, as well as energy smearing¹. However, as will be explained in section 5.1.3 below, $\epsilon_{\text{reco}}^\gamma$ contained two quantitatively different components which were used to separately correct the raw photon yield from π^0 decays and from the complementary sources.

5.1.1 Neutral Hadron Contamination

The term C_0 in equation 5.5 was defined as the number of reconstructed showers generated by neutral hadrons relative to the total number of showers in the photon candidate sample. The STAR detector has no means of directly identifying neutrons (n) and antineutrons (\bar{n}). Therefore the contamination had to be simulated and subtracted using the measured (anti)proton spectra to estimate its size.

Internal STAR measurements of the p and \bar{p} yields in d+Au (2003) and p+p (2001) collisions were reported in [90]. These yields were parametrized as

$$\frac{1}{2\pi p_T} \frac{d^2 N}{dp_T dy} = B \left(1 + \frac{m_T - m_0}{nT} \right)^{-n} \quad (5.8)$$

with the parameters listed in table 5.1 and m_0 equal to the proton mass. We assumed that their primary production rates were equal to those of the n and \bar{n} yields, respectively. However, the contribution from Λ and $\bar{\Lambda}$ was not subtracted in case of the STAR p and \bar{p} measurements.

The ratio of hyperon and proton spectra, $\Lambda/p \equiv \delta_\Lambda$, was estimated to be approximately 20% [90]. The hyperons contribute to the proton yield through the decay $\Lambda \rightarrow p + \pi^-$. The latter has a branching ratio equal to 63.9% which is different from the decay $\Lambda \rightarrow n + \pi^0$ (35.8%). Hence, the estimated yield of neutrons was determined from the measured proton yield as

$$n = (1 - \delta_\Lambda) p_{\text{prod}} + \delta_\Lambda \frac{\Gamma(\Lambda \rightarrow n\pi^0)}{\Gamma(\Lambda \rightarrow p\pi^-)} p_{\text{prod}} + \frac{A - Z}{Z} p_{\text{part}} \quad (5.9)$$

The last term on the right is the scaled yield of participant protons (p_{part}) to account for the different number of neutrons versus protons in the gold core ($A = 197$, $Z = 79$). The yield of protons produced in the actual collision is written as p_{prod} . The sum of those two was, by definition, equal to the measured inclusive proton yield. Finally, the produced proton spectrum p_{prod} was assumed to match that of the antiprotons since the latter does not

¹Hence, the inverse correction factor $\epsilon_{\text{reco}}^\gamma$ is in principle not an efficiency, as was already discussed in section 4.2.

par.	d+Au (p)	d+Au (\bar{p})	p+p (p)	p+p (\bar{p})
B	0.3 ± 0.01	0.23 ± 0.01	0.072 ± 0.005	0.061 ± 0.005
T	0.205 ± 0.004	0.215 ± 0.005	0.179 ± 0.006	0.173 ± 0.006
n	11.00 ± 0.29	12.55 ± 0.41	10.87 ± 0.43	10.49 ± 0.40

Table 5.1: The parameters used to describe the proton and antiproton spectra [90].

contain participant contributions. The expression for the antineutron yield is similar to equation 5.9 without the participant term p_{part} .

The largest neutral contamination was caused by antineutrons. The annihilation process, e.g. $\bar{n} + p \rightarrow 2\pi^+\pi^-\pi^0$, in the lead of the calorimeter could initiate an electromagnetic shower which did not necessarily develop in the same direction as the incident antineutron. Moreover, the available energy for the reaction products included the energy of the nucleon at rest (~ 1 GeV). The measured energy of especially the slow antineutrons could therefore be significantly increased as compared to the detection of photons with similar momenta, the potential shift being as large as approximately twice the rest mass of a nucleon.

To study the contamination of our photon candidate spectrum, approximately 3×10^6 antineutrons were generated and processed through the GEANT simulation with the following settings:

- $0 < p_T < 10 \text{ GeV}/c$
- $-0.3 < y < 1.2$
- $0 < \phi < 2\pi$
- $dN/dy = dN/d\phi = \text{constant}$, $dN/dp_T \sim \exp(-p_T/(2 \text{ GeV}/c))$

The non-uniform p_T distribution was chosen to provide sufficient statistics at low values of p_T where the slow antineutrons constituted a significant source of contamination. The GEANT framework was initialized with the FLUKA program [89] to describe the particle transport and the interactions in the detector material. Note that the parametrizations of the p and \bar{p} yields were not only used to assign a weight to the Monte-Carlo events but also to determine the absolute contamination of the photon sample. The latter was divided by the number of photon candidates from experiment which resulted in C_0 .

Figure 5.2 qualitatively illustrates the bin migrations which had to be considered to evaluate the \bar{n} reconstruction efficiency as defined by equation

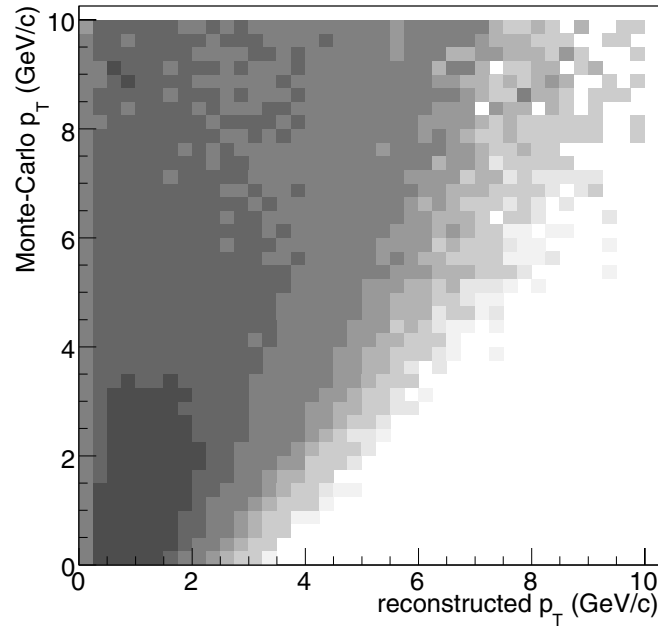


Figure 5.2: Generated Monte-Carlo p_T of antineutrons versus their reconstructed p_T assuming that the incident particles were photons.

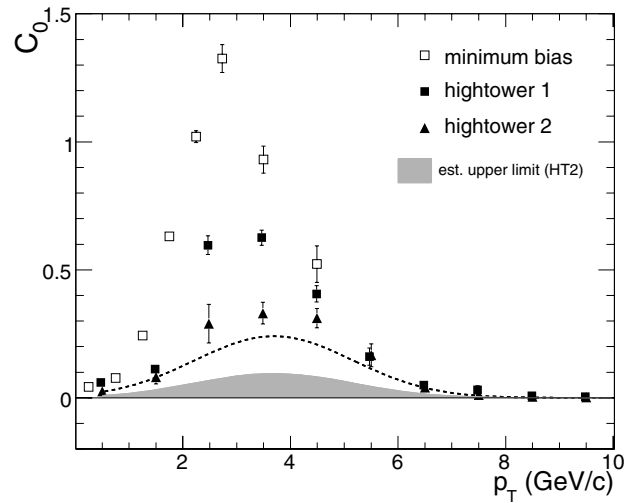


Figure 5.3: The relative neutral hadron contribution to the photon candidate yield in terms of C_0 versus p_T . The filled area represents the upper limit to C_0 for our hightower 2 data sample, the dashed curve is the upper limit in the extreme scenario that all photon candidates were a result of showering antineutrons.

4.6. The vertical axis represents the generated p_T of the \bar{n} and the horizontal axis its measured p_T . The latter was calculated with the assumption that the incident particle was a photon, similar to what would happen in our experiment in case a neutral hadron would be misidentified as a photon candidate. This result confirms that the lowest p_T intervals will receive the largest contribution from relatively slow antineutrons. Hence, the precise shape of the \bar{n} input distribution of the Monte-Carlo simulation in this p_T region was crucial to quantitatively determine the contamination.

The final contamination fraction C_0 is shown in figure 5.3 in case of p+p collisions. The graphs show that, in a limited p_T range, C_0 appeared to be larger than unity. The latter would not be possible (see equation 5.5) unless the associated systematic uncertainties are extremely large.

Two natural limits to the contamination can be considered. First of all, the requirement that $C_0 \leq 1$ constitutes a hard upper limit by definition. This is not very realistic though, as it implies that the inclusive photon yield would be zero. An alternative limit follows from the assumption that in the range around the annihilation peak ($\sim 2.5 \text{ GeV}/c$) the direct photon signal would be zero. In both cases, a scaling factor for C_0 was derived which was subsequently applied to the hightower 2 graph in figure 5.3. The hard upper limit $C_0 \leq 1$ is shown by means of the dashed curve, the shaded band represents the limit assuming that only background photons have been detected in the range $1 < p_T < 4. \text{ GeV}/c$. We have chosen the latter as our estimate of the upper limit on the neutral contamination C_0 .

As a cross-check, the possible contamination by long-lived neutral kaons (K_0^L) was studied. The reconstruction efficiency of these particles was found to be negligibly small for $p_T > 5 \text{ GeV}/c$. The upper graph in figure 5.4 shows the generated K_0^L spectrum and the lower graph the resulting raw yield of fake photon candidates. The ratio of these two would be by definition equal to the reconstruction efficiency (see equation 4.6). The figure indicates that the contribution to $N_{\text{raw}}^{\text{cand}}$ in case of the K_0^L can be ignored at higher values of p_T .

In addition, we show in figure 5.5 the reconstruction efficiencies of antineutrons, long-lived kaons, and positively charged pions. These results were obtained for hightower 2 data from which we will eventually reconstruct our direct photon spectra. The figure illustrates how the π^+ and K_0^L interactions with the BEMC resulted in a negligible contamination as compared to that of the antineutrons as shown in figure 5.3. According to our simulations, the clusters from neutrons caused a similar contribution to the photon sample as those from the charged pions and could therefore be ignored as well.

Two important remarks should be made here. First of all, the simulation of the charged pions contained a full track reconstruction in the TPC. Hence,

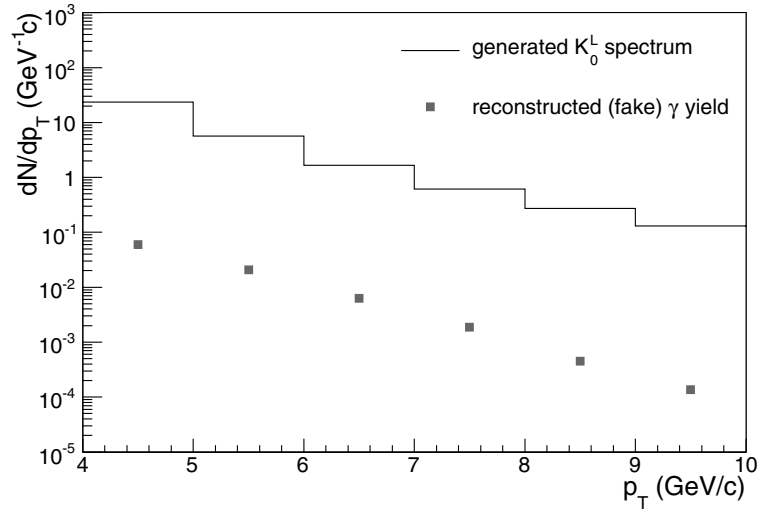


Figure 5.4: Generated K_0^L yield and the corresponding yield of fake photon candidates as obtained from a Monte-Carlo simulation.

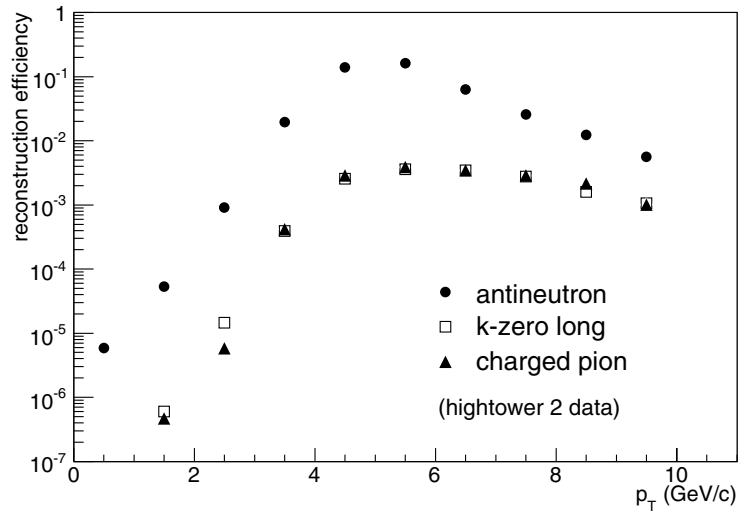


Figure 5.5: The photon reconstruction efficiencies (as defined in the text) in case the shower was initiated by antineutrons, long-lived kaons, and positively charged pions. Note that the input particles were simulated within $0 < p_T < 10 \text{ GeV}/c$.

many clusters were rejected with the charged particle veto which was also applied in our analysis of the experimental data. However, the irregular nature of the hadronic shower made it possible that these clusters were outside the veto area. Nevertheless, the spatial correlation with the reconstructed charged track remained and the contamination associated with showering charged hadrons will therefore be addressed in the next section in terms of C_{\pm} (c.f. equation 5.5).

A second remark concerns the p_T values and the reconstruction efficiencies in figure 5.5. These were determined with the assumption that the shower was initiated by a photon. The number of anomalous photon candidates from neutral hadrons is then calculated as the sum of the products of each efficiency with the corresponding hadron spectrum. Dividing this sum by the total number of uncorrected photon candidates (c.f. γ_{cand} in equation 5.5) yields the final value of C_0 which, in practice, was fully determined by the antineutrons.

5.1.2 Background from Charged Particles

The contamination of the photon candidate sample by charged particles was suppressed with a charged particle veto (CPV). All candidates with a charged track closer than $D_{\text{CPV}} = 15$ cm were excluded from further analysis. The erroneous rejection of genuine photons, due to random overlaps with a charged track, was corrected for by the term $\epsilon_{\text{CPV}}^{\gamma}$ as can be seen from equations 5.6 and 5.7. The method to determine the correction for false vetoes was already described in section 4.2.7. The only difference was that in case of $\epsilon_{\text{CPV}}^{\gamma}$ we used the closest distance of a track to a single photon cluster instead of a pair. Figure 5.6 shows the results for $\epsilon_{\text{CPV}}^{\gamma}$ in case of HT1 d+Au collisions. The correction was parametrized with a linear function and the obtained parameters are listed for completeness in table 5.2.

However, contrary to the π^0 analysis, an additional correction had to be derived to eliminate the remaining fraction of charged particles from the photon candidate sample. This correction factor was denoted by C_{\pm} and was already introduced in equation 5.5 above. The factor C_{\pm} was obtained from the integrated excess of the D_{track} distribution over the fit to the random associations, in the interval $15 < D_{\text{track}} < 25$ cm. The D_{track} distributions of single clusters and the corresponding fit results were very similar to those shown in figure 4.18. The factor C_{\pm} was finally defined as the number of counts in this excess divided by the total number of candidates and evaluated for consecutive p_T bins. The resulting correction was relatively small, $C_{\pm} < 5\%$, over the entire p_T range. The final estimates of C_{\pm} are listed in table 5.2 as well.

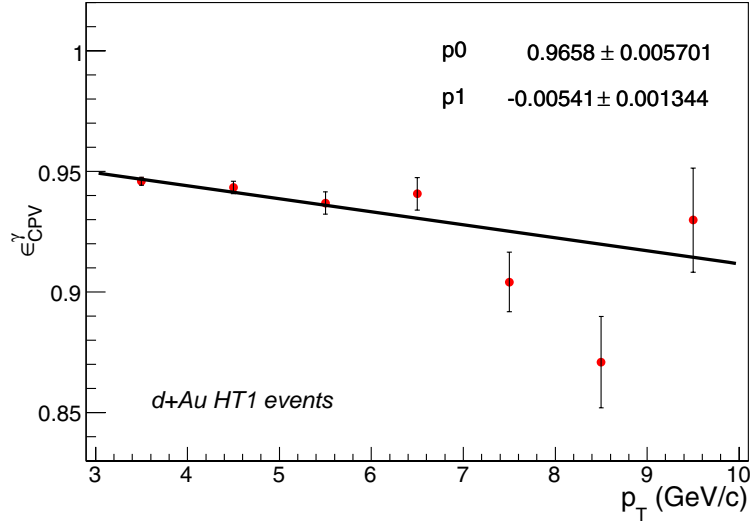


Figure 5.6: The false veto correction $\epsilon_{\text{CPV}}^{\gamma}$ for single photons in case of d+Au HT1 events. The full line represents the fit with the linear function and the resulting parameters for all trigger classes are listed in table 5.2.

system	par.	MB	HT1	HT2
p+p	c	0.028 ± 0.007	0.002 ± 0.005	0.004 ± 0.008
	d	0.000 ± 0.005	-0.011 ± 0.001	-0.011 ± 0.001
	C_{\pm}	0.015 ± 0.005	0.020 ± 0.007	0.040 ± 0.015
d+Au	c	0.041 ± 0.002	0.034 ± 0.006	0.049 ± 0.007
	d	-0.004 ± 0.001	-0.005 ± 0.001	-0.003 ± 0.001
	C_{\pm}	0.020 ± 0.005	0.020 ± 0.005	0.035 ± 0.015

Table 5.2: The parameters of the fit to $\epsilon_{\text{CPV}}^{\gamma}$ with the function $f_{\text{cpv}} = c + dx$, and the remaining contamination by charged particles C_{\pm} .

5.1.3 Photon Reconstruction Efficiency

The photon reconstruction efficiency $\epsilon_{\text{reco}}^\gamma$ was calculated analogously to the definition in equation 4.6 in case of neutral pions. We have evaluated $\epsilon_{\text{reco}}^\gamma$ for two types of photons separately. First of all, for those which originated from a decaying π^0 and, in addition, for events containing only a single photon. The latter was then used to correct the fraction of the photon yield from other sources than the decay $\pi \rightarrow \gamma\gamma$, as will be demonstrated below.

To determine $\epsilon_{\text{reco}}^\gamma$ in case of the π^0 decay photons, we used the Monte-Carlo event sample which was introduced in section 4.2.1. Next to that, the same parametrization of the π^0 yield was used as a weight in order to simulate a realistic input distribution. Note, however, that the frequency at which a given event occurs should depend on the simulated p_T of the π^0 and not on the p_T of any of the two photons. Hence, it was crucial that an identical weight was applied to all reconstructed photons in an event.

Furthermore, the simulation included all the possible losses of photon candidates as listed in section 4.2.1, except for those associated with the invariant mass window and the cut on the energy asymmetry $Z_{\gamma\gamma}$. An important aspect concerned those showers which were initiated by a high p_T π^0 . Since there was no requirement on the relation between the reconstructed p_T and the Monte-Carlo input p_T , the correction implicitly accounted for events where one of the two decay photons remained unidentified and the total energy was assigned to a single cluster. This merging of photon showers constituted the main difference with respect to the reconstruction efficiency of single photons.

Similar to the above, $\epsilon_{\text{reco}}^\gamma$ for single photons followed from a Monte-Carlo sample of $\sim 1 \times 10^6$ events where each event contained a single photon with

- $0 < p_T < 20 \text{ GeV}/c$
- $-0.3 < y < 1.2$
- $0 < \phi < 2\pi$
- $dN/dp_T = dN/dy = dN/d\phi = \text{constant}$

The corresponding weight function would in principle follow from considering the spectrum of photons from decaying hadrons other than the π^0 , as well as that of the direct photons. However, we will demonstrate in section 5.2.2 that the shape of the decay photon spectrum and the measured π^0 spectrum were very similar, at least, for the p_T range which we are considering in this analysis. Although the direct photon spectrum was expected to exhibit a

slightly different p_T dependence, varying the input spectrum correspondingly did not yield quantitatively different results.

Finally, we have implemented the correction to the measured photon yields as follows. The yield of photons which originated from the process $\pi^0 \rightarrow \gamma\gamma$ was determined from the measured π^0 spectrum. This part of $N_{\text{incl}}^{\text{raw}}$ was corrected with the result for $\epsilon_{\text{reco}}^\gamma$ in case of π^0 decay photons. The remaining part of the raw photon yield was assumed to consist of single photons which were not correlated to the other photon candidates in the event. This assumption was based on the observation that the reconstruction efficiency for photons from the process $\eta \rightarrow \gamma\gamma$, the next largest source of decay photons ($\sim 15\%$), was equivalent to that of single photons. The latter can be understood considering the minimum opening angle between the two photons which is approximately proportional to the mass of the decaying meson (see appendix C). The mass of the η is ~ 4 times larger than the π^0 mass and the angular separation between its decay daughters therefore extends well beyond the dimensions of a calorimeter tower: $\Delta\eta \times \Delta\phi = 0.05 \times 0.05$ rad.

Figure 5.7 shows the reconstruction efficiency $\epsilon_{\text{reco}}^\gamma$ of the π^0 decay photons in case of minimum bias, HT1, and HT2 triggered p+p collisions. The single photon reconstruction efficiency is shown in figure 5.8. The two results were found to be very similar in the low p_T region where the angular separation of the decay photons was still large compared to the size of a BEMC tower. However, at higher values of p_T the challenge to separate the two photons increased, particularly in case of the most symmetric decays. When such a merged event occurred, the remaining photon candidate was erroneously assigned the energy of both showers. This led to significantly larger reconstruction efficiencies as compared to those for single photons (see the discussion on energy smearing in section 4.2.5). Eventually, at the highest p_T values considered in this analysis, the decay photon efficiency even exceeded unity, as can be seen from figure 5.8.

Equations 5.6 and 5.7 define how the final corrections were applied to the raw inclusive photon sample N_{raw}^γ . The vertex efficiency ϵ_{vert} , the correction accounting for photon conversions in the missing material c_{miss} , and the bin centering factor c_{bin} were already discussed in chapter 4. These, combined with the CPV efficiency $\epsilon_{\text{CPV}}^\gamma$ and the reconstruction efficiency $\epsilon_{\text{reco}}^\gamma$ for single photons and decay photons, were used to convert N_{raw}^γ to the fully corrected inclusive photon yield.

In principle, $N_{\text{incl}}^{\text{raw}}$ followed from the subtraction of the charged and neutral backgrounds from the raw photon candidates, as indicated in equation 5.5. The contamination by charged particles was subtracted according to the procedure explained in section 5.1.2, however, the neutral hadron correction turned out to be rather problematic. Although an upper limit for

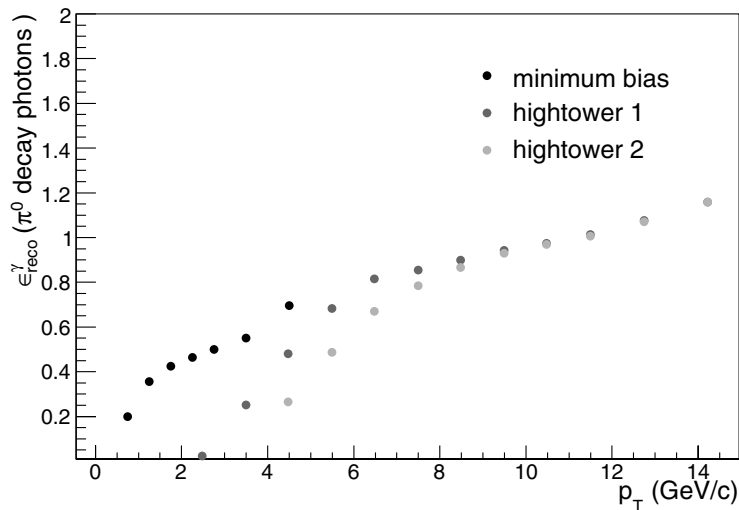


Figure 5.7: The reconstruction efficiency $\epsilon_{\text{reco}}^{\gamma}$ for photons exclusively from the decay $\pi^0 \rightarrow \gamma\gamma$. The observed rise of the efficiency at high p_T is caused by the merging of the π^0 decay daughters, as explained in the text.

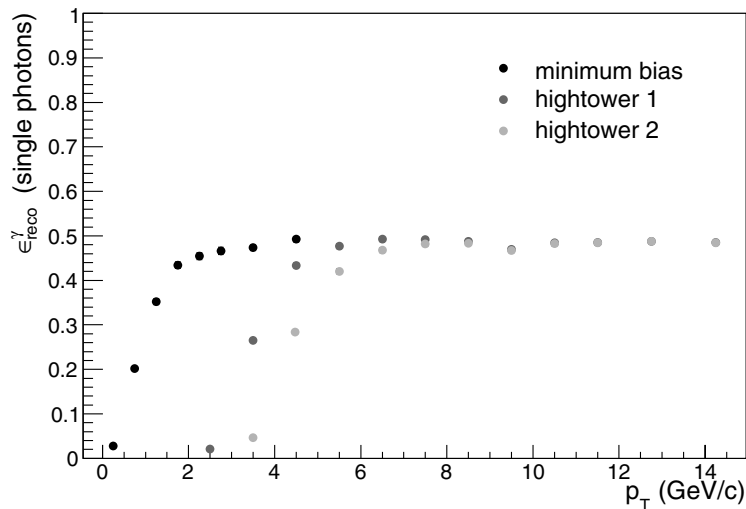


Figure 5.8: The reconstruction efficiency $\epsilon_{\text{reco}}^{\gamma}$ for photons as determined from a Monte-Carlo sample containing a single photon per event. This result was used to correct the fraction of the photon sample which exceeded the simulated contribution from the decay process $\pi^0 \rightarrow \gamma\gamma$.

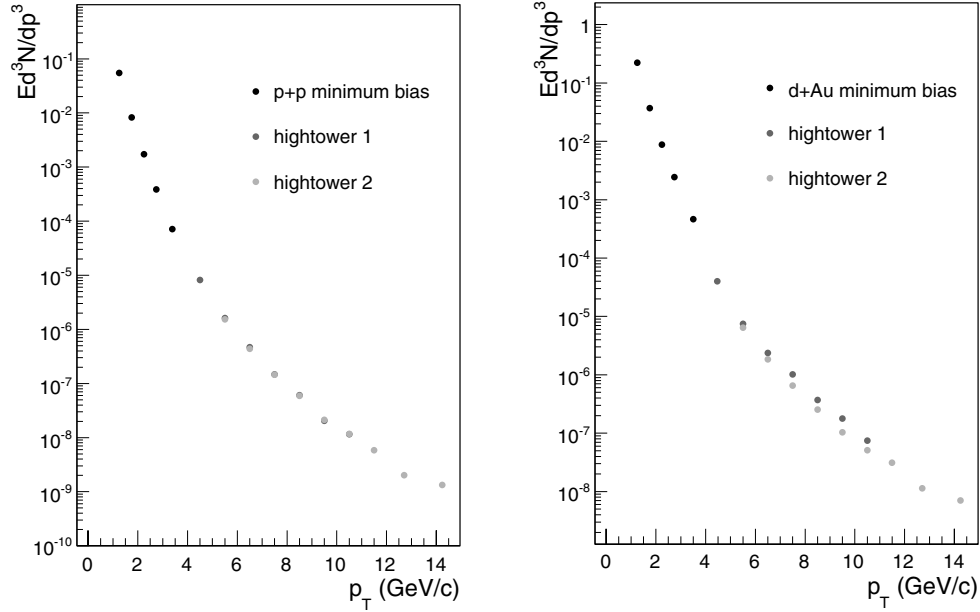


Figure 5.9: Inclusive photon invariant yield Ed^3N/dp^3 from p+p collisions (left) and from d+Au collisions (right). Note that the neutral hadron contamination was not subtracted (see text).

the contamination fraction C_0 has been derived in section 5.1.1, we did not find any means to reduce the associated systematic uncertainty on C_0 to a level where a significant subtraction could be performed. This was particularly true for minimum bias events, as can be seen from figure 5.3. In case of hightower triggered collisions, the upper limit on the contamination fraction reduces to a vanishing level at higher values of p_T . Our final results, which will be introduced in the next chapter, were therefore obtained in the range $6.0 < p_T < 15.0$ GeV/c and the photon candidates obtained from the minimum bias data were discarded.

Figure 5.9 shows the corrected inclusive photon spectra in case of p+p (left) and d+Au (right) collisions, without the subtraction of the neutral hadron contribution. The discrepancy between the spectra from hightower-1 and hightower-2 d+Au collisions was already mentioned in section 4.3.3 in case of the π^0 analysis. As stated there, the deviation of the hightower-1 data points from the overall trend was the reason to assign a somewhat larger systematic uncertainty on the π^0 yield than what was quoted in [56]. However, the questionable hightower-1 results were not used in the final direct photon reconstruction. The measured hightower-2 yields turned out

to be statistically more significant: we reconstructed 17684 and 3738 photon candidates from the hightower-2 and hightower-1 d+Au data, respectively, in the range $6 < p_T < 10$ GeV/ c . In the following section, we will include both triggered data sets for completeness. The final differential cross sections of direct photon production presented in chapter 6 were obtained exclusively from the hightower-2 triggered data.

5.2 Direct Photon Analysis

The measured inclusive neutral pion spectra combined with the inclusive photon yields constitute the basis of our direct photon analysis. Below, it will be demonstrated how these two results, together with the simulated decay photons from other sources than π^0 decay, will be used to determine the direct photon yields in terms of the double ratio.

5.2.1 Double Ratio

The double ratio is a common and convenient way of expressing the ratio of all measured photons and the simulated background photons. It was schematically written in the introduction of this chapter as

$$R_\gamma = \frac{\gamma_{\text{incl}}/\pi^0}{\gamma_{\text{decay}}/\pi^0} = 1 + \frac{\gamma_{\text{direct}}}{\gamma_{\text{decay}}}. \quad (5.10)$$

The numerator $\gamma_{\text{incl}}/\pi^0$ represents the ratio of the measured and fully corrected γ_{incl} and π^0 yields given by equations 5.6 and 4.15, respectively. The denominator $\gamma_{\text{decay}}/\pi^0$ corresponds to the simulated yield of decay photons divided by a fit to the measured π^0 yield. The latter will be discussed in detail in section 5.2.2. The last term in equation 5.10 illustrates that a direct photon signal is observed when the double ratio exceeds unity.

This double ratio had the advantage that many experimental uncertainties, common to the measurement of π^0 and γ_{incl} spectra, partially or even completely canceled. An exact cancelation occurred in case of the normalization uncertainties listed in table 4.4. In addition, the uncertainties associated with

- the BEMC calibration and in particular the overall energy scale
- the rejection of beam background events
- the correction for conversions in the missing material

decay	branching ratio
$\pi^0 \rightarrow \gamma\gamma$	98.80%
$\pi^0 \rightarrow e^+e^-\gamma$	1.20%
$\eta \rightarrow \gamma\gamma$	39.23%
$\eta \rightarrow \pi^+\pi^-\gamma$	4.78%
$\eta \rightarrow e^+e^-\gamma$	0.49%
$\omega(782) \rightarrow \pi^0\gamma$	8.69%

Table 5.3: Dominant contribution of hadronic decays to the inclusive photon yield.

- the false charged particle vetoes
- the π^0 and γ_{incl} reconstruction efficiencies

either largely or partially canceled. The error caused by the uncertainty of the overall energy scale was most significantly reduced. This was the primary motivation to study the direct photon yield by means of the double ratio. Note that many other contributions were reduced since the π^0 reconstruction can be viewed as the reconstruction of two separate photons.

5.2.2 Background from Hadronic Decays

The γ_{decay} yield, that is, those photons which came from hadronic decays, was determined with a simulation of the decay processes listed in table 5.3. The other possible contributions, from processes such as $\eta' \rightarrow \rho^0\gamma$, were found to be negligible ($< 1\%$). A fit to the measured π^0 yield served as an input to this simulation. The used function was of the form $\sim (1 + p_T)^{-\alpha}$ and the p_T interval of the fit was equal to $4.0 < p_T < 15.0 \text{ GeV}/c$. This reduced p_T range was chosen since the decay background at a given $p_T = p'_T$ was fully determined by the meson spectra at $p_T > p'_T$. Hence, a more precise result could be obtained since we did not consider direct photon production below $p_T = 6 \text{ GeV}/c$. The final exponents of the fit were given by $\alpha = 9.1 \pm 0.1$ and $\alpha = 9.0 \pm 0.1$ for d+Au and p+p collisions, respectively. The normalization was irrelevant because it eventually canceled upon taking the ratio $\gamma_{\text{decay}}/\pi^0$.

We made use of the experimental observation that the spectra of the η and $\omega(782)$ mesons scale with the π^0 spectrum when determined as a function of their transverse mass m_T . This phenomenological m_T scaling law, in case of the η yields, is given by

$$\left. \frac{dN}{dp_T}(m_T) \right|_{\eta} = R_{\eta/\pi^0} \left. \frac{dN}{dp_T}(m_T) \right|_{\pi^0}, \quad (5.11)$$

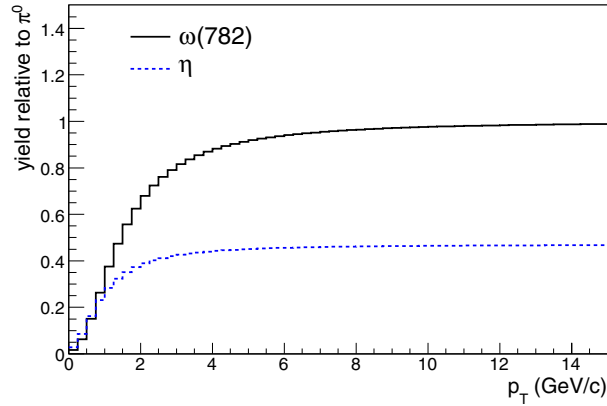


Figure 5.10: The estimated yield of η and $\omega(782)$ mesons in d+Au collisions, relative to the measured π^0 yield, as determined from the m_T scaling relation in equation 5.11.

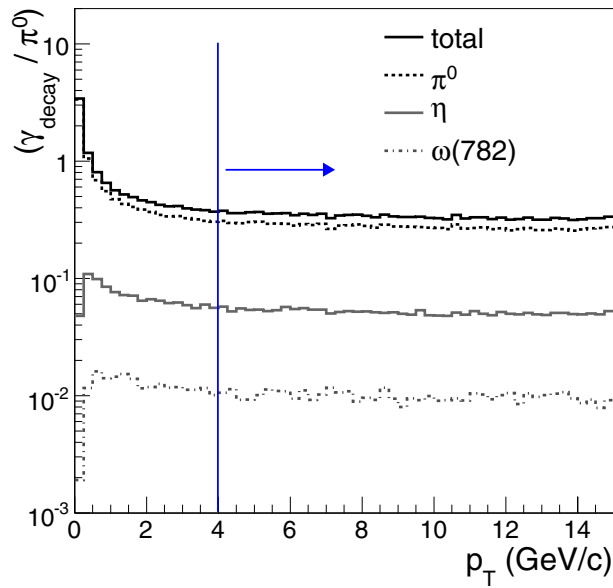


Figure 5.11: The simulated number of photons per input pion $\gamma_{\text{decay}}/\pi^0$ from hadronic decays in d+Au collisions as a function of p_T . The included decay processes are listed in table 5.3. The vertical line indicates the lower limit of the p_T range which was used to fit the π^0 spectrum. Note that the value of $\gamma_{\text{decay}}/\pi^0$ below $p_T = 4 \text{ GeV}/c$ is therefore less accurate, however, it was not used for further analysis (see text).

The applied scaling factors were $R_{\eta/\pi^0} = 0.48 \pm 0.05$ and $R_{\omega/\pi^0} = 0.47 \pm 0.05$ for p+p and d+Au events, respectively. These values are in agreement with a first measurement of η production at STAR [56] as well as the world average over a variety of different collision systems. Furthermore, the PHENIX collaboration at RHIC reported consistent values obtained from identical collision systems [92].

In case of the $\omega(782)$ yields, we used $R_{\omega/\pi^0} = 1.0 \pm 0.2$ which is in agreement with recent measurements at RHIC [93] which resulted in

$$\begin{aligned} R_{\omega/\pi^0} &= 0.94 \pm 0.08 \text{ (stat.)} \pm 0.12 \text{ (sys.)} \quad (\text{d + Au}) \\ R_{\omega/\pi^0} &= 0.85 \pm 0.05 \text{ (stat.)} \pm 0.09 \text{ (sys.)} \quad (\text{p + p}) \end{aligned}$$

The η and $\omega(782)$ yields, relative to the π^0 yield, are shown in figure 5.10 as a function of p_T . It can indeed be seen that these yields approach the constants R_{η/π^0} and R_{ω/π^0} at high values of p_T , meaning that $m_T \rightarrow p_T$.

The final ratio $\gamma_{\text{decay}}/\pi^0$ is shown in figure 5.11 for d+Au collisions. The curves represent the contributions of the separate processes and the total decay photon yield, each of them divided by the parametrization of the measured π^0 spectrum. Although the normalization uncertainty canceled upon taking this ratio, the uncertainty coming from the shape of the π^0 spectrum and the estimated values of the scaling coefficients had to be taken into account. This was done by varying the exponents of the fit as well as the values for the scaling coefficients R_{η/π^0} and R_{ω/π^0} by their standard error leading to the corresponding values quoted in table 5.4.

5.2.3 Direct Photon Results

Figure 5.12 shows the ratio $\gamma_{\text{incl}}/\pi^0$ in case of p+p (upper panel) and d+Au collisions (lower panel). This is the point-to-point ratio of the γ_{incl} spectrum and the π^0 spectrum, and corresponds to the numerator of the double ratio R_γ defined in equation 5.10. The background from decay photons, which is the denominator of R_γ , is expressed as $\gamma_{\text{decay}}/\pi^0$. The latter is shown in the same figure in terms of the full (upper) curve in each of the panels. The dashed curve represents those background photons which came from π^0 decays. A significant excess of the experimental data points over the full curve can be interpreted as a direct photon signal. Note that the minimum bias data are absent due to the substantial antineutron contamination and the large systematic uncertainties mentioned earlier.

The measured double ratio R_γ is shown in figure 5.13 as obtained from p+p (upper panel) and d+Au (lower panel) collisions. The error bars represent the statistical uncertainty of the data points only. To draw conclusions

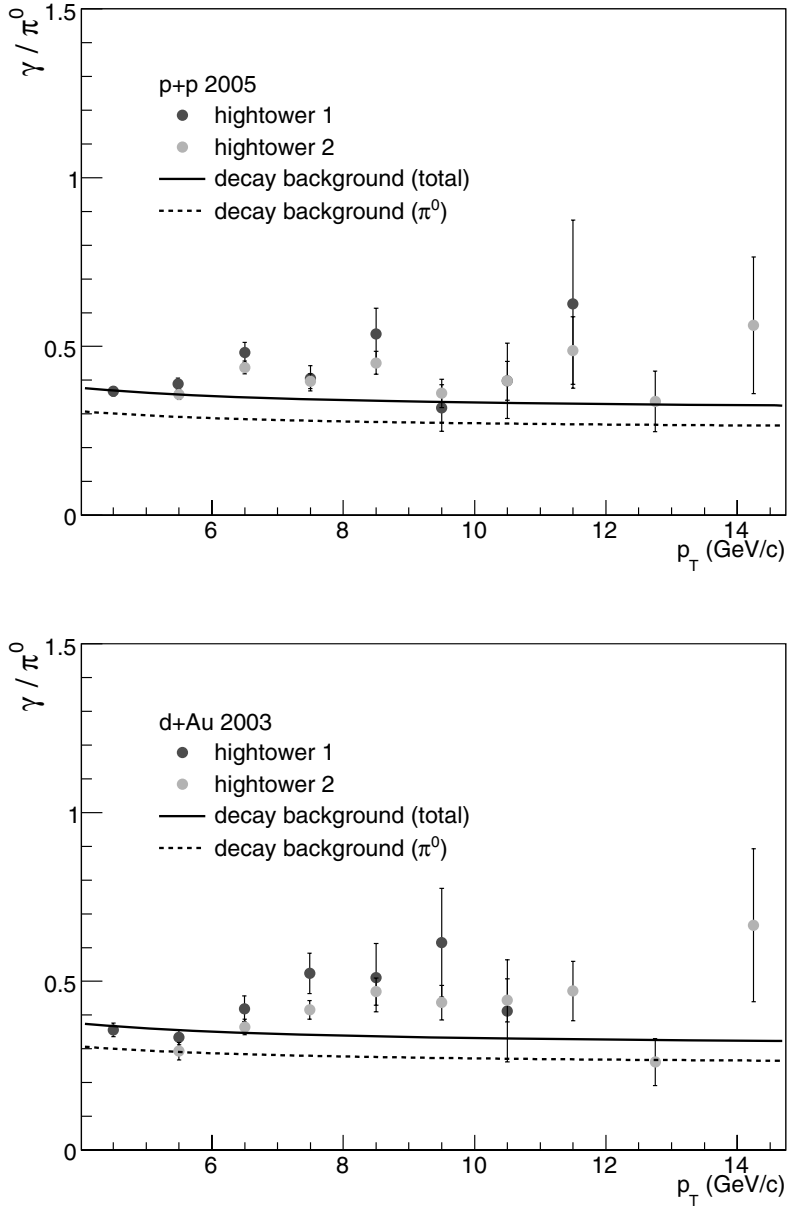


Figure 5.12: The ratio $\gamma_{\text{incl}}/\pi^0$ as measured in the p+p (upper panel) and d+Au (lower panel) data for the separate hightower trigger conditions. The full curve represents $\gamma_{\text{decay}}/\pi^0$, the background photons divided by the parametrized π^0 spectrum, and the dashed curve is that same quantity but only for those photons coming from the π^0 decay. The double ratio R_γ can be obtained from these data by dividing the data points by the full curve as indicated in equation 5.10.

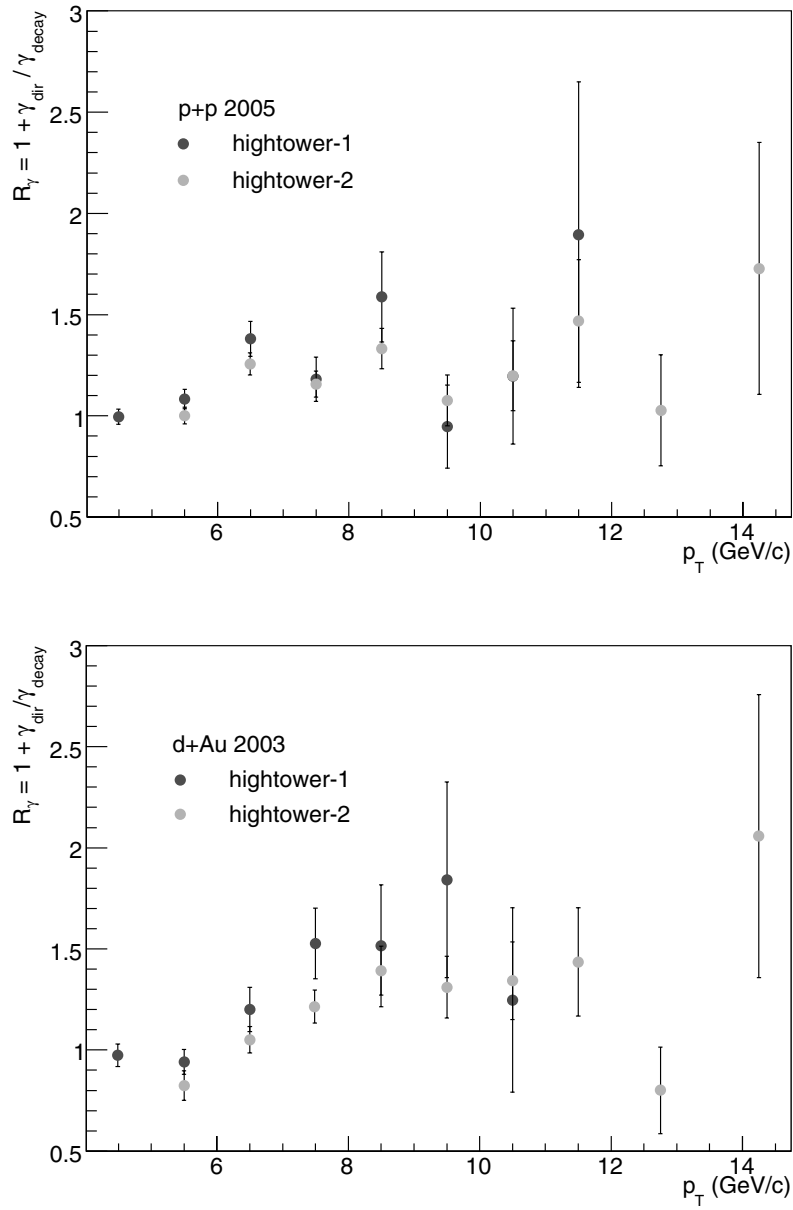


Figure 5.13: The direct photon signal, in terms of the double ratio $R_\gamma = 1 + \gamma_{\text{dir}}/\gamma_{\text{decay}}$ as defined in equation 5.10, from p+p (upper panel) and d+Au (lower panel) collisions as a function of p_T . The error bars represent the statistical uncertainties only, the systematic uncertainties will be included when we compare these results to theoretical predictions in the next chapter.

from these data with respect to a possible excess over the simulated background requires a careful analysis of the systematic uncertainties. In addition to what was presented in section 4.3.3, we discuss the resulting systematic uncertainties of R_γ below. The final numbers are given in table 5.4 for typical values of p_T . The statistically most significant data points of the double ratio were selected for the final result and will be used in the discussion presented in the next chapter. The final data are listed in appendix A.

5.2.4 Systematic Uncertainties

The summary of the systematic uncertainties of the double ratio R_γ is given by table 5.4. It clearly indicates that the major advantage of expressing the direct photon yield in terms of R_γ is the large reduction of the uncertainty coming from the BEMC energy scale. Consequently, the largest sources of uncertainty were those associated with the π^0 yield extraction and the BSMD energy scale.

One could naively expect that the BSMD energy scale uncertainty would cancel upon taking the ratio of the photon and pion spectra. However, as this uncertainty enters the analysis mainly due to threshold effects in the clustering routine, the raw photon and neutral pion yields were not similarly affected. For example, a deviation of the BSMD energy scale from its true value could result in the loss of the least energetic photon from an asymmetric π^0 decay. The other photon, with its energy closer to that of the π^0 , could then still be reconstructed. As a consequence of the steeply falling π^0 spectrum, the raw inclusive photon yield at a given value of p_T has a large contribution especially from photons with their energy close to that of the π^0 . Hence, the loss of the softer of the two photons has a mild effect on the inclusive photon yield whereas the π^0 is truly lost. We have evaluated this uncertainty explicitly for the double ratio R_γ , by carrying out the full analysis while changing the global BSMD energy scale by $\pm 10\%$. The resulting variation of R_γ from this source was estimated to be $\sim 6\%$, independent of p_T for values of p_T greater than $6 \text{ GeV}/c$.

The uncertainty associated with the parametrization of the π^0 yield was estimated from the statistical error ($\sim 1\%$) on the exponent. Furthermore, the fit was carried out for varying p_T ranges, leading to a $\sim 1\%$ variation of the exponent as well. Hence, we assigned a total relative error 1.5% to the exponent of this parametrization. At sufficiently high p_T values the invariant yield of neutral pions can be approximately described as a power law function $\sim p_T^{-\alpha}$. The corresponding yield of decay photons with transverse momentum

equal to p_T is then given by

$$\frac{dN}{dp_T} = \frac{2}{p_T} \int_{p_T}^{\infty} k_T^{-\alpha+1} dk_T = \frac{2}{\alpha-2} p_T^{-\alpha+1}. \quad (5.12)$$

The last factor on the right is then precisely the π^0 yield such that the ratio

$$(\gamma_{\text{decay}}/\pi^0) \sim \frac{2}{\alpha-2}. \quad (5.13)$$

Hence, we assumed that the error estimate of 1.5% for the exponent α translated to a similar relative error on the double ratio R_γ .

In the next chapter, we will use the corrected inclusive photon spectrum to reconstruct our final direct photon yields with the relation

$$\gamma_{\text{direct}} = (1 - R_\gamma^{-1}) \times \gamma_{\text{incl}}. \quad (5.14)$$

A correct evaluation of the absolute direct photon yield γ_{direct} therefore required that the systematic uncertainties associated with γ_{incl} , which canceled in the ratio R_γ , were included again. However, it should be noted that a relatively small error on R_γ causes a large error on γ_{direct} as a result of the subtraction in equation 5.14. This, in combination with the error on γ_{incl} from the energy scale uncertainty ($\sim 30\%$) will dominate the final error on γ_{direct} .

Besides the fact that the systematic uncertainties which canceled in the double ratio were included again, we have derived upper limits for those p_T values where R_γ did not correspond to a significant direct photon signal. We have assumed that the statistical and systematic errors both followed a Gaussian distribution and have summed these in quadrature. We have assigned an upper limit to the signal in terms of a 95% confidence limit, thereby using that the true value of R_γ cannot be smaller than unity, by definition.

p_T (GeV/ c)	p+p		d+Au	
	6.5	12.75	6.5	12.75
<i>correlated</i>				
BEMC energy scale	3.0%	3.0%	3.0%	3.0%
BEMC gain spread	1.0%	1.0%	1.0%	1.0%
BSMD energy scale	6.0%	6.0%	6.0%	6.0%
BSMD gain spread	1.0%	1.0%	1.0%	1.0%
R_{η/π^0}	2.0%	2.0%	2.0%	2.0%
π^0 yield fit	1.5%	1.5%	1.5%	1.5%
<i>uncorrelated</i>				
π^0 yield extraction	5.0%	7.1%	5.0%	7.1%
beam background	-	-	1.0%	3.0%
ϵ_{reco} (stat.)	2.4%	1.7%	4.2%	2.2%
<i>total</i>				
point-by-point	8.8%	10.2%	8.9%	10.6%
statistical	4.4%	26.7%	6.4%	26.3%

Table 5.4: The relative uncertainties on the double ratio as obtained from the p+p and d+Au data. The statistical uncertainty from the efficiency correction was included in the total statistical error.

Chapter 6

Discussion

In this chapter, we present and discuss the results of our analysis of inclusive neutral pion and direct photon production in proton-proton and deuteron-gold collisions at $\sqrt{s_{NN}} = 200$ GeV. The data corresponding to our measurement can be found in appendix A.

6.1 Neutral Pions in p+p Collisions

Our final result for the differential cross section of inclusive neutral pion production in p+p collisions is shown as a function of p_T in figure 6.1. The curves were obtained with a NLO pQCD calculation with the CTEQ6M parton distributions [10] and the KKP set of fragmentation functions [12] for three different values of the common factorization scale μ [19]. The bottom panel shows the data divided by the calculation for $\mu = p_T$. The total systematic uncertainty is indicated by the shaded band around the data points and clearly dominates over the statistical uncertainty which is given by the error bars.

Figure 6.1 illustrates the predictive power of pQCD (and the factorization theorem) for inclusive hadron production in p+p collisions at RHIC. The experimental data are consistent with the theoretical curves over the entire transverse momentum range $2 < p_T < 15$ GeV/ c . Note that the latter corresponds to a change in the differential cross section of approximately 7 orders of magnitude. Similar results for π^0 production at $\sqrt{s} = 200$ GeV were reported by the PHENIX collaboration [94].

These observations are different from what has been observed in case of high p_T π^0 production at lower center-of-mass energies ($\sqrt{s} \sim 30$ GeV), as discussed in, e.g., [95]. The experimental cross sections were found to deviate from the NLO pQCD predictions, mostly by an overall normalization

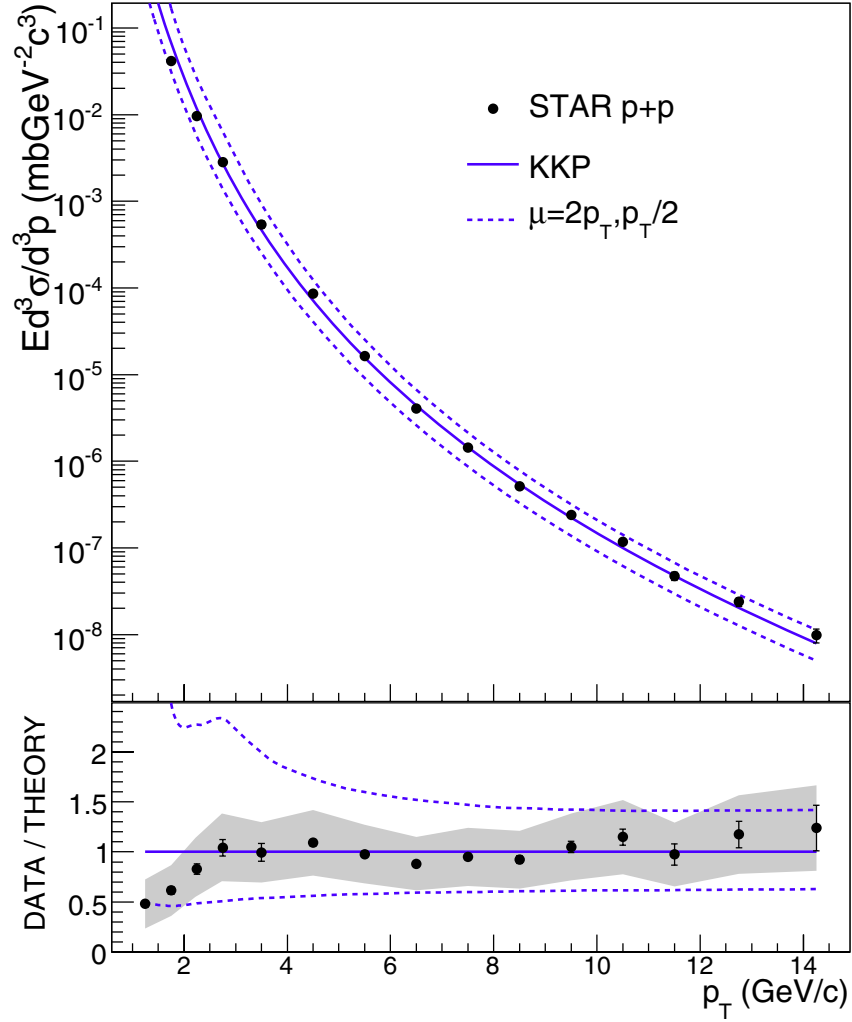


Figure 6.1: Neutral pion production in p+p collisions compared to a pQCD calculation with the KKP set of fragmentation functions [19]. The dashed lines illustrate the dependence on the specific choice of the factorization scale μ with the upper curve the result for $\mu = p_T/2$. The lower panel shows the data divided by the pQCD calculation for $\mu = p_T$. The error bars represent the statistical uncertainty of the data points and the shaded band indicates the systematic uncertainty.

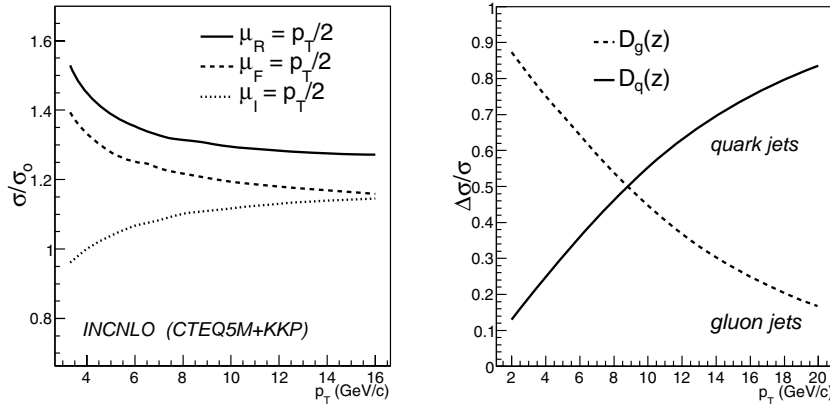


Figure 6.2: Left panel: the variation of the π^0 cross section relative to the calculation with a common scale $\mu = p_T$. Right panel: the relative contribution to the π^0 cross section from quark ($D_q(z)$) and gluon ($D_g(z)$) initiated fragmentation. Both panels correspond to p+p collisions at $\sqrt{s} = 200$ GeV. The horizontal axes label the p_T of the π^0 .

factor of ~ 2.5 . However, good agreement with theory has been observed at higher values of the collision energy. In case of single inclusive jet production $p + \bar{p} \rightarrow \text{jet} + X$ at $\sqrt{s} = 1.96$ TeV, for example, where consistency with NLO pQCD was obtained over the jet momentum range $50 < p_T < 700$ GeV/c [96]. Our result and, more generally, those obtained at RHIC show that π^0 production in p+p collisions at $\sqrt{s} = 200$ GeV can be properly described with pQCD as well.

The theoretical uncertainty in figure 6.1 comes from the change in the cross section upon varying the common factorization scale, here denoted by μ . We have used the INCNLO program [98] to calculate the explicit dependence on the initial state factorization, the final state factorization (or fragmentation), and the renormalization scale, denoted by μ_I , μ_F , and μ_R , respectively. Figure 6.2 demonstrates the sensitivity to each of these scales separately. It shows the ratio of the π^0 cross section to the nominal cross section, with $\mu_I = \mu_F = \mu_R = p_T$, in case that one of the scales was set equal to $p_T/2$. When calculated up to all orders, the cross section is independent of these scales. In practice, pQCD calculations are known up to finite order in α_s and the compensation of the scale dependence by the included higher order terms is incomplete.

When comparing the measured π^0 cross section to the results from a pQCD calculation as described above, an additional uncertainty should be considered. The theoretical curves are subject to experimental uncertainties

as well. Namely, those of the data which were used to determine the initial parametrization of the parton density functions and the fragmentation functions. Our measurement probes the former in a region of x where they are well under control: $\sim 0.1 < \bar{x} < 0.3$ [100]. The latter, and especially the gluon-to-pion fragmentation function $D_{\pi/g}(z)$, has been less accurately constrained. The parametrizations have been determined from data which were predominantly obtained with electron-positron annihilation experiments. In such reactions, gluon fragmentation is only a sub-leading contribution to the production of hadrons. Hence, the resulting measurements of $D_{\pi/g}(z)$ are not precise and generally degrade towards larger values of the momentum fraction z of the pion.

The right panel in figure 6.2 shows how gluon initiated fragmentation (denoted by D_g) dominates the size of the theoretical cross section of π^0 production below $p_T \sim 8 \text{ GeV}/c$. Furthermore, it can be shown that the value of z to which our π^0 measurement is sensitive is relatively large, $\bar{z} \sim 0.6$ [100]. The above are consequences of the interplay between the parton distribution functions, the matrix element of the hard scattering, and the shape of the parton-to-pion fragmentation functions in p+p collisions at RHIC energies. Various sets of fragmentation functions are available and they differ mostly in their description of $D_{\pi/g}(z)$. The present discrepancies are as large as a factor of 3–4 at $z \sim 0.5$ and $\mu_F^2 = 10 \text{ GeV}^2$ [101] and increase towards $z = 1$.

To illustrate the above, figure 6.3 shows the normalized spectrum of charged particles produced by gluon initiated jets [97]. It demonstrates that the uncertainty of the experimental data points rapidly increases when the momentum fraction of the hadron with respect to the jet (x_E) becomes larger. The curves represent the results from calculations based on different sets of fragmentation functions and their predictions increasingly differ when x_E approaches unity.

The top panel in figure 6.4 shows our neutral pion cross section in p+p collisions compared to the results of the calculation introduced above and to those determined with two alternative sets of fragmentation functions, denoted AKK [102] and Kretzer [103]. The bottom panel depicts the ratio of all data to a parametrization of the measured π^0 spectrum. Again, the shaded band indicates the sum of all systematic errors added in quadrature. Presently, our results can not be used to discriminate between the various fragmentation scenarios. The largest contribution to the systematic uncertainty comes from the error on the absolute energy scale of the calorimeter. The latter was found to be strongly correlated over the entire p_T range and therefore precludes too stringent claims. When this source of uncertainty would be reduced, our data can be of great value in a global analysis of fragmentation functions as reported, e.g. in [101], thereby constraining the

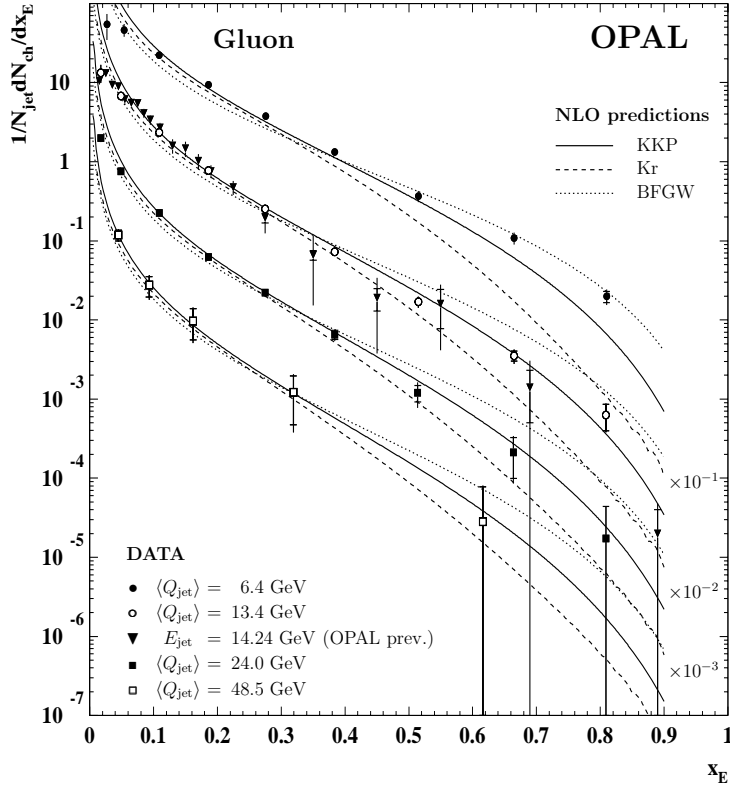


Figure 6.3: The gluon initiated fragmentation into charged hadrons for different jet energy scales Q . The vertical axis represents $N_{\text{jet}}^{-1} dN_{\text{ch}}/dx_E$, the number of charged hadrons with momentum fraction x_E normalized to the total jet count. The curves correspond to the results from a NLO calculation with different sets of fragmentation functions. The figure was taken from [97].

shape of the gluon-to-pion fragmentation function at large values of z .

We conclude this section by returning to our main objective, namely, the study of matter which is produced in the most central Au+Au collisions at RHIC. Figure 6.5 shows the nuclear modification factor R_{AB} obtained by the STAR collaboration for charged hadron production in Au+Au and d+Au collisions [40] at $\sqrt{s_{NN}} = 200$ GeV (see equation 4.26 for the definition of R_{AB}). These data were determined with respect to a reference spectrum from p+p collisions where the final state can be considered nearly a vacuum. The absence of strong nuclear effects in the d+Au system, combined with the large ($\times 5$) suppression of the particle yields in central Au+Au collisions, has contributed to the conclusion that a strongly interacting QGP-like plasma has indeed been produced in Au+Au collisions at RHIC [104, 105, 106, 107]. The presented cross section of π^0 production can serve as an important baseline to

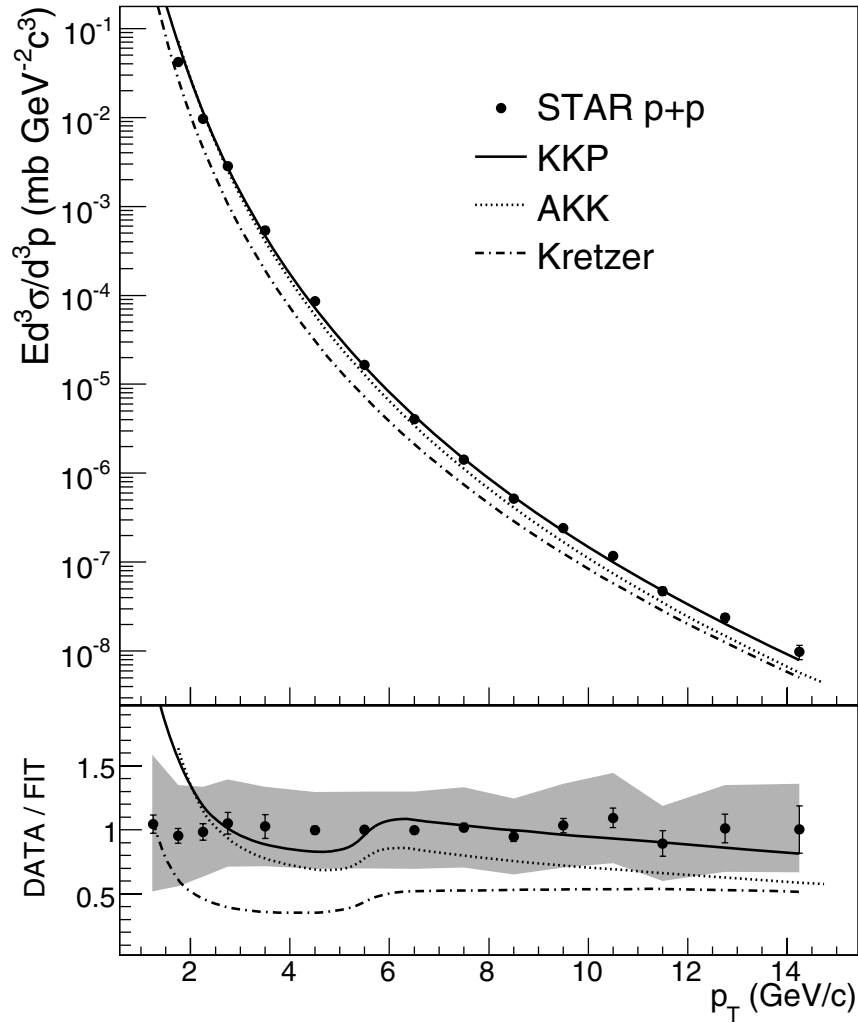


Figure 6.4: Neutral pion production in p+p collisions compared to different sets of fragmentation functions. All calculations were performed for $\mu = p_T$. The lower panel shows the data divided by a fit to the measured cross section. The error bars represent the statistical uncertainty of the data points, the shaded band indicates the systematic uncertainty.

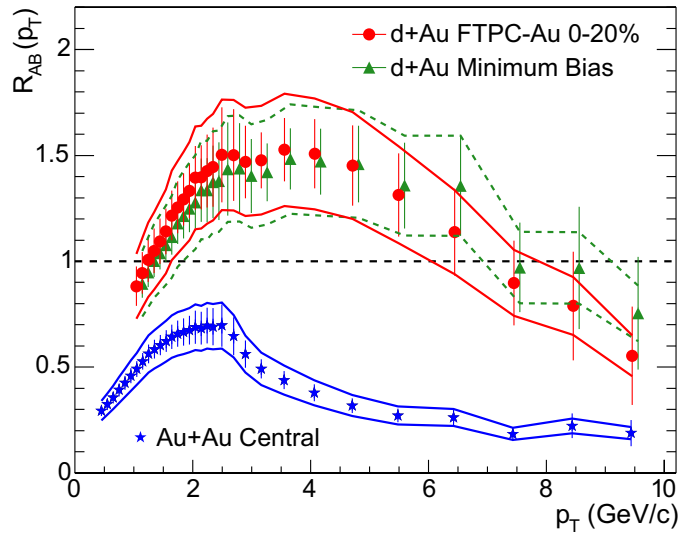


Figure 6.5: The nuclear modification factor R_{AB} for charged hadron production in d+Au and Au+Au collisions as obtained by STAR. The d+Au results were obtained from minimum bias and the 20% most central collisions.

further study and quantify the nature of this suppression and hence, study the properties of the plasma which is produced in heavy ion collisions at RHIC.

6.2 Nuclear Modification in d+Au collisions

The top panel in figure 6.6 shows our data for the Lorentz invariant yield Ed^3N/d^3p of neutral pions from d+Au collisions at $\sqrt{s_{NN}} = 200$ GeV. The systematic uncertainty is represented by the shaded band around the data points. The statistical uncertainties are given by the error bars. The curves represent the calculated NLO pQCD cross section for p+p collisions, scaled with the nuclear overlap T_{dAu} which was determined with a Monte-Carlo Glauber calculation (see equation 4.26). In the same figure, we have included the results from the PHENIX collaboration [108, 109] obtained from d+Au collisions as well. The corresponding nuclear modification factor R_{dAu} , as defined by equation 4.26, for neutral pion production is shown in the bottom panel of this figure. Our yields are in agreement with those from PHENIX over the full range in transverse momentum. Note that in the ratio of spectra the uncertainty from the energy scale largely canceled resulting therefore in a relatively precise measurement of R_{dAu} .

The obtained values of R_{dAu} impose limits on the possible enhancement

(Cronin effect, anti-shadowing) or suppression (shadowing, Color Glass Condensate) of particle yields in d+Au collisions, as compared to those in the p+p system. The measured values of R_{dAu} are consistent with unity for all p_T values above ~ 2 GeV. However, the predicted modifications in the kinematic regime of this measurement ($x_T \sim 0.05$) are comparable in size to the uncertainties, see e.g. [110, 111]. It will therefore be a challenging task to eventually discriminate between the available theoretical models.

Despite the limitations mentioned above, our conclusion that there is no evidence for strong nuclear effects in the gold core constitutes an important result. It has serious implications for a future measurement of thermal photons in Au+Au collisions. Initial state effects could introduce an additional uncertainty in the yield of prompt photons at low p_T . In order to isolate the thermal component, the prompt photon yield eventually has to be subtracted from the total direct photon signal in this p_T region, as shown in figure 1.10. An incorrect treatment of initial state effects could therefore artificially enhance or suppress the measured thermal photon spectrum. In addition, this measurement of R_{dAu} constitutes an independent proof that the suppression of high p_T particles in Au+Au collisions, as shown in figure 6.5, can not be attributed to initial state effects in the gold core. Moreover, the p_T range of this observation has been extended to 15 GeV/ c , when compared to the earlier STAR result obtained from charged hadron spectra.

6.3 Direct Photon Cross Sections

The final results for the double ratio R_γ in p+p and d+Au collisions are shown in figure 6.7. The shaded band near $R_\gamma = 0$ indicates our estimate of the upper limit of the remaining contamination by neutral hadrons. The curves correspond to a NLO pQCD calculation [19] which was further evaluated as

$$R_\gamma|_{\text{theory}} = 1 + \frac{(\gamma_{\text{dir}}/\pi^0)_{\text{NLO}}}{(\gamma_{\text{decay}}/\pi^0)_{\text{simu}}} \quad (6.1)$$

where the numerator equals the ratio of the NLO pQCD prompt photon and neutral pion cross section. The latter was already introduced in section 6.1 (see e.g. figure 6.1). The denominator is given by the number of decay photons per neutral pion, as determined with the simulation described in section 5.2.2.

The theoretical prompt photon cross sections had the CTEQ6M [10] parton densities and the GRV parametrization [99] of the parton-to-photon fragmentation functions as an input [19]. The scale dependence of this calculation is illustrated by the dashed curves in the figure and was obtained by

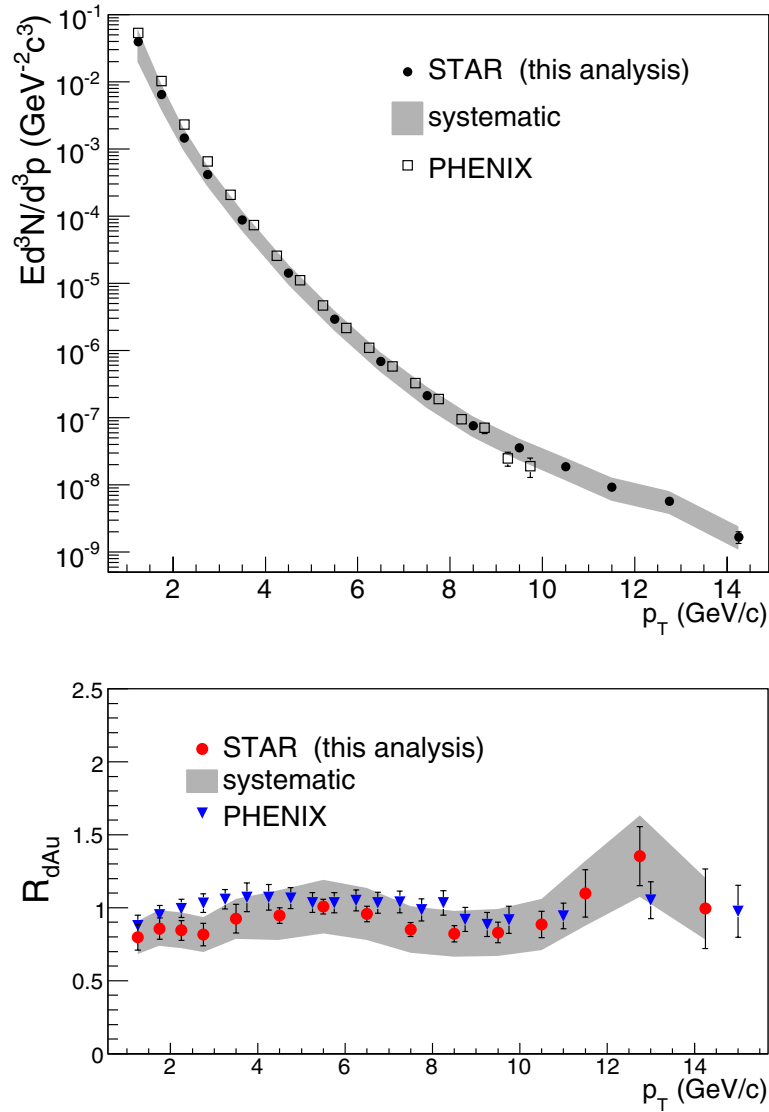


Figure 6.6: Top panel: Lorentz invariant yield Ed^3N/d^3p of inclusive neutral pions in d+Au collisions as a function of p_T and averaged over $0.1 < y < 0.9$. The error bars show the statistical uncertainty of the data and the systematic uncertainty is indicated by the shaded band. The data are compared to the result from the PHENIX collaboration at RHIC. Bottom panel: the nuclear modification factor R_{dAu} at $\sqrt{s_{NN}} = 200$ GeV from this analysis compared to the measurement by PHENIX. The latter has systematic and statistical uncertainties summed in quadrature. The normalization uncertainties were not included and equal to 13% and 9.7% in case of the STAR and PHENIX measurement, respectively.

changing μ in the calculation of prompt photon production while keeping the scale corresponding to the π^0 cross section fixed at $\mu = p_T$. In addition, we have varied the factorization scale for both cross sections simultaneously. The observed variation was quantitatively similar, although in the opposite direction. Since the measured neutral pion spectrum favors the result of the pQCD calculation with $\mu = p_T$, we have used this value for all three curves.

Although figure 6.7 demonstrates that the measured values of R_γ are consistent with the calculated direct photon signal, the interpretation in this context has its limitations. First of all, the curves do not follow directly from the theory but depend on our simulation of the decay photon yields, as shown in equation 6.1. In addition, the NLO pQCD cross section of π^0 production is less accurately constrained than that of prompt photon production. This can be seen by comparing the results for different sets of fragmentation functions, as shown in figure 6.4, to the curves for prompt photons in figure 1.6. To allow for a more solid comparison to theoretical predictions as well as other experimental data, we have converted R_γ to an absolute cross section and invariant yield in case of p+p and d+Au collisions, respectively.

Figure 6.8 shows the measured cross section $Ed^3\sigma/d^3p$ and invariant yield Ed^3N/d^3p of direct photon production in p+p and d+Au collisions, respectively. The bar on top of the arrows indicates the 95% confidence limit. The normalization uncertainties (c.f. table 4.4) are not explicitly given. The NLO pQCD cross section of prompt photon production was scaled with the nuclear thickness function T_{dAu} to account for the number of binary collisions in the d+Au system (see equation 4.27). The precision of the presented measurement is limited by systematic uncertainties for $p_T \leq 9 \text{ GeV}/c$ and by statistical uncertainties for larger values of transverse momentum. Nevertheless, our results are compatible with the curves from the NLO pQCD calculation. A further interpretation of these data will follow in the next section from a comparison to the results of other experiments.

Note that we have included the fragmentation component in the pQCD calculations since our measurement was based on an inclusive sample of photons. This is in contrast to a measurement where only isolated photon candidates are counted. In that case, an isolation criterion is used to reject photons when the amount of hadronic energy in a jet-like cone around their trajectory exceeds a certain threshold value. Consequently, the prompt photons produced in the fragmentation process of quark or a gluon will be suppressed. The relative size of the two separate components is shown in figure 1.7. A first measurement of the contribution from fragmentation photons to the total prompt photon cross section in case of p+p collisions at RHIC was reported in [112].

The interest in disentangling photons from the fragmentation process and

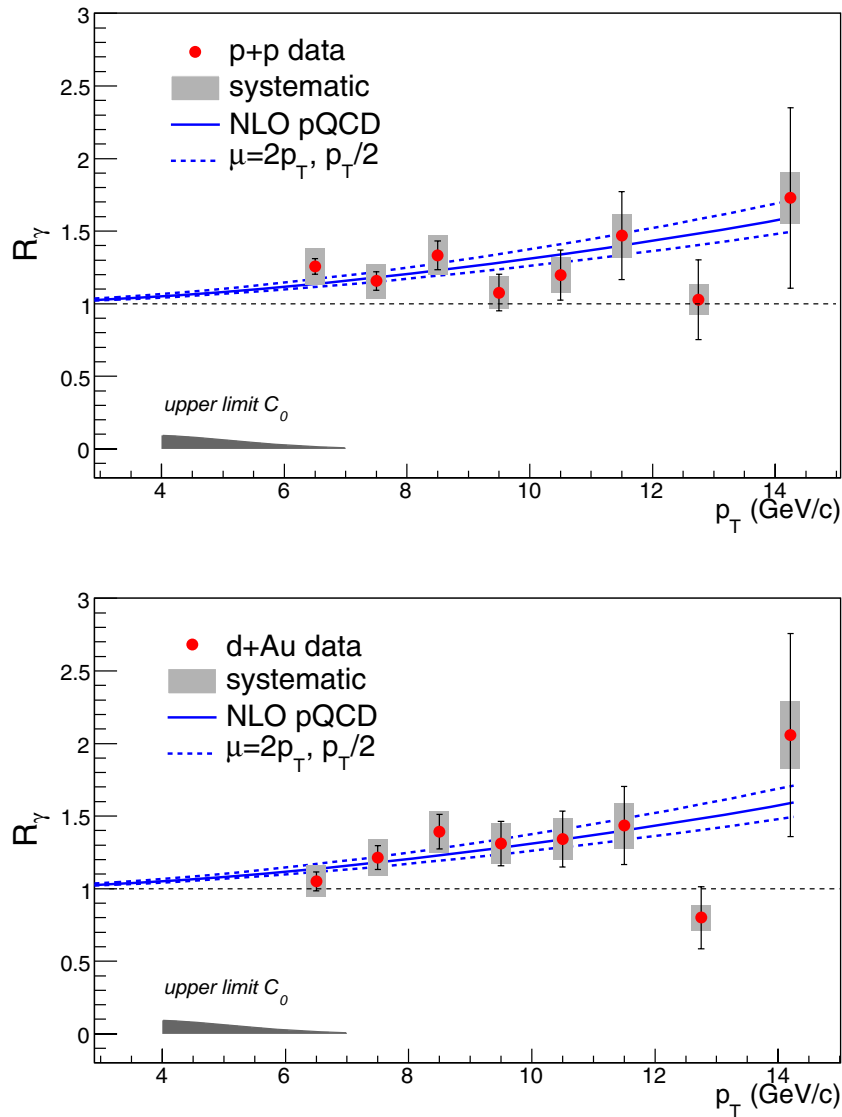


Figure 6.7: The direct photon yields from p+p and d+Au collisions in terms of the double ratio R_γ . The error bars represent the statistical uncertainty of the data and the systematic uncertainty is indicated by the shaded rectangles. The curves correspond to a NLO pQCD calculation of the differential cross sections of direct photon and inclusive pion production in p+p collisions for different factorization scales μ . The upper limit of the fractional neutral hadron contamination C_0 is explicitly shown as the shaded band at $R_\gamma = 0$. The upper pQCD curve corresponds to the scale $\mu = p_T/2$.

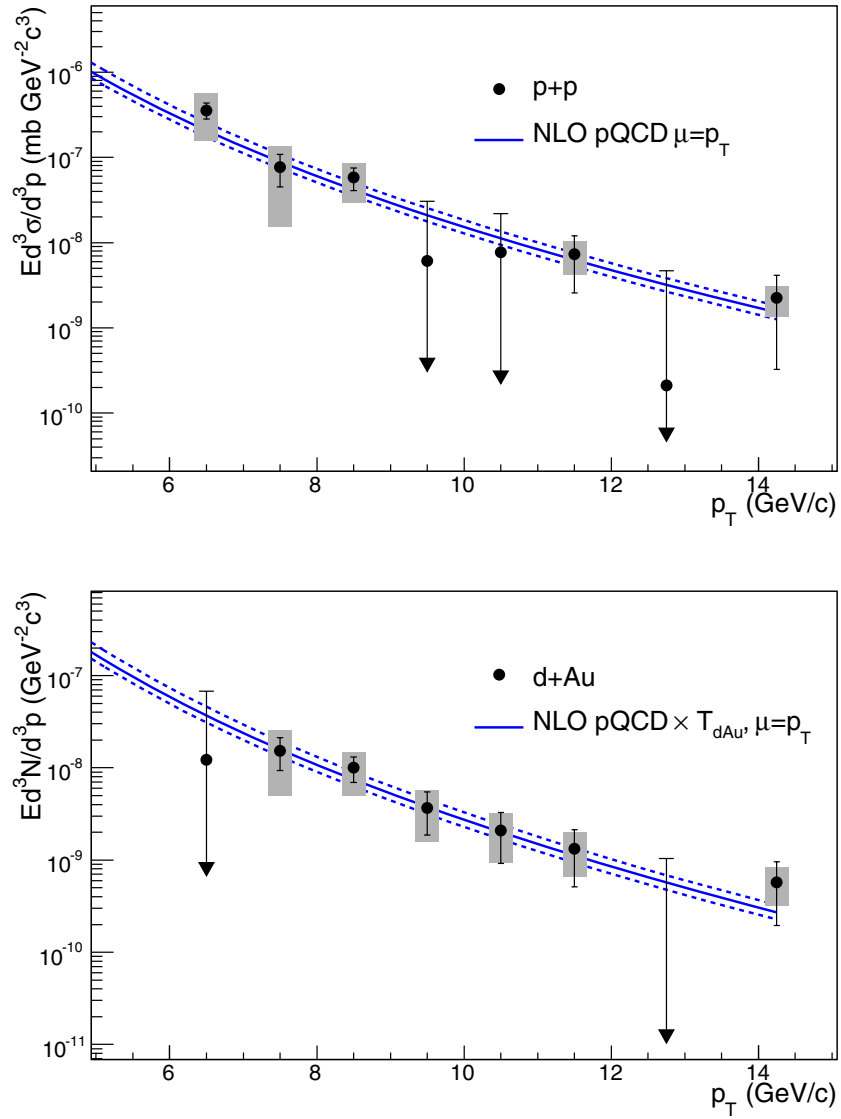


Figure 6.8: The differential cross section $Ed^3\sigma/dp^3$ of direct photon production in p+p collisions (upper panel) and the Lorentz invariant yield Ed^3N/dp^3 in d+Au collisions (lower panel), both shown as a function of p_T and averaged over $0.1 < y < 0.9$. The error bars represent the statistical uncertainty of the data and the systematic uncertainty is indicated by the shaded rectangles. The arrows correspond to the 95% confidence limits as defined in the text. The curves are the result of a NLO pQCD calculation which, in case of d+Au collisions, was scaled with T_{dAu} (see equation 4.27).

the initial hard scattering is twofold. First of all, it has been observed that the hot and dense final state of central heavy ion collisions at RHIC causes a suppression of particle yields. This jet quenching has been attributed to induced gluon radiation from a parton traversing the Quark Gluon Plasma. The same mechanism could lead to a suppression of fragmentation photons, although we should stress that an enhancement of directly produced photons has been proposed as well [113]. Furthermore, the main objective of the RHIC spin program is to constrain the polarization of the gluons inside the proton ($\Delta G(x)$). The isolation criterion has a bias towards the final state of the quark-gluon Compton process (c.f. figure 1.4) and therefore enhances the sensitivity of the cross section to the gluon content of the proton. Although the presented analysis has been performed from a different perspective, the developed experimental techniques can eventually contribute to a study of the proton spin structure as well (see e.g. [114]).

6.4 Comparison to Other Experiments

Prompt photon production in hadronic collisions is considered a high precision test of pQCD. Hence, many experimental facilities, over approximately the last two decades, have put effort in a measurement of prompt photons. The presently covered kinematic domain extends over 4 orders of magnitude in p_T^2 and $0.01 < x_T < 0.6$ and was explored at fixed target experiments as well as hadron colliders¹.

In what follows, we will compare our results to a selection of prompt photon measurements which has overlap with the kinematic range probed at RHIC. Our definition of direct photons, namely those which do not originate from hadronic decays, is common to the field of heavy ion physics. However, there are no medium-induced direct photons (e.g. thermal photons) in p+p and p+ \bar{p} collisions and consequently, the direct photons become equivalent to the prompt photons. Note that in that case we will use these two terms synonymously in our discussion below.

Photons from p+p and p+ \bar{p} Collisions

A compilation of recent experimental data on prompt photon production in p+p and p + \bar{p} collisions is shown in figure 6.9 in terms of the differential cross section $E d^3\sigma/d^3p$ as a function of p_T . The measurements were

¹The momentum fraction x_T is defined as $x_T = 2p_T/\sqrt{s}$ and can be considered an approximate measure of the initial momentum fraction x of the incoming parton, as discussed in appendix B.

performed at RHIC [112] and at the Tevatron collider [115, 116, 117] and cover the energy range $200 < \sqrt{s} < 1960$ GeV. The data points have error bars which represent the systematic and statistical uncertainties summed in quadrature. The curves in the figure correspond to NLO pQCD calculations which we have performed with the INCNLO routine [98]. This routine had the earlier CTEQ5M parton distribution functions and the BFG-II [118] set of photon fragmentation functions as an input. The difference of the former with respect to the latest CTEQ6M parametrizations is small though, as discussed in [10].

All theoretical cross sections were evaluated with $\mu = p_T/2$ in order to maintain consistency with preceding literature [119]. The choice $\mu = 2p_T$, however, would cause a $\sim 30\%$ decrease of the theoretical cross section without significantly altering its shape. In addition, we should stress that we have not accounted for the isolation criterion used in the CDF and D0 analyses. The INCNLO routine is much faster than Monte-Carlo algorithms which include the specific definition of such an isolation cut. The implementation of the isolation criterion for the CDF and D0 results would lead to a $\sim 10\%$ decrease of the cross sections without significantly altering their shape in the presented p_T range [119]. Note that in the upper panel of figure 6.9, we have omitted the CDF and D0 data points above $p_T = 100$ GeV/ c to improve the overall visibility.

The bottom panel in figure 6.9 presents the experimental results divided by the NLO pQCD curves, as a function of x_T . It demonstrates that the \sqrt{s} dependence of prompt photon production in hadronic collisions can be properly described with the NLO calculations. The data do not seem to exhibit any p_T or x_T dependent deviations from theory and the results of our measurement, albeit within large errors, are fully consistent with these observations.

This is in contrast to what has been reported by the E706 collaboration [120]. Figure 6.10 shows the cross section obtained with two different beam energies at the E706 fixed target experiment. There is an apparent discrepancy with the theory which increases towards smaller values of p_T . The lower center-of-mass energy ($\sqrt{s} = 31.6, 38.8$ GeV), however, can not explain the origin of this effect as other experiments at similar energies have obtained results which are consistent with NLO pQCD [119]. Our data, as well as those published by PHENIX, have significant overlap in p_T with the E706 data and yield no evidence of such a p_T dependent enhancement.

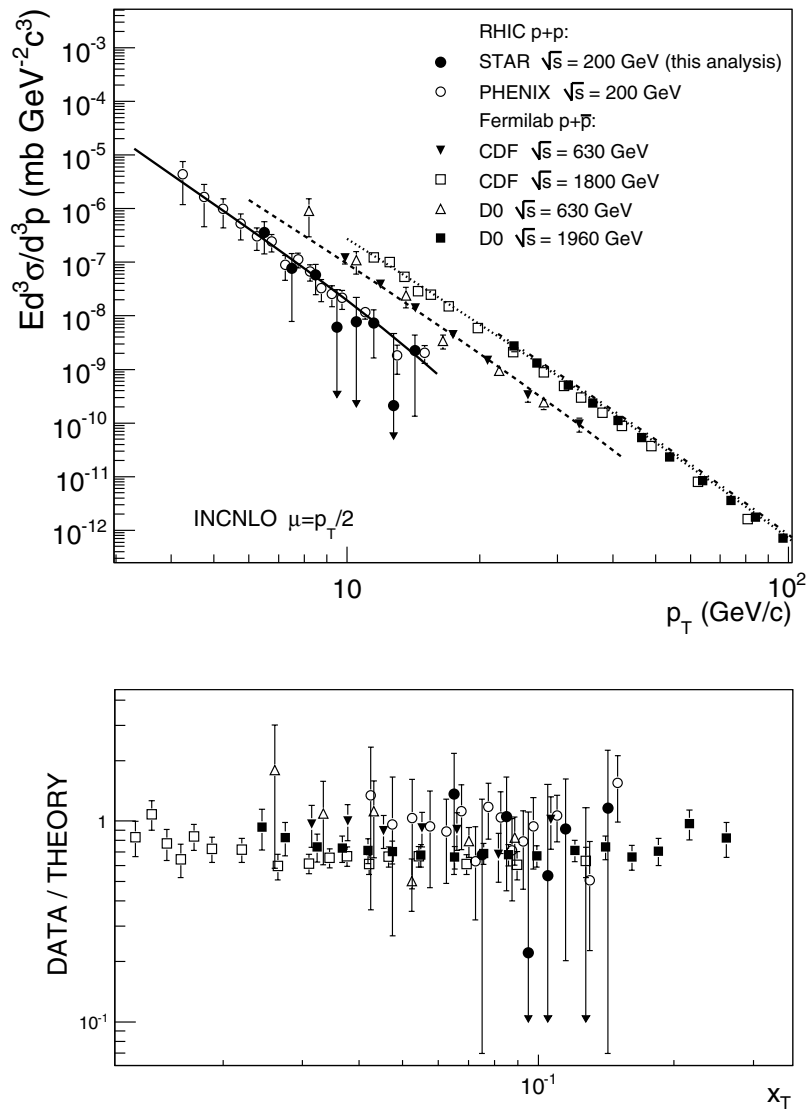


Figure 6.9: Upper panel: cross sections of (isolated) direct photon production obtained in p+p and p+p collisions at the RHIC and Tevatron collider. The curves correspond to the INCNLO calculation with $\mu = p_T/2$. All data have statistical and systematic uncertainties summed in quadrature. The bar on top of the vertical arrows indicates our estimate of the 95% confidence level. The CDF and D0 data points with $p_T > 100$ GeV/c have been omitted to improve visibility. Bottom panel: the data divided by the calculation as a function of x_T .

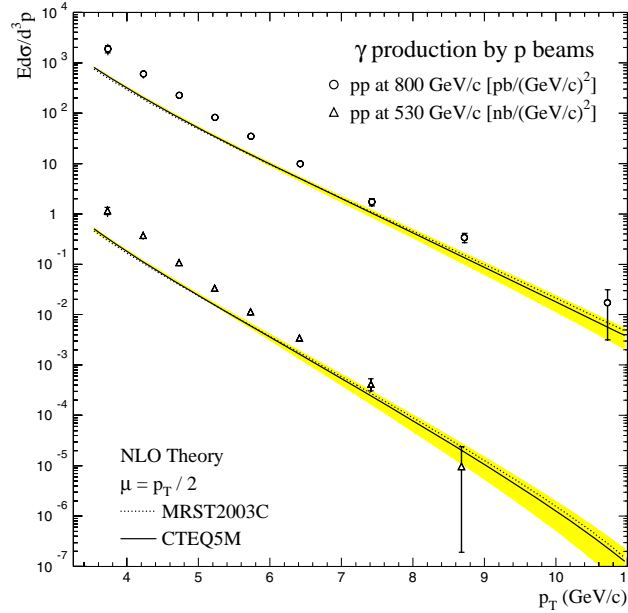


Figure 6.10: Direct photon production in p+p collisions with beam energy equal to 530 GeV and 800 GeV as reported in [120]. The curves represent the cross section obtained with a NLO calculation and the bands the uncertainty obtained from varying the factorization scale μ .

Photons from p+A Collisions

Experimental data on direct photon production in ultra-relativistic collisions of protons (or deuterons) and nuclei is scarce. In fact, RHIC is the first collider facility which can provide such asymmetric collisions. For our comparison in figure 6.11, we have used data obtained with a 530 GeV and 800 GeV proton beam and a fixed beryllium target [120]. Measurements of direct photons in p+A systems at lower center-of-mass energies ($\sqrt{s_{NN}} \sim 20$ GeV) were reported in, e.g., [121, 122].

The STAR data comes from our analysis of d+Au collisions with a center of mass energy per nucleon pair $\sqrt{s_{NN}} = 200$ GeV. All cross sections were divided by the number of possible nucleon-nucleon collisions ($A \times B$) and we have assumed that the total hadronic cross section in d+Au collisions was equal to 2.2 ± 0.1 b [69]. The curves in the figure illustrate the results from a NLO pQCD calculation with the INCNLO program with $\mu = p_T/2$, as described earlier in this chapter.

The bottom panel of figure 6.11 shows the ratio of the measured cross section of the reaction $p + A \rightarrow \gamma_{\text{direct}} + X$, normalized to the theory predictions, as a function of $x_T = 2p_T/\sqrt{s_{NN}}$. Although the PHENIX collaboration have

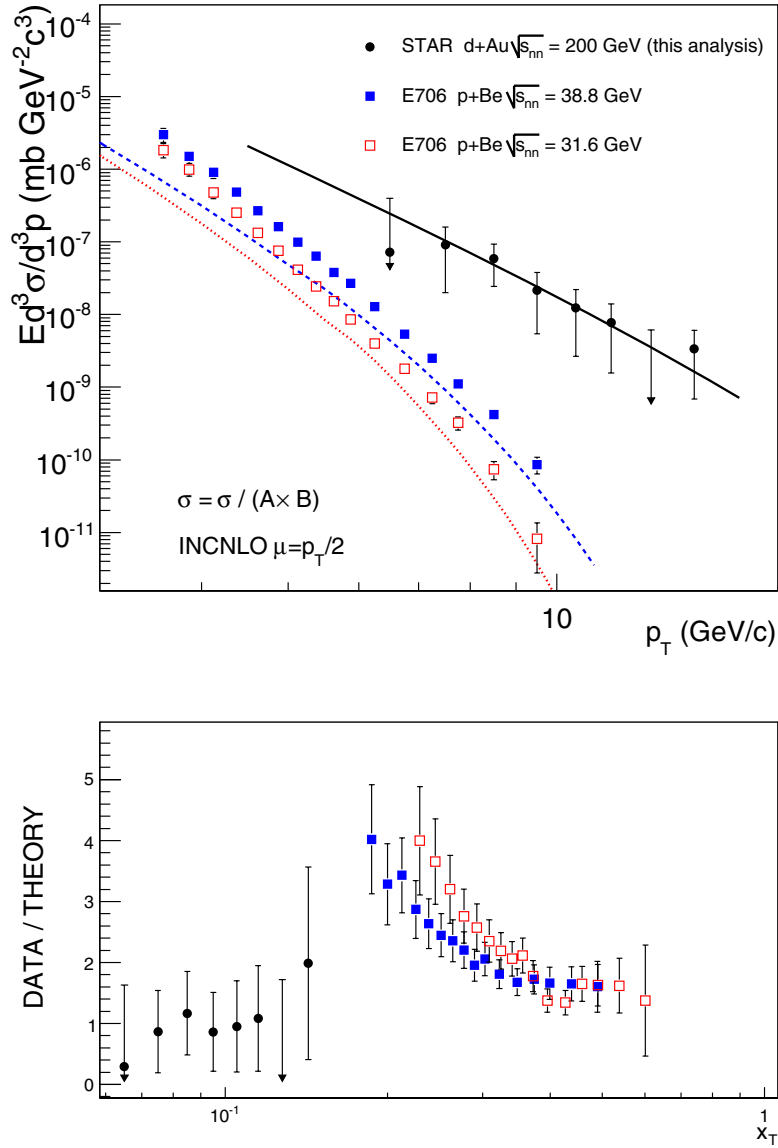


Figure 6.11: Upper panel: the cross sections per nucleon of direct photon production in p+A collisions. The E706 data were determined from scattering protons on a fixed Beryllium target with proton energy $E_{\text{beam}} = 800$ GeV and 530 GeV. The theoretical curves were calculated with the INCNLO program with $\mu = p_T/2$. All data have statistical and systematic uncertainties summed in quadrature. The bar on top of the vertical arrows indicates our estimate of the 95% confidence level. Bottom panel: the ratio of these data and the corresponding curves as a function of x_T .

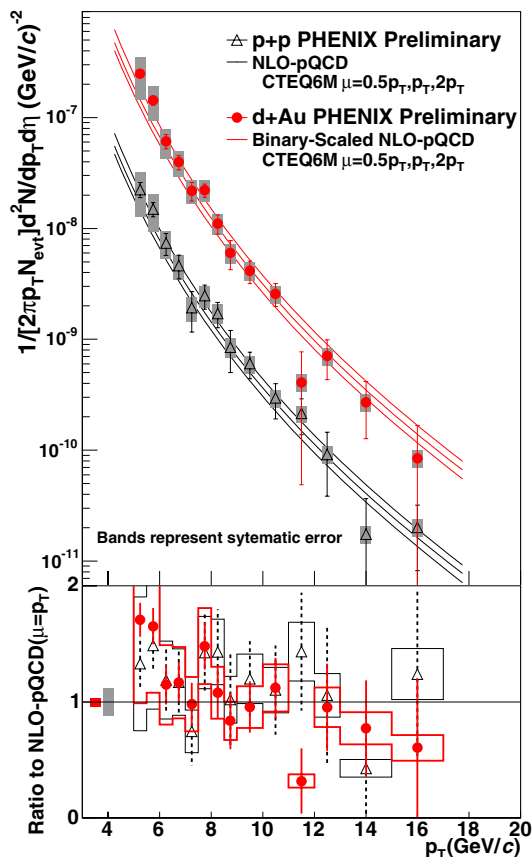


Figure 6.12: Preliminary measurement of direct photon production in $\sqrt{s_{NN}} = 200$ GeV p+p and d+Au collisions, by the PHENIX collaboration. The upper panel shows $E d^3N/dp^3$ and the bottom panel shows the direct photon yields divided by the results from a NLO pQCD calculation. The figure was taken from [123].

presented direct photon data in $\sqrt{s_{NN}} = 200$ GeV d+Au collisions, see for instance [123], these have not been published at the time of writing this thesis. Nevertheless, the preliminary results of their measurement are shown, together with the pQCD curves, in figure 6.12. From the lower panel of the figure it can be seen that the data from this analysis are consistent with the results from PHENIX. Note, however, that the ratio in this case is with respect to the theory prediction with $\mu = p_T$.

As in case of p+p collisions discussed earlier in this chapter, the E706 results from p+Be collisions demonstrate a p_T dependent deviation from the theoretical prediction. The discrepancy persists, even when the NLO calculation is performed with the smaller factorization scale $\mu = p_T/3$ as it

concerns not only an overall normalization factor [98]. An energy-dependent transverse momentum broadening ($\langle k_T \rangle \sim 1.2$) of the scattering partons was proposed in order to reconcile the p+Be data with theory [120]. We did not find evidence to support an extrapolation of these non-perturbative effects to a larger center-of-mass energy $\sqrt{s_{NN}} = 200$ GeV and the significantly heavier d+Au system.

Our results on direct photon production in d+Au collisions are compatible with the preliminary data obtained by PHENIX as well as NLO pQCD calculations. However, these measurements do not rule out nuclear modification or multiple scattering effects in the gold core, but provide an upper limit to the possible size of these phenomena instead. Similar to our discussion in section 6.2, we point out that a thorough understanding of direct photons from d+Au collisions will be important to interpret a possible thermal photon excess in Au+Au collisions.

6.5 Outlook

First and foremost, the techniques and results presented in this thesis serve as a foundation for future analyses of direct photon production in Au+Au collisions. The ultimate goal of our efforts is a measurement of the thermal photon spectrum, accurate enough to provide information on the temperature evolution of the created plasma. Next to many theoretical complications and uncertainties, the experimental challenge will be considerable. The backgrounds from decay photons and neutral hadrons in the thermal range, although suppressed by jet quenching, are extremely large. Note that in case of the current analysis of p+p and d+Au collisions, it was not possible to extract a direct photon signal below $p_T \sim 6$ GeV/c. Furthermore, the analysis of meson production in Au+Au collisions, which is essential to determine the decay backgrounds, will be more involved as a consequence of the high particle multiplicities in central events.

As an illustration, figure 6.13 shows the invariant mass distribution of photon pairs obtained from $\sim 4.5 \times 10^4$ minimum bias Au+Au collisions (Run-4), for $p_T > 1$ GeV/c. The inset of the figure, which zooms in on the invariant mass range $0.0 < m_{\text{inv}} < 0.5$ GeV/c², demonstrates that there is no discernible π^0 signal on top of the combinatorial background. The latter does not imply though, that a neutral pion mass peak is not present. A more careful study would show that the peak resides on top of a large and rapidly rising combinatorial background. To extract the peak content in such an environment, this background would have to be reconstructed by means of the technique of mixed events.

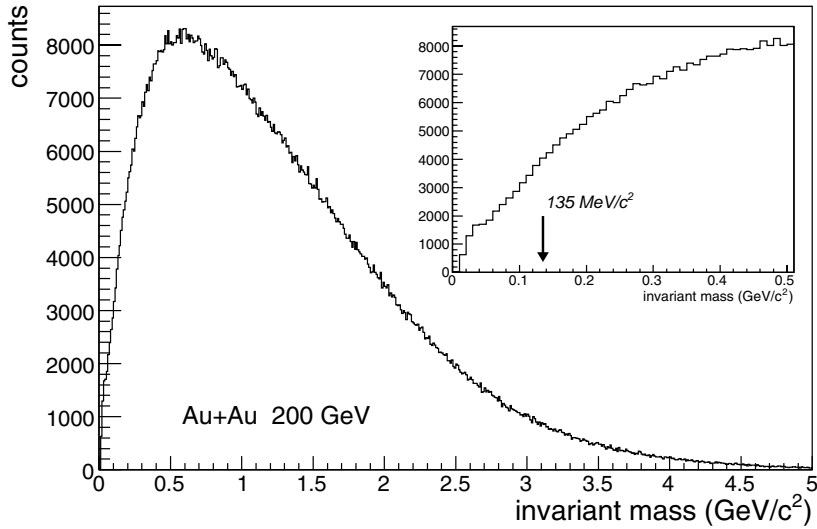


Figure 6.13: The invariant mass distribution of photon pairs obtained from $\sim 4.5 \times 10^4$ minimum bias Au+Au events for $p_T > 2 \text{ GeV}/c$. The inset zooms in on the range $0.0 < m_{\text{inv}} < 0.5$ and the arrow illustrates the theoretical value of the π^0 mass.

Furthermore, it should be stressed that this mass distribution was obtained with the same framework as was used to analyze p+p and d+Au collisions. It is not evident that the developed routines are sufficiently advanced to be used in the environment of the most central heavy ion collisions. The clustering algorithm, for example, which was used to reconstruct the profile and position of the electromagnetic showers, will be challenged by more frequent random overlaps. This will inevitably reduce the position and energy resolution of the photon candidates. Likewise, the rejection of genuine photons by random associations with a charged track will be enhanced. These and other complications will demand an optimum performance of the calorimeter, the shower maximum detector, and the applied reconstruction routines.

The precision of the current measurements was predominantly affected by two sources of uncertainty. First of all, the uncertainty associated with the global BEMC energy scale which at present will inevitably lead to systematic uncertainties up to $\sim 40\%$ when reconstructing a photon or neutral pion momentum spectrum. In addition, the uncertainty attributed to the BSMD calibration procedure was the source of the dominant systematic error of the double ratio and, hence, of the absolute direct photon yield. The precision

of future direct photon studies and the continuation of this analysis to the environment of heavy ion collisions, would most certainly benefit from a reduction of these systematic uncertainties.

Based on our analysis we conclude that the following two studies will be extremely valuable to improve on the significance of the presented measurements:

- the absolute calibration of the BEMC based on the position of the neutral pion mass peak
- the in situ calibration of the BSMD based on electron tracks in the Time Projection Chamber

An example, similar though not identical to the first of these two, was already discussed in section 4.3.3. In that case it concerned a calibration of the overall BEMC energy scale during one period of data recording relative to another. When the backgrounds in the π^0 mass window are sufficiently well under control, such an analysis can be used to perform an absolute energy calibration of the individual calorimeter towers and determine the global energy scale.

The in situ energy calibration of the BSMD could improve the capability of disentangling nearby showers, e.g. those from a highly energetic neutral pion decaying into two photons, and additionally increase the efficiency to identify backgrounds from neutral hadrons. The electrons can be tracked with the Time Projection Chamber, which extends beyond the calorimeter surface. The BSMD response could then be calibrated relative to the momentum and thus the energy of the identified electron. Both these calibration techniques are currently under investigation within the calorimeter working group.

We conclude by showing two observations of direct photons in ultra-relativistic heavy ion collisions. Figure 6.14 shows the very first measurement of a direct photon signal in ultra-relativistic heavy ion collisions, performed by the WA98 collaboration [124]. These data were found to be consistent with a thermal source, either the Quark Gluon Plasma or a Hot Hadron Gas, for photons below $p_T = 2.5 \text{ GeV}/c$. However, it was not possible to claim the existence of a QGP phase in central Pb+Pb collisions at a beam energy of 158 AGeV [29].

In figure 6.15 we shows a more recent result obtained by the PHENIX collaboration in $\sqrt{s} = 200 \text{ GeV}$ Au+Au collisions at RHIC [125], together with the results from the calculation presented in section 1.2.3 [31]. The measured spectrum of direct photons at high p_T is well described by the NLO pQCD cross section, scaled with the nuclear thickness function for the 10%

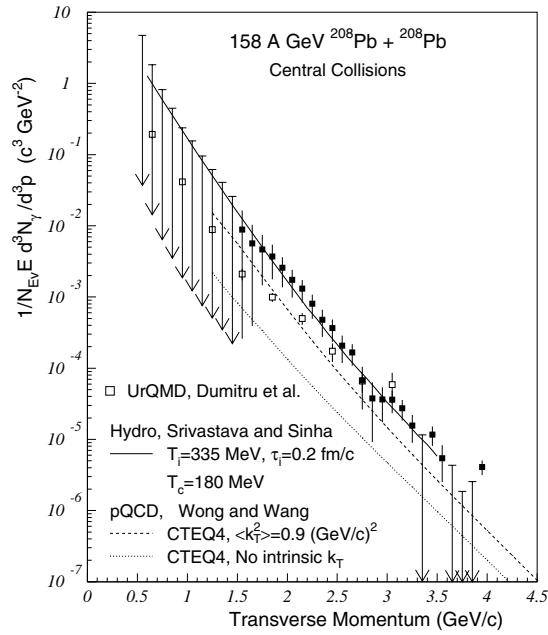


Figure 6.14: The direct photon excess at low p_T measured by the WA98 collaboration in $\sqrt{s_{NN}} = 17.3$ GeV Pb+Pb collisions, compared to theoretical predictions including the production of thermal photons. The figure was taken from [124].

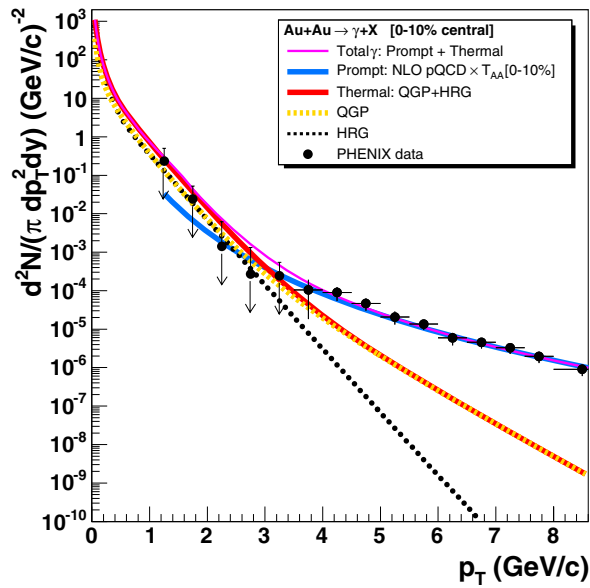


Figure 6.15: The direct photon signal in Au+Au collisions at $\sqrt{s_{NN}} = 200$ GeV from PHENIX. The figure was taken from [31].

most central Au+Au collisions. The arrows through the data points, in the p_T range where a thermal excess is expected, indicate the 90% confidence limits of the signal. The PHENIX data are consistent with the evolution scenario from section 1.2.3 in case of an initial QGP temperature equal to 590 MeV and formation time $\tau_0 = 0.15 \text{ fm}/c$. However, the use of direct photons to acquire more detailed information on the thermodynamical evolution of the QGP can only be successful when the precision of theoretical predictions and future measurements will be improved.

From the start of the 2006 p+p run at RHIC, the Barrel Electromagnetic Calorimeter has been fully commissioned and operational. The detector currently spans 2 units of pseudo-rapidity and the full azimuthal angle, and is complemented by the Barrel Shower Maximum Detector covering the entire calorimeter acceptance. The Barrel Preshower Detector approaches its full installation as well. The latter can contribute to a suppression of the large hadronic backgrounds present in Au+Au collisions. These developments, combined with the large amount of high-quality data from p+p, d+Au, and Au+Au collisions, provide a unique opportunity to study direct photons at STAR.

Summary

The primary goal of heavy ion physics is the study of the Quark Gluon Plasma (QGP). In this exotic state of matter, the quarks and gluons, which make up ordinary hadronic matter, decouple and behave as free particles. The QGP exists at extremely high temperatures and baryon densities, for example, in the early universe or in the ultra-dense core of neutron stars. The thermal radiation from the quarks in the plasma can provide information on the temperature of the matter and, hence, on the equation of state of the QGP. To isolate these thermal photons, precise knowledge is required on alternative sources of photon production in hadronic collisions. This was the principle argument to study the production rates of direct photons in p+p and d+Au collisions.

The analyzed data were recorded with the STAR experiment and correspond to p+p and d+Au collisions from the RHIC run in the years 2003 and 2005, respectively. The principle detectors for our analysis were the Barrel Electromagnetic Calorimeter and the Barrel Shower Maximum Detector. The former is a lead-scintillator sampling calorimeter located at mid-rapidity ($0 < \eta < 1$) and covering the full azimuthal angle. The latter is a gaseous wire-proportional counter with cathode strip readout and is embedded in the calorimeter with equal acceptance. The signals from these two detectors were used to reconstruct the energy, the position, and the shower profile of the photon candidates.

Direct photons are defined as those photons which do not originate from hadronic decays. The largest background to a direct photon measurement is formed by the decay of a neutral pion into two photons. Therefore, the first step was the reconstruction of the neutral pion yields. To accomplish this, a combinatorial technique was used, based on the invariant mass of pairs of photons from the same collision. The spectra of other hadrons decaying into photons were assumed to exhibit a phenomenological scaling law. With the resulting hadron yields as an input, the total number of decay photons was simulated. The direct photon spectrum then followed from a subtraction of these decay photons from the total photon yield.

However, instead of directly performing this subtraction, our ansatz was to express the direct photon yield in terms of the so called double ratio. This is the point-to-point ratio of the inclusive photon and neutral pion spectrum, divided by the total number of decay photons relative to a parametrization of the neutral pion spectrum. It has the advantage that many experimental uncertainties, common to the detection of neutral pions and single photons, largely cancel. The final step in our analysis was the conversion of this double ratio to absolute direct photon yields.

The cross section of inclusive neutral pion production in p+p collisions was found to be in agreement with the results from a next-to-leading order pQCD calculation with the KKP set of fragmentation functions and the CTEQ6M parton densities as an input. The results from alternative calculations differ mostly in their description of the gluon-to-pion fragmentation function which, at least up till now, is poorly constrained. The dominant uncertainty ($\sim 30\%$) of the measured cross section resulted from a 4% uncertainty of the global energy scale of the calorimeter. A future reduction of this uncertainty is anticipated and would yield valuable data to constrain gluon-to-pion fragmentation in the kinematic regime at RHIC. In addition, the neutral pion cross section in p+p collisions serves as an important reference to study the modification of particle yields by jet quenching effects in heavy ion collisions at RHIC.

The neutral pion yield from d+Au collisions has been analyzed by means of the nuclear modification factor R_{dAu} . We have measured that R_{dAu} is consistent with unity over the transverse momentum range $2 < p_T < 15$ GeV/c, indicating the absence of strong nuclear effects. Furthermore, it can be viewed as an independent confirmation that the strong suppression of particle yields, as observed in central Au+Au collisions at RHIC, cannot be attributed to possible nuclear effects in the gold core.

The measured direct photon differential cross section in p+p collisions is consistent with the results from a next-to-leading order pQCD calculation. This calculation included the GRV parton-to-photon fragmentation functions and the CTEQ6M parton density functions. Both systematic and statistical uncertainties were found to be relatively large and preclude more stringent claims. Nevertheless, the data appear to follow the current global trend, namely, that next-to-leading order pQCD provides an accurate description of the direct photon cross sections in relativistic hadronic collisions with center-of-mass energies ranging approximately from 30 GeV up to 1.96 TeV.

Experimental data on ultra-relativistic proton(deuteron)-nucleus collisions are scarce. Moreover, RHIC is the first collider facility to provide such asymmetric collisions. Hence, the data reported in this thesis for direct photon production in d+Au collisions can be considered valuable by them-

selves. We have not observed a strong p_T dependent deviation from the NLO pQCD predictions. Such a discrepancy has been previously reported in case of p+Be collisions. However, the current uncertainties of our results are too large to completely exclude the presence of such effects.

In general, the results in this thesis constitute a solid baseline for further studies of photon production at RHIC. A future effort at STAR to extract a thermal photon signal from Au+Au collisions will greatly benefit from the presented research.

Samenvatting

Het belangrijkste doel binnen de zware-ionenfysica is de studie van het quark-gluonplasma (QGP). In deze exotische toestand van materie gedragen de quarks en gluonen, de bouwstenen van alledaagse hadronische materie, zich nagenoeg als vrije deeltjes. Het QGP bestaat bij extreem hoge temperaturen en dichtheden zoals, bijvoorbeeld, in het vroege heelal of in de zeer dichte kernen van neutronensterren. De thermische straling van de quarks in het plasma kan directe informatie verschaffen over de temperatuur van de materie en, zodoende, over de toestandsvergelijking van het QGP. Het isoleren van deze thermische fotonen vereist precieze kennis van alternatieve bronnen van fotonproductie in botsingen tussen hadronen. Dit was het voornaamste argument om de productie van fotonen in p+p en d+Au botsingen te bestuderen.

De geanalyseerde data zijn verkregen met het STAR experiment en afkomstig van p+p en d+Au botsingen bij RHIC in de jaren 2003 en 2005, respectievelijk. De voornaamste detectoren voor onze analyse waren de Barrel Electromagnetic Calorimeter (BEMC) en de Barrel Shower Maximum Detector (BSMD). De BEMC is een lood-scintillatie calorimeter die geplaatst is bij centrale rapiditeit ($0 < \eta < 1$) en zich uitstrekt over de volledige azimutale hoek. De BSMD is een gasachtige dradenkamer met uitleesbare cathodestrips en bevindt zich binnenin de calorimeter. De signalen van deze twee detectoren werden gebruikt om de energie, de positie, en het profiel van de electromagnetische cascade van de fotonen te meten.

Directe fotonen zijn gedefinieerd als fotonen die niet afkomstig zijn van het verval van een hadron. De grootste achtergrond bij een meting van directe fotonen wordt zodoende veroorzaakt door het verval van een neutraal pion naar twee fotonen. Daarom was het belangrijk om in eerste instantie de spectra van de neutrale pionen te bepalen. Dit werd bereikt met behulp van een combinatoriële techniek op basis van de invariante massa van fotonparen. We hebben daarnaast aangenomen dat de spectra van andere hadronen die een verval kennen naar een of meer fotonen, beschreven kunnen worden middels een fenomenologische schalingswet. Het totale aantal vervalstofotonen

werd gesimuleerd op basis van de resulterende hadronspectra. Het spectrum van directe fotonen werd vervolgens bepaald door de vervalsfotonen af te trekken van de volledige opbrengst van fotonen.

In plaats van het verschil tussen alle fotonen en de vervalsfotonen direct te bepalen, hebben we ervoor gekozen om de productie van directe fotonen te analyseren in termen van de zogenaamde dubbele ratio. Hiervoor is de ratio van het spectrum van inclusieve fotonen ten opzichte van het spectrum van neutrale pionen bepaald. Deze ratio is vervolgens gedeeld door het spectrum van vervalsfotonen, dat genormaliseerd werd ten opzichte van een parameterisatie van het neutrale-pionspectrum. Het voordeel van deze methode is dat de experimentele onzekerheden die gemeenschappelijk zijn voor een meting van neutrale pionen en fotonen, significant verkleind kunnen worden. De laatste stap in de analyse betrof de omzetting van deze dubbele ratio naar absolute spectra van directe fotonen.

De werkzame doorsnede van de productie van inclusieve neutrale pionen in p+p botsingen is in overeenstemming met de resultaten van een NLO pQCD berekening op basis van de KKP set van fragmentatiefuncties en de CTEQ6M partondichtheden. De uitkomsten van alternatieve berekeningen verschillen met name van elkaar vanwege hun beschrijving van de gluon-naar-pion fragmentatiefunctie die, tot dusver althans, niet erg nauwkeurig bepaald is. De grootste onzekerheid ($\sim 30\%$) van de gemeten doorsnede werd veroorzaakt door een 4% onzekerheid op de energieschaal van de calorimeter. Een toekomstige verkleining van deze onzekerheid zal waardevolle data opleveren om de gluon-naar-pion fragmentatiefunctie te bepalen voor het kinematische domein bij RHIC. Daarnaast geldt dat de werkzame doorsnede van pionproductie in p+p botsingen een belangrijke referentie vormt om de effecten van jet quenching te onderzoeken in botsingen tussen zware ionen bij RHIC.

De opbrengst van neutrale pionen in d+Au botsingen is geanalyseerd middels de nucleaire-modificatiefactor R_{dAu} . We hebben gemeten dat R_{dAu} consistent is met één binnen het impulsinterval $2 < p_T < 15$ GeV/c, hetgeen al te sterke nucleaire effecten uitsluit. Bovendien vormt dit een onafhankelijke bevestiging dat de suppressie van de deeltjesopbrengst in Au+Au botsingen, de zogenaamde jet-quenching, geen gevolg is van nucleaire effecten in de goudkern.

De gemeten werkzame doorsnede van directe fotonen die geproduceerd zijn in p+p botsingen is consistent met de resultaten van een NLO pQCD berekening. Deze berekening was gebaseerd op de GRV parton-naar-foton fragmentatiefuncties en de CTEQ6M partondichtheden. Zowel de systematische als de statistische onzekerheden waren relatief groot en maken al te precieze claims onmogelijk. Desalniettemin lijken de data de huidige trend

te volgen, namelijk, dat NLO pQCD de werkzame doorsnedes van de productie van directe fotonen in hadronische botsingen succesvol beschrijft. Dit laatste betreft botsingen met een zwaartepuntsenergie variërend van 30 GeV tot 1.96 TeV.

Er zijn relatief weinig experimentele data beschikbaar met betrekking tot ultra-relativistische proton(deuteron)-nucleus botsingen. RHIC is dan ook de eerste colliderfaciliteit die dergelijke asymmetrische botsingen mogelijk maakt. De meting van directe fotonen in d+Au botsingen, zoals beschreven in dit proefschrift, kan dan ook als een belangrijk, afzonderlijk resultaat beschouwd worden. We hebben geen bewijs gevonden voor een sterke p_T -afhankelijke afwijking van de voorspellingen op basis van NLO pQCD. Een dergelijke afwijking is wel gerapporteerd in eerdere publicaties in het geval van p+Be botsingen. De huidige onzekerheden in onze resultaten zijn echter te groot om de aanwezigheid van dit effect volledig uit te kunnen sluiten.

In het algemeen geldt dat onze resultaten een belangrijk referentiekader vormen voor verdere fotonmetingen bij RHIC en ten goede zullen komen aan een toekomstige analyse van thermische fotonen in Au+Au botsingen.

Acknowledgements

First of all, I would like to take this opportunity to thank my promotor, Thomas Peitzmann. His interest and guidance, as well as his constructive criticism, were essential to the successful completion of this thesis. I also want to thank my co-promotor, André Mischke, for, among other things, his technical assistance in the beginning and his careful reading of many preliminary manuscripts during the final stages of my research. I want to thank Oleksandr Grebenyuk, a fellow PhD student of our group, who graduated on a closely related subject. I have greatly benefited from our discussions, especially those related to programming and the STAR software environment. In general, I would like to express my gratitude to all the people in our research group at Utrecht University and NIKHEF, as well as the people from the STAR collaboration, who contributed, one way or another, to this project.

I am especially grateful to the people who are most important in my life. Without the unconditional support of my family and friends, I would have never been able to complete this.

Appendix A

Tabulated Results

p_T (GeV/ c)	$Ed^3\sigma/d^3p$ (mb GeV $^{-2}c^3$)	uncertainty	
		stat.	sys.
1.25	2.771e-01	1.891e-02	1.413e-01
1.75	4.172e-02	2.516e-03	1.724e-02
2.25	9.601e-03	6.176e-04	3.419e-03
2.75	2.838e-03	2.258e-04	9.196e-04
3.50	5.383e-04	4.836e-05	1.622e-04
4.50	8.595e-05	2.670e-06	2.584e-05
5.50	1.640e-05	4.751e-07	4.923e-06
6.50	4.048e-06	1.149e-07	1.226e-06
7.50	1.425e-06	4.495e-08	4.375e-07
8.50	5.156e-07	2.140e-08	1.607e-07
9.50	2.402e-07	1.306e-08	7.610e-08
10.50	1.173e-07	8.230e-09	3.780e-08
11.50	4.726e-08	5.200e-09	1.550e-08
12.75	2.377e-08	2.649e-09	7.963e-09
14.25	9.797e-09	1.812e-09	3.368e-09

Table A.1: The differential cross section of inclusive π^0 production in p+p collisions at $\sqrt{s} = 200$ GeV averaged over the rapidity range $0.1 < y < 0.9$.

p_T (GeV/c)	$Ed^3\sigma/d^3p$ (mb GeV ⁻² c ³)	uncertainty	
		stat.	sys.
6.50	3.577e-07	7.711e-08	2.007e-07
7.50	7.655e-08	3.152e-08	6.105e-08
8.50	5.809e-08	1.736e-08	2.841e-08
9.50	6.112e-09	(95%CL=3.070e-08)	
10.50	7.716e-09	(95%CL=2.198e-08)	
11.50	7.314e-09	4.739e-09	3.151e-09
12.75	2.121e-10	(95%CL=4.659e-09)	
14.25	2.238e-09	1.913e-09	8.748e-10

Table A.2: The differential cross section of prompt photon production in p+p collisions at $\sqrt{s} = 200$ GeV averaged over the rapidity range $0.1 < y < 0.9$.

p_T (GeV/c)	Ed^3N/d^3p (GeV ⁻² c ³)	uncertainty	
		stat.	sys.
1.25	3.944e-02	3.469e-03	2.072e-02
1.75	6.386e-03	3.772e-04	2.763e-03
2.25	1.449e-03	7.031e-05	5.500e-04
2.75	4.138e-04	2.149e-05	1.452e-04
3.50	8.800e-05	4.331e-06	2.922e-05
4.50	1.413e-05	6.681e-07	4.721e-06
5.50	2.951e-06	1.223e-07	9.933e-07
6.50	6.916e-07	3.336e-08	2.365e-07
7.50	2.147e-07	9.892e-09	7.483e-08
8.50	7.564e-08	4.087e-09	2.690e-08
9.50	3.560e-08	2.303e-09	1.293e-08
10.50	1.870e-08	1.409e-09	6.941e-09
11.50	9.274e-09	9.133e-10	3.516e-09
12.75	5.744e-09	5.647e-10	2.237e-09
14.25	1.673e-09	3.273e-10	6.722e-10

Table A.3: The Lorentz invariant π^0 yield in d+Au collisions at $\sqrt{s_{NN}} = 200$ GeV averaged over the rapidity range $0.1 < y < 0.9$.

p_T (GeV/c)	Ed^3N/d^3p (GeV ⁻² c ³)	uncertainty	
		stat.	sys.
6.50	1.218e-08	(95%CL=6.784e-08)	
7.50	1.535e-08	6.004e-09	1.033e-08
8.50	1.001e-08	3.064e-09	5.017e-09
9.50	3.682e-09	1.812e-09	2.077e-09
10.50	2.099e-09	1.180e-09	1.150e-09
11.50	1.325e-09	8.153e-10	6.727e-10
12.75	6.660e-21	(95%CL=1.039e-09)	
14.25	5.735e-10	3.793e-10	2.533e-10

Table A.4: The Lorentz invariant direct photon yield in d+Au collisions at $\sqrt{s_{NN}} = 200$ GeV averaged over the rapidity range $0.1 < y < 0.9$.

p_T (GeV/c)	R_{dAu}	uncertainty	
		stat.	sys.
1.25	0.797	0.089	0.113
1.75	0.857	0.072	0.123
2.25	0.845	0.068	0.122
2.75	0.816	0.078	0.119
3.50	0.924	0.098	0.137
4.50	0.945	0.053	0.171
5.50	1.008	0.051	0.184
6.50	0.957	0.054	0.177
7.50	0.851	0.047	0.160
8.50	0.822	0.056	0.157
9.50	0.830	0.070	0.162
10.50	0.885	0.092	0.176
11.50	1.099	0.162	0.222
12.75	1.353	0.201	0.280
14.25	0.993	0.272	0.212

Table A.5: The nuclear modification factor R_{dAu} in d+Au collisions at $\sqrt{s_{NN}} = 200$ GeV averaged over the rapidity range $0.1 < y < 0.9$.

p_T (GeV/ c)	R_γ	uncertainty	
		stat.	sys.
6.50	1.256	0.055	0.128
7.50	1.156	0.064	0.118
8.50	1.332	0.099	0.136
9.50	1.076	0.126	0.110
10.50	1.198	0.172	0.122
11.50	1.469	0.304	0.150
12.75	1.027	0.274	0.105
14.25	1.728	0.623	0.176

Table A.6: The double ratio $R_\gamma = 1 + \gamma_{\text{dir}}/\gamma_{\text{decay}}$ in p+p collisions at $\sqrt{s} = 200$ GeV averaged over the rapidity range $0.1 < y < 0.9$.

p_T (GeV/ c)	R_γ	uncertainty	
		stat.	sys.
6.50	1.051	0.066	0.108
7.50	1.215	0.082	0.126
8.50	1.393	0.120	0.146
9.50	1.310	0.153	0.138
10.50	1.342	0.192	0.143
11.50	1.435	0.268	0.155
12.75	0.800	0.214	0.088
14.20	2.058	0.700	0.231

Table A.7: The double ratio $R_\gamma = 1 + \gamma_{\text{dir}}/\gamma_{\text{decay}}$ in d+Au collisions at $\sqrt{s_{NN}} = 200$ GeV averaged over the rapidity range $0.1 < y < 0.9$.

Appendix B

Coordinates and Kinematic Variables

The STAR coordinate system is a right-handed Cartesian system with its origin located at the center of the solenoid. The \hat{z} direction is along the beam line towards the west and the \hat{y} direction is upwards. Consequently, \hat{x} runs from north to south. This means that the clockwise rotating beam moves in the direction of positive z (c.f. figure 2.1). We have used cylindrical coordinates such that

$$x = r \cos \phi \tag{B.1}$$

$$y = r \sin \phi \tag{B.2}$$

$$z = z \tag{B.3}$$

with $-\pi < \phi < \pi$. However, we have denoted the cylindrical radius by r , contrary to ρ which is the official STAR notation. The variable θ (spherical coordinate) is the angle between the vector (x, y, z) and the z axis and therefore runs from 0 to π . The coordinate system of the analyzed events was equivalent to the above with the measured event vertex replacing the nominal STAR origin.

Throughout this thesis we have made use of relativistic kinematics with the speed of light equal to unity: $c = 1$. The four-momentum of a particle is then given by

$$p_\mu = (E, p_x, p_y, p_z) \tag{B.4}$$

with the Minkowski metric defined by the tensor

$$\eta_{\mu\nu} = \begin{pmatrix} 1 & 0 & 0 & 0 \\ 0 & -1 & 0 & 0 \\ 0 & 0 & -1 & 0 \\ 0 & 0 & 0 & -1 \end{pmatrix} \tag{B.5}$$

such that $p^\mu = \eta^{\mu\nu} p_\nu$. The inner product of the four-vector p_μ with itself is given by

$$p_\mu p^\mu = E^2 - p_x^2 - p_y^2 - p_z^2 = m^2 \quad (\text{B.6})$$

and is invariant under transformations of the Lorentz group. The square root of the above inner product corresponds to the invariant mass.

In case of a 2-to-2 interaction of particles with incoming four-momenta p_a^μ and p_b^μ and outgoing momenta p_c^μ and p_d^μ , the Mandelstam variables are given by

$$s = (p_a^\mu + p_b^\mu)^2 \quad (\text{B.7})$$

$$t = (p_a^\mu - p_c^\mu)^2 \quad (\text{B.8})$$

$$u = (p_a^\mu - p_d^\mu)^2 \quad (\text{B.9})$$

and the center-of-mass energy of the partonic reaction is equal to \sqrt{s} . In heavy ion physics, a common expression is the center-of-mass energy of a collision between a single nucleon from the projectile and a single nucleon from the target: $\sqrt{s_{NN}}$. In case of proton-proton collisions, we use \sqrt{s} for the center-of-mass energy of the two protons.

The rapidity y of a particle with four-momentum p_μ , is defined as

$$y = \frac{1}{2} \ln \frac{E + p_z}{E - p_z} = \frac{1}{2} \ln \frac{1 + \beta \cos \theta}{1 - \beta \cos \theta} \quad (\text{B.10})$$

with $\beta = v/c$. In case of ultra-relativistic particles, such that $v \rightarrow c$, y becomes equal to the pseudo-rapidity:

$$\eta = -\ln \tan \frac{\theta}{2}. \quad (\text{B.11})$$

The transverse momentum of the particle is given by

$$p_T = \sqrt{p_x^2 + p_y^2} = |\vec{p}| \sin \theta \quad (\text{B.12})$$

and the transverse components of the energy and mass follow from

$$E_T = E \sin \theta \quad (\text{B.13})$$

$$m_T = \sqrt{m^2 + p_T^2}. \quad (\text{B.14})$$

For our comparison of photon cross sections from experiments with different center-of-mass energies, we used the variable

$$x_T = \frac{2p_T}{\sqrt{s_{NN}}}. \quad (\text{B.15})$$

This variable can be related to the longitudinal momentum fractions x_a and x_b of the incoming partons in the 2-to-2 partonic process, $a + b \rightarrow \gamma + d$. The initial partonic momenta are given by

$$p_{\mu,a} = \frac{\sqrt{s}}{2}(x_a, 0, 0, -x_a) \quad (\text{B.16})$$

$$p_{\mu,b} = \frac{\sqrt{s}}{2}(x_b, 0, 0, x_b) \quad (\text{B.17})$$

and conservation of energy leads to

$$\frac{\sqrt{s}}{2}(x_a + x_b) = E_\gamma + E_d. \quad (\text{B.18})$$

Assuming that the produced photon has momentum perpendicular to the incoming particles ($x_a = x_b$), we find that

$$x_a = \frac{E_\gamma + E_c}{\sqrt{s}} \approx \frac{2p_T}{\sqrt{s}} \quad (\text{B.19})$$

such that $x_a \sim x_T$. Consequently, the variable x_T is sensitive to the momentum fraction of the partons entering the hard scattering process.

Appendix C

Neutral Pion Decay

The decay of a neutral pion $\pi^0 \rightarrow \gamma\gamma$ is isotropic in the pion rest frame. This means that $dN/d\Omega^*$ is a constant and that

$$\frac{dN}{d\cos\theta^*} = \frac{1}{2} \quad (\text{C.1})$$

which is normalized over the interval $-1 < \cos\theta^* < 1$ and the $*$ is used to label variables corresponding to the rest frame. We start with determining the energy distribution (and therefore the energy asymmetry $Z_{\gamma\gamma}$) of the photons in the laboratory frame.

The distribution of the photon energy E_γ in the laboratory frame is related to equation C.1 by

$$\frac{dN}{dE_\gamma} = \frac{dN}{d\cos\theta^*} \frac{d\cos\theta^*}{dE_\gamma} = \frac{1}{2} \frac{d\cos\theta^*}{dE_\gamma}. \quad (\text{C.2})$$

The photon energy in the laboratory frame as a function of the angle θ^* follows from a Lorentz transformation with $\gamma = E_{\pi^0}/m_{\pi^0}$ and

$$\beta = \sqrt{1 - \frac{1}{\gamma^2}} = E_{\pi^0}/p_{\pi^0}. \quad (\text{C.3})$$

The energy E_γ^* is equal to $m_{\pi^0}/2$ and the four-momentum of the photon in the pion rest frame is given by

$$p_\mu^* = \frac{m_{\pi^0}}{2}(1, \sin\theta^*, 0, \cos\theta^*). \quad (\text{C.4})$$

After the Lorentz boost we find that

$$E_\gamma = \frac{\gamma m_{\pi^0}}{2}(1 + \beta \cos\theta^*). \quad (\text{C.5})$$

Hence, $dE_\gamma/d\cos\theta^* = p_{\pi^0}/2$ and therefore

$$\frac{dN}{dE_\gamma} = \frac{1}{p_{\pi^0}} \quad (\text{C.6})$$

which is a constant. The resulting energy distribution, as well as that of the energy asymmetry, is therefore flat. From equation C.5 and the limits of $\cos\theta^*$ mentioned above, we find that the photon energy is limited to the range $(E_{\pi^0} \pm p_{\pi^0})/2$. Note that the maximum and minimum energy are obtained when the photons are emitted parallel to the Lorentz boost.

A minimum opening angle between the two photons occurs when the decay in the pion rest frame is perpendicular to the boost. In that case, the transverse momentum of a photon, in both frames of course, is equal to $m_{\pi^0}/2$. The total momentum of the two photons, which is in the direction of the boost, is just the neutral pion energy E_{π^0} . Denoting the minimum opening angle by ψ_{\min} , we find that

$$\tan \frac{\psi_{\min}}{2} = \frac{m_{\pi^0}}{E_{\pi^0}}. \quad (\text{C.7})$$

For sufficiently large π^0 energy, we can approximate that $\tan\epsilon \sim \epsilon$ and

$$\psi_{\min} \sim \frac{2m_{\pi^0}}{E_{\pi^0}} \quad (\text{C.8})$$

which gives the minimum opening angle as a function of the π^0 energy in the laboratory frame.

Appendix D

Acronyms

ADC Analog-to-Digital Converter; unit of the resulting digital number

AKK Albino-Kniehl-Kramer fragmentation functions

AGS Alternating Gradient Synchrotron

BBC Beam-Beam Counter

BEMC Barrel Electromagnetic Calorimeter

BNL Brookhaven National Laboratory

BSMD Barrel Shower Maximum Detector

BSMDE Barrel Shower Maximum Detector eta-plane

BSMDP Barrel Shower Maximum Detector phi-plane

CERN Conseil Européen pour la Recherche Nucléaire

CGC Color Glass Condensate

CPV Charged Particle Veto

CTB Central Trigger Barrel

CTEQ the Coordinated Theoretical-Experimental project on QCD

DAQ Data AcQuisition system

DD Double-Diffractive

DGLAP Dokshitzer-Gribov-Lipatov-Altarelli-Parisi equations

- DIS** Deep Inelastic Scattering
- DSM** Data Storage and Manipulation (boards)
- EMC** European Muon Collaboration; ElectroMagnetic Calorimeter
- EVB** EVent Builder
- FEE** Front End Electronics
- GEANT** GEometry ANd Tracking
- GRV** Gück-Reya-Vogt set of fragmentation functions
- HG** Hadron Gas
- HHG** Hot Hadron Gas
- HIJING** Heavy Ion Jet INteraction Generator
- HRG** Hadron Resonance Gas
- HT1,HT2** HighTower 1 and 2 (trigger condition)
- HTL** Hard-Thermal-Loop
- HPSS** High Performance Storage System
- IFC** Inner Field Cage
- INCNLO** routine to calculate INclusive hadron and direct photon production at NLO
- IR** InfraRed
- KKP** Kniehl-Kramer-Pötter fragmentation functions
- L0–L3** trigger Level 0 up to 3
- LINAC** LINear ACcelerator
- LPM** Landau-Pomeranchuk-Migdal
- MB** Minimum Bias
- MC** Monte-Carlo (simulation)
- MIP** Minimum Ionizing Particle

MP Mixed Phase

MuDST Micro (μ) Data Summary Tape

MWPC Multi-Wire Proportional Chamber

ND Non-Diffractive

NLO Next-to-Leading Order

NSD Non-Single-Diffractive

NMC New Muon Collaboration

PED mean value of noise PEDESTAL

PMT Photo-Multiplier Tube

pQCD perturbative Quantum ChromoDynamics

QCD Quantum ChromoDynamics

QED Quantum ElectroDynamics

QGP Quark Gluon Plasma

RCF RHIC Computing Facility

RHIC Relativistic Heavy Ion Collider

SD Single-Diffractive

STAR Solenoidal Tracker At RHIC

SVT Silicon Vertex Tracker

SSD Silicon Strip Detector

TCD Trigger and Clock Distribution

TCU Trigger Control Unit

TDC Tower Data Collector

TOF Time-Of-Flight detector

TPC Time Projection Chamber

TPT Time Projection Chamber Tracker

TRG the TRiGger system

TRS TPC Response Simulator

WLS WaveLength Shifting (fiber)

ZDC Zero Degree Calorimeter

Bibliography

- [1] M.E. Peskin and D.V. Schroeder, *An Introduction to Quantum Field Theory*, Westview Press (1995).
- [2] L.H. Ryder, *Quantum Field Theory*, Cambridge University Press, 2nd edition (1996).
- [3] K.G. Wilson, Confinement of Quarks, *Phys. Rev. D* **10** (1974) 2445–2459.
- [4] E.V. Shuryak, *The QCD Vacuum, Hadrons and Superdense Matter*, Volume 71 of World Scientific Lecture Notes in Physics (2004).
- [5] R.C. Wha and X-N. Wang, *Quark Gluon Plasma 3*, World Scientific (2004).
- [6] Y-G. Ma *et al.*, *Proceedings of Quark Matter 2007*, *J. Phys. G* **34** (2007) issue 8.
- [7] F. Karsch *et al.*, *Phys. Lett. B* **478** (2000) 447.
- [8] G. Sterman *et al.*, *Rev. Mod. Phys.* **67** (1995) 157–248.
- [9] V.N. Gribov and L.N. Lipatov, *Sov. J. Nucl. Phys.* **15** (1972) 438;
G. Altarelli and G. Parisi, *Nucl. Phys. B* **126** (1977) 298;
Y.L. Dokshitzer, *JETP* **46** (1977) 641.
- [10] J. Pumplin *et al.*, *JHEP* 0207 (2002) 012.
- [11] L. Bourhis *et al.*, *Eur. Phys. J. C* **19** (2001) 89–98.
- [12] B.A. Kniehl *et al.*, *Nucl. Phys. B* **582** (2000) 514–536.
- [13] J.A.M. Vermaseren, *Comp. Phys. Comm.* **83** (1994) 45.
- [14] P. Aurenche *et al.*, *Phys. Lett. B* **140** (1984) 87.

-
- [15] P. Aurenche *et al.*, Nucl. Phys. B **297** (1988) 661.
- [16] L.E. Gordon and W. Vogelsang, Phys. Rev. D **50** (1994) 1901.
- [17] F. Aversa *et al.*, Nucl. Phys. B **327** (1989) 105.
- [18] P. Aurenche *et al.*, Nucl. Phys. B **399** (1993) 34.
- [19] W. Vogelsang, personal communication (2006).
- [20] K. Koller *et al.*, Z. Phys. C **2** (1979) 197.
- [21] J. Kapusta *et al.*, Phys. Rev. D **44** (1991) 2774;
Erratum-ibid. D **47** (1991) 4171.
- [22] R. Baier *et al.*, Z. Phys. C **53** (1992) 433.
- [23] C. Gale and J. Kapusta, Nucl. Phys. B **357** (1991) 65.
- [24] E. Braaten and R.D. Pisarski, Nucl. Phys. B **337** (1990) 569.
- [25] P. Aurenche *et al.*, Phys. Rev. D **58** (1998) 085003.
- [26] L.D. Landau and I.J. Pomeranchuk, Dokl. Akad. Nauk SSSR **92** (1953) 535; A.B. Migdal, Phys. Rev. **103** (1956) 1811.
- [27] P. Arnold *et al.*, JHEP **0112** (2001) 009.
- [28] J.D. Bjorken, Phys. Rev. D **27** (1983) 140.
- [29] T. Peitzmann and M.H. Thoma, Phys. Rept. **364** (2002) 175–246.
- [30] S. Turbide *et al.*, Phys. Rev. C **69** (2004) 014903.
- [31] D. d’Enterria and D. Peressounko, Eur. Phys. J. C **46** (2006) 451-464.
- [32] C-Y. Wong, High-Energy Heavy-Ion Collisions, World Scientific (1994).
- [33] M. Arneodo, Phys. Rept. **240** (1994) 301;
D.F. Geesaman *et al.*, Ann. Rev. Nucl. Part. Sci. **45** (1995) 337.
- [34] N. Armesto, J. Phys. G **32** (2006) R367–R394.
- [35] P. Amandruz *et al.*, Nucl. Phys. B **441** (1995) 3–11.
- [36] J.J. Aubert *et al.*, Phys. Lett. B **123** (1983) 275.

-
- [37] I. Iancu *et al.*, Nucl. Phys. A **692** (2001) 583;
E. Ferreiro *et al.*, Nucl. Phys. A **703** (2002) 489.
- [38] E. Iancu and R. Venugopalan, hep-ph/0303204 (2003).
- [39] J. Cronin *et al.*, Phys. Rev. D **11** (1975) 3105.
- [40] J. Adams *et al.*, Phys. Rev. Lett. **91** (2003) 072304.
- [41] Brookhaven National Laboratory, <http://www.bnl.gov>.
- [42] A. Bravar *et al.*, Nucl. Phys. A **755** (2005) 313c–361c.
- [43] H. Hahn *et al.*, Nucl. Instrum. Meth. A **499** (2003) 245–263.
- [44] T. Ludlam, Nucl. Instrum. Meth. A **499** (2003) 428–432.
- [45] T. Satogata *et al.*, proceedings of the 2003 Particle Accelerator Conference, Portland, Oregon, (2003).
- [46] M. Bai *et al.*, proceedings of the 2005 Particle Accelerator Conference, Knoxville, Tennessee (2005).
- [47] BNL accelerator division, <http://www.bnl.gov/cad/accelerator/>.
- [48] K.H. Ackermann, Nucl. Instrum. Meth. A **499** (2003) 624–632.
- [49] M. Anderson *et al.*, Nucl. Instrum. Meth. A **499** (2003) 659–678.
- [50] F. Bergsma *et al.*, Nucl. Instrum. Meth. A **499** (2003) 633–639.
- [51] Particle Data Group, <http://pdg.lbl.gov/>.
- [52] H. Bethe, Ann. Phys. **397** 3 (1930) 325–400.
- [53] M. Beddo *et al.*, Nucl. Instrum. Meth. A **499** (2003) 725–739.
- [54] F.S. Bieser *et al.*, Nucl. Instrum. Meth. A **499** (2003) 762–765.
- [55] B. Bonner *et al.*, Nucl. Instrum. Meth. A **508** (2003) 181–184.
- [56] O. Grebenyuk, Ph.D. dissertation, Utrecht University (2007).
- [57] S. Bennet *et al.*, STAR internal note 351 (1998).
- [58] E. Longo and I. Sestili, Nucl. Instrum. Meth. **128** (1975) 283;
Erratum-ibid. **135** (1976) 587.

-
- [59] S.A. Akimenko *et al.*, Nucl. Instrum. Meth. A **365** (1995) 92–97;
S.A. Akimenko *et al.*, Prib. Tekh. Eksp. N3 39 (1997).
- [60] O.D. Tsai, personal communication (2007).
- [61] C. Adler *et al.*, Nucl. Instrum. Meth. A **470** (2001) 488–499
- [62] J. Kiryluk, AIP Conference Proceedings **675** (2003) 424–428
- [63] J.M. Landgraf *et al.*, Nucl. Instrum. Meth. A **499** (2003) 766–777.
- [64] <http://www.rhic.bnl.gov/RCF/>.
- [65] C. Adler *et al.*, Nucl. Instrum. Meth. A **499** (2003) 778–791.
- [66] R.E. Kalman, Transactions of the ASME–Journal of Basic Engineering **82** series D (1960) 35–45.
- [67] A. Drees *et al.*, Proceedings of the Particle Accelerator Conference 2003, volume 3 (2003) 1688–1690.
- [68] J. Adams *et al.*, Phys. Rev. Lett. **91** (2003) 172302.
- [69] C. Adler *et al.*, Phys. Rev. Lett. **89** (2002) 202301;
B. Choi, Ph.D Dissertation, University of Texas (2003).
- [70] D. Kharzeev *et al.*, hep-ph/0212316;
L. Hulthén and M. Sagawara, Handbuch der Physik **39** (1957).
- [71] J.E. Gans, Ph.D. dissertation, Yale University (2004).
- [72] M. Cormier *et al.*, Nucl. Instrum. Meth. A **483** (2002) 734–746.
- [73] J. Adams *et al.*, Phys. Rev. C **70** (2004) 054907.
- [74] CERN program library, <http://cernlib.web.cern.ch/cernlib/>.
- [75] R. Brun and F. Carminati, Detector Description and Simulation Tool, GEANT v3.21, <http://wwwasd.web.cern.ch/wwwasd/geant/>.
- [76] F. Abe *et al.*, Nucl. Instrum. Meth. A **271** (1988) 387.
- [77] F. Abe *et al.*, Phys. Rev. D **48** (1993) 2998–3025.
- [78] M. Calderón de la Barca Sánchez, Ph.D. dissertation, Yale University (2001).

-
- [79] W.R. Leo, *Techniques for Nuclear and Particle Physics Experiments*, Springer-Verlag (1987)
- [80] V.L. Rykov, STAR internal note 301 (1997).
- [81] G.F. Knoll, *Radiation Detection and Measurement*, John Wiley and Sons (1979).
- [82] Mount Sinai, NY (11766), <http://www.wunderground.com/>
- [83] X-N. Wang and M. Gyulassy, *Phys. Rev. D* **44** (1991) 3501–3516.
- [84] A.A. Wetzler, Ph.D. dissertation, J.W. Goethe-University (2006).
- [85] G. Lin, personal communication (2007).
- [86] T. Sjostrand *et al.*, Pythia 6.3 physics and manual, hep-ph/0308153.
- [87] G.J. Alner *et al.*, *Z. Phys. C* **33** (1986) 1–6.
- [88] R.E. Ansorge *et al.*, *Z. Phys. C* **33** (1986) 175–185.
- [89] A. Fasso *et al.*, hep-ph/0306267.
- [90] J. Adams *et al.*, *Phys. Lett. B* **637** (2006) 161.
- [91] S. Frixione, *Phys. Lett. B* **429** (1998) 369;
S. Frixione and W. Vogelsang, *Nucl. Phys. B* **568** (2000) 60–92.
- [92] S.S. Adler *et al.*, *Phys. Rev. C* **75** (2007) 024909.
- [93] S.S. Adler *et al.*, *Phys. Rev. C* **75** (2007) 051902.
- [94] S.S. Adler *et al.*, *Phys.Rev.Lett.* **91** (2003) 241803.
- [95] P. Aurenche *et al.*, *Eur. Phys. J. C* **13** (2000) 347–355.
- [96] A. Abulencia *et al.*, hep-ex/0701051 (2007), *submitted to Phys. Rev. D*.
- [97] G. Abbiendi *et al.*, *Eur. Phys. J. C* **37** (2004) 25–47.
- [98] P. Aurenche *et al.*, *Eur. Phys. J. C* **9** (1999) 107–119;
http://wwwlapp.in2p3.fr/lapth/PHOX_FAMILY/readme_inc.html
- [99] M. Gluck *et al.*, *Phys. Rev. D* **48** (1993) 116;
Erratum-ibid. *D* **51** (1995) 1427.
- [100] S. Kretzer, *Acta Phys. Polon. B* **36** (2005) 179–186.

-
- [101] D. de Florian *et al.*, Phys. Rev. D **76** (2007) 074033.
- [102] S. Albino *et al.*, Nucl. Phys. B **725** (2005) 181–206.
- [103] S. Kretzer, Phys. Rev. D **62** (2000) 054001.
- [104] J. Adams *et al.*, Nucl. Phys. A **757** (2005) 102.
- [105] I. Arsene *et al.*, Nucl. Phys. A **757** (2005) 1.
- [106] B.B. Back *et al.*, Nucl. Phys. A **757** (2005) 28.
- [107] K. Adcox *et al.*, Nucl. Phys. A **757** (2005) 184.
- [108] S.S. Adler *et al.*, Phys. Rev. Lett. **91** (2003) 072303.
- [109] S.S. Adler *et al.*, nucl-ex/0610036 (2006), *submitted to Phys. Rev. Lett.*
- [110] P. Levai *et al.*, nucl-th/0306019
- [111] K. Eskola *et al.*, Eur. Phys. J. C **9** (1998) 61–68.
- [112] S.S. Adler *et al.*, Phys. Rev. Lett. **98** (2007) 012002.
- [113] R.J. Fries *et al.*, Phys. Rev. Lett. **90** (2003) 132301.
- [114] G. Bunce *et al.*, Ann. Rev. Nucl. Part. Sci. **50** (200) 525–575.
- [115] D. Acosta *et al.*, Phys. Rev. D **65** (2002) 112003.
- [116] V.M. Abazov *et al.*, Phys. Rev. Lett. **87** (2001) 251805.
- [117] B. Abbott *et al.*, Phys. Rev. Lett. **84** (2000) 2786–2791.
- [118] L. Bourhis *et al.*, Eur. Phys. J. C **2** (1998) 529–537.
- [119] P. Aurenche *et al.*, Phys. Rev. D **73** (2006) 094007.
- [120] L. Apanasevich *et al.*, Phys. Rev. D **70** (2004) 092009.
- [121] M. McLaughlin *et al.*, Phys. Rev. Lett. **51** (1983) 971.
- [122] J. Badier *et al.*, Z. Phys. C **31** (1986) 341.
- [123] D. Peressounko *et al.*, Nucl. Phys. A **783** (2007) 577–582.
- [124] M.M. Aggarwal *et al.*, Phys. Rev. Lett. **85** (2000) 003595.
- [125] S.S. Adler *et al.*, Phys. Rev. Lett. **94** (2005) 232301.